



HAL
open science

Synthesis and characterizations of 2D nanoparticles with controlled folding for circularly polarized optical properties

Jiunn Hong Po

► **To cite this version:**

Jiunn Hong Po. Synthesis and characterizations of 2D nanoparticles with controlled folding for circularly polarized optical properties. Material chemistry. Université Paris sciences et lettres, 2023. English. NNT: 2023UPSL047 . tel-04458939

HAL Id: tel-04458939

<https://pastel.hal.science/tel-04458939>

Submitted on 15 Feb 2024

HAL is a multi-disciplinary open access archive for the deposit and dissemination of scientific research documents, whether they are published or not. The documents may come from teaching and research institutions in France or abroad, or from public or private research centers.

L'archive ouverte pluridisciplinaire **HAL**, est destinée au dépôt et à la diffusion de documents scientifiques de niveau recherche, publiés ou non, émanant des établissements d'enseignement et de recherche français ou étrangers, des laboratoires publics ou privés.



THÈSE DE DOCTORAT

DE L'UNIVERSITÉ PSL

Préparée à l'Ecole Supérieure de Physique et de Chimie Industrielles de la Ville de Paris, Laboratoire de Physique et d'Etude des Matériaux (UMR 8213)

Synthesis and characterizations of 2D nanoparticles with controlled folding for circularly polarized optical properties

Synthèses et caractérisations des nanoparticules 2D à enroulement contrôlé pour des propriétés optiques circulairement polarisées

Soutenue par

Hong PO

Le 16/10/2023

École doctorale n°397

Physique et Chimie des Matériaux

Spécialité

Chimie des Matériaux

Composition du jury :

José BICO Professeur, ESPCI Paris	<i>Président</i>
Thierry GACOIN Directeur de Recherche, Ecole Polytechnique	<i>Rapporteur</i>
Myrtil KAHN Directrice de Recherche, Université de Toulouse	<i>Rapporteuse</i>
David NORRIS Professeur, ETH Zürich	<i>Examineur</i>
Sandrine ITHURRIA Maître de Conférences, ESPCI Paris	<i>Directrice de thèse</i>

“ Thank you, next. ”

Ariana Grande

ECOLE SUPÉRIEURE DE PHYSIQUE ET DE CHIMIE INDUSTRIELLES DE LA VILLE DE
PARIS

Abstract

Laboratoire de Physique et d'Études de Matériaux

Doctor of Science

Synthesis and characterizations of 2D nanoparticles with controlled folding for circularly polarized optical properties

by Hong PO

Belonging to II-VI semiconductors, cadmium chalcogenide nanoplatelets exhibit narrow optical features in the visible region. These particles can measure up to hundreds of nanometers in length and width, while presenting a few nanometers along their quantum confined thickness direction. During surface functionalization of ligands onto these ultra-thin nanosheets, residually stressed bodies are created. This originates from the mismatch between the inorganic crystal lattice and layer of anchoring atoms, in addition to the steric repulsion brought by aliphatic chains. These three acting components are captured via a quantitative mechanical analysis to result in a model that allows for the prediction of curling in nanoplatelets. The resulting nanohelices radii are shown to be able to be tuned by linearly varying the associated organic chain lengths, for a given thickness population of nanoplatelets. Despite the important surface stress induced by thiolate headgroups, the average in-plane lattice parameter of these nanocrystals remains equal to that of zinc blende bulk as demonstrated experimentally and theoretically by wide-angle X-ray diffraction. Specific orientation of these anisotropic and distorted objects reflects an impact on the form and intensity of their corresponding scattered peaks.

Ways to obtaining cadmium chalcogenide nanoplatelets that display chiroptical properties in absorption are addressed. The most promising route consists in substituting pristine surface achiral carboxylates by chiral enantiomers of tartaric acid. The dissymmetry values appear to increase with the number of stereocenters and show much stronger polarized signals with carboxylate than thiolate functional groups. These absorptive-like line shapes associated to the excitonic transition wavelength of the inorganic core, result from a hybridization effect between their hole level and the ligands' molecular orbital. On the other hand, gold decorated chiral silica helices, synthesized from the benefit of the gemini surfactant molecules' self-assembly, are also capable of exhibiting circular dichroism in their plasmon resonance region. This increases with the strength of the interparticle plasmonic coupling, in agreement with simulations performed under discrete dipole approximation. An opening towards sorting chiral objects via optoacoustophoresis is documented. This proof-of-concept demonstrates distinct average in-plane migration speeds between separate chiral moieties, as a function of the acoustics and optical working conditions. The effect of particles' shape and concentration in solution show that upon jamming, an object's compressibility can lead to self-organizing behaviors similarly to cases of active matters, bacteria and cells.

Acknowledgements

“Thanks, thanks, thanks...” a word that has been much repeated to express my deepest gratitude over the course of my doctoral studies. To the greatest extent, I owe my supervisor Sandrine the highest form of recognition. I have always appreciated her support, valued the discussions that we have had, treasured her enormous sense of humor and kept thoughts of her willingness to push us to be at our best state. Among many other things that I will carry along with me leaving this laboratory, is certainly the recipe to her legendary chestnut chocolate cake!

At the same time, food topics have always had their fair share of being the most discussed subject during meet-ups. I cherish Nicolas for his infamous source of piping hot stories coming straight out from the Dean Office’s oven, Alexandra for her ever-lasting kindness that shines through her smile, Thomas for his never-ending helpfulness that always manages to find time for those in need and Céline for her cheerful youthfulness that drives the bonding of the whole gang. Needless to state, there is Xiangzhen who has since ages been in the picture, well-known for her generosity and over-flooding cuteness which exceed her reputation.

Y’all could not believe the chance I have got to collaborate with other amazing researchers, notably from the PMMH laboratory. A huge shoutout to Benoît R., Étienne and José who have actively contributed to the very beginning of my work. I had the pleasure to meet Benoît B. from IMPMC who has also lent us a hand. Not forgetting Jean-Luc, Mauricio, Ludovic and Jean for willingly opening up their doors, to try out certain of my crazy ideas. Nevertheless, I thank many other people with whom I have interacted over the course like Anthony, Lucas, Isabelle, Nathan, Jérôme, Bruno and Mohamed.

Looking up to those students who have previously graduated, I was fortunate enough to be in their good hands upon my arrival at LPEM. Among which, the geeky Antoine H. with his all-rounded knowledge, the fabulous Sheila bella with her French raps and ever-present ears for others, the man Mogha best known for his level-headedness, plus composed personality in every single situation and the bro Subha who shines through his quirkiness and unbeatable integration ability. Then, the two queens of their class, we have the bubbly Fanny and the impeccable Sophia. Alongside them, I have had my tears and joy pouring my heart out over afternoon teas and countless other alcoholic beverages.

On and off, up and down, no one understands my PhD journey better than my fellow NPLs teammates. Herein, Coco the lead of the herd, demonstrates such leadership by guiding others with a tremendous amount of detailed care. I thank him from the bottom of my heart for putting up with my crap over these past years and the number of times where I got excessively tipsy, sat on his bed and somehow, ended up spending the night without recalling what happened. Speaking of formerly mentioned queens, we have got two adorable, yet feisty princesses: Lina and Ningyuan. It seems to me as if we have known each other since the previous lifetime and I hold them both close like little sisters that I have never had. There come the star prodigies: Henri and Leo, for wonderfully showing up in our group. Their spontaneous, charming and warm addition no doubt shakes up the dynamics into forming a more cohesive one.

Running down the list, I am deeply blessed to have shared my last three years with other mates who have together started our journey as doctoral students. Yuzhou, who

has painted an unfazed and serene image of him ever since the beginning, exhibits such ease steering through his way in the laboratory. I cherish every single moment we have gone through, from spending most Wednesday nights learning Japanese to our huge excursion in California, where I was literally sick like a dog. From the optical team, it was thrilling to meet Mathias and Charlie. It appears exceedingly easy to approach and engage with these welcoming bunch. Needless to say, their carefree and easy-going traits leave an important footprint on my general way of acting and I am forever grateful for them.

Soon after, the arrival of newbies ought to carry on our laboratory traditions as the renewal of young blood. At all times, I have appreciated the outspokenness of Alice and her blunt points of view. She would have made a staggered presence if she were not to have moved. Nour a.k.a. my sassy baby girl, partner in crime, perfect-pitched karaoke duet and the list goes on, crossing the finishing line of my thesis would not have been possible without having her genuine presence around. I enjoy each memorable in- and out-of-the-office minute with her and still could not believe how her ears remain intact after all my constant venting, whining and let's not forget about the series of spamming of Instagram shorts during late nights.

Without the presence of interns, clearly my work would have been less fruitful. In this perspective, Antoine A. came in as my first while exuding a complete independence and became rapidly proficient in his tasks. Second shoutouts to Henri and Jean, who were equally proactive, for the honor, excitement and gratification working alongside them both. Furthermore, the comes-and-goes include Edwige, Pierre, Méline, Pauline, Nicolas, Juichi and Simone. Especially remarkable highlights are allocated to Sanya, Beatrice and Antony for simply being extraordinary as themselves. We had the immense pleasure to bond over a shared office, that swiftly became a safe place where we were able to talk freely and I would not have given in to anything in exchange for you people.

Independently of the laboratory, my closest friends definitely represent several fundamental pillars of my journey up to this point. Dating back to preparatory classes, Clément F. and Justin have been supportive and protective as always. This translates precisely into the purest form of exhilaration by looking back after these years, how far we have navigated and blossomed. Let's not get confused with the other Clément bibi, who understands me accurately inside out as much as Laëtitia and Gabriel. The ESPCI experience would have been a complete noxious and unlivable disaster in their absence. Nowadays, I am truly adjusted to seeing Edouard and Yuna on a near daily basis, which I hope would not come as a shock when I finally move out. I thoroughly treasure all the splendid and quality time that we have had, no surprise they are delightful.

Family has, on all occasions and levels, played a key role in my life ever since I took my first breath. Even though I might talk lightly and rarely of them, knowing that my father and sisters have got my back means the whole world to me. Despite our physical distance, there are aspects that I could not imagine living in a universe without them.

Towards the end of this lengthy monologue, I would like to dedicate much attention to Luc. This person stood along, endured some of my harshest words, accompanied me through hardships and explored jointly unseen places, that ultimately taught us lifelong lessons mutually. It is unthinkable to relive these instants in each other's absence and let's see what the future holds!

Overview

For about a decade, it has been possible to fabricate televisions with QLED, which stands for Quantum Dots Light Emitting Diode. This refers to a type of display technology which uses tiny particles which emit different hues when hit by light sources, for more vibrant and fine color displays than traditional LED televisions. The insertion of quantum dots that possess exceptional optical properties in terms of absorption and emission within these flat screens, is executed in the form of films. These particles were first synthesized in 1993 by the Bawendi group. The authors reported the first organometallic synthesis of colloidal quantum dots of cadmium chalcogenide CdE, where E = S, Se, Te. These spherical nanoparticles exhibited unprecedented monodispersity in solution and possessed at least one of their dimensions smaller than the Bohr radius, implying that their optical properties were directly size-related.

Over time, numerous groups have optimized the synthesis of II-VI semiconductor nanocrystals. Significant efforts have been notably made to create nanocrystals with different morphologies. In 2006, the Hyeon group developed the first synthesis of wurtzite CdSe nanoribbons with a thickness in the order of nanometers and lengths up to several hundred nanometers. Then in 2008, Ithurria *et al.* synthesized colloidal zinc blende CdSe nanosheets for the first time and these latter were subsequently named nanoplatelets, exhibiting controllable thickness down to the scale of atomic monolayers. Given that the quantum confinement effect only applied along the direction of their thickness, the associated optical properties presented fine spectral features.

The combination of a high absorption cross-section and a short radiative recombination time renders II-VI semiconductor nanoplatelets interesting for applications as diodes and lasers. Among which, CdSe is the most extensively studied candidate and its direct synthesis leading to different thicknesses have been reported. Herein, this thesis addresses rather nanoplatelets with defined helical morphologies and their characterizations to yield chiroptically active materials. Circular dichroism spectroscopy is a technique that has found diverse applications in studying the properties of helical objects due to their inherent asymmetry. For instance, this spectroscopy tool has proven useful for chiral sensing and analysis with chiral molecules. It also provides valuable insights into the structural and conformational changes of a chiral absorbing medium and in particular, dealing with nanoparticle-ligand interactions.

Herein, the manuscript is divided into five following chapters:

- Chapter 1 introduces the idea of two-dimensionally shaped semiconductor nanoplatelets. The synthesis leading to these atomically defined materials, whose optical properties are essentially controlled through their thickness will be discussed. The occurrence of curling that results from these ultrathin flexible sheets will be elucidated as a link to their surface chemistry. Finally, we will detail the different routes toward building inorganic chiral structures, going from an individual single particle level to supramolecular assemblies.
- Chapter 2 demonstrates the ability of cadmium-based nanoplatelets to react promptly as flexible substrates for the self-assembly of surface ligands. The reason for which these quantum particles curl into nanohelices will be explained from a mechanical

point of view, which originates from the adsorption of molecules onto their outer surface. This part also highlights the structural studies made by using X-ray diffraction on highly distorted anisotropic objects.

- Chapter 3 explores various methods capable of synthesizing chiral cadmium selenide nanoplatelets. Strategies that include symmetry-breaking in terms of geometry and ligand exchange by chiral compounds will be shown. In particular, the adequate choice of a ligand candidate that allows an efficient coupling with the inorganic core will be addressed, via its molecular structure and chemical composition. This work also underlines the dependence of dissymmetry factors on their exchange rate, as evidenced by distinct characterization techniques.
- Chapter 4 reveals another system based on hybrid gemini surfactant-silica that is fabricated under its pure enantiomeric form. The use of this matrix to host incoming guests of different natures will be displayed. A proof-of-concept to sort chiral objects built on opto-acoustophoresis will be presented. This constitutes a contactless means to selectively promote the migration speed of either population of chiral moieties in suspension, under simultaneous opto- and acousto-perturbations.
- Chapter 5 summarizes the main findings from these previous chapters. A list of perspectives that still represents on-going work in our research group will be discussed, that would undoubtedly require further effort and understanding.

Contents

Abstract	iii
Acknowledgements	v
Overview	vii
1 Introduction	1
1.1 Two-dimensional semiconductor nanocrystals	1
1.1.1 Generalities	1
Charge carriers description	1
Quantum confinement effect	2
Quantum well description	3
1.1.2 Colloidal cadmium chalcogenide NPLs	4
Crystalline structure	4
Surface-stabilizing ligand shell	5
Surface stresses due to ligand footprint	6
Optical properties	7
Mechanical analogs	8
1.1.3 Synthesis of colloidal nanoparticles	8
Hot-injection synthesis leading to the discovery of NPLs	10
Growth mechanism of anisotropic NPLs	11
Post-synthetic ways to size-control NPLs	13
1.2 Inorganic chiral materials	16
1.2.1 Characterization of chirality	16
CD formalism	16
Conceptualizing a CD spectrometer	18
1.2.2 Introducing chiral semiconductor nanocrystals	19
Intrinsic chiral defects	19
Nonracemic ensemble of chiral geometries	20
Shell of chiral surface ligands	21
Hierarchical chirality	23
1.2.3 Mechanical sorting of chiral objects	24
Acoustophoresis formalism	25
Primary force	26
Secondary forces	26
Established examples in microfluidics	29
1.3 Conclusion	32
2 Folding of nanoplatelets	35
2.1 Studies on CdSe homostructures	36
2.1.1 Modifications of surface chemistry	36
Structural details within a helix	40
2.1.2 Mechanical modeling of bending	42

	Two considered misfit layers	43
	Three considered misfit layers	46
2.2	Extension onto core-only CdS and core-shell CdSe-CdS	49
2.2.1	CdS homostructures	49
2.2.2	CdSe-CdS heterostructures	50
2.2.3	Validation of mechanical model	52
2.3	Structural implications of anisotropic objects	54
2.3.1	XRD of flat undistorted NPLs	56
2.3.2	Scattering of curved nanohelices	58
2.3.3	Bypass between simulation and experimental data	60
2.4	Conclusion	64
3	Chiral imprints on nanoplatelets	65
3.1	Effect of particles' shape	66
3.1.1	Studies on uniquely-shaped 3 MLs CdSe NPLs	67
	Factors leading to shape-selective synthesis	67
	Observations under CD	68
3.1.2	Further investigations on 4 MLs	69
	Observations under CD	70
	Enantiomeric excess assessment	70
3.2	Direct ligation with chiral compounds	72
3.2.1	Thiol functional groups	72
	Cysteine molecules	72
	Dithiothreitol molecules	75
3.2.2	Carboxylic functional groups	77
	Tartaric acid molecules	77
	Malic acid molecules	81
	Characterizations of exchanged surface ligands	86
3.3	Surface modification with halides	88
3.3.1	Two-steps ligand exchange towards ibuprofen molecules	89
	Characterizations on 3 and 4 MLs CdSe NPLs	89
	Extension onto different shapes of 3 and 4 MLs structures	94
3.4	Conclusion	97
4	Tribrid silica-based chiral helices	99
4.1	Synthesis of surfactant-silica helices	100
4.1.1	Self-assembly of gemini surfactants	100
4.1.2	Surface patterning with CdSe NPLs	104
4.1.3	Functionalization with gold nanoparticles	106
	CD properties of tribrid surfactant-silica-gold structures	108
	Simulation of plasmonic CD under discrete dipole approximation	114
	Validation on a single and aligned particle(s)	116
	Effect of gold nanoparticles' size with respect to the helical substrate	118
4.2	Manipulating fluorescently-labelled silica objects	120
4.2.1	Setting up samples and opto-acousto resonator	121
4.2.2	Tracking of particles under migration	123
	Influence of illuminated light intensity	124
	Influence of dilution	126
	Influence of particles' shape	127
4.3	Enhanced-aggregation phenomenon under opto- and acousto-coupling	130
4.3.1	Electric field and heat transfer simulations	130

4.3.2	Choice of materials and geometry of objects	131
4.3.3	Influence of individual particle's size and number	133
4.4	Conclusion	136
5	Conclusions et perspectives	137
5.1	Conclusions	137
5.2	Perspectives	139
A	Publications and communications	143
B	Materials and Methods	145
C	Folding of nanoplatelets	155
D	Chiral imprints on nanoplatelets	161
E	Tribrid silica-based chiral helices	169
	Bibliography	173

List of Abbreviations

Ac	Acetates
APTES	3-aminopropyl-triethoxysilane
ARF	Acoustic Radiation Force
c-ALD	Colloidal Atomic Layer Deposition
CD	Circular Dichroism
CPL	Circularly Polarized Light
D	Dextrogyre
DFT	Density Functional Theory
DNA	Deoxyribonucleic Acid
DFT	Density Functional Theory
EDX	Energy Dispersive X-ray
FITC	Fluorescein Isothiocyanate
FTIR	Fourier Transform Infrared
FWMH	Full Width at Mid-height
hh	heavy hole
HAADF	High-angle Annular Dark-field
HOMO	Highest Occupied Molecular Orbital
HRTEM	High-resolution Transmission Electron Microscope
L	Levogyre
lh	light hole
LUMO	Lowest Unoccupied Molecular Orbital
MLs	Monolayers
MPTMS	3-mercaptopropyl-trimethoxysilane
NMR	Nuclear Magnetic Resonance
NPLs	Nanoplatelets
OA	Oleates
ODE	1-Octadecene
OLam	1-Oleylamine
PDMS	Poly Dimehtylsiloxane
PEM	Photoelastic Modulator
PVP	Polyvinyl Pyrrolidone
SEM	Scanning Electron Microscope
STEM	Scanning Transmission Electron Microscope
so	spin orbit
TEM	Transmission Electron Microscope
UV	Ultraviolet
QDs	Quantum Dots
XRD	X-ray Diffraction

Physical Constants

Boltzmann constant	$k_B = 1.38 \times 10^{-23} \text{ J K}^{-1}$
Dynamic viscosity of water	$\eta = 0.9 \times 10^{-3} \text{ kg m}^{-1} \text{ s}^{-1}$
Electron mass	$m_e^* = 9.11 \times 10^{-31} \text{ kg}$
Elementary charge	$e = 1.60 \times 10^{-19} \text{ C}$
Planck's constant	$h = 6.63 \times 10^{-34} \text{ kg m}^2 \text{ s}^{-1}$
Vacuum permittivity	$\epsilon_0 = 8.85 \times 10^{-12} \text{ F m}^{-1}$

List of Symbols

a	particle's dimension under quantum confinement	m
A	absorbance	-
c	speed of sound	m s^{-1}
d	particle's diameter	m
D_r	rotational diffusion coefficient	s^{-1}
E	energy (resp. Young's modulus)	J (resp. $\text{kgm}^{-1}\text{s}^{-2}$)
f	time frequency	s^{-1}
F	force	kgms^{-2}
G	free energy	J
h	thickness	m
I	intensity	A
k	wavevector	m^{-1}
L	length	m
m	particle's mass	kg
n	carbon number	-
p	pitch	m
r	particle's radius	m
t	time	s
T	temperature	K
V	potential	V
w	width	m
x	position along Cartesian x -axis	m
y	position along Cartesian y -axis	m
z	position along Cartesian z -axis	m
α	tilt angle (resp. deformation)	rad (resp. -)
β	compressibility	$\text{kg}^{-1}\text{ms}^2$
γ	shear rate	s^{-1}
Γ	free energy per unit surface	Jm^{-2}
ϵ	permittivity (resp. strain)	F m^{-1} (resp. -)
η	dynamic viscosity	$\text{kgm}^{-1}\text{s}^{-1}$
θ	ellipticity	rad
κ	curvature	m^{-1}
λ	wavelength	m
ρ	density	kgm^{-3}
σ	absorption cross-section	m^2
τ	relaxation time	s
ϕ	helical angle	rad
φ	rotation angle in the xy -plane	rad
ψ	wavefunction	-
ω	angular frequency	s^{-1}

Chapter 1

Introduction

1.1 Two-dimensional semiconductor nanocrystals

In this first part of introduction, the generalities and state of art for II-VI semiconductor nanoplatelets will be presented. This concerns in majority the characteristics of cadmium selenide, which is the body of our work. The properties in terms of physico-chemistry of these nanocrystals obtained through colloidal synthesis will be discussed, which has mainly led to their morphology and size control under the quantum confinement regime. Through the leverage of this concept, helical nanoplatelets (NPLs) with large lateral sizes, herein also noted as nanohelices, have been synthesized and thoroughly investigated. By making use of their inorganic lattice core with respect to the coordination of organic ligands, the importance of surface chemistry play in such colloidal systems will be outlined.

1.1.1 Generalities

Widely known semiconductor materials, from the point of view of solid state physics, are objects possessing an electron-rich valence band and a conduction band, separated by an energy gap (Fig. 1.1). This energy gap dictates the overall electrical conductivity behavior of an object, as it constitutes a barrier between electron-hole pairs, also called excitons. In presence of an external source like heat or electromagnetic excitations whose energy input is superior or equal to the gap, this enables the transit of an initial electron from the valence band into the conduction band, by hereby creating and leaving behind a hole. The bound state of an electron and a hole interacting via Coulomb force constitutes then a quasiparticle, named as exciton that can move through the medium for energy transport. Upon relaxation, the electron-hole pair recombines radiatively along the band edges by emitting a photon, which gives rise to the photoluminescence properties of such materials for applications in optoelectronics and solar-harvesting cells [1, 2, 3].

Charge carriers description

Due to the Coulombic attraction existing between the electron and the hole of an exciton, the internal states of a semiconductor nanocrystal is analogous to those of the hydrogen atom, where some of the lower energy states lie below the conduction band by a difference equivalent to its exciton binding energy. For a weakly bound exciton, the electron-hole distance is larger than the lattice constant of the crystal and the exciton is delocalized over several atoms. The Mott-Wannier solution, similar to the hydrogen atom problem, treats this two-particles weakly interacting system with an effective Hamiltonian to yield an expression of the exciton Bohr radius given by [4]:

$$a_0 = \frac{4\pi\epsilon_0\epsilon_r\hbar^2}{e^2} \left(\frac{1}{m_e^*} + \frac{1}{m_h^*} \right) \quad (1.1)$$

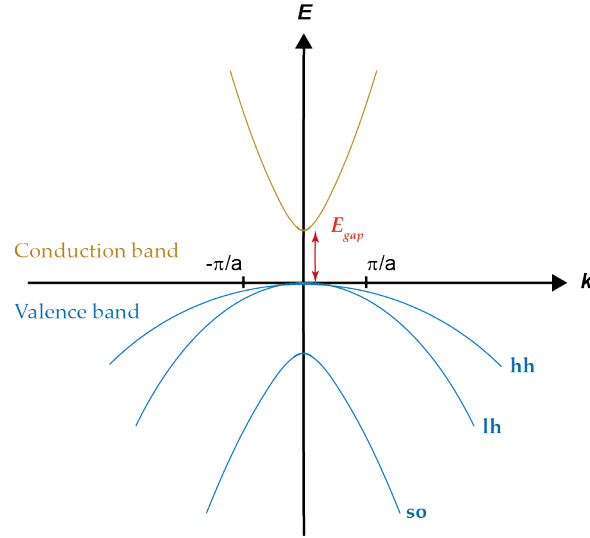


FIGURE 1.1: Band structure of bulk semiconductor CdSe, where the valence and conduction bands are separated by an energy gap. For $k \neq 0$, three-fold degeneration of the valence band leads to the appearance of subbands, named as heavy hole (hh), light hole (lh) and spin orbit (so).

where ϵ_0 is the vacuum permittivity, ϵ_r the material's dielectric constant, \hbar the reduced Planck constant, e the elementary charge, m_e^* the electron mass and m_h^* the hole mass.

In other words, this length scale characterizes the average distance between the electron-hole pair and varies differently for distinct cadmium chalcogenides (Tab 1.1).

Composition	CdS	CdSe	CdTe
Bohr radius (nm)	2.8	5.6	7.5

TABLE 1.1: Values of Bohr radius for bulk semiconductor cadmium chalcogenides. Adapted from [5].

Quantum confinement effect

When it comes to semiconductor crystals on a nanoscale, where at least one of their dimensions a in real space is inferior to the magnitude of its associated Bohr radius, the exciton is said to be quantum confined. The eigenfunctions of the electron and the hole, written as a product of an envelope function and a lattice periodic function, becomes confined in an environment that is smaller than its characteristic size a_0 [6, 7]. As a result in reciprocal space, the transit of the electron from the valence band into the conduction band occurs with a momentum that scales to $\frac{\pi}{a}$. This leads therefore to the discretization of each level in terms of transition energies, in contrary to bulk semiconductors that are composed of two continuous densities of states in their valence and conduction bands (Fig. 1.2).

Via precise and controlled chemical synthesis over the years, it has been reported that different degrees of quantum confinement can be achieved for these cadmium-based semiconductor nanocrystals by finely tuning their morphology. The most common case is reported for spherical quantum dots that experience a three-dimensional confinement [8]. Whereas, examples of two-dimensional confinement can be found for nanorods [9]. Herein, NPLs that

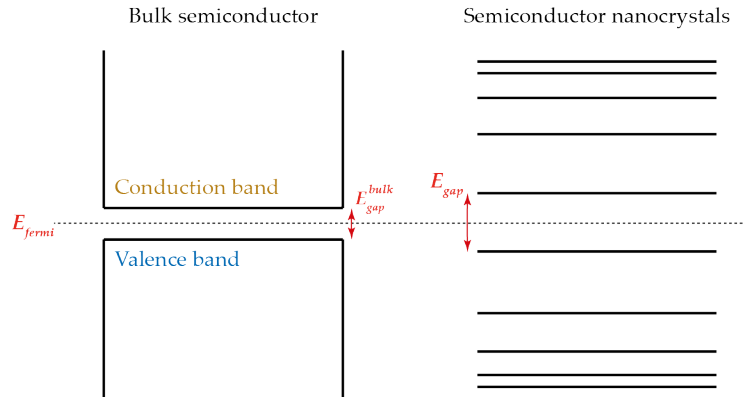


FIGURE 1.2: Effect of nanometric downscale of a bulk semiconductor. The initial energy continuums constituting both the valence and conduction bands discretize into step-like energy levels.

are assimilated to quantum wells possess a one-dimensional confinement since the dimension along their thickness direction \vec{z} only is inferior to the Bohr radius, while presenting an infinitely large lateral facet in the xy -plane as depicted by Fig. 1.3 [10, 11].

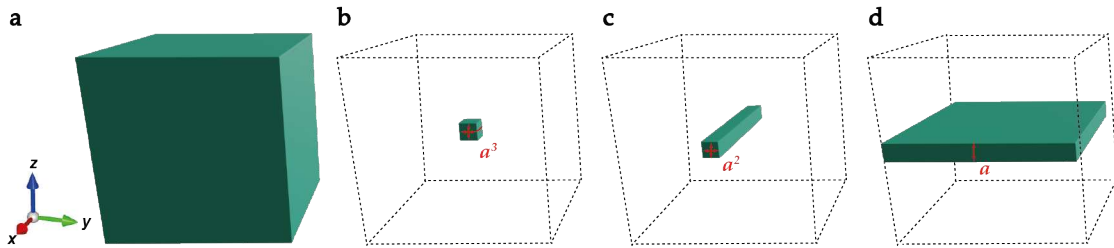


FIGURE 1.3: Various degrees of quantum confinement resulting from the nanometric downscale of (a) a bulk semiconductor. This leads to (b) quantum dots in the case of a three-dimensional confinement, (c) nanorods that experience a two-dimensional confinement along the yz -plane and (d) nanoplatelets that are solely confined along their thickness \vec{z} direction.

Quantum well description

The simplest model for this phenomenon is to consider an infinite potential well in a one-dimensional system. A particle may only travel upward or downward with impenetrable barriers on both ends. The walls of such one-dimensional box may be seen as regions of space with an infinitely large potential energy. Conversely, the interior of the box has a constant, zero potential energy for free-moving particles. The wavefunction ψ containing measurable properties of a particle like its position, momentum and energy can be obtained by solving the Schrödinger equation for this described system:

$$i\hbar \frac{\partial}{\partial t} \psi(z, t) = -\frac{\hbar^2}{2m} \frac{\partial^2}{\partial z^2} \psi(z, t) + V(z) \psi(z, t) \quad (1.2)$$

where m is the particle's mass, i the imaginary unit and t the time.

Inside the box, zero forces act upon the particle and therefore, the wavefunction oscillates through space and time with the exact form of a free particle:

$$\psi(z, t) = [A \sin(kz) + B \cos(kz)] \cdot e^{-i\omega t} \quad (1.3)$$

where A and B are arbitrary complex numbers, k the wavenumber and ω the angular frequency of the oscillations. These are both related to the total energy of the particle given by the expression:

$$E = \hbar\omega = \frac{\hbar^2 k^2}{2m} = n^2 \frac{\hbar^2 \pi^2}{2ma^2} \quad (1.4)$$

where n is a whole number and this constitutes the dispersion relation of a free particle.

Indeed, one notices that a discrete set of energy values and wavenumbers are only allowed for the computation. Finally, the previously unknown constant A may be found by normalizing the wavefunction in a fashion that the total probability density of finding the particle in the system be 1 ($\int_0^a |\psi(z)|^2 dz = 1$). This gives $|A| = \sqrt{\frac{2}{a}}$ and yields ultimately the spatial part of the wave function as:

$$\psi_n(z) = \begin{cases} \sqrt{\frac{2}{a}} \sin(k_n z) & \text{for even } n \\ \sqrt{\frac{2}{a}} \cos(k_n z) & \text{for odd } n \end{cases} \quad (1.5a)$$

$$\quad (1.5b)$$

Herein for semiconductors, the two respective charge carriers that are distinct in terms of associated wavefunction are to be taken into account. Thus, the bandgap energy in these one-dimensionally confined semiconductor nanocrystals, can be expressed as the sum of the bandgap energy of the bulk material, the confinement energy of the electron and the hole, plus their Coulombic interaction. In the case of spherical quantum dots (QDs), this expression writes as [12]:

$$E_{gap} = E_{gap}^{bulk} + \frac{\hbar^2 \pi^2}{2m_e^* a^2} + \frac{\hbar^2 \pi^2}{2m_h^* a^2} - 1.8 \frac{e^2}{\epsilon_r a} \quad (1.6)$$

1.1.2 Colloidal cadmium chalcogenide NPLs

This following section details the structure of these cadmium-based semiconductor NPLs, from the description of their inorganic core to the surface-stabilizing ligand shell. The effect of anchoring ligands onto these ultrathin nanosheets will notably be highlighted. In addition to discussing their resulting morphology, the induced consequence on the optical properties will also be presented. This point, later on, gives rise to the appearance of nanohelices, which are large wide pieces of NPLs with a well-defined principal curvature and a certain handedness.

Crystalline structure

Cadmium chalcogenide nanocrystals can crystallize as either cubic zinc blende or hexagonal wurtzite structures, depending on the experimental conditions during synthesis [10, 11]. It has been shown that in the case of bulk semiconductor CdSe for instance, the energy gap differed between these two crystal structures and gave 1.66 eV as cubic zinc blende (resp. 1.74 eV as hexagonal wurtzite) [13]. In this manuscript, the body of our work concerns that of the cubic zinc blende, whose unit cell is made up of two face-centered sublattices represented by cadmium and chalcogen, offset from one another by a quarter of its lattice

parameter (Fig. 1.4). Hereby, the associated space group is $F\bar{4}3m$.

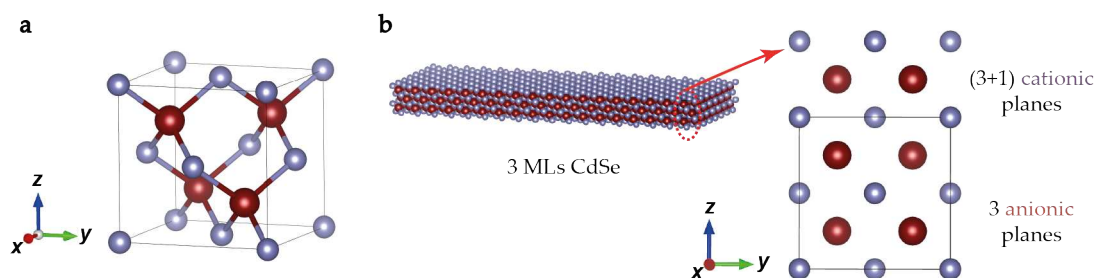


FIGURE 1.4: (a) Unit cell of a cadmium chalcogenide crystalized as cubic zinc blende structure. (b) An example of 3 MLs CdSe, possessing 3 anionic planes and (3+1) cationic planes.

The atomic planes of cadmium and chalcogen situate alternately along the NPLs' short axis, or in other words, along the [001] direction of its cubic crystal structure. Under this manner, NPLs are defined in terms of number of atomic layers that constitute their thickness. A so-called N MLs is composed of N planes of chalcogen and $(N+1)$ planes of cadmium. Therefore, the top and bottom wide facets possess an identical chemical composition, which is both metal-rich.

Surface-stabilizing ligand shell

Since there is a presence of one extra cationic plane than the anionic ones, this results in an excess of global positive charges on the surface of a NPL. Therefore, the intervention of ligands in solution is necessary on one hand, to guarantee the charge neutrality of the material itself and on the other, to ensure the colloidal stability of these nanoparticles suspended mostly in organic solvents. Due to their anisotropic shape compared to spherical QDs, the top and bottom wide facets of NPLs constitute in huge majority their outer exposed surface. These basal planes can be extended over thousands of nm^2 on a single-particle level and the stabilizing layer of ligands can be viewed as a process of self-assembly of organic molecules onto an inorganic nanosubstrate, rendering these quantum objects interesting candidates for a precise surface chemistry play.

According to the formalism of existing covalent bonds on organometallic complexes and as suggested by Owen and co-workers about its application onto nanocrystals, three categories of ligands have been classified as either L , X or Z type [14, 15, 16]. In the first case, neutral L -ligands possessing a free doublet, are capable of bringing in two electrons together to create a bond with a surface metal atom. Examples from this family of ligands are found to be amines and phosphines, which stabilize neutral facets like the (1 1 0) ones in a cubic zinc blende structure. Whereas, single-electron donors X -ligands form only covalent bonds when the surface metal atoms themselves contribute one too during the course. These include carboxylates, halides, phosphonates and thiolates which bind to facets exhibiting dangling bonds like the (0 0 1) and (1 1 1) ones. While the neutral electron-accepting Z -ligands act like Lewis acids to passivate surfaces that are analogue to Lewis bases, such as chalcogenide rich crystal facets.

As cubic zinc blende NPLs present an additional cationic plane compared to the chalcogenide ones, in average one X -ligand is needed to passivate one surface cation. Under typical experimental conditions, carboxylates originating from the introduced metal precursors,

constitute the native ligands that are used to stabilize these nanocrystals in a nonpolar solvent upon synthesis.

Surface stresses due to ligand footprint

As mentioned, the associated space group of these cadmium-based NPLs is $F\bar{4}3m$, which translates into the presence of a four-fold rotoinversion axis along their thickness direction. Therefore, the chemically equivalent top and bottom metal-rich wide facets as seen beforehand, are in fact rotated by 90° from one another. This implies that the way the surface ligands are bound onto the basal planes remains identical, however these latter, from a structural point of view, are shifted by 90° from one another (Fig. 1.5).

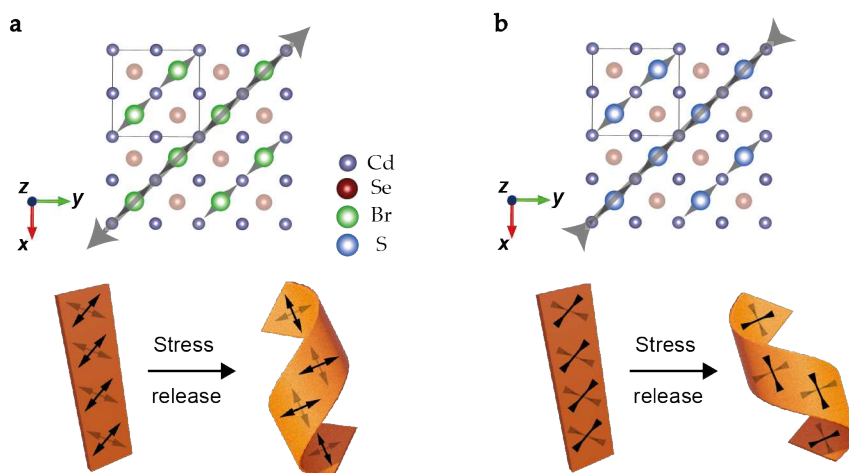


FIGURE 1.5: Scheme of the top facet of a NPL capped by ligands like (a) bromides that bring a tensile strain and (b) thiolates that induce a contractile strain. The associated cartoons display stresses that are oriented at 90° from one another on their top and bottom wide facets and upon the release of their stored elastic energy, these NPLs fold as chiral nanohelices.

The footprint of a carboxylate anchoring group is typically estimated in the order of 0.3 nm^2 [17, 18]. If one were to compare this value with respect to the available area of a surface cadmium displayed by CdSe in the order of 0.18 nm^2 , then a strong in-plane tensile strain would be expected upon the fixation of these carboxylate headgroups. It is estimated that the magnitude of this induced tensile strain is to decrease with the increasing atomic size of chalcogens going from sulfur, selenium to tellurium, as their corresponding cadmium chalcogenide lattice parameter increases in this sense. Thereby, as-synthesized CdTe NPLs are often entirely flat with negligible internal lattice distortions [19, 20].

Whereas for CdS and CdSe subjected to a higher deformation rate, the ideal cubic zinc blende structure becomes tetragonally distorted with an in-plane lattice elongation and an out-of-plane lattice compression [21, 22]. X-ray diffraction (XRD) studies revealed important structural information such as the thickness and crystal orientation of these discrete two-dimensional nanostructures that behaved differently than bulk with the same internal atomic packing. Artemyev and co-workers reported that this tetragonal distortion was greatly reflected through the splitting of the (220) diffraction peak, in agreement with the observed spectroscopic shifts [23].

Optical properties

The former experimental ligand-induced redshifts in the CdSe NPLs were shown to be correlated to the modification in the semiconductors' quantum well width [24]. As the surface ligands were exchanged from native oleates to either hexadecanethiolates or hexadecylphosphonates, the optical spectra became considerably redshifted up to 240 meV. Earlier reports on the lattice shrinkage of thiolates-capped CdTe nanoclusters also pointed towards a length mismatch between the Cd-Te bonds of the inorganic core and the ones of Cd-S on the particle's interface [25]. Since the density of terminal cadmium atoms does not necessarily match the spacing of surface stabilizers, the ligand headgroups in interaction with the surface cations result in lattice distortions. As a result, the strain-induced change in crystals' unit cell translates into a modification of the quantum confinement and hence, the excitonic band gap of semiconductor NPLs.

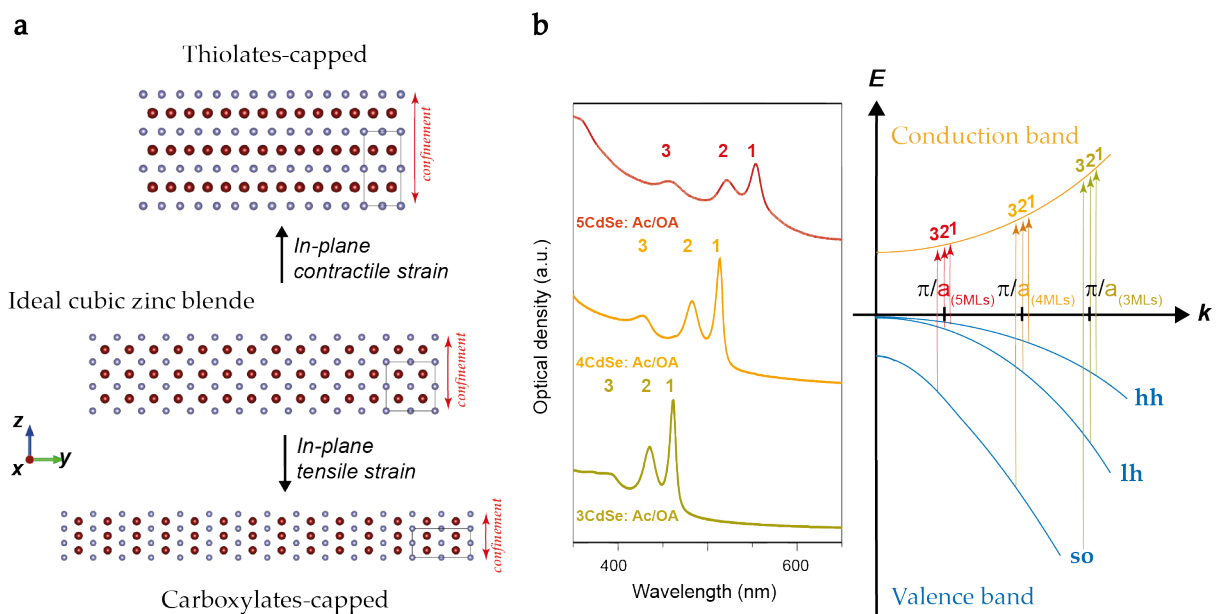


FIGURE 1.6: (a) Scheme of the tetragonal deformation of a cubic zinc blende crystal structure applied onto a piece of 3 MLs NPL upon surface chemistry alteration. The cartoons are not to scale, in order to accentuate on the distortion of unit cells. (b) Absorption spectra of carboxylates-capped 3 (resp. 4 and 5 MLs) CdSe with the indexation of the different excitonic transitions reported onto the band structure.

For this reason, absorption spectroscopy constitutes one of the common techniques frequently employed to characterize these nanoparticles in solution. This enables essentially the thickness determination of a population of NPLs and its purity. If other foreign bodies were to be present, then the resulting spectrum would give a superposition of their respective absorbance. An absorption spectrum of NPLs is interpreted by three main peaks that correspond to the first three excitonic transitions (Fig. 1.6). They reflect the transitions of an electron from the heavy hole (hh) (resp. light hole (lh) and spin orbit (so)) bands to the conduction band. Therefore, each successive increase in terms of MLs for a NPL and hence its thickness, will induce a discrete shift in wavelength that is inversely proportional to the excitonic band gap. For instance from 3 to 5 MLs, the band gap of CdSe varies from 2.69 eV (462 nm), 2.42 eV (512 nm) and 2.25 eV (555 nm) respectively.

Mechanical analogs

Due to the manifestation of a four-fold rotoinversion axis in a NPL and that in-plane stresses are being applied in perpendicular directions on its top and bottom wide facets, a geometrically-frustrated structure is obtained. Similarly in nature, such cases can be found in the seed pods opening of *Bauhinia variegata* [26, 27]. The authors suggested that any residually-stressed bodies would experience a change in configuration upon the release of their stored elastic energy. This has essentially led to multiple forms of helical objects characterized by various curvatures and pitches, by starting off from a saddle-like shape (Fig. 1.7). Besides, the competition between the stretching and bending terms in incompatible thin sheets yielded a geometrically-dependent phenomenon that dictated the shape transition of residually-stressed strips [28, 29].

This mechanical description corresponds well to our case of NPLs, whose width extension can indeed vary for a given length. Predominantly for NPLs with a wide (resp. narrow) width, one finds the scenario of a stretching-dominated (resp. bending-dominated) regime. Upon minimization of the system's elastic energy, these objects curl into helices (resp. twists) as predicted by the macroscale study of Sharon and co-workers.

Overall, wide rectangular and large square NPLs respectively form helices and rolls at final state [31, 32]. Referring back to their top wide crystal facet, one realizes the importance of surface ligands' induced stress that is always directed along the [1 1 0] direction. In fact, this hints already at the resulting morphology of a NPL. If its length and width were in the $\langle 1\ 0\ 0 \rangle$ or $\langle 1\ 1\ 0 \rangle$ directions, then either helices or rolls will ultimately be obtained. This interesting reasoning used to basically couple surface chemistry studies to a mechanical analysis performed at nanoscale, will be further detailed in **Chapter 2**. These nanohelices that are hereby chiral objects, can indeed present themselves as either left- or right-handed structures. In the following section, it is essential to elaborate on the chemical routes that have contributed toward the synthesis of these cadmium-based semiconductor nanoparticles.

1.1.3 Synthesis of colloidal nanoparticles

Classical nucleation theory is a widely accepted model employed in the formation of nanoparticles in standard liquid-phase protocols [33]. LaMer and Dinegar leveraged this nucleation basis to elaborate on a postulate of their diffusion-controlled growth in solutions [34]. This process is divided into four main stages: (i) the rapid increase in concentration of free monomers, (ii) the formation of nuclei due to the monomers' supersaturation, (iii) the growth of particles dictated by the monomers' rate of diffusion and ultimately (iv) the Ostwald ripening, where the large particles continue to grow at the expense of the smaller ones on a longer time scale.

In such descriptions of suspension, it is essential that the creation of solid-liquid interface be favorable. According to Gibbs, the free energy of a particle assumed to be a spherical nucleus writes as:

$$\Delta G = -\frac{4}{3}\pi r^3 |\Delta G_v| + 4\pi r^2 \Gamma \quad (1.7)$$

where r is the particle's radius, ΔG_v the difference of free energy per volume and Γ the free energy of the surface per unit area [35].

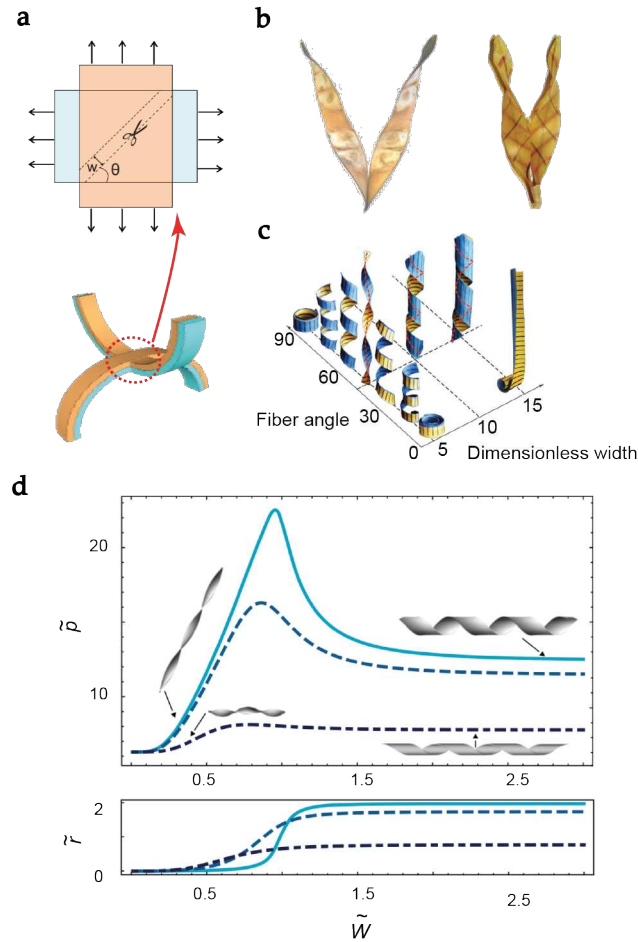


FIGURE 1.7: (a) Fabrication of a mechanical analog of chiral seed pods opening, where two uniaxially-prestretched planar latex sheets along perpendicular directions are glued together, forming saddle-like geometrically-frustrated compound sheet. A strip is then cut from this sheet along a direction that forms an angle θ with one of the stretching directions. (b) Actual seed pods opening of *Bauhinia variegata* represented on the left panel, while on the right, the model reproduction is shown. (c) Different configurations of reproduced latex strip by varying the cut angle and its dimensionless width. (d) Analytic solutions for the dimensionless ribbon-pitch \tilde{p} , and radius \tilde{r} , as a function of the dimensionless width \tilde{W} for different values of deformation $\alpha = 0.01$ (solid cyan), 0.1 (dashed light blue) and 1 (dot-dashed dark blue). As the deformation increases, the twist-to-helical transition becomes smoother and occurs earlier. Insets show selected realizations of ribbon configurations. Adapted from [26, 27, 30].

This allows essentially the assessment of a critical radius, under which particles that are smaller than this limit tend to redissolve as monomers, for the continuous growth of the more stable ones. The key parameter herein to achieve a high monodispersity of particles in solution relies on a neat separation of the two fore-mentioned stages during synthesis: nucleation and growth. For this reason, a swift way of introducing precursors into a heated environment that could in theory lead to a rapid nucleation burst upon supersaturating the medium has been introduced [8]. This pioneer work, based on the thermolysis of organometallic reagents injected into a hot coordinating solvent, has led to the production

of nearly monodispersed II-VI semiconductor QDs. This has later opened doors into better optimized routes for the improved quality control of quantum nanoparticles, which will further constitute the paragraphs of our next section and in particular, a dive into growth instabilities behind these anisotropically-shaped and atomic-scale thick NPLs.

Hot-injection synthesis leading to the discovery of NPLs

Through the work of Bawendi and co-workers, a three-neck flask was set-up under which synthesis were done under an inert atmosphere, with the presence of a temperature probe and an entry for the addition of chemical precursors (Fig. 1.8). This defines one of the staple mountings that is generally used in most chemical synthesis that do not exceed a reaction temperature of $450\text{ }^{\circ}\text{C}$, as limited by the use of heating mantles.

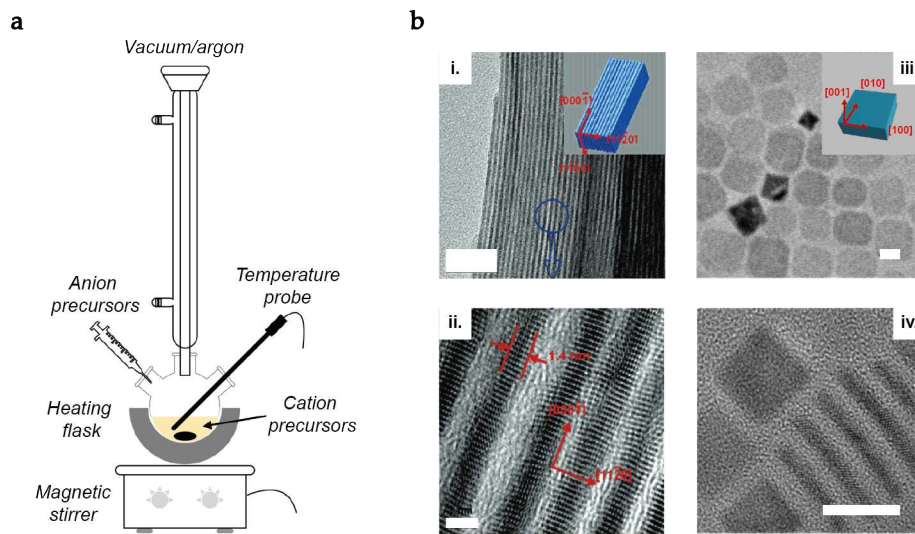


FIGURE 1.8: (a) Scheme of a three-neck flask mounted onto a heating and stirring device adapted for the synthesis of colloidal nanoparticles. (b) TEM and HRTEM images of (i, ii) hexagonal wurtzite CdSe nanoribbons. Scale: 20 and 2 nm. Whereas in (iii, iv), cubic zinc blende CdSe NPLs are shown. Scale: 10 nm. Adapted from [10, 11].

The first report of a free-standing quantum well system was published by Hyeon and co-workers, on nanoribbons of hexagonal wurtzite CdSe that were synthesized at low temperatures around $70\text{ }^{\circ}\text{C}$ [10]. This work that made use of the efficient reaction between Lewis acidic cadmium cations and Lewis basic selenocarbamates to attain ribbon-shaped two-dimensional structures of 1.4 nm thick, exhibited their first and second excitonic transitions located at 2.75 eV (449 nm) and 2.92 eV (423 nm), respectively. Whereas, the counterpart cubic zinc blende CdSe was not discovered until two years later by Dubertret and co-workers [11]. The synthesis of nanoparticles relied once again on the liquid-phase decomposition of both cadmium and selenium precursors, but in a non-coordinating solvent like octadecene instead of octylamine which was formerly employed.

One distinct point from this latter case in contrary to the majority of previous experimental procedures is the addition of an acetate salt towards the beginning of the heated reaction. This has seemingly broken the growth symmetry to yield NPLs whose shape, aspect ratio and thickness can be systematically controlled through the reaction time, growth temperature and ratio between the various added cadmium and the selenium

compounds. Via this work, cubic zinc blende CdSe that were 3 (resp. 4 and 5 MLs) thick possessing first excitonic peak absorption situated at 462 (resp. 512 and 550 nm) were obtained upon removal of certain polyhedral QDs present in solution.

This purification step, which relies on the play of Van der Waals interactions between objects, appears to be essential in separating platelet-like particles from the spherical ones. Since the attractive force between bodies of different geometries scales to the Hamaker constant and is demonstrated to be much important in the case of two parallel plates, this latter will hence sediment at a faster rate [36, 37]. Nonetheless, this washing step enables also the removal of unreacted precursors and the transfer of as-synthesized carboxylates-capped NPLs into other solvents like hexane or toluene.

Growth mechanism of anisotropic NPLs

Initially, zinc blende NPLs were synthesized in octadecene using an acetate salt, mesh precursor of selenide and cadmium carboxylate whose associated carboxylic acid part presented long aliphatic chains like myristic [38]. At that point, it seemed necessary to introduce a mixture of two carboxylic acids whose aliphatic chain length was significantly different in order to induce a symmetry-breaking colloidal synthesis. However, several reports later highlighted the possibility of obtaining such CdSe NPLs with just one single cadmium carboxylate precursor that possessed in fact any lengths like myristic, octanoic or propionic [39, 40, 41].

On one hand, this was due to the reactivity difference between the chalcogenide precursors that were employed, either as mesh form, selenourea or trioctylphosphine selenide [42]. In contrary to the initial report, where the selenium mesh was heated in a mixture that sort of already resembled the synthesis of cadmium chalcogenide QDs themselves, the addition of either selenourea or trioctylphosphine selenide was rather done through hot-injection into a pot that contained only one single cadmium carboxylate precursor [43]. Asaula and co-workers postulated the formation of a smectic mesophase composed of an assembly of octanoate chains, that would aid the template growth of two-dimensional structures. However, this theory was mainly debunked by the absence of liquid-crystal phases during this process through in-situ small-angle X-ray scattering [44].

Norris and co-workers also amended the requirement of a mixed-surfactant system during the formation of NPLs. Instead, the authors carried out the synthesis under melt conditions which showed that either short or long carboxylates can favor the formation of CdSe NPLs. They concluded that the addition of short chains is critical only in standard liquid-phase protocols as these latter phase-separated the cadmium precursors to form two-dimensional structures in a solvent-free environment. Thereby, under working conditions that were kinetically limited, a theory of two-dimensional nucleation and growth was proposed to explain the reasons why an isotropic crystal structure can exhibit a resulting anisotropic crystal shape [45].

By comparing the two growth modes on either wide or narrow facets of a NPL, the authors deduced different energy expressions that corresponded to either a growing square island parallel to the facet edges in the first case or a short step-edge nucleate zipping across the narrow facet in the second (Fig. 1.9). Upon completing each wide (resp. narrow) facets through addition to the crystallite's volume, area and edge length, this displayed in other words, an increase in thickness (resp. lateral size) of the initial NPL. In order for a nucleate to span across the facet, it must first attain a critical island size to remain stable and possess

a sufficient thermodynamic driving force to expand [46]. Since the computed nucleation barriers for narrow facets of various thicknesses (colored dots) appeared to always situate below the one obtained for wide facets (black dot), this means that the short step-edge nucleates spanned always quicker along the narrow facets. Thus, lateral growth of a NPL is strongly favored for even cubical nuclei, leading to the appearance of anisotropic objects.

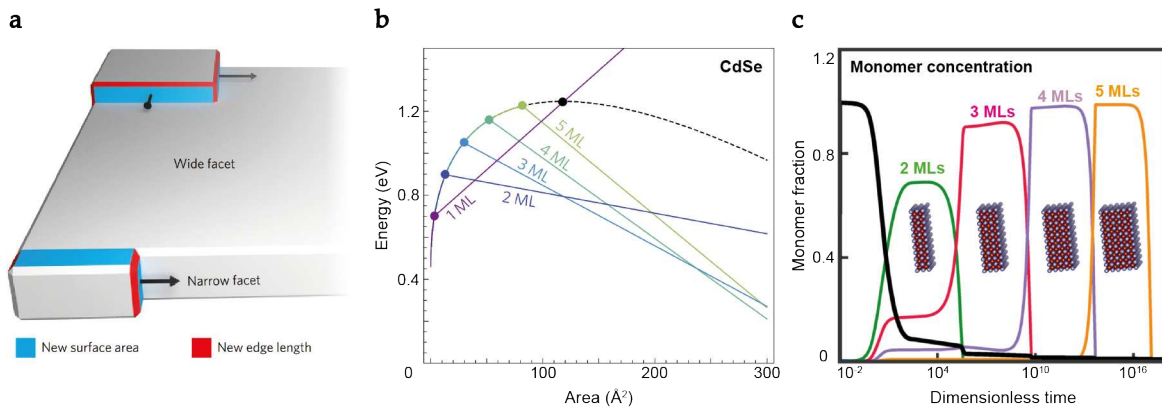


FIGURE 1.9: (a) Scheme of the two different growth modes on wide and narrow facets of a NPL. In the first case, a nucleated island grows isotropically as square to minimize its energy and the corresponding nucleation barrier is determined by the critical island size. On narrow facets whose thickness is less than this critical size, the island zips rapidly over the entire facet and grows along them. (b) Calculated energy as a function of island's size on facets of various thicknesses. (c) Calculated evolution of thickness populations with the fraction of initial free monomers remaining in solution represented in black and NPLs whose thickness ranges from 2 to 5 MLs plotted as colored curves. Adapted from [40, 47].

This concept has been developed even further to describe the evolution of NPLs over time due to thermodynamic driving forces like longer heating for instance [47]. For a given thickness population, laterally smaller objects redissolved at lower monomer concentrations and could eventually disappear from the medium. As this step began to broaden the lateral size distribution of a given thickness, thicker NPLs arose from initially present nuclei during reaction. This agreed coherently with conventional Ostwald ripening, but pursued in a two-dimensional fashion. The as-released material was subsequently captured by these thicker NPLs for their lateral expansion. Experiments of annealing smaller-sized CdS in the presence of thicker CdSe NPLs, have also pointed toward the formation of core-crown nanostructures, where the former served as material reservoirs during the interparticle two-dimensional Ostwald ripening [48].

It is worth mentioning that recently a report from Peng and co-workers demonstrated the formation of a CdS NPL with multiple embedded CdSe QDs through epitaxial fusion in solution of initial CdSe/CdS core-shell spherical nanoparticles [49]. The experimental proofs given by temporal evolution of high-angle annular dark-field (HAADF) images revealed that the NPLs were formed by a process of oriented attachment and exhibited an atomically coherent lattice of zinc blende structure, where the $\langle 0\ 0\ 1 \rangle$ axis defined their thickness direction (Fig. 1.10(c)). In fact, this work goes back to justifying a postulate by oriented attachment of preformed two-dimensional seeds into yielding nanosheets [50]. The presence of single-dot intermediates attached to grown two-dimensional embryos

essentially through $\{1\ 1\ 0\}$ active facets and the ultimate symmetry break was attributed to an intraparticle ripening that only favored their lateral extension along one single dimension.

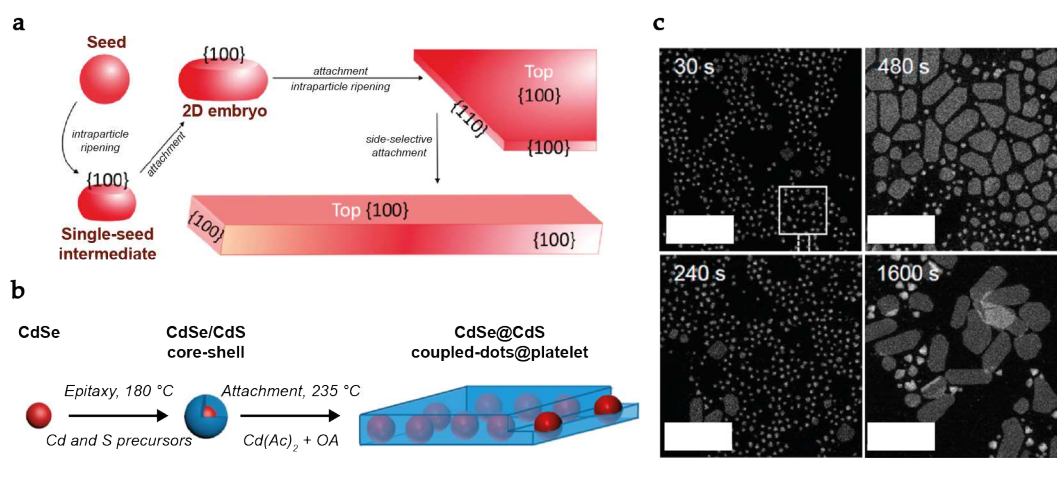


FIGURE 1.10: (a) Growth postulate of NPLs by a process of oriented attachment through active facets. (b) Similar concept that has led to the creation of a structure where multiple CdSe QDs are embedded in a CdS platelet. (c) Temporal evolution of HAADF images during the chemical reaction. Scale bar: 50 nm. Adapted from [50, 49].

Despite the classical intuition of growth postulate proposed by Peng and co-workers, most experimental results still tend to suggest a continuous supply of monomer precursors toward the formation of NPLs and agree to the rational model of Norris and co-workers [51, 52]. Commonly, the highlight is that a symmetry breaking mechanism is required for the synthesis of NPLs with a lateral dimension ranging from tens to hundreds of nm and about a unity thick. The vast amount of efforts in optimizing these nanoparticles has led to directly-synthesized homogenous objects in thickness that is utmost 5 or 6 MLs depending on their surface chemistry [53, 54]. In such cases, the kinetic insight of their chemical reaction often traces back to the nucleation barrier of islands on wide facets due to modifications in surface energy as hinted by the former group.

Going further, small NPLs that were initially synthesized have been laterally extended to form nanohelices of a given thickness. The following section will discuss about chemical protocols that have led to an efficient way of laterally growing them. Nonetheless, thicker NPLs have also been produced where the method used to achieve growth this time around, along their quantum confinement thickness direction will be presented. All of these possible means render NPLs to be flexible and easily moldable for shape-dedicated studies and in particular, I am leaning towards handling and manipulating helical objects in general that could unveil peculiar optical properties that will further be introduced in the second part of this introduction.

Post-synthetic ways to size-control NPLs

Via a two-steps seeded growth technique, carboxylates-capped NPLs are resuspended in a non-coordinating solvent like ODE and can be laterally extended up to fifty times their initial size. This is carried out under a growth condition that consists of placing cadmium acetate and oleic acid in a three-neck flask, while over time slowly adding the chalcogenide

precursor to avoid unwanted secondary nucleation. This procedure was in fact, first introduced to fabricate CdSe-CdS core-crown heterostructures as depicted in the top panel of Fig. 1.11(a), where the photogenerated excitons were passed from the crown to the core to result in the band edge emission of this latter [55, 56]. Thereby, a critical parameter that provoked the CdS addition as crown instead of shell in the bottom panel of Fig. 1.11(a), was attributed to the chemical reactivity of sulfide precursor. The milder version, S-ODE complex was employed compared to the more reactive ones like bis(trimethylsilyl) sulfide or thioacetamide [57, 58].

Besides, the importance of keeping in mind the lattice concordance between different materials was pointed out. Upon growing an environment of CdS around that of CdSe possessing both an identical thickness, whose bulk lattice parameter is 0.58 and 0.61 nm respectively, a 5 % compression of the crystalline structure of this latter along its $\langle 2\ 2\ 0 \rangle$ direction was obtained via electron diffraction analysis. It has as well resulted in noticeable bending of these atomic-scale ultrathin sheets, that agrees in fact with the previously presented mechanical reasoning on residually-stressed bodies. In the same vein, Vasiliev and co-workers have promoted the lateral extension of 2 MLs CdSe homostructures, which led to the formation of helical objects in this case, multiwall rolled-up nanoscrolls [59]. This indicated that either helices or rolls can be ultimately synthesized depending on the orientation of crystal lattice with respect to that of its terminating narrow facets.

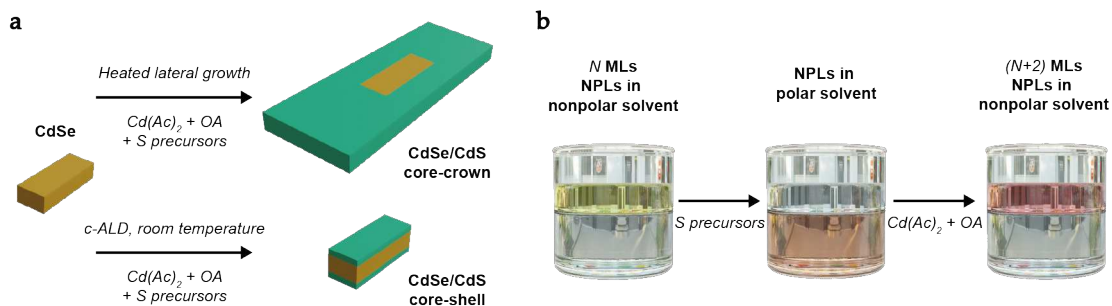


FIGURE 1.11: (a) Scheme to grow either core-crown or core-shell nanostructures from core only NPLs, illustrated for a CdSe/CdS system. (b) Different steps at achieving axial thickness growth via c-ALD technique, going from N to $(N+2)$ MLs in a biphasic mixture.

On the other hand, the axial growth of NPLs along their thickness direction used in this manuscript is based on the route first proposed by Talapin and co-workers [57]. The so-called colloidal atomic layer deposition (c-ALD) technique relies on a layer-by-layer successive growth of subsequent cationic and anionic planes by phase transferring them between immiscible nonpolar and polar solvents (Fig. 1.11(b)). In contrary to conventional successive ionic layer adsorption and reaction method, c-ALD promises a self-limiting half-reactions procedure that enables a facile removal of unreacted molecular precursors and prevents the accumulation of the reaction by-products, via possible purification and washing steps in between additions of ionic planes [60, 61].

Herein, chalcogenide precursors are present in the form of inorganic salts like sodium hydrochalcogenide or ammonium chalcogenide for instance. It consists of firstly exchanging the surface carboxylates of NPLs by these latter, which allows their transfer into a polar solvent like *N*-methylformamide that constitutes a biphasic mixture with hexane. Upon the addition of these anions onto the basal planes of NPLs, the subsequent introduction of a

cadmium salt completes the final and outer cationic planes. As one can imagine, these layer-by-layer steps of growth can be repeated for a given amount of times to reach thicker nanostructures, which exhibit optical properties that are shifted to longer wavelengths. In order to improve on the materials' crystallinity, since the as-described procedure is performed at room temperature, a heated annealing step is done later on in the presence of additional cadmium acetate, oleic acid and phosphines. This has been demonstrated to neatly passivate and amend the atomic disorder and surface roughness found at the interface of growing colloidal semiconductor nanoparticles [62, 63].

1.2 Inorganic chiral materials

Upon introducing the fundamental concepts of the cadmium-based II-VI semiconductor NPLs which constitute the body of this manuscript, these candidates are explored for their potential in exuding chiroptical light properties. This point is essentially characterized through the study of circular dichroism (CD), an aspect that will be detailed in this second part of introduction. Notably, ways to achieve this goal and origins to this phenomenon will be presented, as showcased by the great number of work published over these recent years. Jointly, the notions introduced in this following section hint at the work of **Chapter 3** based on CdSe NPLs and the one of **Chapter 4** based on silica helices. An eventual opened-up avenue that could lead to the sorting of chiral objects will also be evoked.

1.2.1 Characterization of chirality

Herein, the formalism for the measurement of CD for absorption is due to the transitions between two distinct electronic states. Presented under the form of absorption spectroscopy, at a particular wavelength, it defines the difference in the absorbance of left- and right-circularly polarized lights [64]. This term is treated as an observable experimental parameter, which by convention, can be expressed in various unit systems.

CD formalism

In most literatures, CD is given in terms of ellipticity θ rather than absorbance, that are in fact shown to be related by a linear relationship. The definition of ellipticity relies on the resulting electric vector of a light beam \vec{E} , whose intensity is proportional to the square of the amplitude of this vector: $I = |\vec{E}|^2$. According to the principle of superposition, a linearly polarized light can be described as the sum of two circularly polarized beams with equal amplitudes and opposite directions of in-phase rotation [65]. In the presence of a chiral absorbing medium, this results in the attenuation of one of the two circular polarizations more than the other and also, induces a shift between their relative phases.

As a result, the difference in absorption causes the light emerging from the sample to be elliptically polarized, while the phase shift rotates the major axis by an angle α with respect to the incident beam (Fig. 1.12). Via optical rotatory dispersion, or in other words, the Kramers-Kronig transform of CD, this angle can be measured experimentally [66, 67]. Herein, the ellipticity θ expressed in radians, is written as the angle, whose tangent is given by the ratio of the semi-minor to the semi-major axis of the resulting ellipse.

Through computation with the square root of the corresponding intensities of left- and right-circularly polarized lights and by adopting the convention of right-minus-left, one can obtain:

$$\begin{aligned} \theta_{rad} &\sim \frac{\sqrt{I_R} - \sqrt{I_L}}{\sqrt{I_R} + \sqrt{I_L}} = \frac{10^{-\frac{A_R}{2}} - 10^{-\frac{A_L}{2}}}{10^{-\frac{A_R}{2}} + 10^{-\frac{A_L}{2}}} = \frac{e^{-\frac{a_R}{2}} - e^{-\frac{a_L}{2}}}{e^{-\frac{a_R}{2}} + e^{-\frac{a_L}{2}}} \\ &= \frac{e^{\frac{\Delta a_{CD}}{4}} - e^{-\frac{\Delta a_{CD}}{4}}}{e^{\frac{\Delta a_{CD}}{4}} + e^{-\frac{\Delta a_{CD}}{4}}} = \tanh\left(\frac{\Delta a_{CD}}{4}\right) \sim \frac{\Delta A \ln 10}{4} \end{aligned} \quad (1.8)$$

where a and A are the Eulerian and decadic absorbances respectively, that are related by $a = A \ln 10$. The indices L and R indicate the left- and right-circular components, while

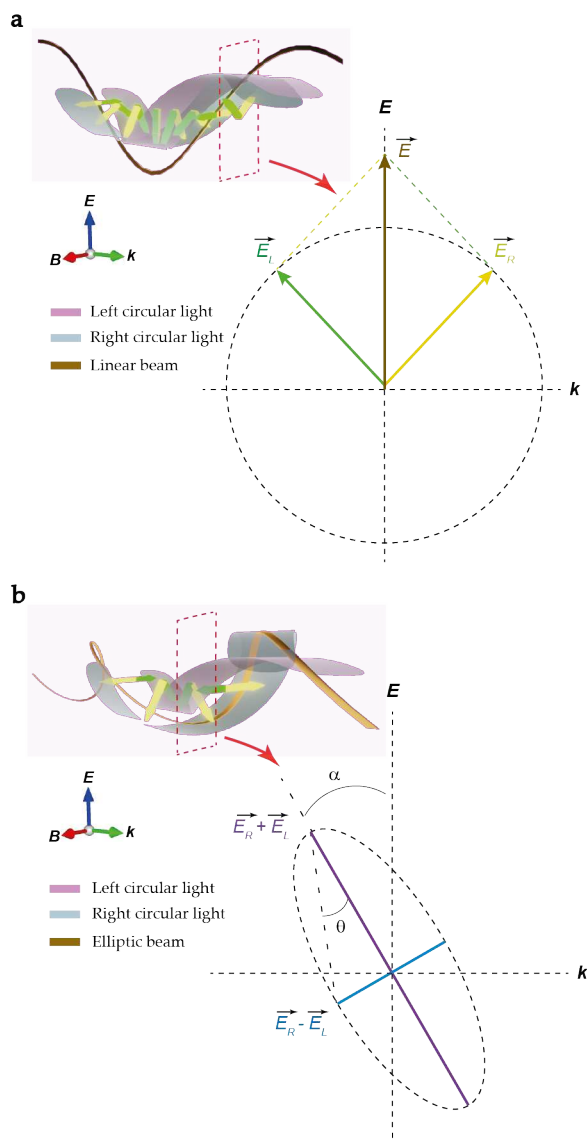


FIGURE 1.12: (a) Decomposition of the electric vector of a vertically polarized beam into two circularly polarized components of equal magnitude and opposite directions of in-phase rotation. Inset displays a propagating beam along the wavevector direction \vec{k} and a slice of the electrical field projected onto the EB -plane is shown. (b) Effect of passing through a chiral absorbing medium on the components of the electric vector. Their different magnitudes are decreased due to CD and absorption, resulting in an elliptical trajectory. The major axis of the ellipse is twice the sum of the magnitudes of the left- and right-circularly polarized components, whereas the minor axis is twice their difference. The ellipticity θ , is the angle whose tangent is the ratio of the semi-minor to the semi-major axes as depicted. The difference in refractive indices for the two circularly polarized components results in rotation of the major axis by an angle α with respect to the initial polarization of the incident beam.

$$\Delta a_{CD} = a_L - a_R.$$

Soon later expressed in mdeg, the ellipticity θ writes as:

$$\theta_{mdeg} \sim 32980\Delta A \quad (1.9)$$

For a sample containing a single chiral species, the ratio of CD to absorbance is an intrinsic parameter that can be obtained without knowledge of optical path length, absorber concentration or their associated product. This is because $\frac{\Delta A_{CD}}{A} = \frac{\Delta a_{CD}}{a} = \frac{\Delta \epsilon_{CD}}{\epsilon} = \frac{\Delta \sigma_{CD}}{\sigma}$, where ϵ and σ are the molar absorbance coefficient and effective absorption cross-section of the absorber respectively. This ratio denoted by g , is the intrinsic chiral anisotropy that depends on the spectral region where the sample absorbs [68, 69].

Conceptualizing a CD spectrometer

From the instrumental viewpoint, the measurement of CD can be recorded using (i) a photomultiplier or avalanche photodiode to quantify the intensity of a light beam, (ii) a photoelastic modulator to periodically alter the beam's polarization states and (iii) a monochromator located between the light source and the modulator to refine the excitation wavelength. The spectral domain of focus spans about a decade in wavelength (photon energy) from roughly 1.2 μm (1 eV) in the near infrared to 120 nm (10 eV) in the vacuum ultraviolet.

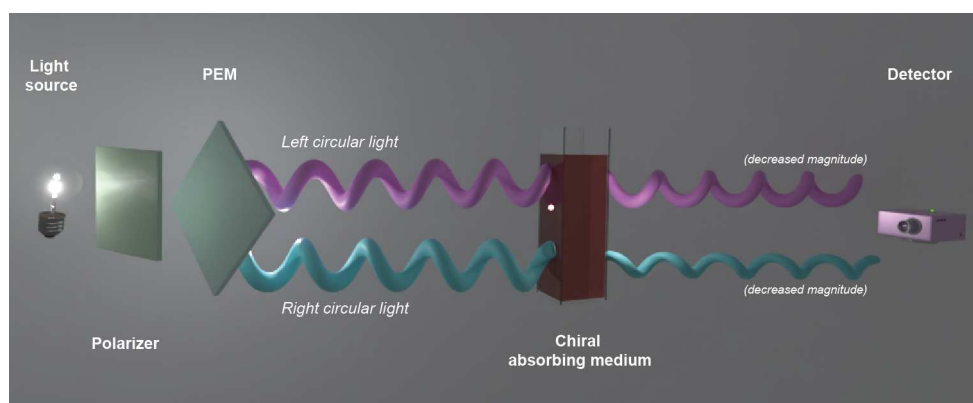


FIGURE 1.13: Schematic diagram displaying the conceptual relationships of the typical subsystems found in a CD spectrometer.

In such instruments, a xenon arc light source and a double-prism monochromator are best implemented [70]. Fig. 1.13 illustrates the arrival of an incident beam of monochromatic, linearly polarized light on a photoelastic modulator (PEM). This latter ought to be oriented with its stress axis making an angle of 45° , with respect to the polarization state of the incident optical beam that could either be vertically or horizontally polarized. PEMs operate as an isotropic material bonded to a quartz crystal that acts as the frequency-determining element in an electronic oscillator circuit. As the alternate current flowing in this circuit causes the crystal to mechanically vibrate due to the piezoelectric effect, this induces similar vibrations in a transparent optical element that modify the refractive index for the direction parallel to the long-axis of the optical elements, with respect to that for the orthogonal direction. Therefore, the phase of these two components becomes sinusoidally shifted with respect to each other over time.

When the instantaneous phase shift equals zero, the light emerging from the PEM will have the same polarization as the incident beam. However, when the phase shift equals $\frac{\pi}{4}$,

the exiting beam will be circularly polarized. In this case, the instantaneous intensities of the exiting beam can be represented as the sum of left- and right-circularly polarized components. As these latter pass through a chiral absorbing medium and become attenuated, their intensities are in fact computed as voltages that depend on the incident beam power, the sensitivity of the device at a particular wavelength and the internal gain of the photomultiplier. Thus, the device calibration for the measurement of CD represents an important operation at avoiding artifacts due mainly to linear dichroism signals [71].

1.2.2 Introducing chiral semiconductor nanocrystals

Generally, colloidal nanoparticles as a macroscopic ensemble in solution ought not to show any chiroptical properties for the intuitive reason that their chirality is random, producing equal portions of the possible enantiomers. However, these nanocrystals are also known to exhibit low symmetries and reports have previously revealed the presence of hidden chiral defects in bulk and on their surface that were in fact responsible for these CD observations. With this being said, chiral inorganic nanocrystals can still be readily designed and fabricated through a range of approaches. This area has notably received a great deal of attention, since they demonstrate potential applications in chiral sensing, catalysis and as metamaterials in advanced optical devices [72, 73, 74]. Herein, the essential identified factors that have contributed to the appearance of chiral II-VI semiconductor nanoparticles in particular, will be broken down.

Intrinsic chiral defects

The first concept of proving the basis of chiral crystal symmetry groups was carried out on HgS [75]. The use of colloidal chemistry to bring in an environment of a large concentration of chiral penicillamine molecules that could bind strongly to the surface of forming crystals, induced a symmetry breaking from the achiral β -phase to the thermodynamically favored chiral α -phase of the cinnabar structure. As supported by high-resolution transmission electron microscopy (HRTEM) and XRD data, these latter displayed strong chiroptical response that was several orders of magnitude higher than the one of achiral semiconductors from the same family, passivated by the identical chiral surface ligands.

Theoretically, it is believed that chiral dislocations of a lattice are a naturally occurring phenomenon during a crystal growth like semiconductor nanowires, whose optical activity can be inherently varied owing to the size quantization of their energy spectra [78]. Building up from the semiclassical Rosenfeld approximation, the presence of a screw dislocation as illustrated by Fig. 1.14 has led to interferences of transitions due to the radial and angular derivatives, that were shown to be dependent on the momentum of sub-bands. Similar analysis applied onto QDs, rods and disks have revealed increasing CD with the nanocrystal's length and the magnitude of dislocation [76].

The observation of intrinsic chirality for CdSe/ZnS systems have also been reported which were initially formed in an equal dextrogyre (D -) to levogyre (L -) ratio, along with achiral nanocrystals [77]. An enantioselective separation method based on a phase transfer approach, demonstrated that chiral molecules bind with different affinities to the surface of QDs' enantiomers. Upon selective ligand exchange of levorotatory (resp. dextrorotatory) nanoparticles in the case of using L - (resp. D -) cysteine molecules, the initial phase containing unexchanged nanocrystals of opposite handedness exhibited mirrored CD spectra despite being capped by achiral trioctylphosphine oxide. The intrinsic behavior underlined here originating from achiral wurtzite lattices arose from the symmetry breaking,

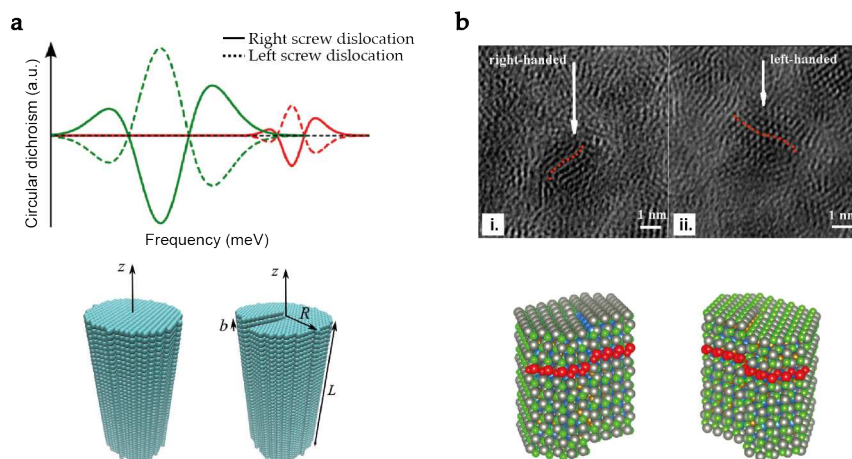


FIGURE 1.14: (a) Scheme of cylindrical nanocrystals made up of cubic lattice unit cells with and without the presence of screw dislocations. The general calculated CD spectra upon intraband transitions for right-handed (solid curves) and left-handed (dashed curves) screw dislocations are shown. (b) TEM images of CdSe/ZnS QDs, where the arrows indicate possible screw dislocations. Atomistic models of these core-shell nanoparticles are displayed with dislocations set in the (0 1 0) plane of CdSe core. Red dotted lines indicate the direction of the dislocations. Adapted from [76, 77].

induced by the presence of naturally forming chiral defects during uniaxial growth of these nanocrystals.

Nonracemic ensemble of chiral geometries

Moving onto an inorganic material possessing a chiral shape itself, if one were to be interested in the manifestations of chirality in such system, it is crucial to firstly obtain a nonracemic ensemble of such nanoparticles. Typically, this requires a chiral bias at atomic scale during their growth. Markovich and co-workers have explored colloidal tellurium and selenium nanostructures with shape chirality by using thiolated chiral biomolecules like glutathione [79]. These compounds managed to induce enantioselective nucleation and growth, leading to the crystallization of chiral open-scissors geometry for instance as depicted in Fig. 1.15(a).

The photoconversion of spin angular momenta into structural changes in matter has also been harvested to yield chiral twisted nanoribbons with an exceeding enantiomeric excess of 30 % [80]. This method of templating left- (resp. right-) circularly polarized light to fabricate left- (resp. right-) handed structures relied on the photooxidation of thioglycolic acid ligands on the surface of initially truncated nanoparticles by over time, absorbing left- (resp. right-) photons. These photoexcited tetrahedrons with a size of 3.6 nm then self-assembled to form left- (resp. right-) handed nanoribbons with a pitch of 1.65 μm in average as shown by Fig. 1.15(b), that revealed correspondingly positive (resp. negative) mirror-image CD signals.

Similarly, semiconductor helices reaching an exceeding enantiomeric excess of 98 % have also been prepared from the aging and assembly of chiral cysteine-stabilized CdTe nanoparticles dispersed in methanol [81]. This intriguing and spontaneously occurring process was attributed to a phenomenon of chiral self-sorting based on the thermodynamic preference of

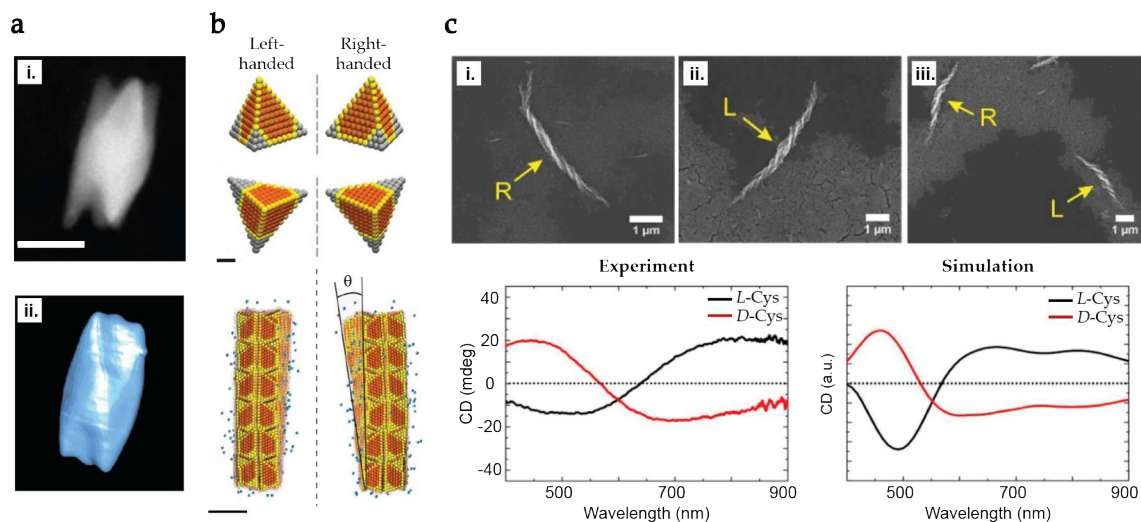


FIGURE 1.15: (a) Dark field STEM imaging and tomography of tellurium sample obtained with hydrazine and glutathione. Scale bar: 100 nm. (b) Atomistic models of nanoparticles with left- and right-handed truncations used during molecular dynamics simulations. These latter then self-assemble into nanoribbons in an isothermal-isobaric ensemble at temperature $T=300$ K during several ns. Scale bar: 1 and 5 nm. (c) SEM images of *D*-Cys (left), *L*-Cys (middle) and *DL*-Cys (right) CdTe nanoparticles assembly, along with their associated experimental and simulated CD spectra. Adapted from [79, 80, 81].

building blocks to assemble with those of the same handedness. Thereby, an achirally stabilized system by thioglycolic acid did not lead to any observable helicity, while a *DL*-cysteine dispersion contained surprisingly helical structures of both opposite handedness. The absence of neither intrahelical racemization, nor achiral objects in general, indicated a strong preference towards homochirality, an effect that is as well observed for fibrous hydrogels and supramolecular columns [82, 83].

Shell of chiral surface ligands

If one were to look back at the first publication on chiral semiconductor nanoparticles, Kelly and co-workers have synthesized penicillamine stabilized CdS QDs using the microwave induced heating technique [84]. These latter were obtained by mixing cadmium perchlorate, a basic solution of either *D*-, *L*- or *DL*-penicillamine, plus thioacetamide to form luminescent chiral nanoparticles possessing broad emission bands in the visible region. Later on, a similar method has also been used for the fabrication of chiral CdTe nanostructures functionalized by other thiolated compounds like cysteine and glutathione [21, 85].

As for the origin of observed CD in this case, a cluster of CdS cut out from the bulk wurtzite structure whose surface is bound by a penicillamine molecule has been computed by density functional theory [86, 87]. Such models showed that the ligand bind via the nitrogen and sulfur atoms to one surface cadmium, while simultaneously introducing distortions by an additional bonding of carboxylate to another neighboring cadmium. This strong ligand-cluster interaction has led to the enantiomeric distortion of outermost cadmiums, whereas the core geometry still remained.

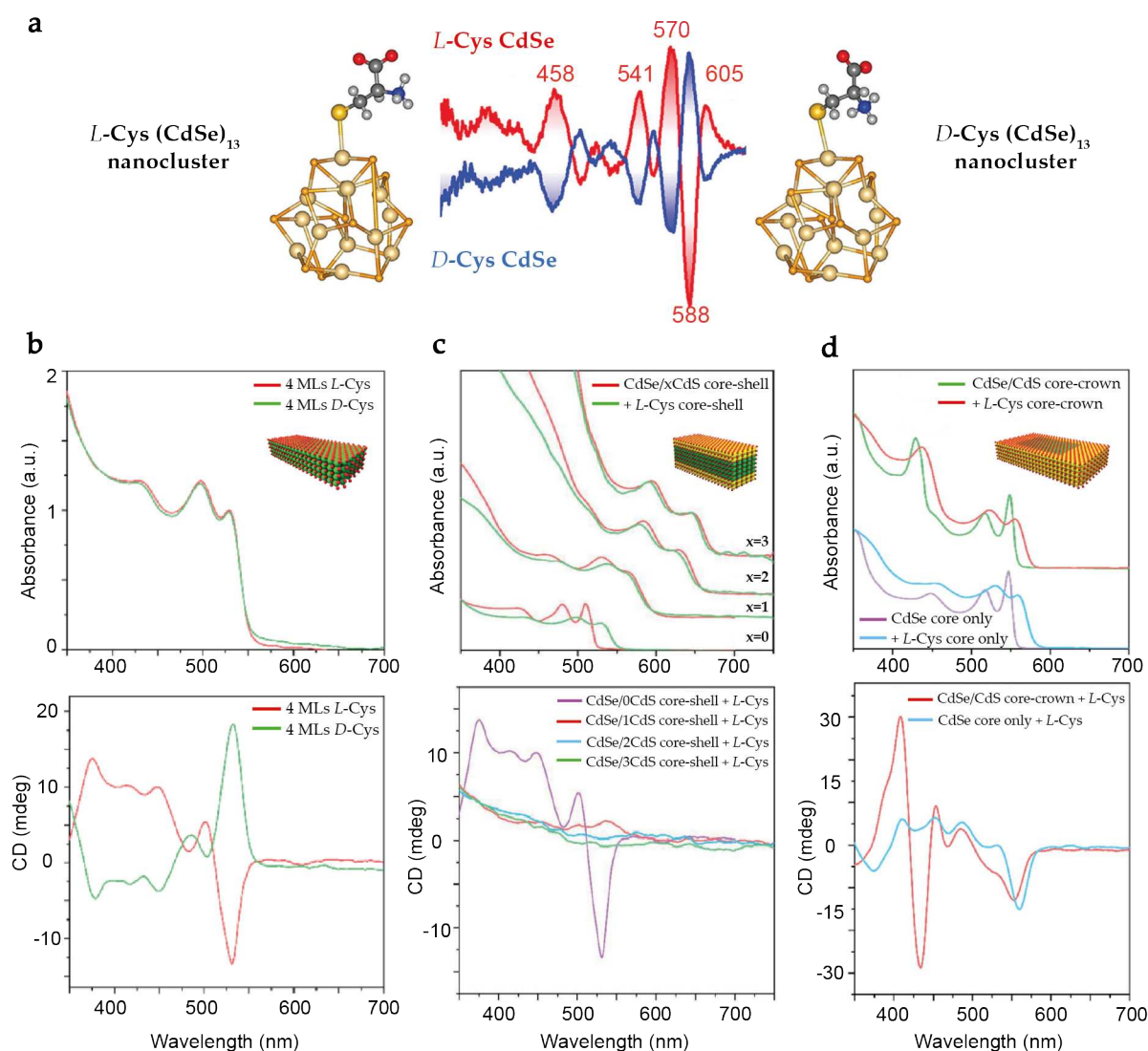


FIGURE 1.16: (a) CD spectra of CdSe QDs capped by chiral *L*-cysteine (red curve) and *D*-cysteine (blue curve) molecules. Scheme of the optimized geometries under density functional theory is illustrated. (b) Absorption and CD spectra associated to 4 MLs CdSe zinc blende NPLs upon ligand exchange with both enantiomers of chiral cysteine. (c) Similar spectra for 4 MLs CdSe/*x*CdS core-shell structures before and after ligand exchange with *L*-cysteine, where *x* denotes the varying thickness of grown CdS shell ranging from 0 to 3 MLs on each wide facet of the NPLs. Herein, the strong CD signal decreases with the thickness of this latter. (d) Similar spectra for 4 MLs CdSe core only and CdSe/CdS core-crown structures before and after ligand exchange with *L*-cysteine. The core-crown system exhibits two strong CD bands corresponding to the CdSe and CdS band edges. Adapted from [88, 89].

In addition to this surface distortion factor, a phenomenon of chiral ligand induced CD onto originally achiral CdSe QDs has been reported by Balaz and co-workers through a process of post-synthetic chiral ligand exchange [88]. Theoretical calculations indicated that the induced CD was predominantly due to hybridization between the ligand's highest occupied molecular orbital (HOMO) and the QD's valence band, which yielded structural and energetic aspects of this interaction. Subsequently, Oron and co-workers have furthered this scope onto atomically flat two-dimensional NPLs [89]. In a similar fashion, the authors have replaced the initially achiral oleic acid ligands by chiral cysteine molecules onto cadmium-based NPLs that were core only, core-shell and core-crown heterostructures (Fig. 1.16(b,c,d)).

This work has notably highlighted the interest of NPLs in exhibiting a much strong quantum confinement along the transverse direction and at the same time, a large surface-to-volume ratio which appeared to be critical parameters for the induction of chirality. In comparison to spherical QDs and nanorods, the flexibility of such ultrathin sheets can undeniably be leveraged for the enhancement of CD as discussed theoretically [90, 91, 92]. And so, this beginning point drives us into further exploring this class of material as an active chiral-absorptive system by simultaneously playing with the inorganic core and the organic shell of stabilizers surrounding it. Details on this part of our work will be covered later in **Chapter 3**.

Hierarchical chirality

The ability of small building blocks to spontaneously assemble into forming supraparticles of unique geometries has been introduced as a way to achieve chiral superstructures. Thereby, even if an individual starting unit does not reveal any chiroptical activity, the higher order of superstructures can [93, 94]. These assemblies can be constructed by biological linkages like single-strand DNA for instance, to create a tetrahedral shape whose corners are composed of four different types of objects as illustrated by Fig. 1.17(a) [95]. Via hybridization of the complementary chains, the most promising structure was made of a combination of CdSe/ZnS core-shell QDs, gold and silver nanoparticles. The enantiomeric constructs were obtained by switching the position of two of these nanoparticles through conjugation with the opposite strand and hence, resulted in strong scalable mirrored CD signals.

This combination of metal and semiconductor nanoparticles has benefited yet another hybrid plasmon-exciton assembly that gives rise to unusual chiroptical properties of plasmon-exciton states [96]. By using cysteine-stabilized chiral CdTe nanoparticles and gold nanorods, two geometries: (i) nanorod dimers with twisted scissor-like shape spaced in between and around with CdTe or (ii) single nanorods in an entire shell of CdTe, were essentially obtained depending on the molar ratio of these latter as shown by Fig. 1.17(b). Different configurations yielded distinct CD signals that were either associated in large part to the plasmonic material itself or the coupling between these two. As for the supraparticles' enantiomeric preference, it appeared that the chiral interactions between CdTe units in the shell dictated the final outcome of the bisignated pattern of a resulting CD.

Nonetheless, chirality transfer onto assemblies of achiral building blocks with the use of chiral templates has also been rendered possible [98, 99]. Among which, the functionalization of achiral CdSe/CdS quantum rods of various aspect ratios onto silica helical ribbons demonstrated an effect of grafting orientation on the induced CD signals as displayed by Fig. 1.17(c) [97]. Thanks to the facile tunability of silica's morphology that was in fact obtained by a sol-gel transcription of previously reported self-assembled

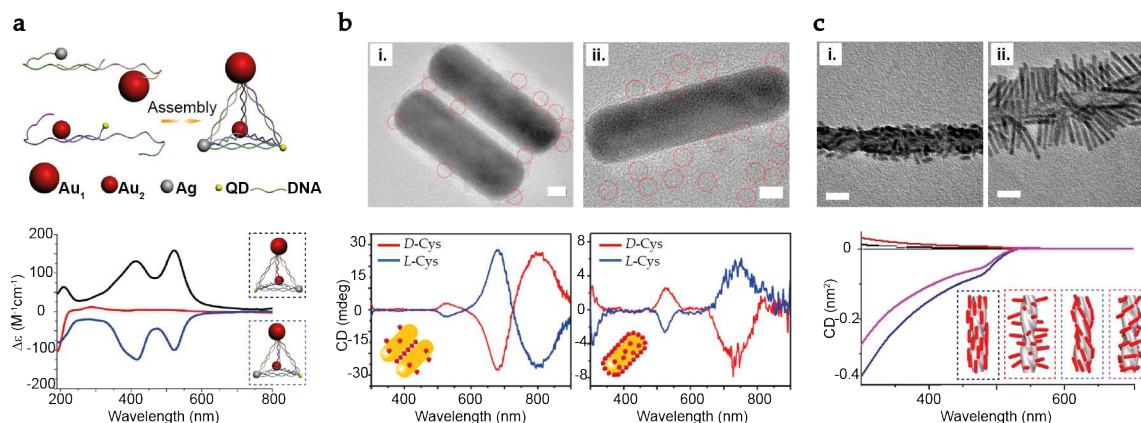


FIGURE 1.17: (a) Scheme displaying the assembly of various components into a tetrahedral superstructure, bridged by 26 bp double-strand DNAs that equal 8.8 nm. The resulting CD spectra of the *S*-enantiomer (black curve), racemic mix (red curve) and *R*-enantiomer (blue curve) are shown. (b) TEM images of CdTe-gold nanorod(s) assemblies and their corresponding CD spectra for both enantiomers of chiral cysteine used to stabilize the semiconductor nanoparticles. Red circles indicate the identification of CdTe units around the plasmonic structure. Scale bar: 5 nm. (c) TEM images of silica twists functionalized by CdSe/CdS quantum rods of different lengths and the simulated CD spectra of these latter with four various grafting orientations, with respect to the helical substrate. Scale bar: 20 nm. Adapted from [95, 96, 97].

gemini surfactants, both helical and twisted structures were prepared to host incoming semiconductor nanoparticles [100, 101]. This difference in morphology has led to a stronger *g*-factor dependence in the former case, that was suggested to vary with its curvature and pitch, thus shedding light on the design of efficient chiral superstructures based on inorganic silica-nanocrystal components.

In Chapter 4, this chiral silica template will notably be adopted, modified and leveraged for the functionalization of various compounds such as semiconductor CdSe NPLs, plasmonic gold nanoparticles and fluorescein organic fluorophores. These fascinating candidates that bind either electrostatically or covalently onto the surface of these micrometric helical ribbons demonstrate induced CD signals in solution, whose sign can be controlled by the handedness of these silica helices in agreement to previous reports [102, 103]. In addition to this aspect of enantiomeric excess control over an ensemble of chiral objects and owing to the robustness of silica materials, a proof-of-concept for sorting crystals of opposite handedness under an acoustic resonant field will be discussed.

1.2.3 Mechanical sorting of chiral objects

In particular for pharmacological reasons, it is crucial to control the enantiomeric form and purity of certain commercialized biomolecules that could either be beneficial or severely harmful like thalidomide for instance. Standard chiral resolution techniques rely most frequently on specific chemical interactions to separate a racemic mixture through chromatography or electrophoresis [104, 105, 106, 107]. When it comes to mechanical resolution methods, a huge focus is spanned on microfluidic systems in view of their low sample volumes, short processing times, cost-effective and portable advantages.

The general thought is to apply shear flows on chiral bodies, in order to create lift that is specific to their orientation and thanks to which, these latter ought to migrate separately from one another [108, 109]. One of the many criteria to be satisfied is that the thermal fluctuations should be neatly overcome. Specifically by assessing the rotational diffusion coefficient of a spherical object of diameter d , this gives an expression of $D_r \sim \frac{k_B T}{\pi \eta d^3}$, where k_B is the Boltzmann constant, T the absolute temperature and η the dynamic viscosity of the medium. Since the associated relaxation time of orientation persistence writes as $\tau = \frac{1}{2D_r}$, a typical 1 μm -sized object in aqueous solution at room temperature can thus in theory, maintain its orientation for several seconds.

However, for objects tinier than this length scale, random walk may outcompete these so-called chiral drift [110]. Thereby, advanced methods involving the juxtaposition of a second force coupled to microfluidics have been introduced over the recent years by optical means, that contributed to field-induced chiral sorting strategies based on the use of light angular momentum [111, 112, 113]. Brasselet and co-workers have succeeded at deflecting cholesteric liquid crystal droplets of a given chirality under two counter-propagating circularly polarized beams with opposite helicities. Such optofluidic toolbox intelligently harvested the factor of discrimination that these microspheres acted as circular Bragg reflectors. The light propagation of circular polarization states depended on the actual cholesteric helical axis over a region of Bragg wavelength, as determined by its parallel and perpendicular refractive indices.

Herein, our strategy is by deliberately taking the advantage of particles' helical morphology and subjecting them under an acoustic resonant field [114, 115]. The resulting motor force that drives their migration in solution in a phenomenon known as acoustophoresis, will be addressed in this section. As preliminary tests, it is important to map out the particles' migration behavior like traveling velocities for instance and to compare them with actual existing reports before implementation in microfluidic devices. Therefore, a brief overview of work that has forecast this chiral sorting technique will be presented later and serves as basis to actually constructing an acoustofluidic resonator.

Acoustophoresis formalism

This novel rising area of research benefits notably from the blooming performance of microfluidics and piezoelectrical sources. Its basic principle is to contactlessly manipulate micrometric objects in suspension by employing an acoustic leverage called acoustic radiation force and this has opened tremendous perspectives particularly in the field of cell biology [116, 117]. This method consists of firstly generating an ultrasonic standing wave in a microcavity, in order to create an acoustic pressure gradient whose node is located at its mid-height. Under the gradient effect thus established, objects are forced to migrate towards the pressure node to gather in the mid-plane. Later in **Chapter 4**, this phenomenon turns out to be more subtle than it seems since the applied forces depend strongly on the acoustic conditions and vary as a function of the nature of the handled objects, their concentrations in solution and also, their intrinsic physical properties like compressibility.

In general, two technological approaches stand out in the generation of acoustic radiation force (ARF) in a microchannel, that is either by surface acoustic waves or bulk acoustic waves. In the former case, it consists of propagating an acoustic wave along an elastic material into a cavity of interest to create the ultrasonic environment [118]. The most noticeable difference between these two methodologies lies on the form of piezoelectrical transducer used to produce these acoustic sources. An interdigital transducer made up

of two metal electrodes manufactured by photolithography in the form of intersecting combs, allows the flow of current to be translated into physical deformations of a material (Fig. 1.18(a)). These associated displacements are at the origin of surface acoustic waves, whose frequency in the order of 35 MHz in average is far greater than the one in volumetric systems [119].

By correctly sizing the network of interdigital transducers with respect to the width of the microchannel, a pressure node can be expressed in its mid-plane along the longitudinal direction. Whereas in the second approach of bulk acoustic waves, an incident wave is directly conveyed into a fluid that is found between two opposite parallel walls (Fig. 1.18(b)). Thanks to the existence of these two hard surfaces, it enables the incident wave to be reflected into creating a stationary one, which is basically the result of in-phase superposition between the initial and reflected parts. Herein, the acoustic source is emitted by a cylindrical piezoelectrical transducer placed at the bottom of a cavity of height h , that satisfies the resonance condition of a stationary wave of wavelength λ_{ac} , where $h = \frac{\lambda_{ac}}{2}$.

Primary force

This phenomenon of acoustophoresis, firstly discovered by Kundt and Lehmann in 1866, was not formally theorized until later in 1884 by Rayleigh [122]. The revised model proposed by Yosioka-Kawasima on spherical compressible objects suspended in a compressible fluid and subjected to an interaction with plane waves is adapted throughout our work [123]. This gives an expression of ARF that writes:

$$\mathbf{F}_{ac}(z) = \frac{\pi}{2} \langle E_{ac} \rangle k d_p^3 F_Y \sin(2kz) \cdot \mathbf{e}_z \quad (1.10)$$

where d_p is the diameter of a particle, k the wavenumber given by $\frac{2\pi}{\lambda_{ac}} = \frac{2\pi f_{ac}}{c_f}$, f_{ac} and c_f represent the resonant frequency and speed of sound in a fluid, respectively. Developing further, $c_f = \frac{1}{\sqrt{\rho_f \beta_f}}$ for which ρ_f and β_f indicate both the density and compressibility of a fluid. Concurrently, one can also deduce a similar expression for the speed of sound in a particle $c_p = \frac{1}{\sqrt{\rho_p \beta_p}}$. On the other hand, $\langle E_{ac} \rangle$ depicts the time-averaged acoustic energy density injected into a system. This term depends essentially on the resonant frequency and its amplitude v_0 , written as $\frac{\rho_f v_0^2}{2}$. Along with the acoustic contrast factor:

$$F_Y = \frac{1 + \frac{2}{3} \left(1 - \frac{\rho_f}{\rho_p}\right)}{2 + \frac{\rho_f}{\rho_p}} - \frac{\rho_f c_f^2}{3 \rho_p c_p^2} \quad (1.11)$$

This term quantifies an object's response to the excitation by acoustic waves, depending on the surrounding environment and also, on its own mechanical properties. For each type of particle, this variable differs in a sense that a positive (resp. negative) sign indicates its migration towards (resp. away from) the acoustic pressure node, while its absolute value represents the magnitude of this acoustic response. Therefore, this constitutes a crucial criterion that allows already the sorting of a population of objects according to their size, density and compressibility.

Secondary forces

In addition to the primary ARF that was previously evoked, several other forces are also in play when the acoustics are switched on in a resonant cavity that lead to the trapping

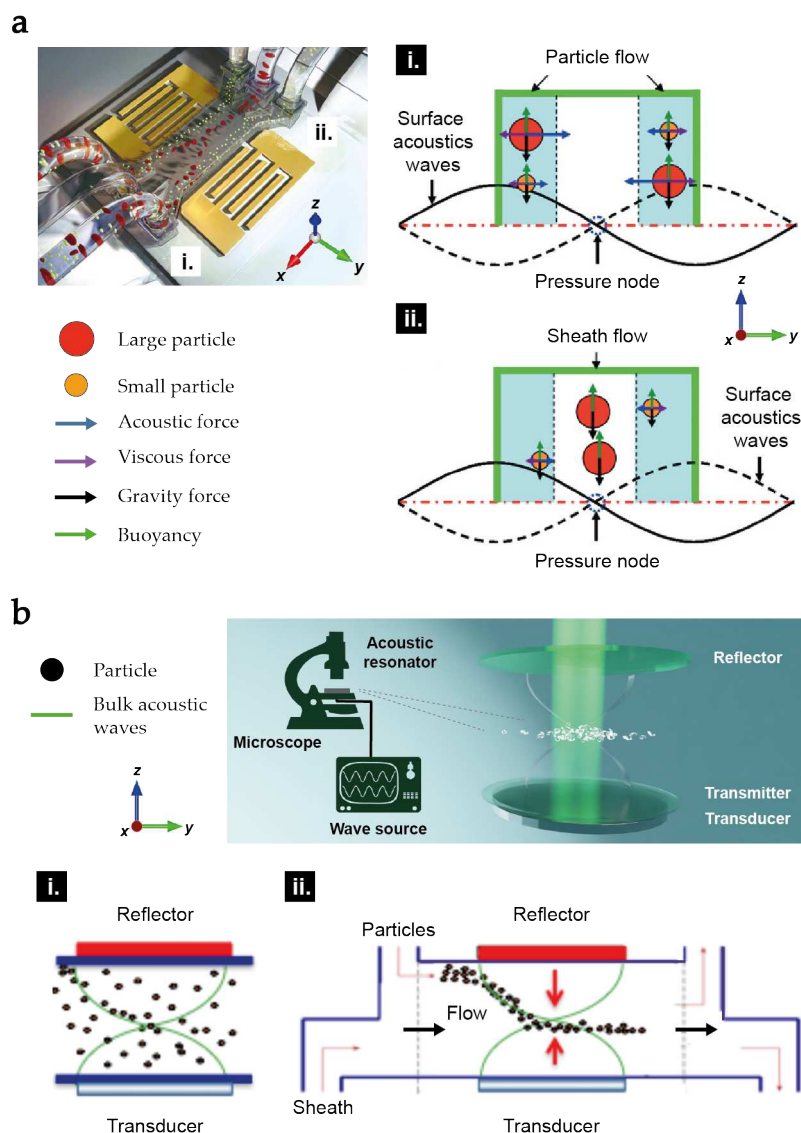


FIGURE 1.18: Principle of acoustic levitation by (a) surface and (b) bulk acoustic waves. In the former case, a flow is imposed in a microchannel composed of three inputs and three outputs, where a mix of small and large particles is injected through side entrances. The ultrasonic environment generated by the interdigital transducers displaces the larger objects into the center, while the smaller ones remain close to the walls as determined by the exposition time to acoustics. Later on, the large particles are collected from the central outlet, whereas the smaller ones exit through the sides. In the latter case, the particles are drawn to the mid-height of the acoustic cavity and observed under an optical microscope. The typical size of the objects that can be moved by ARF ranges from 100 nm to several tens of microns, while the usual thickness of a microchannel can be a few hundreds of microns. Similarly, acoustofluidic sorting devices can be built based on the difference in acoustic response displayed by various materials and an optimal design of the microchip. Adapted from [120, 118, 121].

of particles in the nodal plane as depicted by Fig. 1.18(b). One of which is the transverse component of the ARF given by:

$$F_T = d_p^3 \frac{3(\rho_p - \rho_f)}{\rho_f + 2\rho_p} \vec{\nabla} \langle E_{ac} \rangle \quad (1.12)$$

This force prevails due to the inhomogeneity of acoustic source and the edge effects linked to the walls of a resonant cavity. This term being usually two orders of magnitude lower than the primary ARF becomes predominant only at the pressure node [124, 125]. As the axial component of the ARF zeroes out in the nodal plane, its transverse component F_T comes in to create an acoustic field that moves the objects confined in the lateral plane to a local point, which ultimately ends up in an aggregate [126].

A third party called Bjerknes force joins in to maintain the aggregates intact [127]. This interparticle attractive term applies strongly over short distances, which render the objects quasi-inseparable upon aggregation [128]. It consists of two terms: (i) the hard sphere contribution possessing two components (F_r , F_θ) and (ii) the one due to compressibility F_{comp} [129, 130]. They each write:

$$F_r = F_{r_0} (3\cos^2(\theta_r) - 1) \quad (1.13)$$

$$F_\theta = F_{r_0} \sin(2\theta_r) \quad (1.14)$$

$$F_{comp} = -\frac{\pi^3 \rho_f f_{ac}^2 p^2 d_p^6 (\beta_p - \beta_f)^2}{72 d_{p-p}^2} \quad (1.15)$$

where the constant $F_{r_0} = \frac{\pi}{96} \frac{d_p^6 (\rho_p - \rho_f)^2}{\rho_f d_{p-p}^4}$, θ_r the interparticle angle projected onto the nodal plane, p the acoustic pressure and d_{p-p} the interparticle distance.

Last but not least, the ubiquitous presence of acoustic streaming should be accounted for. This latter defines a generated flow in the surrounding fluid of an object due to the attenuation of acoustic waves [131]. As it was first documented by Rayleigh, this perturbation was later classified into several categories depending on the resonant cavity's height h , with respect to the acoustic wavelength λ_{ac} .

For the resonant cavity's design in our particular case, where $\lambda_{ac} \sim h$, vortices are most likely to occur near the walls. Kutter and co-workers have shown via particle image velocimetry analysis that there was a size-dependence of the particles' motion, either being ARF- or acoustic streaming-dominated [132]. Thereby in the scenario of 1 μm polystyrene beads, these objects acted as tracers for the liquid motion and the resulting vortex-like structure in the flow field prevented these particles from accumulating at the pressure node. This acoustic streaming term, though it may seem disruptive, but it can be harvested to promote the aggregation of cells in certain cases and also, for an efficient fluid mixing in a microchannel [133, 134, 135].

In short, in resonant cavities generated by bulk acoustic waves, the main force acting on a suspension of particles is the primary axial ARF that confines these latter onto the nodal plane (Fig. 1.19(a)). Upon reaching this state, the transverse component of the ARF gathers the particles in an in-plane fashion, along with the Bjerknes force which further compacts

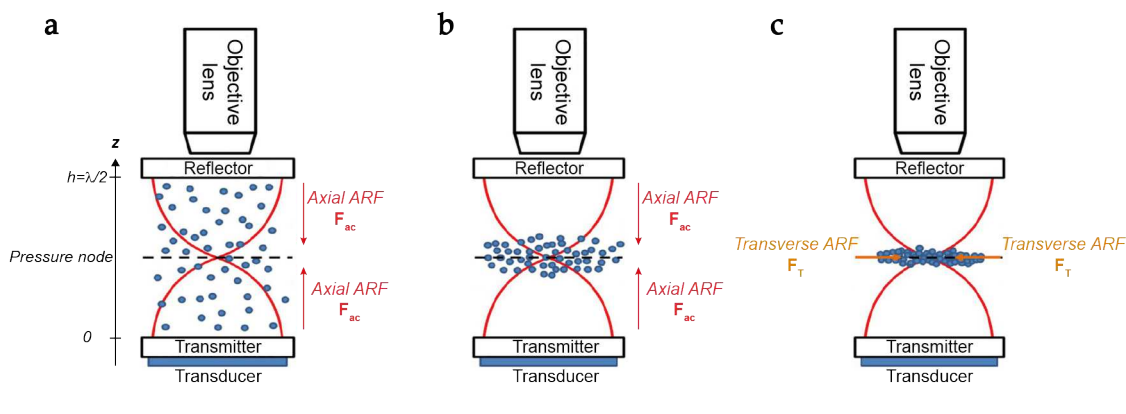


FIGURE 1.19: Scheme of a suspension of particles subjected to ARF manipulation over time. (a,b) The primary axial force F_{ac} drives the objects toward the resonant cavity's mid-height and confines them in the nodal plane. (c) The transverse force F_T then contributes to further compacting these latter into forming an aggregate. Adapted from [136].

them into forming a cohesive aggregate (Fig. 1.19(b,c)). Finally, if there were acoustic streaming rolls occurring in our system, these vortices entrain only a negligible amount of particles near the wall boundaries, while keeping the majority trapped at the pressure node.

Established examples in microfluidics

In **Chapter 4**, this acoustic levitation technique has been tested out with different natures of helical particles and their quantified migration behavior will be discussed later on. In fact, the first suggestion for mechanical chiral separation under microflows was proposed by Hänggi and co-workers' theoretical study, based on the transport properties of a many-bodies system in a spatially variable flow vorticity [137]. The authors demonstrated at stationary state that two different types of fluid vortices with respectively left- and right-handed flow orientations entrained various amounts of a specifically designed chiral enantiomer and thus, motivated several other reports to build distinct computational methods to tackle this exact issue [138, 139, 140].

By cautious design of microchannels and in particular, for those possessing a rectangular cross-section and a high width-to-height aspect ratio, the fluid's flow profile ought to be parabolic along the height-direction, while being uniform over the channel's width. Thereby, Stocker and co-workers studied the motion of helically shaped bacteria of about $16 \mu\text{m}$ long, in such Poiseuille flow where the shear rate varies linearly over the channel's height with a negative (resp. positive) sign in the upper (resp. lower) half of this latter as shown by Fig. 1.20(a) [141]. The authors essentially observed a lateral drift trajectory perpendicularly to the flow that was dependent on both the helices' chirality and the sign of the imposed shear rate. This reached a lateral separation Δz up to several hundreds of microns in a microchannel of $100 \mu\text{m}$ long, pumped by a mean pressure-driven parabolic flow of $3 \text{ mm}\cdot\text{s}^{-1}$ which illustrated a huge leap forward in enabling chiral resolution by shear, in view of feasible manufacturing techniques.

Another demonstration of experimentally separating colloidal chiral particles has been reported by Bechinger and co-workers [142]. The symmetry-breaking of the flow profile in a rectangular microchannel was achieved by topologically patterning slanted grooves on its top wall and thus resulting in a helical flow field, whose circulation direction depended

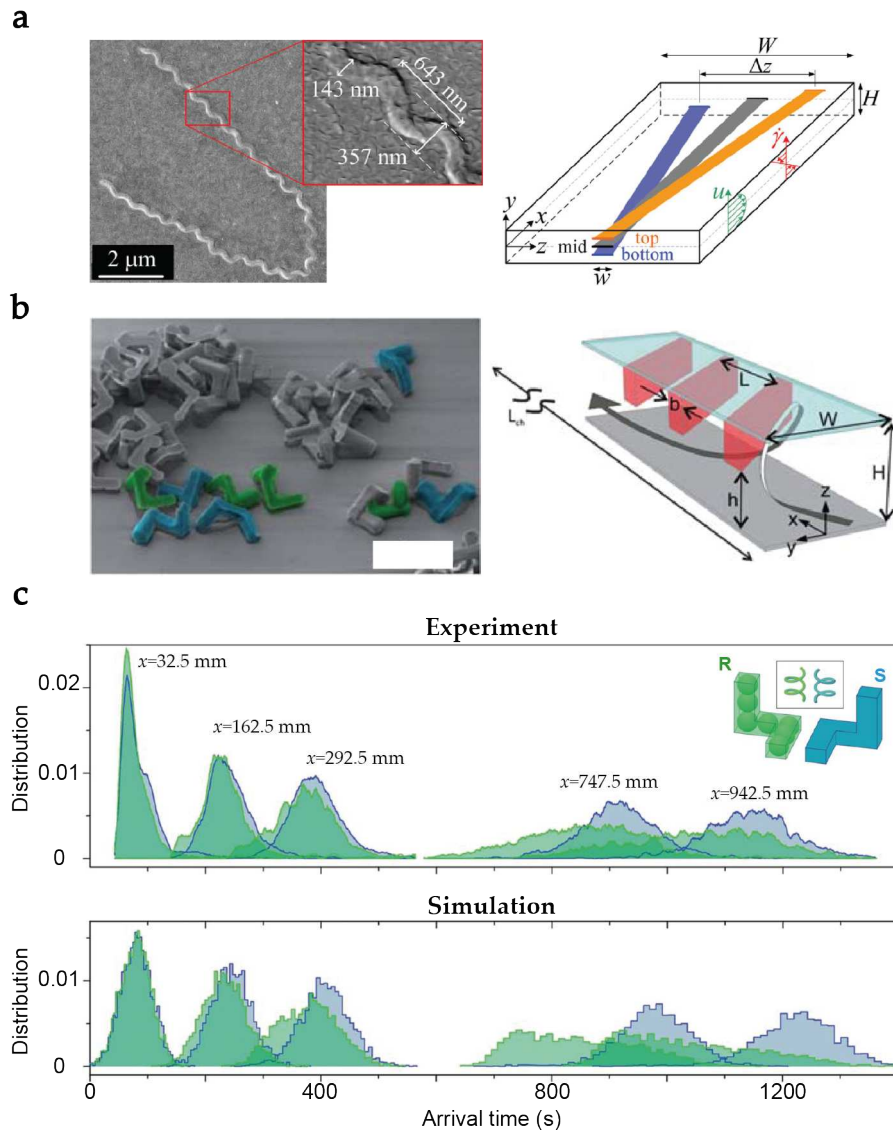


FIGURE 1.20: (a) SEM image of the helically shaped bacteria *Leptospira biflexa flaB* mutant, whose dimensions are noted in the inset. During separation process for one enantiomer in a microchannel, where $W = 1 \text{ mm}$, $H = 90 \text{ }\mu\text{m}$ and $w = 100 \text{ }\mu\text{m}$, the lateral drift direction depends on the sign of the shear rate $\dot{\gamma}$, resulting in divergence of the top and bottom streams. (b) SEM image of chiral particles fabricated from photoresist SU-8 by photolithography and labeled with green Nile Red and blue 2.6-ANS fluorescent dyes. In the microscope image however, these latter are artificially colored to match their chirality. A microchannel displaying polydimethylsiloxane (color-coded in red) that is periodically patterned with obliquely oriented ridges on its top wall, is used in experiment. As a result, the application of a pressure gradient along the channel creates a right-handed helical flow field. Scale bar: $10 \text{ }\mu\text{m}$. (c) Measured and simulated arrival time distributions of R- and S-particles at different channel positions x , relative to the initial injection point. Adapted from [141, 142].

on the orientation of these imprinted grooves as depicted by Fig. 1.20(b). Right-handed particles fabricated from photoresistive materials and measuring several unities of microns, displayed a higher migration speed than their chiral moieties when they were both simultaneously placed in a swirling flow field of right-handed circulation direction. This velocity difference up to several hundreds of $\mu\text{m}\cdot\text{s}^{-1}$ was understood to arise from the minimization of objects' frictional losses to the surrounding fluid. In which case for *S*-particles traveling in a right-handed flow, these latter tend to situate close to the walls to result in greater viscous frictions and thus, a lower migration speed in a microchannel of 1 m long under a flow velocity of $1\text{ mm}\cdot\text{s}^{-1}$.

In principle, the stakes of mechanical chiral resolution for objects that are sized at the limit of $1\ \mu\text{m}$ incline mainly toward lowering their rotational diffusion due to thermal fluctuations. This is shown to be attained by applying secondary forces through fluid mechanical or optical means in lab-on-a-chip approaches for instance. These introduced chiral forces serve to directly couple the orientation of objects with respect to their surrounding and under an optimized flow, sorting of enantiomers is rendered possible. In addition to the existing acoustofluidic method that has been evoked earlier, we suggest herein a supplementary coupling with light excitations of our resonant cavities during experiments of acoustic levitation. This has contributed to the appearance of a novel phenomenon known as opto-acoustophoresis where particles in a suspension migrate promptly and selectively under an excitation of these two coupled-forces. Therefore as a preliminary proof-of-concept, the migration behavior of chiral particles has been mapped in **Chapter 4** for the identification of key parameters that are in play during this occurrence. With these being clarified, further work ought to pronounce a new generation of chiral separation devices in particular, dedicated to particles in the nanometer range.

1.3 Conclusion

In the first part of this introductory chapter, the main idea of two-dimensionally shaped semiconductor nanoparticles known as NPLs has been presented. The size-modulated optical properties of these materials are dictated by the behavior of excitons located in a confinement regime. In this specific case where only one single dimension of the nanocrystals occurs to be smaller than the Bohr radius of its bulk material, these NPLs are assimilated to quantum wells that exhibit atomic-scale thicknesses and large lateral sizes. As first reported in 2008, cadmium-based NPLs that crystallized under the cubic zinc blende structure allow since then a vast manipulation in terms of their shape and composition, to be transformed into adequate candidates for physical and chemical studies.

As to answering the question of symmetry breaking during the growth of NPLs, a plausible explanation widely accepted by the community has been given from an energetic approach of island nucleation. This consists of comparing the growth cost on respectively wide and narrow facets of a cuboid, which justifies its preferred lateral extended version that is thermodynamically driven. As to obtaining thicker NPLs through prolonged heating during synthesis, this is revealed to be due to the interparticle Ostwald ripening from the thinner structures to the thicker ones, taking place in a two-dimensional fashion.

Owing to the flexibility of these ultrathin sheets and how prone they are to deformations upon surface chemistry functionalization, at equilibrium these nanostructures adapt conformations that minimize their internal energy. This has essentially given rise to a panel of helical shapes according to their geometry factor. Occurring chiral objects can be found in the nature, as theorized by macromechanical studies based on the concept of residually stressed bodies. Herein, nanohelices resulting from large pieces of NPLs are perfect analogue to this system at the nanoscale.

Thanks to the crystallographic founding of cubic zinc blende NPLs, their surface features represent a known asset that is leveraged to investigate peculiar properties like interface lattice mismatches between the inorganic core and anchoring groups of ligand shell, plus the induction of chirality brought by the adsorption of surface stabilizers. These two phenomena constitute the majority of this body of work as detailed in **Chapters 2 and 3**, in which our main focus has been dedicated onto CdSe NPLs of various shapes (square, rectangular, twisted and helical) and thicknesses (2, 3, 4, 5, 6 and 7 MLs).

The origin of inorganic chiral materials in particular for II-VI semiconductor nanoparticles can be due to the: (i) presence of intrinsic chiral defects, (ii) manifestation from a nonracemic ensemble of chiral geometries, (iii) stabilizing shell of chiral surface ligands and (iv) hierarchical chirality resulting from an assembly. Factors (ii) and (iii) for instance will be showcased throughout **Chapter 3**, which have resulted in cadmium-based NPLs that are actively chiral-absorptive. A discussion revolving around the effect of selected chiral ligands on the magnitude of induced dissymmetry will also be notably highlighted.

Arriving onto **Chapter 4** that is purely centered on the manipulation of helical objects, the scope of our investigation for CD is evidenced by the previously mentioned factor (iv): hierarchical chirality resulting from an assembly. The fact that hybrid gemini surfactant-silica helices can be synthesized under their pure enantiomeric form, this structure has been taken into advantage to host distinct incoming guests like semiconductor CdSe NPLs, plasmonic gold nanoparticles and fluorescein organic fluorophores. Suspensions of these resulting tribrid systems have later been characterized under opto-acoustophoresis resonant

studies which aim to serve as basis for further mechanical chiral resolution projects.

Chapter 2

Folding of nanoplatelets

Colloidal II-VI semiconductor NPLs present strong, narrow optical transitions and fast exciton recombination, which render them interesting candidates for optical gain and laser applications. For this purpose, it is essential to implement nanocrystals with a high photoluminescence quantum yield, in order to achieve satisfying results. One of the strategies is by synthesizing nanocrystals with small lateral sizes to reduce the presence of exciton traps [143]. On the contrary, I am hereby looking at NPLs with subatomic thicknesses which span up to thousands of nm². These extremely thin nanosheets can indeed be assimilated as flexible substrates which could undergo transitions in morphology, when external stresses are exerted onto them. In our daily life, we could simply picture how a piece of paper is deformed when a weight is placed onto it. The system becomes overall geometrically frustrated due to an applied torque that results in the bending and buckling of objects.

Nature has always been the source of inspiration for a huge number of research works. Often the origin of shape motions might originate from an object's swelling and shrinkage, caused by the variation of water concentration for instance and thus leading to osmosis within membranes. Typically in biological sclerenchymal tissues, these latter expand and shrink in an anisotropic fashion due to the accumulation of elastic energy and build-up of stresses [144]. Besides, changes in air humidity induce such uniaxial modifications as well, in cases of opening and closing of a pine cone and the penetration of wheat seeds into soil [145, 146]. Further examples are also embedded by plant tendrils and horns of mountain goats, in response to adapting suitably to the presence of external stimuli.

An illustration is reported by Armon et al. on the opening of pods of *Bauhenia variegata*, whose valves consist of two perpendicularly oriented fibrous layers, in respect to their longitudinal axis [26]. The flat-to-helical transition that is observed during their opening turns out to be driven by these two actual layers which are shrinking in perpendicular directions. The metric incompatibility that results from this tendency, causes a modification in the curvature tensor that ultimately dictates the local configuration of a surface. Similarly, such mathematical derivations are also unveiled by certain amphiphiles that self-assemble via short-range interactions into chiral nanoribbons, that are proven to be geometrically incompatible [30].

As a bridge to the previously introduced crystal structure of colloidal II-VI semiconductor NPLs, it is fair to say that our system resembles in principle, the reported chiral seed pods. Seemingly, the presence of in-plane perpendicular stresses is strong enough to drive the formation of spontaneous curvatures on these sufficiently large and nonetheless, atomically ultrathin inorganic nanosheets. Findings that are both experimentally and quantitatively supported, reveal a unique shape evolution for such bodies composed of residually stressed layers and suggest a general framework for nanomechanical studies.

2.1 Studies on CdSe homostructures

In the beginning, 3 MLs CdSe NPLs are synthesized according to the protocol as listed in the **Materials and Methods** section, which exhibit an average geometry of around $(300 \times 80 \times 1) \text{ nm}^3$. These pristine synthesized nanohelices are capped with a mix of a short (acetate) and a long (oleate) carboxylate as evidenced by fourrier transform infrared (FTIR) and ^1H nuclear magnetic resonance (NMR) data. Later on, these native carboxylate ligands are thoroughly exchanged with linear thiolate ones $\text{C}_n\text{H}_{2n+1}\text{S}^-$, where $n = 2, 4, 8, 12, 18$. The ligand exchange is carried out in two steps, to ensure a complete surface chemistry substitution before being characterized under FTIR and energy dispersive X-ray (EDX) analysis. Besides, these exchanges induce a redshift of their optical features which arises principally from two effects: (i) the partial delocalization of the exciton wave function over the sulfide planes and (ii) a change from a contractile strain to a tensile strain in the NPLs' thickness direction, which induces an increase in the associated lattice parameter along the z -axis and thus, a decrease of the quantum confinement.

2.1.1 Modifications of surface chemistry

Intuitively, it would be difficult to estimate the actual lateral dimensions of a piece of initially folded nanohelix. However as demonstrated by Ithurria and co-workers, the exchange from COO^- to X^- , halide ligands in particular iodides co-passivated by oleylamine, resulted in NPLs that were completely unfolded and lying flat on their large lateral facets as imaged under transmission electron microscope (TEM) [147]. Via this method, one can then easily deduce a distribution of any NPLs' associated lateral dimensions (Fig. 2.1(a,b)). This yields for instance, over 25000 nm^2 in average for a piece of 3 MLs CdSe NPL. Under FTIR as shown in Fig. 2.1(c), as-synthesized carboxylates-capped nanohelices present intense characteristic peaks of their asymmetrical and symmetrical vibrations, situated around 1525 and 1420 cm^{-1} . Besides, the presence of alkyl parts is shown in the region of 2900 cm^{-1} .

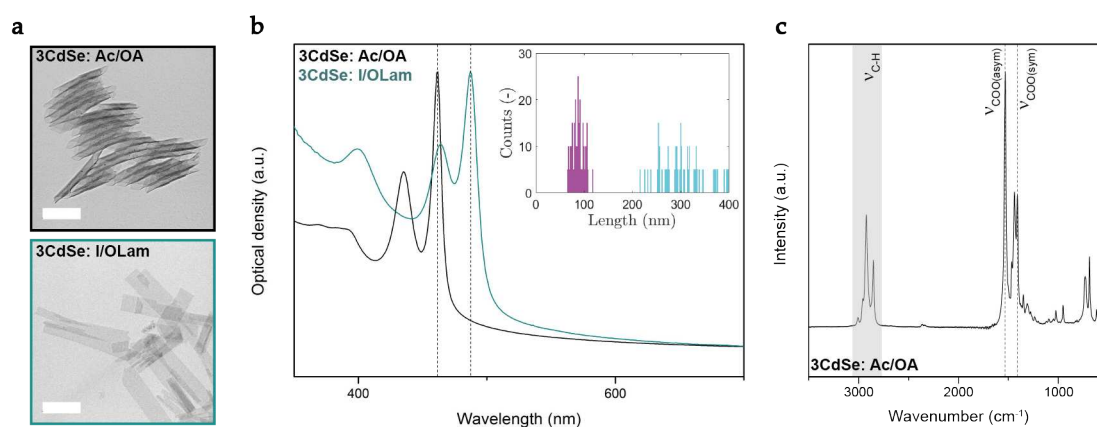


FIGURE 2.1: (a) TEM images of similar 3 MLs CdSe NPLs with two different surface chemistries. They are either capped by a mix of acetates-oleates under folded shapes or flattened with iodides co-stabilized by oleylamine. (b) Absorption spectrum displays a $\sim 30 \text{ nm}$ redshift upon the ligand exchange. The inset shows the distribution of dimensions along the short- (magenta) and long-axis (cyan) of these NPLs. Measured values are respectively $(88 \pm 12) \text{ nm}$ and $(302 \pm 45) \text{ nm}$, analyzed over a population of 100 nanoobjects. Scale bar: 200 nm . (c) FTIR spectrum of the carboxylates-capped nanohelices.

As for ^1H NMR analysis, one ought to observe a mix of proton features originating from acetates and oleates as they are both introduced during the synthesis. Simulations performed with *nmrdb* that are done on acetic and oleic acids, first demonstrate theoretical values of the location of expected peaks and indeed, they are well matched with the experimental spectra obtained for NPLs. Tab. 2.1 recapitulates the peaks' chemical shift and multiplicity calculated separately for these short and long carboxylic acid chains. In side-to-side comparison with NPLs, one could easily distinguish the protons of acetic acids localized around 2.0 ppm and the triplet methyl CH_3 contribution of oleic acids around 0.9 ppm (Fig. 2.2). Upon a fine resonance integration, a molecular ratio of acetates-to-oleates present on a NPL can be estimated in the order of 3.5:1.0, where one assumes primarily a homogenous ligand distribution on each individual particle over the entire ensemble of analyzed NPLs.

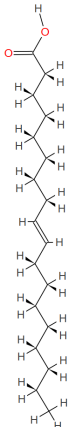
Carboxylic acids	Chemical shift (ppm)	Number of hydrogen atoms	Multiplicity
	2.03	3	Singlet
	0.86	3	Triplet
	1.17-1.34	16	Quintuplet, triplet triplet, hexaplet
	1.36-1.62	6	Triplet triplet
	1.89-2.03	4	Quadruplet
	2.30	2	Triplet
	5.30-5.45	2	Doublet triplet

TABLE 2.1: Associated ^1H NMR chemical shifts and multiplicities simulated for acetic and oleic acids.

As Artemyev and co-workers have detailed about the intrinsic absorption behavior of NPLs that is both strongly thickness- and aspect ratio-dependent, the authors render the possibility to obtain coefficients that can be used for nanoparticles' concentration determination in solution [148]. Via this method of absorbance measurements, one can deduce the NPLs' volume fraction at 309 nm and alongside with the classical Beer-Lambert equation, the concentration of oleates can also be determined at 267 nm which corresponds to the absorption of double-bond in the near-UV region for a given molar extinction coefficient [149]. Hence by combining the prior ratio of acetates-to-oleates evaluated at 3.5:1.0, one can then proceed to estimate the global coverage of both surface ligands through an expression: $\sigma = \frac{C_{\text{ligands}}}{C_{\text{NPLs}}} \cdot \frac{1}{S_{\text{NPL}}}$. At first numerical approximations, this yields a ligand coverage of 2.3 nm^{-2} which is lower than the reported values of 5.3 (resp. 4.0 nm^{-2}) obtained for 5 MLs CdSe NPLs (resp. nanospheroids of 3.4 nm in diameter) by Hens and co-workers [150, 151]. Herein, the difference in values might surely be due to the desorption of certain weakly bound carboxylates after several steps of extensive purification. Undeniably, sophisticated NMR resolved experiments that involve probing of the dynamic nuclear polarization can

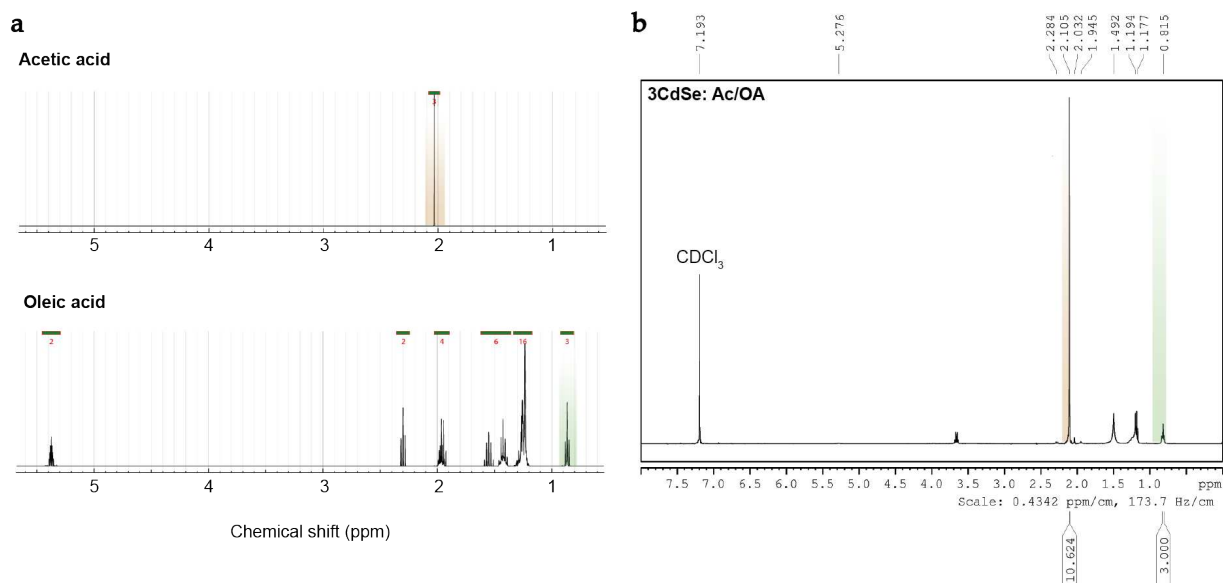


FIGURE 2.2: Simulated ^1H NMR spectra of (a) acetic and oleic acids, along with (b) an experimentally obtained one for carboxylates-capped 3 MLs CdSe NPLs where deuterated chloroform is used as solvent. The contributions originating from acetates (resp. oleates) are highlighted in orange (resp. green).

further confirm the detailed surface structures of such inorganic nanocrystals that consist of elements with spin- $\frac{1}{2}$ isotopes [152].

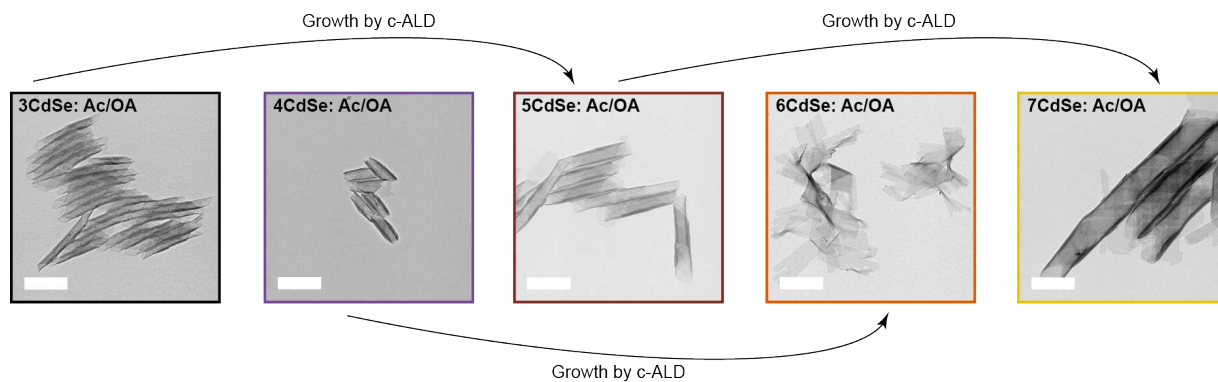


FIGURE 2.3: TEM images of as-synthesized carboxylates-capped CdSe NPLs. Nanohelices which possess an odd (resp. even) number of MLs, are subsequently obtained via the route of c-ALD with 3 (resp. 4 MLs) ones as the starting blocks. Scale bar: 200 nm.

Herein, thicker CdSe NPLs are synthesized via the route of c-ALD which conserves the parity number of MLs of a NPL [57]. Both anions and cations are subsequently deposited onto the initial starting blocks. Thereby, nanohelices with an odd (resp. even) number of MLs can be orderly obtained such as from 3 to 5 and eventually to the population of 7 ones (resp. 4 to 6) as depicted in Fig. 2.3. The surface chemistry of these objects remains globally unchanged, where they are passivated by a mix of carboxylates.

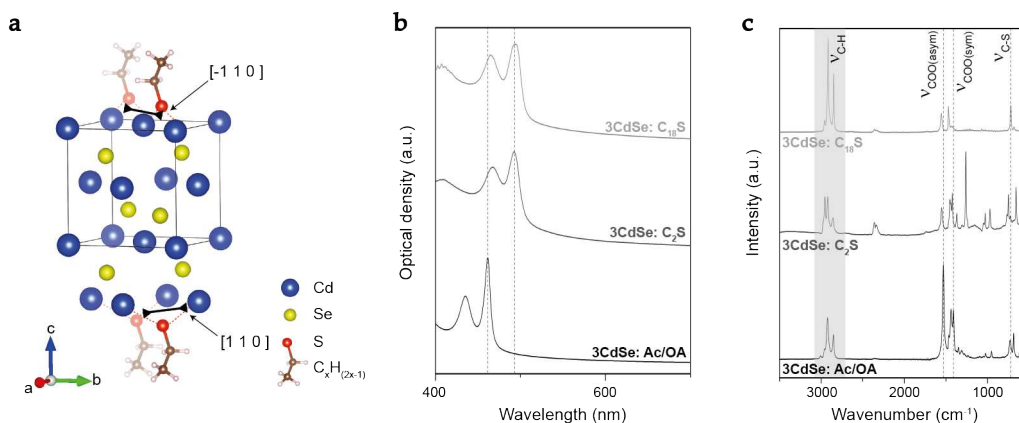


FIGURE 2.4: (a) CdSe zinc blende crystal structure represented by a 3 MLs NPL. The arrows illustrate the compressive stresses brought by ethanethiolate ligands. The presence of a $\bar{4}$ axis along the NPL's thickness direction \bar{c} , induces contractile strain on the top and bottom wide facets oriented at 90° from one another. (b) Absorption spectra of 3 MLs CdSe nanohelices before and after surface ligand modifications, from initially acetates/oleates-capped to either ethanethiolates- or octadecanethiolates-capped. Their corresponding FTIR spectra are shown in (c).

Subsequently by replacing these latter RCOO^- with RS^- ligands of different chain lengths, the fore-mentioned characteristic peaks of the carboxylates disappear with the exchange by various alkanethiolates. Plus, the appearance of a new peak around 700 cm^{-1} confirms the presence of carbonsulfide bonds in the system as displayed in Fig. 2.4(c). The atomic ratio of sulfur-to-surface cadmiums of NPLs is quantified by EDX and demonstrates a good agreement of 1.0:1.0 if the cations were fully passivated by thiolates in a bridging fashion (Tab. 2.2). Furthermore, the two optical transitions attributed to the heavy (resp. light) hole to conduction band transitions located around 463 (resp. 433 nm) for carboxylates-capped 3 MLs CdSe NPLs, shift to 494 ± 1 (resp. 470 ± 1 nm) when they are fully substituted by surface thiolates as shown in Fig. 2.4(b).

3 MLs CdSe NPLs	Carboxylates-capped			Thiolates-capped			
	Number of planes	Atomic ratio in theory (%)	Result (%)	Number of planes	Atomic ratio in theory (%)	Result for C_2S (%)	Result for C_{18}S (%)
Cd	4	57.1	58.0 ± 2.0	4	44.4	46.5 ± 3.5	44.0 ± 2.0
Se	3	42.9	42.0 ± 2.0	3	33.3	32.5 ± 4.0	33.5 ± 1.5
S	-	-	-	2	22.3	21.0 ± 2.5	22.5 ± 0.5

TABLE 2.2: Theoretical and experimental atomic ratios of cadmium, selenium and sulfur for carboxylates- and thiolates-capped 3 MLs NPLs.

Observations under TEM show that the pristine carboxylate-capped 3 MLs CdSe nanohelices possess in average 9 nm in terms of helices' radii. As the native ligands are replaced by alkanethiolates of various chain lengths ($n = 2, 4, 8, 12, 18$), their associated radius increases with the number of carbon which constitutes these aliphatic chains. These

values range from 6.5 to 13 nm and identical ligand exchanges are performed on all thickness populations of CdSe NPLs. Their corresponding radii are measured with the analysis of microscope images under *ImageJ* and later, plotted as a function of carbon number which constitutes the linear alkanethiolates that are anchored onto their outer surface (Fig. 2.5).

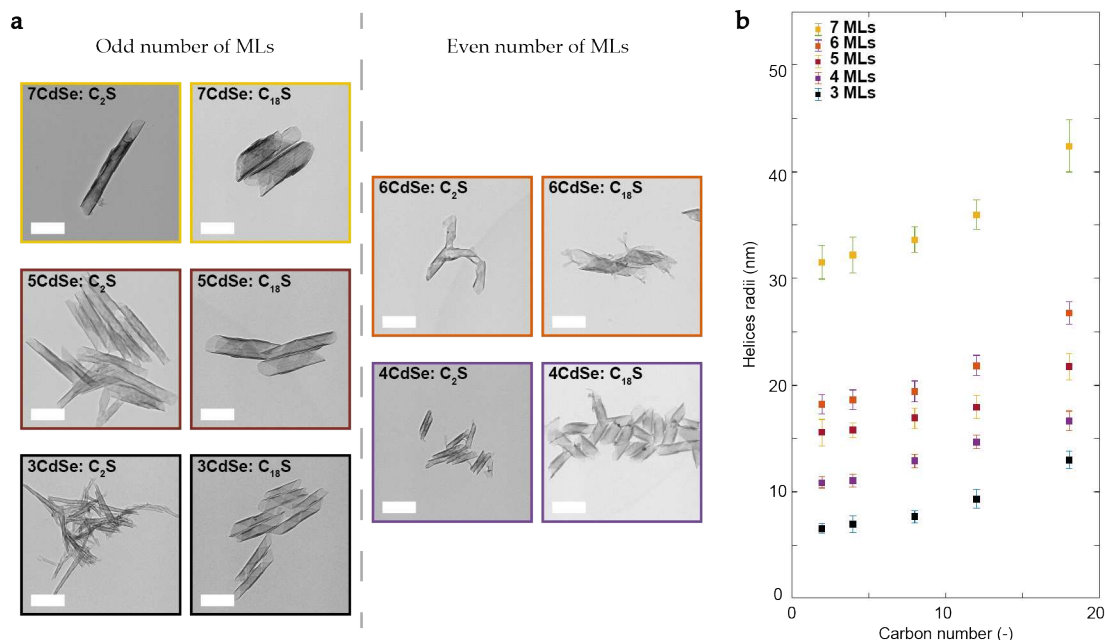


FIGURE 2.5: (a) TEM images of CdSe NPLs which have been chemically surface-modified and present either ethanethiolates or octadecanethiolates on their outer surface. Left (resp. right) panel displays images of odd (resp. even) number of MLs NPLs. Scale bar: 200 nm. (b) Experimental helices' radii deduced from the analysis of microscope images for CdSe NPLs with thicknesses ranging from 3 to 7 MLs, averaged over a population of 100 nanohelices.

Herein, one single thiolate group bridges two surface cadmiums to provide these atoms a tetrahedral environment, which induces compressive stresses along the $[1\ 1\ 0]$ and $[-1\ 1\ 0]$ directions on the two opposite wide facets of a CdSe NPL as displayed in Fig. 2.4(a). Thus at final state, this latter curls with either its top or bottom facets located in the inner side of a helix, both with equal probability. This results in a population of nanohelices of a given handedness, where the compressive stresses are directed perpendicularly to the helical axis on their inner side. Under electronic microscope, it is possible to distinguish the related contrast of nanohelices in a sufficiently diluted environment and both handedness are accounted for the radii measurement over 100 nanoparticles without bias (Fig. 2.6).

Structural details within a helix

When a NPL becomes wide enough, it adopts the geometry of cut-out strips from a cylinder with one single principal curvature along the $[1\ 1\ 0]$ direction (Fig. 2.7(b)). Whereas for narrow NPLs, twisted structures are rather obtained. The continuous transition between these two limiting regimes is manifested by the substrate's geometry itself. Data extracted from the measurement of surface topography by optical profilometry demonstrated values of mean and Gaussian curvatures that dictated the global shape of these helical strips with varying widths [26].

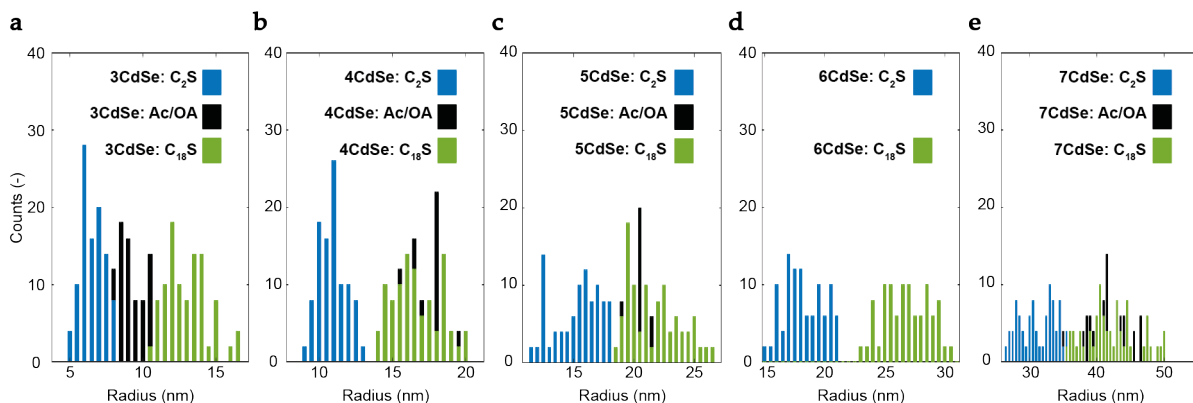


FIGURE 2.6: Distributions of CdSe nanohelices' radii for NPLs with thicknesses ranging from (a) 3 to (e) 7 MLs. Blue (resp. black and green) bars represent nanoparticles which are capped by ethanethiolates (resp. acetates-oleates and octadecanethiolates), analyzed over a population of 100 nanohelices. Bin: 0.5 nm.

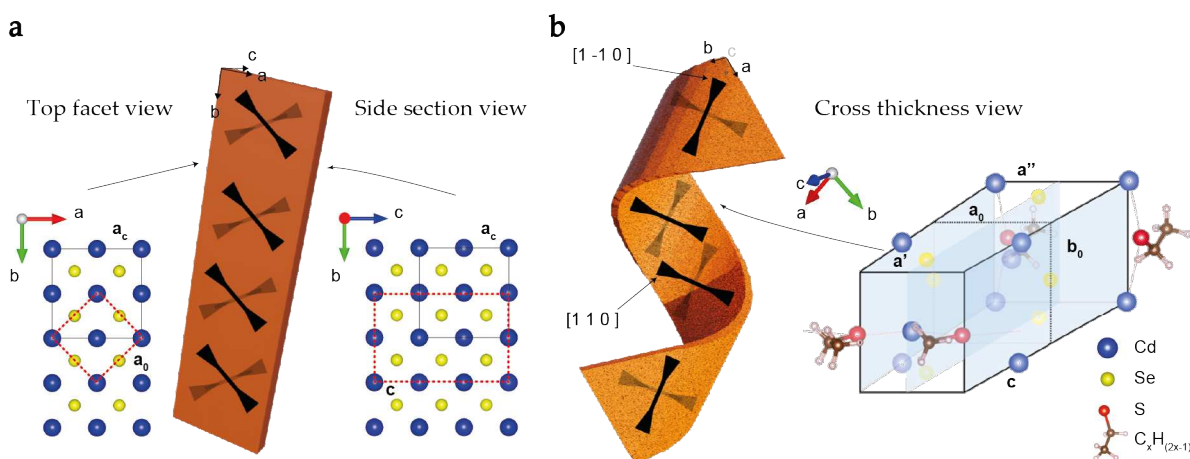


FIGURE 2.7: (a) Scheme of a zinc blende 3 MLs CdSe flat NPL, with a cubic cell (a, b, c). The black arrows illustrate the compressive stresses induced by thiolate ligands on CdSe, which are oriented perpendicularly to one another between top and bottom wide facets. The crystal atomic structure is displayed under two different viewing angles (either top facet or side section), where the initial zinc blende lattice parameter a_c , and the derived one obtained for smaller repeated motifs a_0 , are shown. (b) As the same piece of flat wide NPL curls into a helix in order to minimize its internal elastic energy, the compressive stresses are directed perpendicularly (resp. parallel) to its helical axis on the inner (resp. outer) surface of the structure. The atomic-scale elemental volume with its average dimension (a_0, b_0, c) is drawn. Along the $[1\ 1\ 0]$ direction, the derived lattice parameter varies linearly from a' to a'' with a constant curvature.

Within a piece of nanohelix, an atomic-scale elemental volume as depicted by the inset of Fig. 2.7(b), which possesses a constant curvature can be derived from its initial zinc blende crystal structure. This motif, which in repetition constitutes the helix itself, results from the lattice mismatch that is due to the adsorption of surface thiolates on the inner side of a helix, along the $[1\ 1\ 0]$ direction. On the other hand, the stresses induced along the

[1 -1 0] direction on the outer side of the structure, plays an insignificant role during bending.

In Fig. 2.7(b), the lattice parameter, a varies linearly across the thickness of a piece of helix from a' to a'' along the [1 1 0] direction. The average value in the mid-plane, noted a_0 is given by the expression $a_c \cdot \frac{\sqrt{2}}{2}$, where a_c is the bulk lattice parameter of CdSe. Moving on, the parameter b_0 that situates orthogonally to a , along the [1 -1 0] direction remains unmodified across the thickness direction \vec{c} , of the NPL. Therefore, this variable stays undeformed independently of the nanohelices' handedness and writes similarly to the expression of a_0 .

2.1.2 Mechanical modeling of bending

Adsorbing ligands on a CdSe NPL induces surface stresses on each wide opposite facet of the object. These stresses are contractile and uniaxial with orthogonal orientations at $\pm 45^\circ$ (on wide facets along the [1 1 0] and [1 -1 0] directions), in respect to the [0 1 0] growth direction of NPLs. If these ligands would solely adsorb on one facet, such surface stresses would result in the bending of the NPL dictated by the direction of the uniaxial stress. As a consequence, the helix would wrap around a cylinder whose radius R , is given by the balance between surface stresses and the substrate's bending stiffness. This is identical to the standard case of temperature-activated bilayers which are most commonly observed in the field of engineering [153, 154]. The axis of the cylinder would then be orthogonal to the direction of the applied stresses, which in turn leads to the formation of a helical ribbon.

A general case was studied by Sharon and co-workers with a laminated model involving two pre-stretched layers in orthogonal directions [26]. Once the laminated sheet was cut into strips, twisted ribbons of negative Gaussian curvature or helical ribbons that wrapped around a cylinder may be obtained, depending on the relative width $\tilde{w} = \frac{w}{\sqrt{Rt}}$, of the strips. It is noted that w is its actual width, t its thickness and R the resulting radius that minimizes the bending energy. In the case of wide ribbons ($\tilde{w} \gg 1$), which is relevant to the configuration of our NPLs, the authors predicted the formation of helical ribbons of radius R , as if surface stresses were only present on one single facet. Herein, stresses induced by the ligands adsorbed on the outer surface of a piece of helix do not participate in bending. One can then focus on the misfit between the inorganic part and ligands that are only adsorbed on the helix's inner surface, in order to generate radii predictions as a function of the NPLs' thickness and the length of the various experimentally introduced linear aliphatic chains.

In our case, orthogonal stresses are present on both opposite facets of a single NPL. As explained beforehand, each of these facets will tend to induce bending along its own direction. From a mechanical point of view, the surface will result into a saddle shape with principal curvatures of opposing sign, $\pm \frac{1}{R}$ as illustrated in Fig. 2.8(a). However, such transformation encounters a strong geometrical constraint rationalized by the theory of incompatible elasticity [28, 29]. A quantity referred to Gaussian curvature, is defined as the product of these two principal curvatures at any given location on a surface. Following the Gauss theorem, which states that any modification to the Gaussian curvature such as transforming a flat substrate with zero curvature to a saddle with negative value, induces in-plane distortions [155]. In the case of ultrathin sheets, it is essential to note that in-plane deformations cost highly in terms of elastic energy than the phenomenon of bending itself. Therefore, the transformation of an object possessing opposite facets subjected to orthogonal stresses, into a structure with negative Gaussian curvature is strongly hindered.

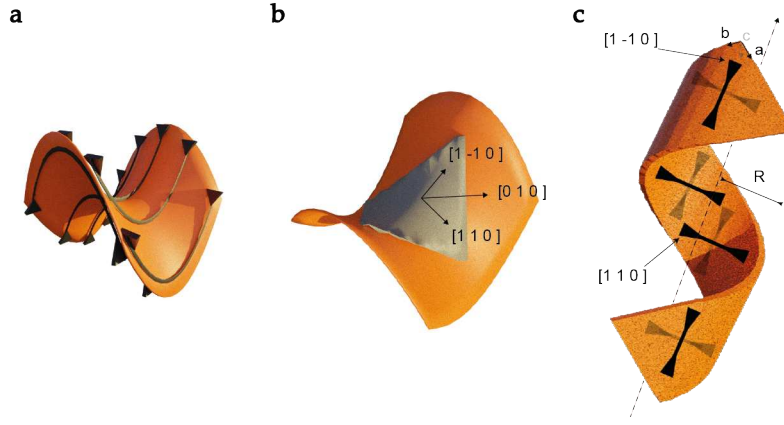


FIGURE 2.8: Scheme of a 3 MLs square nanosheet of zinc blende crystal structure. The arrows represent the compressing directions due to the adsorption of surface ligands. On the top (resp. bottom) facet, the induced stress is directed along the $[1 -1 0]$ (resp. $[1 1 0]$) direction. If a wide strip ($\tilde{w} \gg 1$) were to be cut from the gray zone in the middle of the nanosheet, this would result in a helix at the equilibrium state.

Two considered misfit layers

Firstly, one can consider a simple two-layers misfit strain system composed of a core and a layer of ligands of respective thicknesses, H and h and Young's moduli, E_s and E_d (Fig. 2.9). The length of the core at rest, L is taken as a reference. Due to a modification in lattice parameters, the rest length of the layer of ligands differs from this reference value, L and is given by $L(1 + \Delta\epsilon)$, where $\Delta\epsilon$ corresponds to the initial misfit between both layers of material. When $\Delta\epsilon$ becomes negative, the ligands' anchoring group brings a contractile stress and conversely, a tensile stress for a positive misfit. Intuitively, when both layers are brought into contact, they tend to adjust their final length at equilibrium, which induces internal stresses that result in bending. This transformation can be decomposed into two steps: (i) the bilayer first adopts an average length, $L(1 + \alpha)$ along its neutral axis and (ii) bends subsequently with a curvature, κ expressed by $\frac{1}{R}$. These steps correspond respectively to an application of axial force and the resulting moment equilibria.

Accounting for the listed effects, the strains in both substrate and deposited layers read:

$$\epsilon_s = \alpha - \kappa(z - d) \quad (2.1)$$

$$\epsilon_d = \alpha - \Delta\epsilon - \kappa(z - d) \quad (2.2)$$

where d is the position of the to-be-determined neutral axis across the cross section of a laminated plate.

If we neglect the Poisson effect, the resulting stresses in both substrate and deposited layers should follow:

$$\sigma_s = E_s \epsilon_s = E_s [\alpha - \kappa(z - d)] \quad (2.3)$$

$$\sigma_d = E_d \epsilon_d = E_d [\alpha - \Delta\epsilon - \kappa(z - d)] \quad (2.4)$$

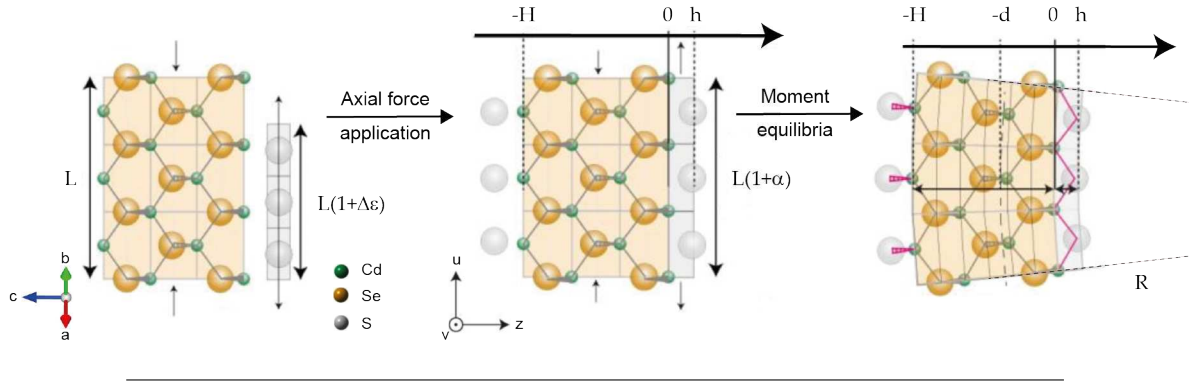


FIGURE 2.9: Schematic decomposition of the cross-section of a NPL into two layers: (i) inorganic core (CdSe) with a thickness H , and (ii) surface ligands' anchoring layer (S^-) with a thickness h . The mismatch, $\Delta\epsilon$ between the two layers along the $[1\ 1\ 0]$ direction of the zinc blende crystal structure (corresponding to \vec{u}) induces residual stresses that result in the phenomenon of bending. Ligands from the outer face are not taken into account as they exert axial forces along the orthogonal direction \vec{v} , and do not participate in the material's deformation.

At equilibrium, the global force and moment corresponding to this stress distribution ought to vanish. Therefore, the force per unit width is given by:

$$f = \int_{-H}^0 \sigma_s dz + \int_0^h \sigma_d dz = \alpha E_s H + (\alpha - \Delta\epsilon) E_d h - \frac{\kappa}{2} [-E_s(H^2 + 2Hd) + E_d(h^2 - 2hd)] = 0 \quad (2.5)$$

As the force balance itself is independent of the curvature, the sum of forces in the two stressed materials should equal to zero. One can then deduce the position of the neutral axis, as well as the effective strain:

$$d = \frac{-E_s H^2 + E_d h^2}{2(E_s H + E_d h)} \quad (2.6)$$

$$\alpha = \frac{E_d h \Delta\epsilon}{E_s H + E_d h} \quad (2.7)$$

Furthermore, in the absence of any external torque such as in the case of free suspending objects, the moment corresponding to its stress distribution calculated in respect to any symmetrical position (for instance, $z = 0$) ought to vanish:

$$M = \int_{-H}^0 \sigma_s z dz + \int_0^h \sigma_d z dz = \frac{-E_s H^2}{2} \alpha + \frac{E_d h^2}{2} (\alpha - \Delta\epsilon) - E_s \left(\frac{H^3}{3} + \frac{H^2 d}{2} \right) \kappa - E_d \left(\frac{h^3}{3} - \frac{h^2 d}{2} \right) \kappa = 0 \quad (2.8)$$

Hence, the induced curvature can be written as:

$$\kappa = \frac{6[E_s E_d H h (H + h) \Delta\epsilon]}{E_s^2 H^4 + E_d^2 h^4 + 6E_s E_d H^2 h^2 + 4E_s E_d H h (H^2 + h^2)} \quad (2.9)$$

For 3 MLs CdSe NPLs capped with sulfides, the thicknesses, H and h of CdSe and the sulfide layer would respectively, be 6 and 1 atomic planes. It is noted that an atomic plane is equivalent to 0.15 nm thick. The outer sulfide layer is neglected, as this latter binds to the cadmium atoms in a direction which is perpendicular to the curvature along the $[1 -1 0]$ crystallographic axis (Fig. 2.9). Therefore, they are not accounted for during the bending of a NPL into a piece of helix. The Young's moduli are taken as those of bulk CdSe and CdS materials, where $E_{s(CdSe)} = 40$ GPa, $E_{d(CdS)} = 46$ GPa. While $\Delta\epsilon$ is first estimated from their bulk lattice mismatch in the order of -3.8% , given that their ideal lattice parameters: $a_{CdSe} = 0.605$ nm and $a_{CdS} = 0.582$ nm. However, with these values, the calculated radius is one order of magnitude larger than the experimentally measured values around 6 nm for 3 MLs CdSe nanohelices capped with ethanethiolates. Surprisingly, only a large misfit strain up to -20% could account for such a large observed curvature via a crude estimation expression: $-\left|\Delta\epsilon\right| \sim \frac{10h}{R}$.

This strong hypothesis is in agreement with results obtained by ab-initio calculations, where a small piece of 4 MLs CdSe NPL capped with HS^- is relaxed by vibrating all of the associated atomic bonds under *Crystal Maker*. Fig. 2.10 demonstrates a piece of NPL before and after energy minimization. In the latter case figure, the sulfide-sulfide distance situates typically around 3.70 \AA , while in zinc blende CdS bulk, it is of 4.11 \AA , with an absolute difference up to 10% . Thus, this goes to show that the electrostatic interactions between the surface cadmiums and sulfides from the ligands, induce a shortening of the Cd-S surface bonds in comparison to the one found for a CdS zinc blende bulk.

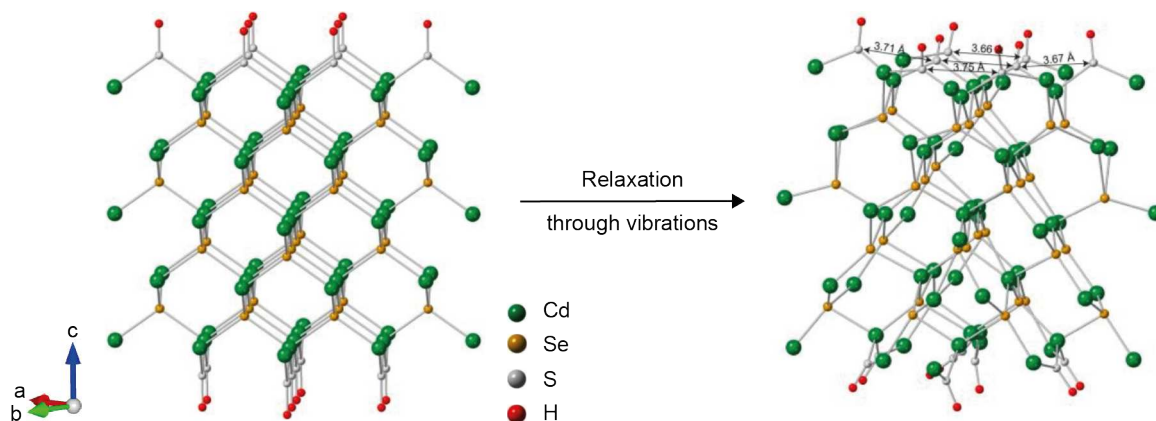


FIGURE 2.10: Relaxation of a tiny piece of 4 MLs NPL capped with bisulfides, possessing the chemical formula HS^- . It demonstrates that the sulfide-to-sulfide distance is reduced compared to the case of a zinc blende CdS bulk, where its lattice parameter equals 4.11 \AA .

Although the order of magnitude of the curling radii of CdSe NPLs indicates unexpectedly important surface stresses induced by thiolates, this strong interaction alone does not explain the variation of the helices radii with the length of the adsorbed ligands. Though, it seems reasonable at first order, to consider a constant mismatch between the inorganic core and sulfides layer, which is independent of the aliphatic chain length. This is because the energetic level of the sulfide orbitals involved in the bridging ought to be unmodified by the length of their organic chains. Secondly, it is essential to account for the steric effect brought by these organic tails, as some of their end-to-end lengths can indeed be larger than a NPL's inorganic core thickness.

Three considered misfit layers

In order to gain more insight, a three-layers model is built from the classical work of Timoshenko, with a supplementary layer of thickness l_n , where its expression is given by $n \cdot d_{(C-C)}$ [156, 157]. Herein, $d_{(C-C)}$ represents the vertical projection of a carbon-carbon bond's distance (Fig. 2.11). In addition, the organic chains are assumed to react with an elastic restoring force during compression with a Young's modulus E_l , that however, do not offer any degree of freedom in stretching. The characteristic rest length of the aliphatic layer is written as $L(1 + \Delta\epsilon'')$. Thus, two misfit strains are considered: (i) $\Delta\epsilon$, the mismatch between the inorganic core and anchoring groups of thiolates and (ii) $\Delta\epsilon''$, the mismatch between the inorganic core and aliphatic chains. Via this reasoning, one can also introduce $\Delta\epsilon'$, which is the dislocation between the anchoring groups and organic tails such that $\Delta\epsilon'' = \Delta\epsilon + \Delta\epsilon'$.

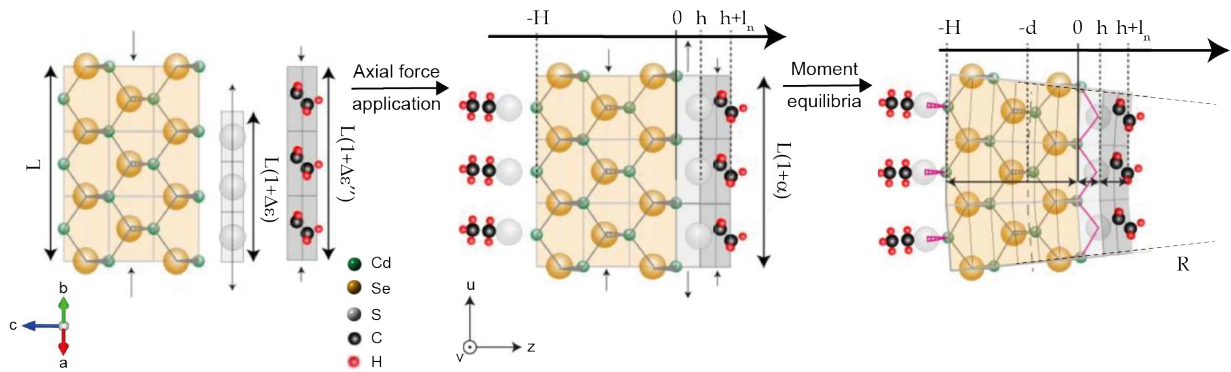


FIGURE 2.11: Schematic decomposition of the cross-section of a NPL into three layers: (i) inorganic core (CdSe), (ii) surface ligands' anchoring layer (S^-) and (iii) aliphatic chain layer (C_nH_{2n+1}) of respective thicknesses H , h and l_n . Mismatches between the layers along the $[1\ 1\ 0]$ direction of the zinc blende crystal structure (corresponding to \vec{u}) induce residual stresses that result in structure's bending. Ligands from the outer face are not taken into account as they exert axial forces along the orthogonal direction \vec{v} and do not contribute to the material's deformation.

As previously, the stresses are written as follows where the Poisson effect is neglected:

$$\sigma_s = E_s \epsilon_s = E_s [\alpha - \kappa(z - d)] \quad (2.10)$$

$$\sigma_d = E_d \epsilon_d = E_d [\alpha - \Delta\epsilon - \kappa(z - d)] \quad (2.11)$$

$$\sigma_l = E_l \epsilon_l = E_l [\alpha - \Delta\epsilon'' - \kappa(z - d)] \quad (2.12)$$

The resulting force per unit width is then given by:

$$f = \int_{-H}^0 \sigma_s dz + \int_0^h \sigma_d dz + \int_h^{h+l_n} \sigma_l dz = \alpha E_s H + (\alpha - \Delta\epsilon) E_d h + (\alpha - \Delta\epsilon'') E_l l_n - \frac{\kappa}{2} [-E_s (H^2 + 2Hd) + E_d (h^2 - 2hd) + E_l [l_n (l_n + 2h) - 2l_n d]] = 0 \quad (2.13)$$

Similarly, the position of the neutral axis and effective strain can be deduced:

$$d = \frac{-E_s H^2 + E_d h^2 + E_l l_n (l_n + 2h)}{2(E_s H + E_d h + E_l l_n)} \quad (2.14)$$

$$\alpha = \frac{E_d h \Delta \epsilon + E_l l_n \Delta \epsilon''}{E_s H + E_d h + E_l l_n} \quad (2.15)$$

The hence associated moment corresponding to the stress distribution calculated in respect to any symmetrical position (for instance, $z = 0$) writes as:

$$\begin{aligned} M &= \int_{-H}^0 \sigma_s z dz + \int_0^h \sigma_d z dz + \int_h^{h+l_n} \sigma_l z dz = \\ &= \frac{-E_s H^2}{2} \alpha + \frac{E_d h^2}{2} (\alpha - \Delta \epsilon) + \frac{E_l l_n (2h + l_n)}{2} (\alpha - \Delta \epsilon) - \\ &= E_s \left(\frac{H^3}{3} + \frac{H^2 d}{2} \right) \kappa - E_d \left(\frac{h^3}{3} - \frac{h^2 d}{2} \right) \kappa - E_l \left(\frac{l_n^3}{3} - \frac{l_n^2 d}{2} + h l_n (h + l_n - d) \right) \kappa = 0 \end{aligned} \quad (2.16)$$

The final expression of the curvature is then determined:

$$\kappa = \frac{6[E_s E_d H h (H+h) \Delta \epsilon + E_d E_l h l_n (h+l_n) \Delta \epsilon' + E_s E_l H l_n (H+l_n) \Delta \epsilon'']}{E_s^2 H^4 + E_d^2 h^4 + 6E_s E_d H^2 h^2 + 6E_d E_l h^2 l_n^2 + 6E_s E_l H^2 l_n^2 + 4E_s E_d H h (H^2 + h^2) + 4E_d E_l h l_n (h^2 + l_n^2) + 4E_s E_l H l_n (H^2 + l_n^2)} \quad (2.17)$$

Herein, the compressive Young's modulus of the aliphatic chains is taken as 0.9 GPa. This value is derived and scales comparably to the estimation of bending moduli done on carbon chains which constitute lipid bilayers in the order of 10^{19} J [158]. It reflects the steric hindrance imposed by the ligands' packing density. Since the organic chains on the outer surface of a piece of helix are uncompressed, they are then omitted from this calculation. Nevertheless, it is important to state that this Young's modulus may be overestimated for shorter aliphatic chains, but due to their smaller length, the resulting steric effect on the estimated helices' radii is also consequently lower in comparison to longer chains. In the end, $\Delta \epsilon$ is adjusted and set to -21 %, in order to obtain a good agreement between the model and experimental value associated with 3 MLs CdSe nanohelices capped by the shortest aliphatic chains, where $n = 2$.

The mismatch, $\Delta \epsilon''$ existing between the inorganic core and aliphatic chain layer is defined from the maximum packing density of carbon chains. On the {0 0 1} zinc blende facets of the NPLs, there is in theory one ligand per surface cadmium which displays a density of 18.3 \AA^{-2} . Experimentally, it has been shown on a Langmuir-Blodgett film that the maximum density of thiolates can reach up to 18.5 \AA^{-2} [159]. One can thus firstly assume that below this limit, the maximum packing is yet to be attained which leads to a reasonable approximation that $\Delta \epsilon'' = 0 \%$. Overall, thiolates anchoring group brings a strong contractile stress onto the CdSe inorganic core, while the layer of packed aliphatic chains exerts in opposite, a tensile stress onto the thiolates. According to our proposed model, one can then expect smaller helical radii for a population of thinner NPLs in comparison to the thicker ones and an increase of these radii as the length of the grafted ligands grow longer, with the input values listed in Tab. 2.3.

The predictions given by our derived model are in excellent agreement with the experimental findings, for increasing NPLs' thicknesses going from 3 to 6 MLs, otherwise from 0.9

3 MLs CdSe NPLs	E_s	E_d	E_l	H	h	l_n					$\Delta\epsilon$	$\Delta\epsilon''$
	(GPa)	(GPa)	(GPa)	(nm)	(nm)	C ₂ S (nm)	C ₄ S (nm)	C ₈ S (nm)	C ₁₂ S (nm)	C ₁₈ S (nm)	(%)	(%)
	40	46	0.9	0.91	0.15	0.2	0.4	0.8	1.2	1.8	-21	0

TABLE 2.3: Input values to three-layers misfit model applied onto a 3 MLs CdSe NPL.

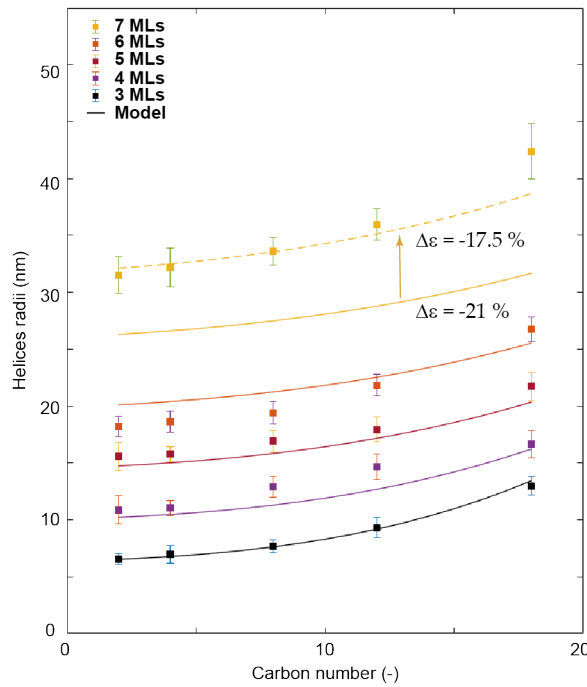


FIGURE 2.12: Experimental helices' radii represented by dots, which are deduced from the analysis of microscope images for CdSe NPLs with thicknesses ranging from 3 to 7 MLs and averaged over a population of 100 nanohelices. The solid lines are predictions from our proposed three-layers mechanical model built from the classical work of Timoshenko. The associated mismatch, $\Delta\epsilon$ existing between the inorganic core and thiolates anchoring layer is set at -21 %, while in the case of predicting the helices radii of 7 MLs CdSe NPLs (dotted line), this parameter is defined at -17.5 %.

to 1.8 nm (Fig. 2.12). For thicker 7 MLs CdSe nanohelices however, a better fit is obtained for $\Delta\epsilon = -17.5\%$, which might mostly be due to the presence of surface defects of the inorganic material explaining larger observed experimental radii. Since the growth of thicker NPLs is carried out through the method of c-ALD, this might introduce certain interstitial imperfections in their resulting crystal structure. Plausible missing surface cadmiums accompanied by the vacancies of ligands, will undoubtedly reduce the induced surface stresses and result in larger helices radii. In another sense, the absolute effective value of $\Delta\epsilon$ is diminished. Thus, our macroscopic model performs well at predicting the curling of NPLs and it reveals simultaneously a major importance of the surface chemistry in play with respect to the coupling between ligands and exposed cadmium atoms.

2.2 Extension onto core-only CdS and core-shell CdSe-CdS

On top of previously elaborated investigations done on CdSe homostructures, the scope of our work has also been extended onto 4 MLs CdS and heterostructured CdSe-CdS core-shell NPLs. This latter is notably composed of 3 MLs of CdSe core with a shell of 1 to 2 MLs of CdS on each lateral side. In the following section, they are then labelled as (3-2)CdSe-CdS (resp. (3-4)CdSe-CdS).

Typically, this allows one to answer the question if surface thioliates bind in a similar tetrahedral way to internally coordinated sulfide anions, which constitute the NPLs' inorganic core. In which sense, zero phenomenon of curling ought to be observed and alkanethiolates-capped CdS NPLs should all exhibit zero curvature independently of the ligands' chain length, if it were the case where surface stresses are absent. To our surprise, flat CdS and CdSe-CdS NPLs are not at all observed. Herein, their corresponding helices radii are recorded (Fig. 2.13 and Fig. 2.14).

2.2.1 CdS homostructures

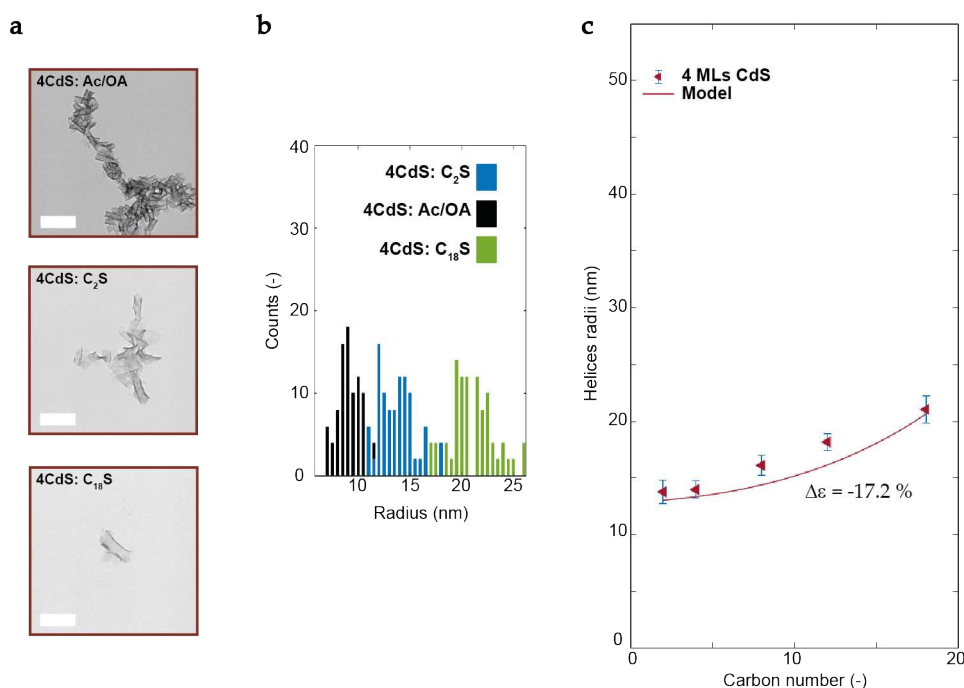


FIGURE 2.13: (a) TEM images of 4 MLs CdS NPLs before and after chemical surface alterations. They are either capped by acetates-oleates, ethanethiolates or octadecanethiolates on their outer surface. Scale bar: 200 nm. While in (b), the distribution of their nanohelices' radii is plotted. Blue (resp. black and green) bars represent nanoparticles which are capped by ethanethiolates (resp. acetates-oleates and octadecanethiolates), analyzed over a population of 100 nanohelices. Bin: 0.5 nm. (c) Experimental helices' radii deduced from the analysis of their corresponding microscope images, averaged over a population of 100 nanohelices with predictions obtained from our derived model that are represented by solid lines.

As demonstrated previously, the absolute bulk lattice mismatch between CdSe and CdS is 3.8 %. In our model, an absolute decrease in the value of $\Delta\epsilon$ is applied to the one which

was employed in the case of CdSe nanohelices, yielding -17.2 % ((-21 + 3.8) %). It is true that one would expect the misfit between the inorganic core and thiolates anchoring layer to be much less, as this time around, the core itself is composed of cadmium sulfides. Therefore, it is reasonable to diminish the absolute value of $\Delta\epsilon$, instead of increasing it while keeping other parameters unmodified.

2.2.2 CdSe-CdS heterostructures

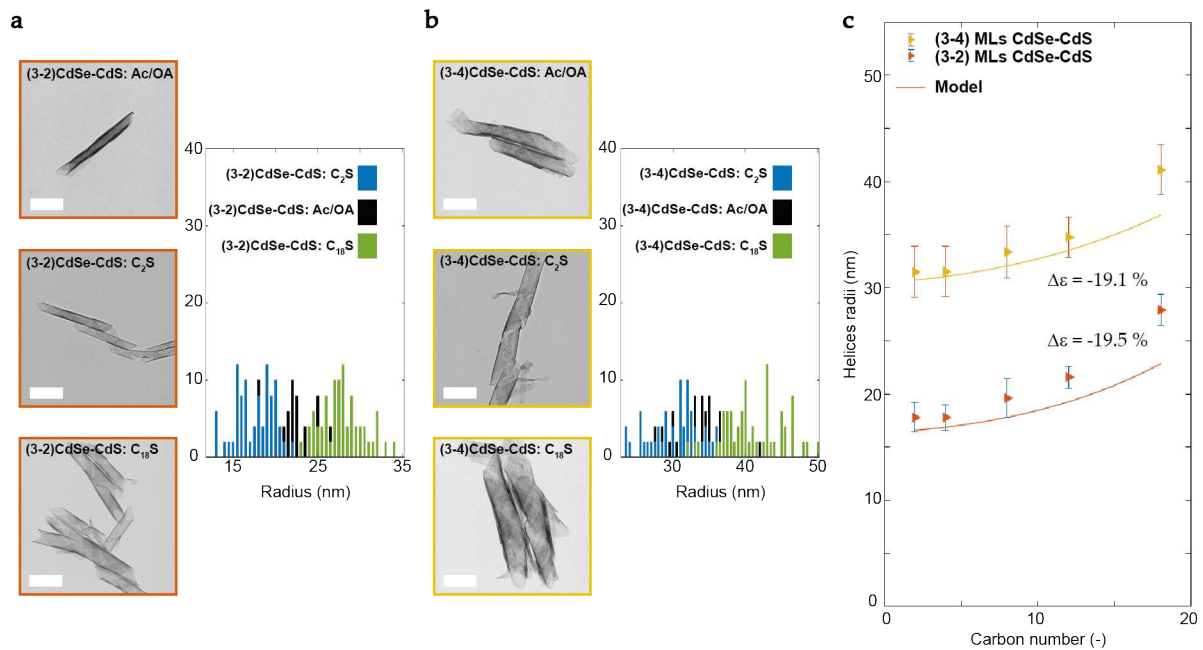


FIGURE 2.14: (a) TEM images of (3-2) MLs CdSe-CdS NPLs before and after chemical surface alterations. They are either capped by acetates-oleates, ethanethiolates or octadecanethiolates on their outer surface, along with the distribution of their nanohelices' radii plotted in black, blue and green respectively. Scale bar: 200 nm. Bin: 0.5 nm. Similarly in (b), the analysis for (3-4) MLs CdSe-CdS NPLs are carried out over a population of 100 nanohelices. (c) Experimental helices' radii deduced from their corresponding microscope images, with predictions obtained from our derived model that are represented by solid lines.

Concerning core-shell heterostructures, it is interesting to note that the thicknesses of these two samples are close to those of 5 and 7 MLs homostructured CdSe NPLs. Herein, to determine the misfit between the inorganic core and surface thiolates, it requires beforehand knowing the lattice distortion of the heterostructures. According to Fig. 2.11, the forces exerted by the inorganic core and thiolates anchoring layer are noted as \vec{F} and $-\vec{F}$ respectively, which contribute to generating a bending moment given by a general expression:

$$M = F \left(\frac{H + h}{2} \right) \quad (2.18)$$

The magnitude of F is found by expressing the mismatch as the difference between the strains resulting from the application of both forces (for instance, by writing the equation of strain balance):

$$\Delta\epsilon = \epsilon_s - \epsilon_d = \frac{F}{HL(1+\alpha)E_s} + \frac{F}{hL(1+\alpha)E_d} \quad (2.19)$$

$$\frac{F}{L(1+\alpha)} = \Delta\epsilon \frac{HE_s h E_d}{HE_s + hE_d + l_n E_l} \quad (2.20)$$

The stress profile as a function of any position across the thickness direction \bar{z} , can then be written in terms of the base level in each constituent which arises from the equation of force balance and the change due to the stress gradient:

$$\sigma_s(z) = \frac{F}{L(1+\alpha)z} - E_s \kappa(z+d) \quad (2.21)$$

$$\epsilon_s(z) = \frac{\sigma_s(z)}{E_s} = \frac{F}{E_s L(1+\alpha)z} - \kappa(z+d) \quad (2.22)$$

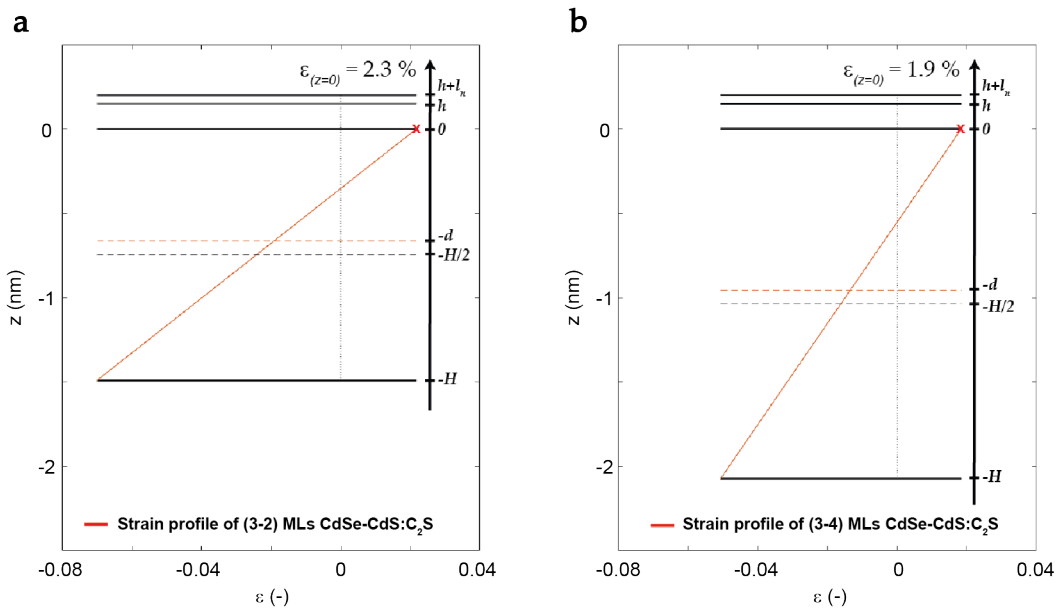


FIGURE 2.15: Strain profiles of a piece of (a) (3-2) and (b) (3-4) MLs CdSe-CdS NPL, plotted as a function of any position across its thickness direction \bar{z} . The represented surface ligands' chain length is equivalent to that of ethanethiolates, where $n = 2$. The inlet scale corresponds to the one used to derive our three-layers model, while the y -axis shows a real associated unity in nm.

Via these stress and strain profile plots, one can then determine the lattice distortions resulting from the application of axial forces in such nanosystems. For instance, a structure made up of six atomic planes of CdSe sandwiched equally between four (resp. eight) atomic planes of CdS, corresponds exactly to that of (3-2) (resp. (3-4) MLs) CdSe-CdS NPLs. According to Fig. 2.15 for objects of (3-2) (resp. (3-4) MLs), the CdS layer which is at the interface between the inorganic core and thioliates anchoring group, experiences an axial deformation up to 2.3 (resp. 1.9) % compared to the case of homostructured CdS. Thus, the lattice mismatch, $\Delta\epsilon$ defined in our three-layers model is to be modified into -19.5 % ((-17.2-2.3) %) and -19.1 % ((-17.2-1.9) %) respectively, for these two core-shell NPLs. Concerning the Young modulus of the core, an intermediate value preponderated by the presence of these two different materials: CdSe and CdS, is considered. These assumptions are shown to agree well with the experimental observations and these core-shell nanohelices fold neither as pure CdSe nor as CdS with equivalent thicknesses (dashed and dotted lines in Fig. 2.16).

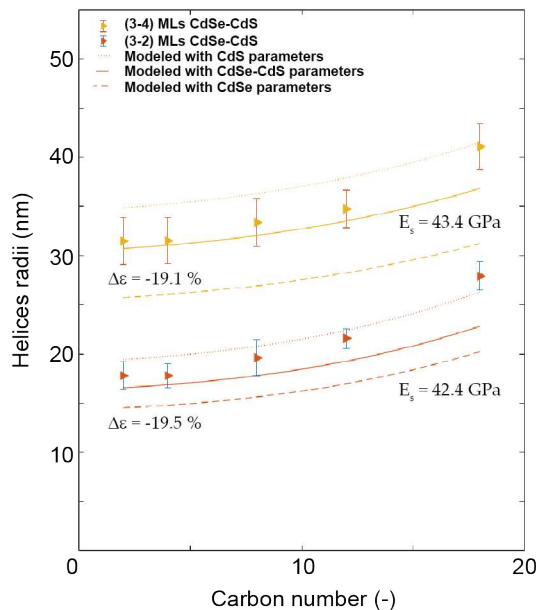


FIGURE 2.16: Comparison between experimental and predicted helices radii for CdSe-CdS core-shell NPLs with a CdSe core of 3 MLs and a CdS shell of either 1 or 2 ML(s) on each lateral side. The dotted (resp. dashed) lines represent the calculated radii when the parameters of CdS (resp. CdSe) are computed into our three-layers model. Concerning CdSe (resp. CdS), the lattice mismatch, $\Delta\epsilon$ equals -21.0 (resp. -17.2 %) and its Young's modulus, E_s equals 40 (resp. 46 GPa).

2.2.3 Validation of mechanical model

According to Eqn. 2.17, the expression of nanohelices' predicted curvature is comprised of a set of eight to-be-determined parameters, namely H , h , l_n , E_s , E_d , E_l , $\Delta\epsilon$ and $\Delta\epsilon''$. In order to fully justify these fore-mentioned variables and their values, it is essential to test out the effect of modifying them individually on helices radii predictions for 3 MLs CdSe NPLs.

Firstly, the effects of the lattice mismatch $\Delta\epsilon$, between the inorganic core and thiolates anchoring group is demonstrated. By considering a value which is close to the one existing between CdSe and CdS bulks, it overestimates the resulting helices radii by an order of magnitude. This may be originating from a rearrangement of the surface atoms that are far from being in their ideal tetrahedral environments. Besides, a modification of the sign of stresses brought by the aliphatic chains can lead to a change in the sense of curvature as displayed in Fig. 2.17(b). If the values of $\Delta\epsilon''$ were to be negative, it is as if an attractive force were to exist between the aliphatic chains, which leads to a decrease in radius when the chain length increases. Moreover, the influences of the Young's modulus of the aliphatic chains E_l , are also looked into. If one had considered a lower value, the consequence observed experimentally while going to longer chains would have been insignificant.

The accuracy of our three-layers model is further tested while taking into account variations in the thicknesses of the different considered layers. It is again worth mentioning that the outer layer of surface ligands is omitted during the helices radii estimation. By looking at the orientation of the inner induced stress along the direction \vec{u} , the outer layer of sulfides binds indeed to the cadmiums along the direction \vec{v} , which is perpendicular to the previous one. As a consequence, the outer contribution is removed since it does not participate in the

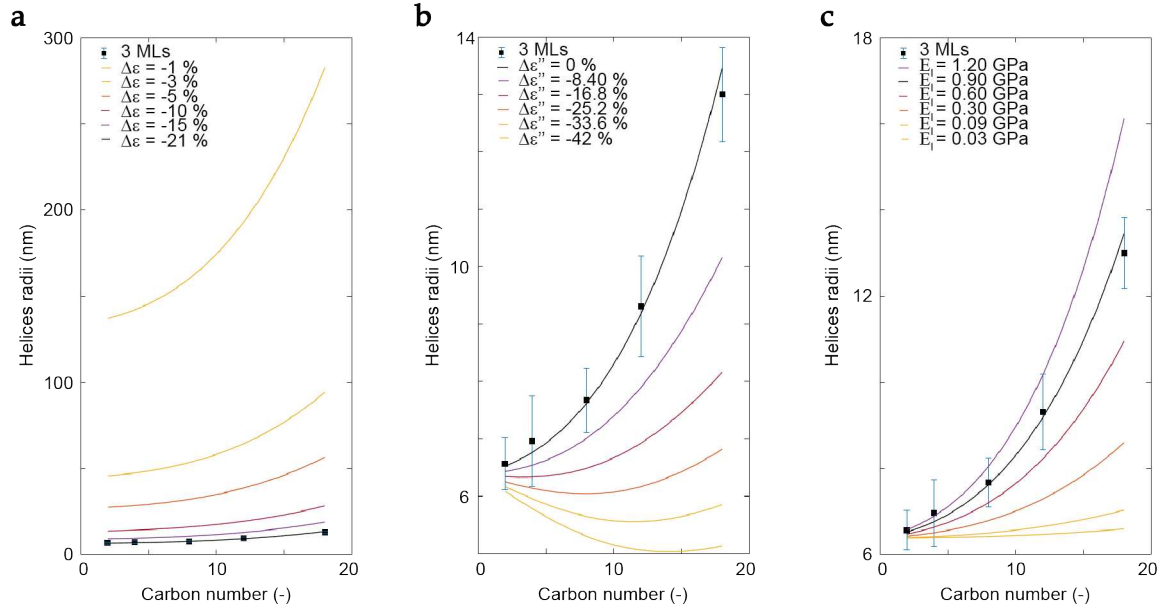


FIGURE 2.17: (a) Calculated helices radii for various values of lattice mismatch $\Delta\epsilon$, between the inorganic core and thioliates anchoring layer, while keeping $\Delta\epsilon''$ constant at 0 %. Other parameters are such, $E_s = 40$ GPa, $E_d = 46$ GPa, $E_l = 0.9$ GPa, $H = (6 \times 1.51)$ Å, $h = (1 \times 1.51)$ Å, and $l_n = (n \times 1)$ Å, where n is the number of carbons constituting the aliphatic chains. (b) Calculated helices radii for a mismatch between the inorganic core and aliphatic chains $\Delta\epsilon''$, that varies from 0 to -42 %. Other parameters are such, $\Delta\epsilon = -21$ %, $E_s = 40$ GPa, $E_d = 46$ GPa, $E_l = 0.9$ GPa, $H = (6 \times 1.51)$ Å, $h = (1 \times 1.51)$ Å, and $l_n = (n \times 1)$ Å. In other words, $\Delta\epsilon'$ is increasing from -21 % (contractile strain) to +21 % (tensile strain). (c) Calculated helices radii for which $\Delta\epsilon = -21$ %, $\Delta\epsilon'' = 0$ % and various Young's moduli of the packing of aliphatic chains. In all figures, the black squares represent the experimental data obtained for 3 MLs CdSe nanohelices.

bending of a piece of NPL towards its inner side. If these outer planes were to be counted, it would lead to an increase of the inorganic core's thickness and hence, the resulting helices radii. Herein, for NPLs capped with thioliates possessing an initial number of MLs N , the ratio of H to h is given by $2N:1$. Moreover, relative errors of ± 8 % in the estimation of an atomic plane's thickness have little effects on the calculated helices radii, as long as the $H:h$ ratio stays 6:1 for an example of 3 MLs CdSe NPLs (Fig. 2.18(b)). It is also important to underline that the carbon-to-carbon distance taken to assess the aliphatic chain length l_n , equals 1 Å, considering the projection of their zig-zag configuration (Fig. 2.18(c)).

In short, our as-proposed three-layers model derived from the classical work of Timoshenko enables an excellent prediction of strains in different atomic planes of a piece of NPL. The inner part of the helix presents an in-plane contractile strain, while the outer side is extended. The amplitude of this latter varies across the thickness's sectioning, as demonstrated by Eqn. 2.22. Independent of the aliphatic chain lengths, the strain in the mid-plane at equilibrium zeroes out. In another sense, the derived zinc blende lattice parameter of the helices a_0 , remains unchanged. In the next section, this structural reasoning is further verified via XRD by evaluating the crystal's associated lattice parameters.

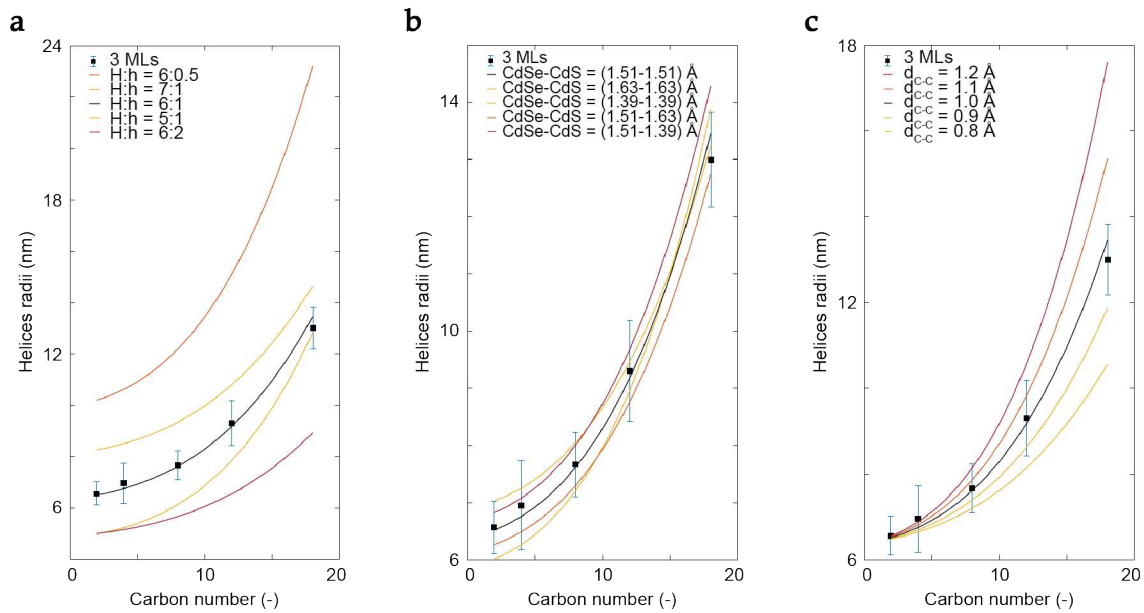


FIGURE 2.18: (a) Calculated helices radii for various ratios of H to h , where $H = (ix1.51) \text{ \AA}$, with $i = 5, 6, 7$ and $h = (jx1.51) \text{ \AA}$, with $j = 0.5, 1, 2$. The values of $i:j$ are given in the inset. Other parameters are such, $\Delta\epsilon = -21\%$, $\Delta\epsilon'' = 0\%$, $E_s = 40 \text{ GPa}$, $E_d = 46 \text{ GPa}$, $E_l = 0.9 \text{ GPa}$ and $l_n = (nx1) \text{ \AA}$, where n is the number of carbons constituting the aliphatic chains. (b) Computed helices radii for various thicknesses of an atomic plane, composing both layers of inorganic core CdSe and anchored thiulates CdS. Their respective ratios are given in the inset. Other parameters are such, $\Delta\epsilon = -21\%$, $\Delta\epsilon'' = 0\%$, $E_s = 40 \text{ GPa}$, $E_d = 46 \text{ GPa}$, $E_l = 0.9 \text{ GPa}$, $l_n = (nx1) \text{ \AA}$, $H = (6xk) \text{ \AA}$, and $h = (1xm) \text{ \AA}$, with both $(k,m) = 1.39, 1.51, 1.69$. (c) Resulting helices radii from modifications of the carbon-carbon distance in the aliphatic chains, where $l_n = (nxd_{C-C}) \text{ \AA}$. Other parameters are such, $\Delta\epsilon = -21\%$, $\Delta\epsilon'' = 0\%$, $E_s = 40 \text{ GPa}$, $E_d = 46 \text{ GPa}$, $E_l = 0.9 \text{ GPa}$, $H = (6x1.51) \text{ \AA}$, and $h = (1x1.51) \text{ \AA}$.

2.3 Structural implications of anisotropic objects

Fig. 2.19 presents the diffraction patterns of 3 MLs CdSe NPLs capped with thiolate ligands that are recorded on two different configurations of diffractometer. In the first experiment, the NPLs suspended in hexane are placed in a glass capillary and the two-dimensional plane detector shows an acquisition of Debye-Scherrer rings. Whereas in the second experiment, the initial NPLs suspended in a solvent are drop-casted on a silicium substrate and the diffracted patterns are obtained under a $\theta - 2\theta$ configuration. For both cases, the diffractograms exhibit Bragg peaks situated near $25, 42$ and 50° , that are respectively, attributed to the $(1\ 1\ 1)$, $(2\ 2\ 0)$ and $(3\ 1\ 1)$ families of planes in a zinc blende crystal structure. These peaks are asymmetric and broad due to the finite size of NPLs. In solution, their scattering patterns show minor differences between different applied surface chemistries, going from ethanethiolates to octadecanethiolates. These latter present both narrow and broad contributions for the $(2\ 2\ 0)$ peak located at $2\theta = 42^\circ$ (Fig. 2.19(a)). In the second experiment however, such narrow peaks are not observed. Instead, there is a doublet of peaks whose splitting broadens with the shortening of aliphatic chain lengths (Fig. 2.19(b)).

The main difference between the two experiments originates from the orientation of the nanohelices. Indeed, owing to their helical shape, the nanohelices in dried state lie down

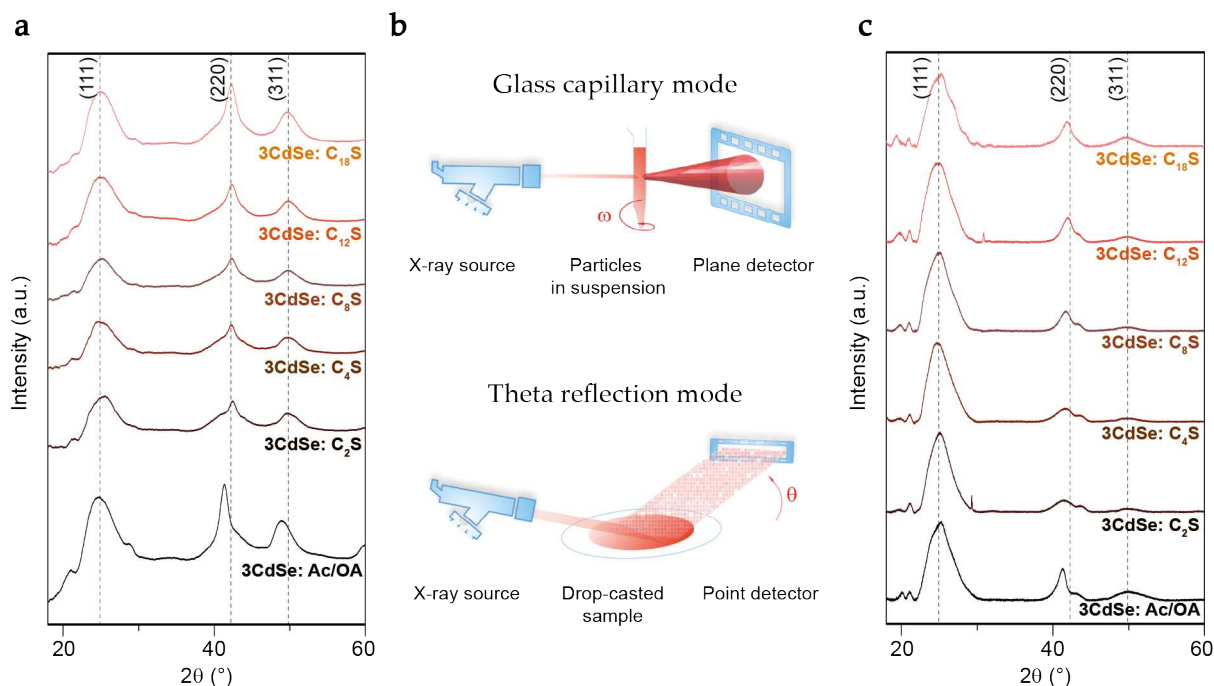


FIGURE 2.19: (a) X-ray diffractograms of 3 MLs CdSe NPLs suspended in hexane, capped by a mix of acetates/oleates and alkanethiolates surface ligands. The initial source is a molybdenum tube, but the data have been plotted as if it were a copper source in order to ease comparison. Vertical lines represent the Bragg angles for zinc blende CdSe with a lattice parameter of 6.05 \AA . (b) Schemes of the two different XRD experimental setups. In the top panel, the particles in suspension are placed in a glass capillary and the resulting scattered pattern is then collected by a plane detector. The bottom panel however, displays NPLs that are deposited and dried on a zero backscattering silicon substrate, defining a $\theta - 2\theta$ configuration. (c) X-ray diffractograms of drop-casted 3 MLs CdSe NPLs capped by Ac/OA and $C_nH_{2n+1}S^-$. The radiation source used originates from copper- K_α .

preferentially on any substrate, as observed experimentally by scanning electron microscope (SEM) in Fig. 2.20(b). Therefore, some planes will diffract with a higher probability, whereas others would not. For instance, equivalences of (2 2 0) family of planes in an unfolded zinc blende NPL split into three distinct contributions in a helix (green, blue and orange representations in Fig. 2.20(a)). The first one exhibits an interplane distance which equals to b_0 and scales independently of the helix's radius, as depicted by the green-colored planes. These latter diffract in a $\theta - 2\theta$ setup solely if the helical axis is orthogonal to the substrate with $\phi = 90^\circ$, which is highly improbable. In the same vein, the second family of blue-colored planes scatters when the helical axis tilts to an angle, $\phi \sim 60^\circ$, which is as well unlikely. Finally, the third family of yellow-colored planes presents an interplane distance which is dependent on a and varies accordingly from a' to a'' . They diffract with much greater importance when the helical axis becomes in line with the substrate, where $\phi = 0^\circ$ just as pictured in a $\theta - 2\theta$ setup.

During XRD experiments carried out via the glass capillary mode, all of these equivalent (2 2 0) families of planes diffract with an equal chance and the broad feature located at $2\theta = 42^\circ$ displays more complexity than the diffractograms obtained through the theta

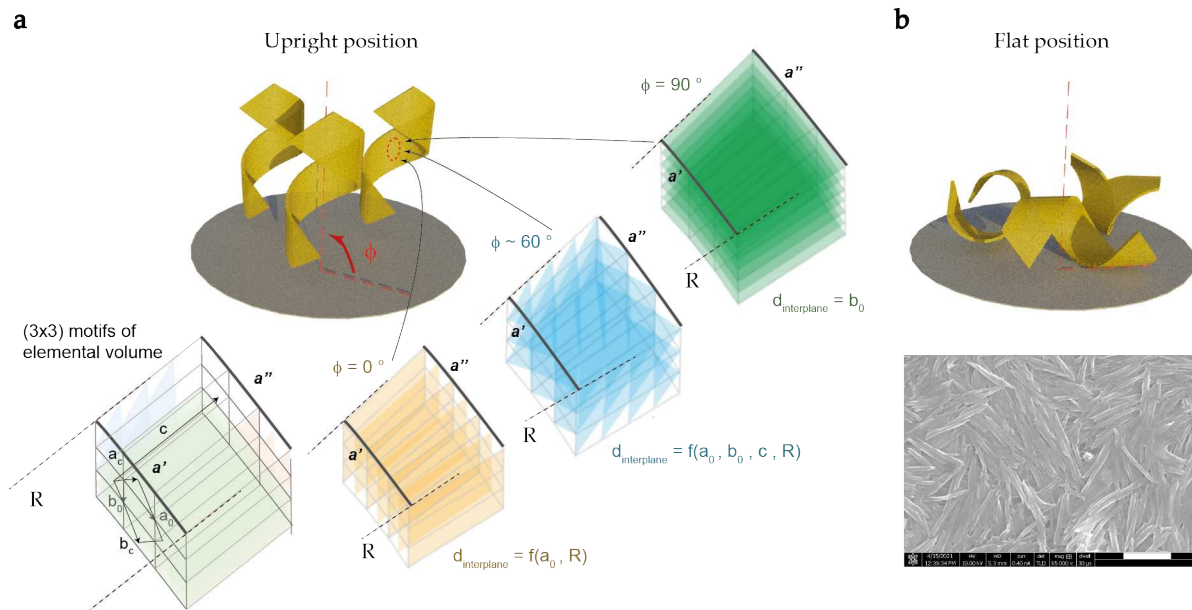


FIGURE 2.20: Schemes displaying nanohelices that are either (a) standing upright at a position perpendicular to their substrate ($\phi = 90^\circ$) or (b) lying down randomly ($\phi = 0^\circ$). Repeated motifs of elemental volume constituting a piece of helix, in which three equivalent (2 2 0) families of planes are represented. The green planes possess a constant interplane distance that equals to b_0 , while the blue ones have an average interplane distance that varies with a_0, b_0, c and R . Whereas, the average interplane distance of the yellow planes writes as a function of a_0 and R . Each of them diffracts with a greater importance when the helical axis is tilted to around $90, 60$ and 0° respectively. The SEM image of 3 MLs CdSe NPLs capped by acetates/oleates, shows a specific orientation of the nanohelices lying down on the silicium substrate. Scale bar: 500 nm.

reflection mode. This is because one would not be able to distinct with ease the superposition of several contributions hidden under a bump. Nevertheless, the narrow peak can still be attributed to the family of planes with a constant b_0 interplane distance, since it barely varies with the different substitutions of surface chemistry. Going from carboxylates to various alkanethiolates, the experimentally extracted parameter b_0 corresponds respectively to (4.36 - 4.25 - 4.27 - 4.26 - 4.27 - 4.27) Å. Therefore, this lattice constant is dilated by 1.9 % in the presence of surface carboxylates ligand compared to the zinc blende bulk value. As for thiolates, b_0 is compressed by (0.7 - 0.2 - 0.45 - 0.2 - 0.2) % respectively for ethanethiolates, butanethiolates, octanethiolates, dodecanethiolates and octadecanethiolates. One can remark that this value stays often close to 4.28 Å, which is the exact value expected for a zinc blende crystal structure of lattice parameter $a_c = 6.05$ Å.

2.3.1 XRD of flat undistorted NPLs

In order to interpret as-obtained experimental observations in Fig. 2.19(a,c), X-ray diffractogrammes of pieces of flat (8x8) nm² 3 MLs CdSe NPLs and nanohelices with a defined curvature have both been simulated. The unit cell of a zinc blende CdSe crystal structure is first coded under its body-centered (I) system under *Matlab*. It is characterized by various geometrical parameters: a , which defines its width; b , its length; c , its height as pictured during the beginning in Fig. 2.7(a). In Cartesian coordinates, this unit cell is

repeated diagonally along its $(\vec{a} + \vec{b})$ and $(-\vec{a} + \vec{b})$ directions, hence forming a NPL of certain dimensions. The same goes in generating nanohelices, except this time around, the expression of its width has to be modified to account for the helix's radius. Anchoring layer of surface ligands can also be added onto such generated structures in a tetrahedral environment, with respect to the surface cadmiums. It is important to point out that all atoms are first coded as punctual space points before attributing associated structural factors to corresponding atoms found in each atomic plane.

The crystal structure's scattered intensity in isotropic environment is then evaluated thanks to the classical Debye equation, by each time considering interactions between paired atoms:

$$I\left(\frac{\sin\theta}{\lambda}\right) = \sum_m^N \sum_{n \neq m}^N f_m f_n \frac{\sin(4\pi \frac{\sin\theta}{\lambda} r_{mn})}{4\pi \frac{\sin\theta}{\lambda} r_{mn}} + \sum_m^N f_m^2 \quad (2.23)$$

where $f = \sum_{i=1}^4 a_i e^{-b_i \frac{\sin^2\theta}{\lambda^2}} + c$, represents the structural factor of considered atoms [160].

Atoms	a_1	a_2	a_3	a_4	b_1	b_2	b_3	b_4	c
Cd	19.151	17.254	4.471	0	0.598	6.806	20.252	0	5.119
Se	17.001	5.820	3.973	4.354	2.410	0.273	15.237	43.816	2.841
S	6.905	5.203	1.438	1.586	1.468	22.215	0.254	56.172	0.867
I	20.233	18.997	7.807	2.887	4.358	0.382	29.526	84.930	4.071

TABLE 2.4: Structural constants of considered atoms.

The previous equation is later modified to take into account the anisotropic aspect of a piece of helix:

$$I\left(\frac{\sin\theta}{\lambda}\right) = \sum_m^N \sum_{n \neq m}^N f_m f_n e^{-2i\pi \vec{q} \cdot \vec{r}_{mn}} + \sum_m^N f_m^2 \quad (2.24)$$

where $\vec{q} = \frac{2\sin\theta}{\lambda} \vec{z}$, is the diffused vector of the excitation source, defining a scalar product with the diffracted rays.

Firstly, Fig. 2.21(a) shows a study of NPLs which diffract in all directions according to Eqn. 2.23 before orienting them specifically with respect to the excitation source, to selectively display contributions of certain family of planes in Fig. 2.21(c), according to Eqn. 2.24. With an unfolded zinc blende NPL, one can easily validate our simulation method by associating the right diffraction peaks to the way the object is oriented in Fig. 2.21(b). Since a crystal lies down on a substrate due to its large lateral dimensions and helical shape, the associated families of planes do not scatter with the same probability. Especially, those twelve multiplicities of (2 2 0) family of planes which were previously equivalent for a flat NPL presenting zero curvature, no longer stay indifferent when it comes to dealing with distorted helical structures. Depending on the nanohelices' orientation, if these latter were to lie down, the (2 2 0) contribution for which $\phi = 90^\circ$ will be extinct. Instead, solely the $\phi = 0^\circ$ (2 2 0) family of planes will diffract under the way they are positioned. It is thus necessary to consider the specific orientation of these helices when one attempts to explain the differences observed in $\theta - 2\theta$ experiments originally presented in Fig. 2.19(c), between alkanethiolates of various chain lengths.

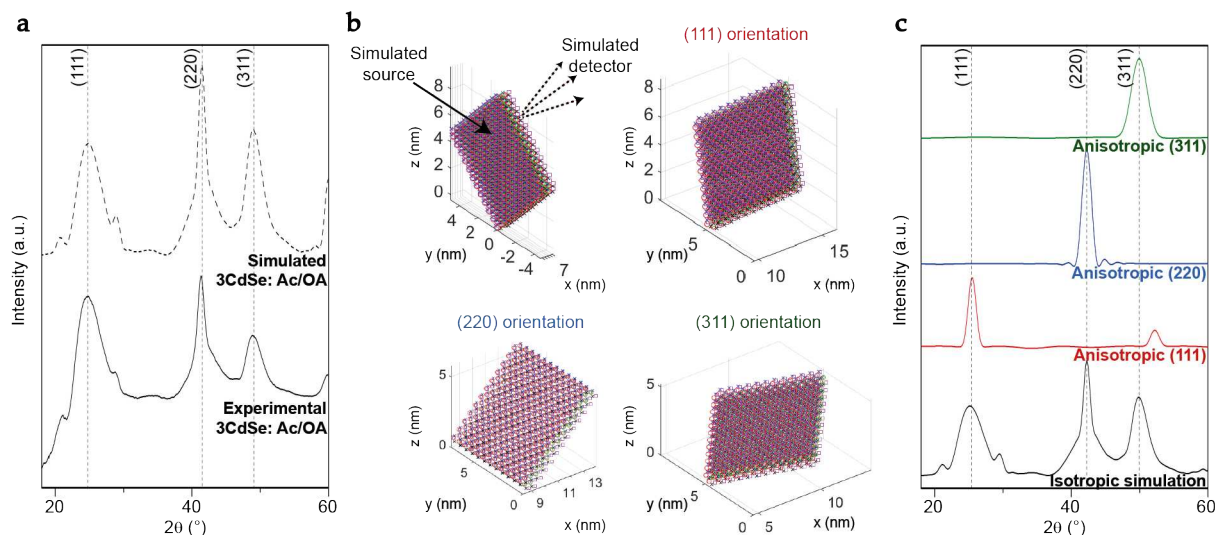


FIGURE 2.21: (a) Comparison between isotropically scattered experimental (solid line) and simulated (dashed line) diffractograms of 3MLs CdSe NPLs capped with carboxylates ligands. The experimental curve is obtained via the glass capillary technique, while the simulated one is computed with Eqn. 2.23. Schemes of different pieces of simulated flat (8x8) nm² NPLs are shown in (b). In order to perform anisotropic diffraction calculations onto these latter, they ought to be oriented under exact scattering positions with respect to the excitation source and the output detector. (c) Separate contributions of an isotropic diffractogram, namely (1 1 1), (2 2 0) and (3 1 1) families of planes, are individually computed with Eqn. 2.24.

2.3.2 Scattering of curved nanohelices

Moving onto nanohelices with a defined curvature, similarly to the first study done on flat NPLs in Fig. 2.21, their diffraction patterns are investigated in all directions in Fig. 2.23(a) according to Eqn. 2.23, before the selective representation of family of planes in Fig. 2.23(b) according to Eqn. 2.24. The observations made from the first experiment via the glass capillary mode are in excellent agreement with the theory computed thanks to the classical Debye formula. The piece of generated nanohelix mimics identical features of 3 MLs CdSe ones that are experimentally capped by ethanethiolates, in a sense where $R = 6.6$ nm and on its inner and outer facets, an anchoring layer of sulfides is added in a tetrahedral fashion with respect to the surface cadmiums. Indeed, the green-colored (2 2 0) family of planes displayed in Fig. 2.22(b) diffracts with a high degree of distortions, as demonstrated by the blue plot found in Fig. 2.23(c). This is mainly due to the paired atoms' local distances r_{mn} , that vary strongly with a' and a'' , as described previously through the atomic-scale elemental volume represented in Fig. 2.7(b), which contribute to a large dispersion in terms of Bragg angles.

If one were to orient this piece of nanohelix in a continuous way along three different space planes, by rotating it: (i) around the y -axis, so that the object transforms from a vertical to a horizontal position lying down on the substrate, (ii) around the z -axis, to maintain the object in rotation on the substrate plane and (iii) around the x -axis, whereby the object is rotated along its centerline and defines a perfect cylindrical envelope, this will further help to underline the importance of specific orientations for anisotropically-shaped particles (Fig. 2.24). By tilting the piece of nanohelix around the y -axis in the first scenario or in other

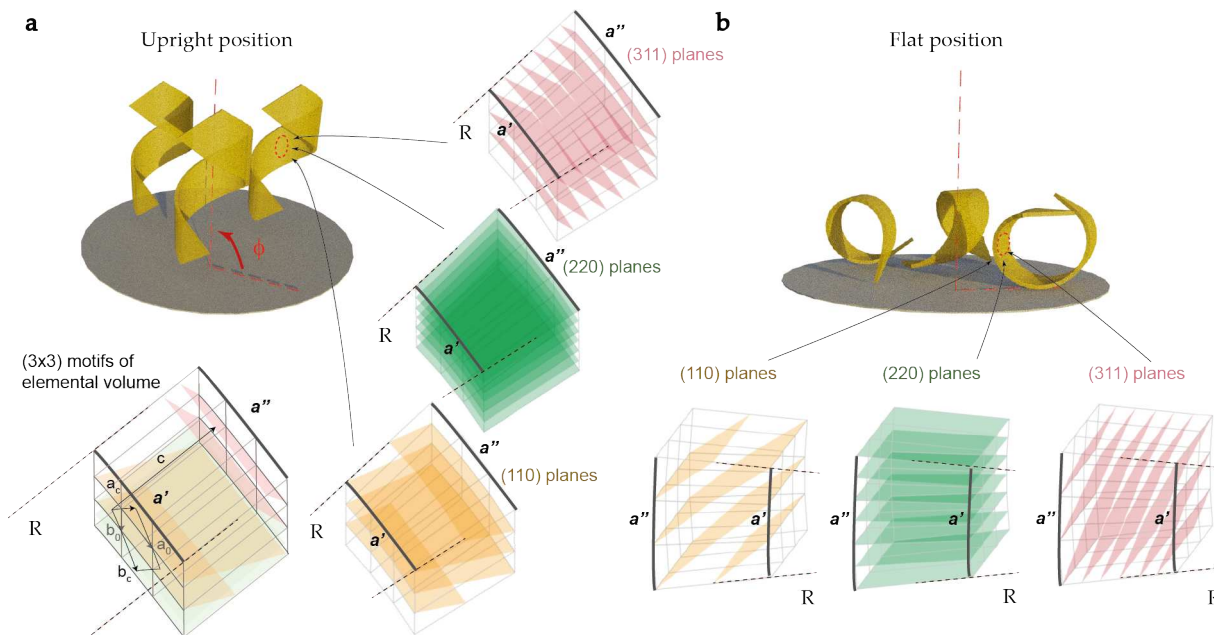


FIGURE 2.22: Different families of planes that diffract as a function of the helices' orientation either being (a) upright or (b) lying down, with respect to the substrate in the case of theta reflection mode. Repeated motifs of elemental volume constituting a piece of helix, display three main families that are looked into: (1 1 0), (2 2 0) and (3 1 1). They are respectively color-coded as orange, green and pink planes. It is essential to note that the (2 2 0) ones represented in the case of lying down position, are exactly identical to the yellow planes shown in Fig. 2.20, whose interplane distance writes as a function of a_0 and R .

words, by changing the angle ϕ , the (2 2 0) family of planes diffracts at different angles as fore-mentioned (Fig. 2.24(a)). Whereas, the rotation around the z-axis does not imply any significant scattering changes as depicted in Fig. 2.24(b). However, when the helical object is rotated along its centerline, notable changes between each scattered pattern can be pointed out (Fig. 2.24(c)). Indeed, as forecast in the anisotropic Debye formula, the associated scalar product which modulates the resulting scattering as a whole is modified for each individual position. Hence, during simulations, the piece of nanohelix is specifically oriented as illustrated in Fig. 2.24(c) in order to fit the experimental data obtained from the second XRD experiment via the theta reflection mode.

On the experimental diffractograms illustrated in Fig. 2.19(c), there is a doublet of peaks noticed around $2\theta = 42^\circ$. Due to the local distortions in nanohelices, we are not exactly investigating the average interplane distances, but rather the pair function between considered atoms. Thus, in Fig. 2.25(b), if one were to look into the probability counts in terms of differences of atomic position along the z-axis, noted d_z and their corresponding Bragg angles 2θ , the resulting pattern matches well with the experimental tendency. Again, these plots are generated for 3 MLs ethanethiolates-capped CdSe helical objects which are oriented in a specific way as shown in Fig. 2.23(b), so that the (2 2 0) family of planes diffracts highly with respect to the incident beam. It is important to note that the diffused vector \vec{q} is collinear with \vec{z} and therefore, it depends on the axial position of different atoms that could contribute to scattering. As a consequence, the histograms represented in Fig. 2.25 display discrete distances between paired atoms which turn out to be the origin of

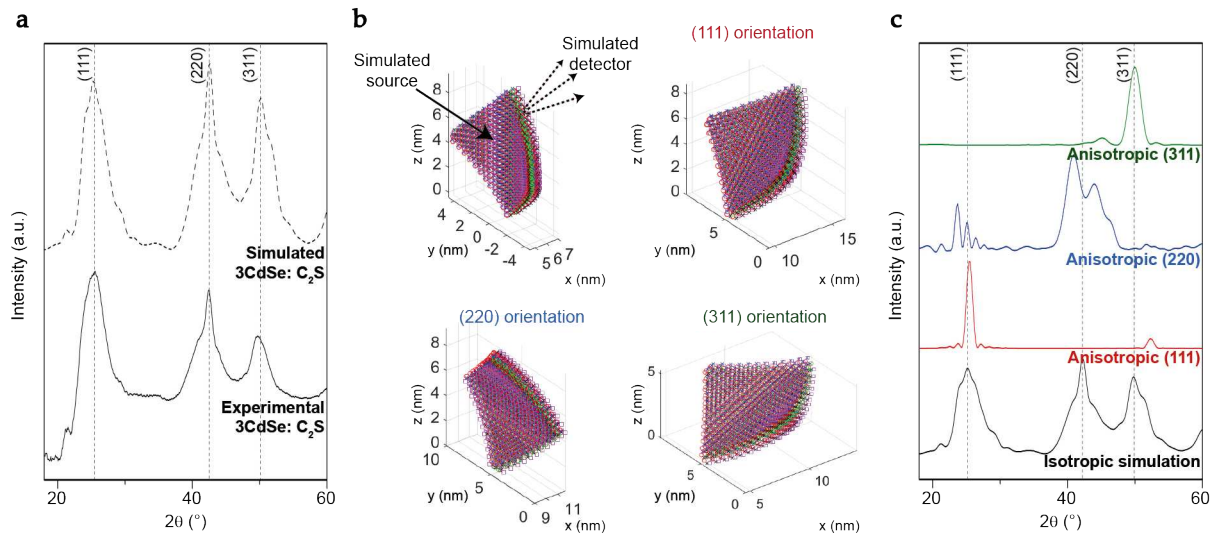


FIGURE 2.23: (a) Comparison between isotropically scattered experimental (solid line) and simulated (dashed line) diffractograms of 3MLs CdSe nanohelices capped with ethanethiolate ligands. The experimental curve is obtained via the glass capillary technique, while the simulated one is computed with Eqn. 2.23. Schemes of different pieces of simulated (8×8) nm² nanohelices are shown in (b). In order to perform anisotropic diffraction calculations onto these latter, they ought to be oriented under exact scattering positions with respect to the excitation source and the output detector. (c) Separate contributions of an isotropic diffractogram, namely $(1\ 1\ 1)$, $(2\ 2\ 0)$ and $(3\ 1\ 1)$ families of planes, are individually computed with Eqn. 2.24.

multiple distorted peaks observed in diffraction.

The bottom (resp. top) panel found in Fig. 2.25 presents the simulated beam patterns diffracted by nanohelices of 6.6 (resp. 13 nm) in radius. The most noticeable difference between these latter as shown in the experiments, originates from the peak located at $2\theta = 42^\circ$. In the case of helices of 6.6 nm, there is a triplet of peaks, whereas for the 13 nm ones, only a doublet of peaks is obtained. Plus surprisingly, none of them is exactly centered around 42.2° , which is the expected value of Bragg angle for a family of planes separated by a distance of $4.28\ \text{\AA}$, as in zinc blende CdSe bulk. This is because even though the mean interatomic distance equals a_0 along the thickness direction of a piece of helix, its distribution however, becomes more dispersed as the helices' radii get smaller. Therefore, the probability counts for the appearance of a_0 are not necessarily correlated, neither higher compared to its neighboring values, in agreement with the interatomic distances plot in Fig. 2.25(b).

2.3.3 Bypass between simulation and experimental data

At the end, in order to obtain a good fit of the experimental anisotropic $(2\ 2\ 0)$ family of planes' scattering patterns, it is essential to take into account the multiple turns of folding made by a single NPL. It thus leads to the possibility where a single helix can exhibit a range of radii values. Typical TEM images of 3 MLs CdSe thiolates-capped NPLs display large sheets which could wind up to four turns in general as shown by Fig. 2.26(a). Hence, during simulations, the final diffracted intensity writes as a sum of contributions from four pieces of nanohelix, with linearly increasing radii. The space which separates these individual objects, noted as e is determined via the analysis of microscope images and gives $(2.3 - 2.6$

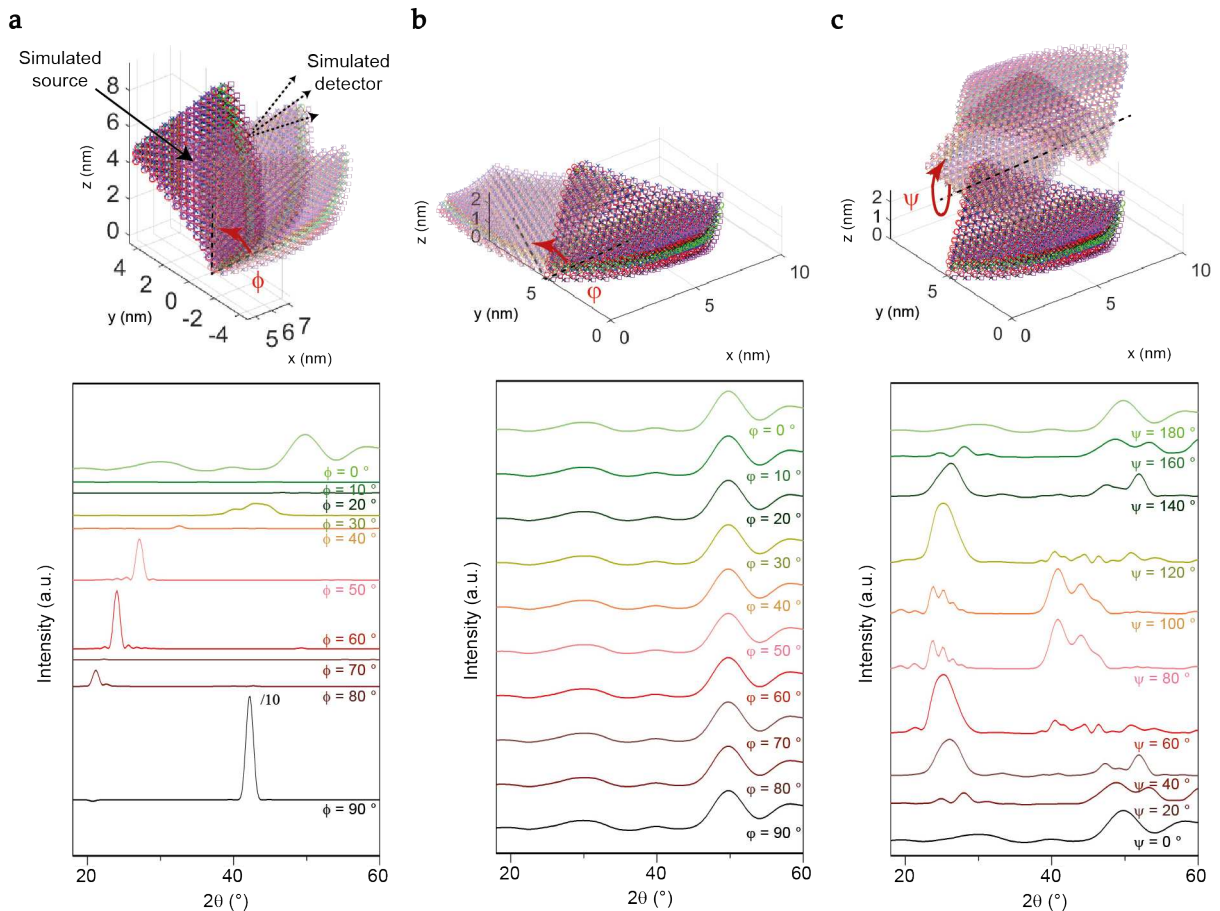


FIGURE 2.24: Simulations of diffracted intensity by a piece of 3 MLs CdSe nanohelix, mimicking the features of those which are experimentally capped by ethanethiolates surface ligands. In (a), the helical object defines a variable angle ϕ which equals 90 (resp. 0 °) with respect to the substrate's surface, when it is at its upright (resp. lying down) position. For a clearer display of other diffractograms, the computed intensity for which $\phi = 90^\circ$ has been reduced by a factor of 10. While in (b), the helix lies down constantly on the substrate with $\phi = 0^\circ$ and rotates in the xy -plane, defining a variable angle ϕ with respect to its initial position. In the case of (c), the object rotates along its centerline and describes therefore a cylinder. The associated angle of rotation is noted as ψ with respect to its initial lying down position.

- 3.0 - 3.8 - 4.9) nm respectively for nanohelices passivated by various alkanethiolates. In general, an increase of the helix's radius smoothens out the resulting diffractogram and changes the intensity ratios between scattered peaks. Despite the strong surface stress induced by thiolate ligands, the average in-plane lattice parameter remains however, equal to that of zinc blende CdSe bulk as shown in Fig. 2.26(b).

Lastly in order to validate our average in-plane bulk lattice parameter hypothesis, positive and negative strains are both applied onto a helix's elemental volume, to look into their effect on the resulting diffractograms. In Fig. 2.27, the importance of the form of the elemental volume constituting our nanohelices, on their scattering pattern is highlighted by varying the lattice parameters (a, b, c). During isotropic diffractions, a shift of the narrow peak located at 42° reflects its corresponding unit cell value b_0 . Whereas, under specific orientations, a change in unit cell value a_0 causes a shift of the triplet of peaks for which $2\theta = 42^\circ$. In both

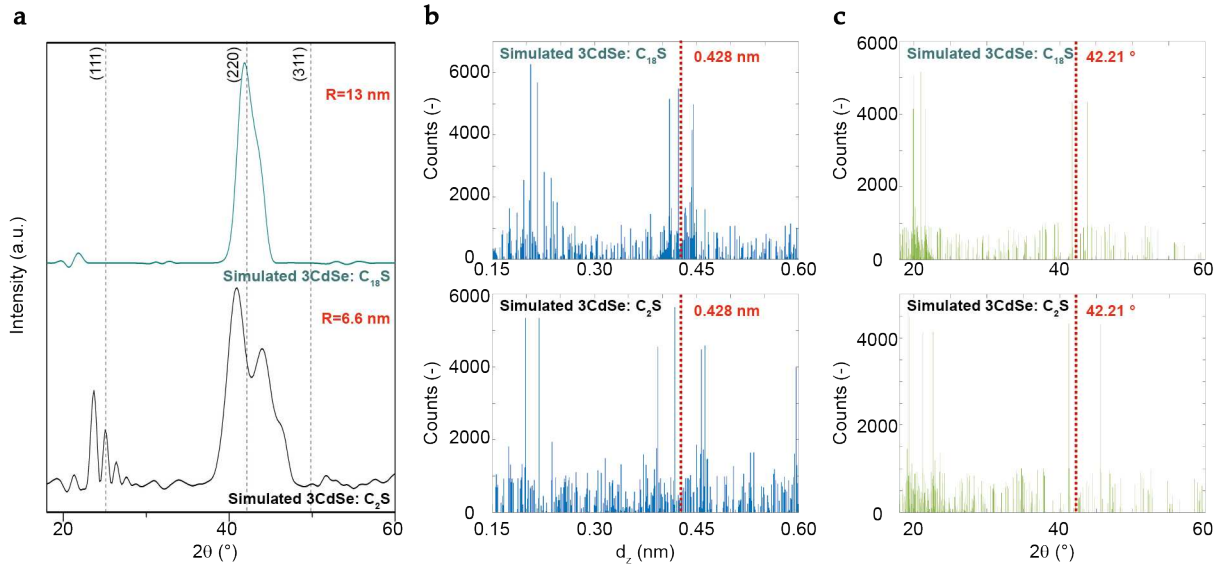


FIGURE 2.25: (a) Simulated diffractograms for anisotropic (2 2 0) family of planes, computed on a piece of 3 MLs CdSe nanohelix which mimics the features of those which are experimentally capped by ethanethiolates and octadecanethiolates. Probability counts for (b) discrete distances between paired atoms along the z -axis and (c) their corresponding Bragg angles are shown. The histograms are respectively plotted with a bin of 0.01 \AA , and 0.01° . Dashed lines in red show values that are associated with an ideal zinc blende CdSe crystal structure of lattice parameter $a_c = 6.05 \text{ \AA}$.

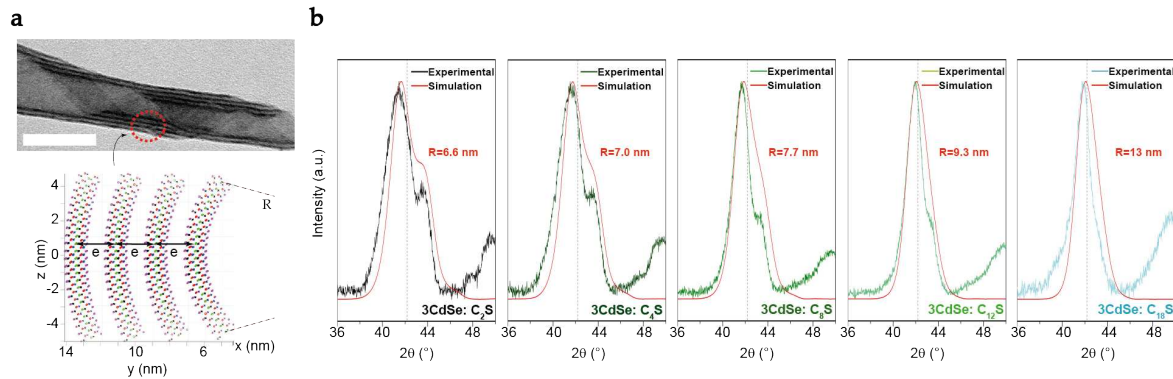


FIGURE 2.26: (a) TEM picture of 3 MLs CdSe NPLs capped by octanethiolate surface ligands. The helix makes up to four turns of folding within a single large sheet of NPL. The illustration shows four pieces of aligned nanohelix, each separated by a spacing e that are considered during simulations. Scale bar: 50 nm . (b) Experimental and simulated diffractograms for anisotropic (2 2 0) family of planes, computed on 3 MLs CdSe NPLs capped by various alkanethiolates. The helices' elemental volume in each scenario is taken equal to that of an ideal zinc blende crystal structure, where $a_c = 6.05 \text{ \AA}$.

studies, it is interesting to note that a modification of unit cell value c is minimal on the position of scattered peaks. Therefore, this agrees well with the fact that the unit cell value b_0 is entirely unscreened even though its value is being increased or decreased in Fig. 2.27(b), due to the lying down position of large helical objects. Out-of-plane across the thickness of a NPL, the induced strain is demonstrated to be negligible by changing the unit cell value

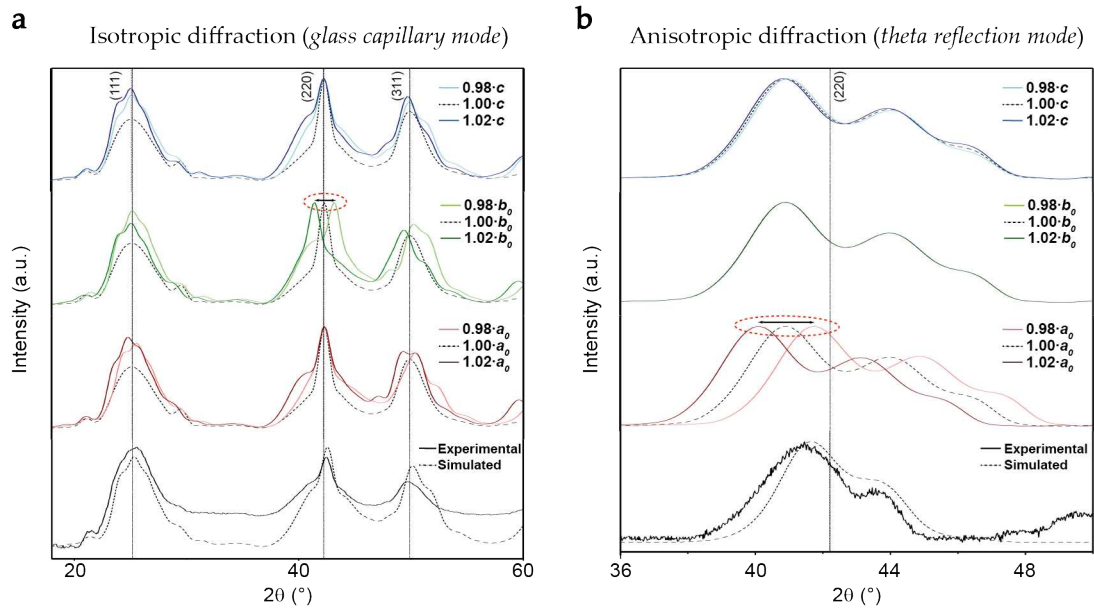


FIGURE 2.27: Comparison between experimental and simulated diffractograms of 3 MLs ethanthyolates-capped CdSe nanohelices which diffract either (a) isotropically in all directions or (b) anisotropically under specific orientations with respect to the (2 2 0) family of planes. The lattice parameters (a_0, b_0, c) used to construct the helix's elemental volume have either been increased or decreased by 2 % compared to the zinc blende bulk ones, where $a_c = b_c = c = 6.05 \text{ \AA}$. As a reminder, both a_0 and b_0 are expressed in terms of $a_c \cdot \frac{\sqrt{2}}{2}$. Zones circled in red display a clear shift of scattered peaks that results from the modification of parameter b_0 (resp. a_0) in the case of glass capillary (resp. theta reflection) mode.

c. Indeed, by taking a step back to a mechanical point of view, the strain exerted along a direction which is perpendicular to that of surface in-plane stresses ought to not exceed this latter.

2.4 Conclusion

In summary, semiconductor CdSe NPLs are flexible substrates that react promptly to various surface chemistries which can in turn, dictate their final shape and morphology. By employing a three-layers misfit strain mechanical model, this enables to predict the bending of NPLs which results from the adsorption of passivating ligands. Our model built from the classical work of Timoshenko, treats the contributions of the anchoring group and linear aliphatic chain of a given ligand separately, while demonstrating good agreement for all studied homo- and hetero-structured NPLs.

The electrostatic interactions that bind the ligands' anchoring group to the surface of an inorganic core induce a strong misfit up to an order of 20 %. Moreover, the consideration of steric repulsion existing between the ligands' aliphatic chains allows for a fine tuning of the nanohelices' radii, by experimentally modifying their chain lengths. Herein, the packing layer of aliphatic chains is estimated to exhibit a Young's modulus in lateral compression, in the order of 1 GPa compared to the literature values of 40 and 46 GPa found for our studied inorganic bulk CdSe and CdS materials.

From a structural point of view, despite the important surface stress induced by thiolate ligands, the average in-plane lattice parameter of CdSe nanohelices remains however, equal to that of zinc blende bulk. Through XRD experiments, it is evidenced that the specific orientation of anisotropic objects play a significant role at determining both the appearance (ratio of intensities, extinction of contributions) and position (full-width dispersion, inter-plane distance) of scattered peaks. Nevertheless, as helices radii become larger when these latter are capped by longer and sterically-occupying ligands, their diffractograms tend to smoothen out as the presence of local distortions due to high surface curvature is much less in this scenario.

The packing of surface ligands has been leveraged as a mean to mechanically induce stresses onto ultrathin bodies. In the beginning of the following chapter, a series of NPLs of a given thickness with various morphologies will be presented as candidates for the study of circular dichroism (CD). Thereby, another role of the organization of these surface stabilizers will also be discussed in view of tuning the shape of inorganic nanoparticles during synthesis. Typically, this yields NPLs possessing a high in-plane aspect ratio that increases with the amount of long-to-short carboxylate chains introduced. Via this control, one can then selectively break an object's symmetry to result in a panel of laterally extended shapes (square, rectangular, twisted, helical) and serve these latter as basis substrates for the surface assembly of either achiral or chiral ligands.

Chapter 3

Chiral imprints on nanoplatelets

Chirality and associated optical CD are intriguing properties of objects which exist at all length scales. In optical spectroscopy, the CD signals are employed for instance, to detect conformational changes of biomolecules and in building switchable sensors [161, 162]. Chirality and non-zero CD effect in a molecule are present if it has neither mirror-symmetry planes nor a center of symmetry. In such a case, a molecule acquires a sense of rotation that could either be clockwise or counter-clockwise. Hence, it reacts with left- and right-handed circularly polarized photons differently and shows a non-zero CD signal.

Modern nanotechnology has the ability to assemble hybrid superstructures composed of nanocrystals and organic molecules as building blocks. These individual starting materials of a hybrid superstructure can be made of different compositions such as metals, semiconductors and biomolecules. The resulting interactions between them usually convey new interesting properties to the superstructure. A recent example is demonstrated by using deoxyribonucleic acid (DNA)-origami-scaffolded plasmonic gold nanohelices attached to a substrate, which can be used to reversibly switch the optical response between two distinct CD spectra corresponding to either a perpendicular or parallel helix orientation with respect to the incident beam [163]. These switchable chiral nanostructures can then be implemented as sensors for the detection of molecules, as well as their sense of chirality and orientation.

From there by taking a step down the hierarchy, one can find individual nanoparticles that produce chiral geometries at a smaller scale compared to the antecedent one at micron level. In general, chiroptical activity can be induced onto quantum nanoparticles by functionalization with chiral ligands via a relatively simple post-synthetic phase-transfer ligand exchange [84, 89]. In this process, the initial hydrophobic ligands-capped nanoparticles produced by the hot injection synthesis in organic media are exchanged by chiral hydrophilic ligands, accompanied by a transfer into the aqueous phase. Subsequently, they exhibit chiroptical activity in their own absorption region, unlike the chiral ligand molecules, which often absorb light only in the deep UV region.

The origin of induced chirality can be understood by the chiral distortion of a nanoparticle's surface atoms upon the adsorption of chiral ligands or the hybridization of their energy levels with the ones of chiral ligand molecules, which then leads to the splitting of the hole-electron levels into two sublevels with different absorptions of circularly polarized light [164, 165]. Via this route of obtaining chiral quantum objects at a single particle level, it seems interestingly enough to begin an investigation with materials such as NPLs that possess already a wide window of optical transitions which does not superimpose with the deep UV region, for such purposes of chirality induction. The as-discussed individual II-VI cadmium-based nanohelix presents a lateral surface that could span up to thousands of nm² and in other words, are capable to host a minimum of tens of thousands of ligands if each

one of the surface cadmiums were to be passivated by a thiolate which occupies roughly 18.5 \AA^2 . Moreover, their versatile surface chemistry play renders them to be easily imagined when it comes to functionalization with various chiral compounds that are interesting to be tested out.

3.1 Effect of particles' shape

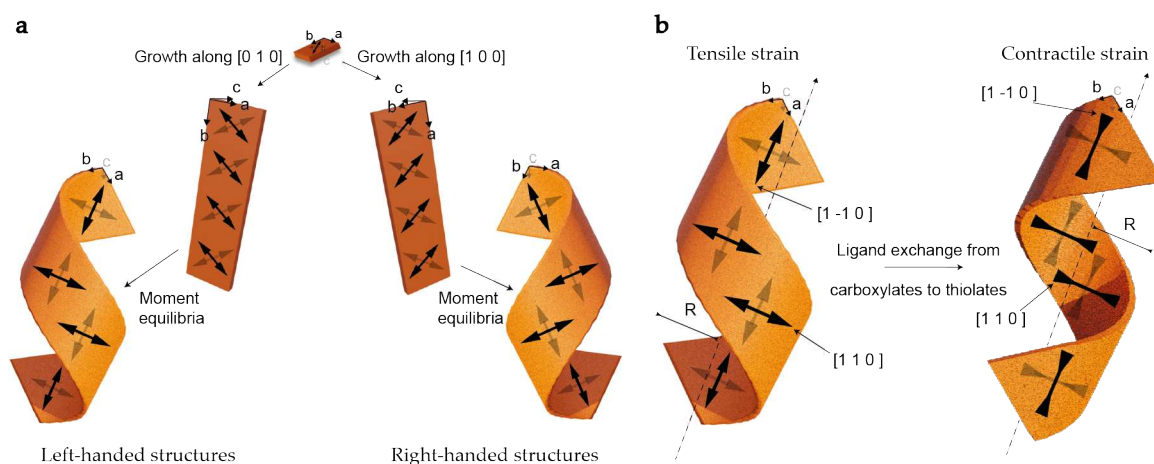


FIGURE 3.1: (a) Two possibilities of presumed growth along the $[0\ 1\ 0]$ and $[1\ 0\ 0]$ directions of a small piece of flat NPL that is capped by positive strain-inducing surface ligands. This leads to the existence of two distinct populations of nanoobjects which are intrinsically chiral, due to the orientation of surface stresses brought by the adsorption of these ligands that is perpendicular to one another on the top and bottom wide facets. At equilibrium, these large ultrathin nanosheets fold as chiral helices in order to minimize their internal elastic energy. (b) By taking the example of a left-handed helical structure, the tensile stresses that are directed perpendicularly (resp. in parallel) to the helical axis on its outer (resp. inner) surface become inverted as the positive strain-inducing surface ligands like carboxylates are exchanged with the negative strain-inducing ones such as thiolates. This process of ligand exchange not only does invert the sense of applied stresses, but also the handedness of these semiconductor nanohelices.

The previous exchange of surface ligands has been done on NPLs that were initially capped by a mix of acetates-oleates, toward different linear alkanethiolates possessing the chemical formula $C_nH_{2n+1}S^-$ where $n = 2, 4, 8, 12, 18$. Theoretically, there should be a racemic mixture of left- and right-handed helices since the growth of nuclei into platelets can be both pictured along its zinc blende $[1\ 0\ 0]$ and $[0\ 1\ 0]$ crystallographic directions with a presumed equal probability Fig. 3.1(a). During the process of surface alteration from carboxylates to thiolates, an unfolding of the nanohelices is first observed before being followed by a refolding of these latter in the opposing direction. TEM pictures in Fig. 3.2 show that a single NPL can exhibit areas where a folding in two opposing directions becomes possible. This arises typically from the presence of a mixture of ligands that simultaneously brings a tensile (resp. contractile) stress originating from the carboxylates (resp. thiolates) anchoring group acting on the inorganic core. The carboxylates-capped CdSe NPLs display indeed a positive strain by 1.9 % of their in-plane lattice parameter compared to the zinc blende bulk value $a_c = 6.05 \text{ \AA}$. In which case, the stress at the origin of curling is directed perpendicularly to the helical axis on the outer surface of the nanohelices. Thus, an exchange from

carboxylates to thiolates demonstrates an entire modification from an induced tensile stress to a contractile one and results in an inversion of the nanohelices' handedness as depicted by Fig. 3.1(b).

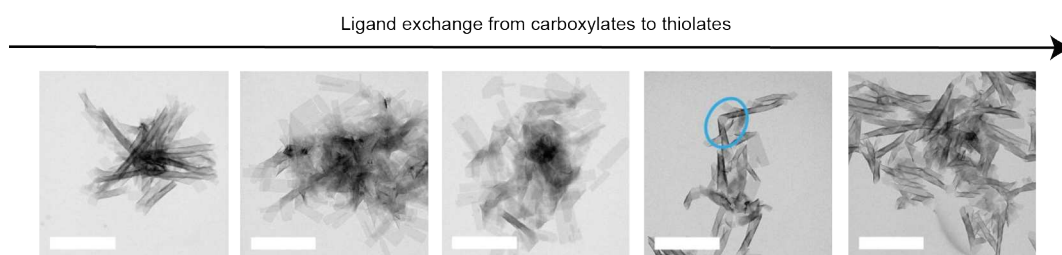


FIGURE 3.2: TEM pictures of aliquots withdrawn during a process of ligand exchange from carboxylates to dodecanethiolates, carried out on 3 MLs CdSe NPLs. In the fourth image, the blue oval highlights a zone where two distinct directions of curling can be observed at both ends of the nanohelix after being unfolded. Scale bar: 500 nm.

If one were to conduct CD measurements of these as-synthesized 3 MLs CdSe nanohelices that are initially capped by carboxylates, to in part verify the enantiomeric excess of these particles in solution, an astonishing result in Fig. 3.3(a,c) shows that their associated spectrum is not quite exactly zero. It is composed of a sum of contributions giving a sigmoid line shape and changing derivative's sign at multiple positions of absorption excitonic maxima. For 3 MLs CdSe NPLs, the excitonic transitions involving light hole (e-lh) and heavy hole (e-hh) states are readily observed as a sharp peak near 462 nm and a corresponding broader one near 435 nm. At these locations, one indeed observes that the CD line shape follows a similar trend as the absorption spectrum, which proves that the chiroptical transitions are associated to the initial excitonic bands of NPLs. The CD signal's magnitude for these achiral ligands-capped nanohelices is however relatively weak, giving an order of $3 \cdot 10^{-5}$ in terms of g-factor, where the maximum (resp. minimum) of the sigmoid situates at 469 (resp. 455 nm).

3.1.1 Studies on uniquely-shaped 3 MLs CdSe NPLs

A series of 3 MLs CdSe NPLs with the same thickness, but various lateral sizes and shapes is synthesized in order to further investigate this intriguing behavior, where achiral ligands-capped quantum particles are able to weakly exhibit chiroptical properties. Therefore, nanoobjects that are squares, polygons and twists have been fabricated by changing the cadmium and selenium chemical precursors involved during synthesis, as well as the different introduced amounts of carboxylic acids. Their lateral dimensions are thoroughly analyzed under TEM after a ligand exchange with iodides, which allows a complete unfolding of the NPLs. This has yielded objects which are respectively $(170 \pm 20, 7350 \pm 560, 2870 \pm 170)$ nm² compared to the helical ones at (53740 ± 4370) nm² (Fig. 3.3(b)). A slight variation in terms of absorption excitonic maxima is noticed for the smallest squared-objects, where their positions are blue-shifted by 4 nm compared to the larger ones. This is indeed related to the stronger quantum confinement effect in the lateral directions of these tiny particles [166].

Factors leading to shape-selective synthesis

In previous studies, the crystalline structures of CdSe nanocrystals with various elongated shapes belong often to the hexagonal wurtzite phase [167]. There was a need for strong ligands such as phosphonic acids, to create a difference in binding energy to the different

available crystal facets [168]. The facets that present a strong ligand binding do not grow as fast as those with a weaker ligand-binding energy, thereby resulting in symmetry-breaking nanoparticles. It is as well possible to leverage the steric hindrance existing between neighboring ligands to result in shape-controlled synthesis. In general, long and bulky chains tend to stay far apart, rendering the local curvature of a particle high and thus, giving a spherical shape. Reports where shorter chains with smaller steric strains, that were either contributing as carboxylic acids or complexing parts of cadmium and selenium precursors, succeeded at favoring crystallization along a preferential axis to yield rods around 12 nm for instance [169].

Whereas by tuning the reactive temperature of synthesis in the case of cubic zinc blende CdSe nanocrystals, distinct morphologies of cube-, sphere-, tetrahedron-shaped and branched particles with a high uniformity can be obtained [170]. According to the calculations of relativistic density functional theory, the adsorption energy of capping ligands on the {1 0 0} facets is usually much lower than that of the {1 1 1} facets due to their higher packing density and the amount of unsaturated atoms. This indicates that the growth of the particles on the {1 0 0} facets possesses a lower activation energy barrier and thus, a preferential growth along this most kinetically favorable direction is facilitated in this example of slab geometry models.

Hereby in our case, the difference in terms of synthesis between polygons and twists is due to the ratio of oleic-to-acetic acids introduced in the reactive medium. It is assumed that in presence of a greater amount of bulkier ligands, the diffusion-controlled mechanism at play, of incoming monomers onto the narrow facets becomes hindered independently of the metal and chalcogenide precursors' concentration [171]. Hence, by adding an adequate quantity of both long and short chains, one is rather able to tune the aspect ratio of as-synthesized NPLs, ranging from roughly 2 to 11.

Observations under CD

According to the CD signals plotted in Fig. 3.3(a,c), an increase of g-factor can be observed going from 0.3, 1.7 to $4.1 \cdot 10^{-5}$ for particles that are squares, polygons and twists. Similarly to the nanohelices, their CD line shape exhibits an identical trend with their own corresponding absorption spectrum. The maximum (resp. minimum) of these sigmoids situates at (465 - 474 - 463) (resp. (449 - 457 - 452) nm). It is worth underlining that the concentration of particles suspended in solution used, during measurements is similar for all samples. In other words, the optical density of the first excitonic peak is aimed to be inferior to 0.1. It can be seen here that the magnitude of the CD response increases with the anisotropy of particles' individual shape. In comparison between the highest and lowest g-factor values obtained for twists and squares, there is around a 20-fold increase. It is important to state that these NPLs are in each case capped by a mix of achiral carboxylates and hence, if these latter exhibit chiroptical activity, the origin might be due to their symmetry-breaking morphologies.

Most recently, the phenomenon of CD has been observed in QDs and nanorods which have not been activated by chiral molecules [76]. This is rather surprising since the observation of chiroptical activity in randomly oriented nanoparticles generally requires chirality. In order to shed light onto this point, the authors have suggested that the QDs possess chiral defects such as screw dislocations, which are affecting the optical properties of small-sized CdSe/ZnS ones and hence, inducing dichroism signals with dissymmetry factors exceeding 10^{-2} . Similarly for single CsPbBr₃ nanocrystals, Lifshitz and co-workers

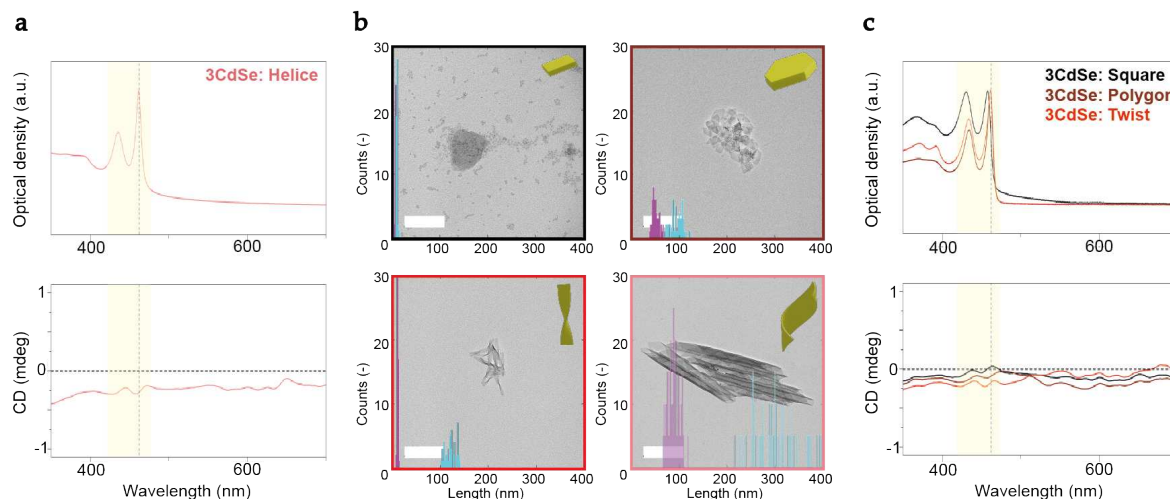


FIGURE 3.3: (a) Optical spectra in terms of absorption and CD for 3 MLs CdSe nanohelices. (b) TEM images of NPLs with the same thickness, but of various shapes like squares, polygons, twists and helices. The histograms show the distribution of dimensions along the short- (magenta) and long-axis (cyan) of these nanoobjects. Measured values are respectively $(7\pm 1, 50\pm 7, 11\pm 1, 88\pm 12)$ nm and $(10\pm 1, 95\pm 12, 122\pm 11, 302\pm 45)$ nm, analyzed over a population of 100 nanoparticles. Scale bar: 200 nm. (c) Optical spectra in terms of absorption and CD for these associated 3 MLs CdSe NPLs, where the first excitonic peak located near 462 nm is represented as dotted line in the highlighted region.

have attributed their elliptical polarization in photoluminescence at zero magnetic fields, to the inversion symmetry-breaking and Rashba effects [172].

Efros and co-workers have demonstrated that achiral structures such as two-dimensionally layered perovskites were theoretically shown to exhibit CD that was observable under an optimal configuration of optical excitation [173]. This latter did not require an external magnetic field, neither the presence of chiral molecules on their outer surface. Polarization-dependent absorption was expected to occur due to the combined effect of Rashba splitting, in-plane crystal symmetry-breaking and the effect of the exciton momentum on its fine structure. Due to the in-plane wave vector dependence on the effective magnetic field that led to the observation of fine structure, helical excitonic states were split in systems of orthorhombic and lower crystal symmetries. Typically, crystals with point symmetry C_{2v} were capable of demonstrating such Rashba spin-splitting effects and the selective coupling of these helical exciton states to circularly polarized light was responsible for the as-predicted CD.

3.1.2 Further investigations on 4 MLs

In order to verify such shape-symmetry-breaking assumption that is being hypothesized here in this work, another series of 4 MLs CdSe NPLs with the same thickness, but various lateral sizes and shapes is again synthesized. Nanoobjects that are squares, rectangles, twists and helices have been fabricated by modifying the introduced ratio of cadmium-to-selenium precursors (Fig. 3.4(b)). Later, their lateral dimensions are thoroughly analyzed under TEM after a similar ligands exchange with iodides. This time around, the objects present respectively $(460\pm 30, 700\pm 50, 4440\pm 240)$ nm² compared to the helical ones at (20500 ± 1250) nm².

Again, a slight variation in terms of absorption excitonic maxima is noticed for the smallest squared-objects, where their positions are blue-shifted by 3 nm compared to the larger ones (Fig. 3.4(c)).

Observations under CD

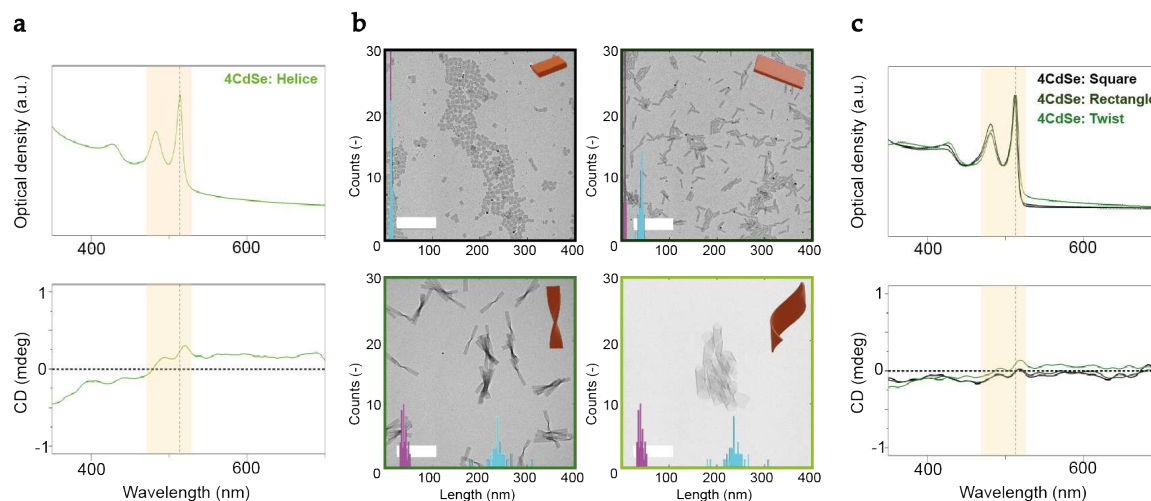


FIGURE 3.4: (a) Optical spectra in terms of absorption and CD for 4 MLs CdSe nanohelices. (b) TEM images of NPLs with the same thickness, but of various shapes like squares, rectangles, twists and helices. The histograms show the distribution of dimensions along the short- (magenta) and long-axis (cyan) of these nanoobjects. Measured values are respectively $(14 \pm 1, 7 \pm 1, 20 \pm 2, 42 \pm 6)$ nm and $(14 \pm 1, 41 \pm 4, 104 \pm 7, 238 \pm 19)$ nm, analyzed over a population of 100 nanoparticles. Scale bar: 200 nm. (c) Optical spectra in terms of absorption and CD for these associated 4 MLs CdSe NPLs, where the first excitonic peak located near 514 nm is represented as dotted line in the highlighted region.

The CD line shape once again demonstrates a similar evolution with the corresponding absorption spectrum of each population of 4 MLs CdSe NPLs. In terms of their magnitude, an increasing trend is observed ranging from $1.2, 3.4$ to $7.4 \cdot 10^{-5}$ for particles that are rectangles, twists and helices respectively. The maximum (resp. minimum) of these sigmoids situates at $(519 - 524 - 526)$ (resp. $(501 - 503 - 506)$ nm). If one were to look at the ratio between the highest and lowest g -factor values obtained for helices and squares, there is around a 4-fold increase. This result are in contrast with the work reported by Oron and co-workers, where there was hardly any change in the relative magnitude of the CD response with the lateral sizes of investigated CdSe NPLs. In their findings, the NPLs were capped by chiral *L*-cysteine molecules, where the effect studied concerned mainly their chiral footprint onto semiconductor nanosubstrates obtained through ligand exchange [89]. Besides, the as-synthesized NPLs in our case display an outer surface that covers differences over two orders of magnitude, thus enabling a broader scope of investigation.

Enantiomeric excess assessment

Undeniably, the primary motivation of developing chiral nanomaterials is the possibility of creating chiral metamaterials with negative refractive indices and for the purposes of biomolecular sensing [174, 175]. However, in order to attain these effects that are fundamentally interesting, one is often limited by the issue of CD coupling's strength. In general,

significant magnitudes can be obtained in systems of achiral nanoparticles arranged in a chiral superstructure with strong interparticle interactions [176]. But the most intuitive approach to obtain a large chiroptical activity is definitely by directly forming nanoparticles with an actual chiral shape such as gammadions or helices. For instance, a report on the formation of chiral shapes with enantiomeric excess was done on semiconductor TiO_2 that was made possible via a transcription of the helical structure of amino acid-derived amphiphile fibres through fine coordination bindings between the carboxylic groups and TiO_2 source [177]. Moreover, nanocrystals of Te and Se with a variety of chiral shapes that exhibited dissymmetry factors in the order of 10^{-3} were readily obtained and hint at the possibility through various chemical transformation processes, of templating other materials into chiral shapes thanks to the reactivity of Te [79].

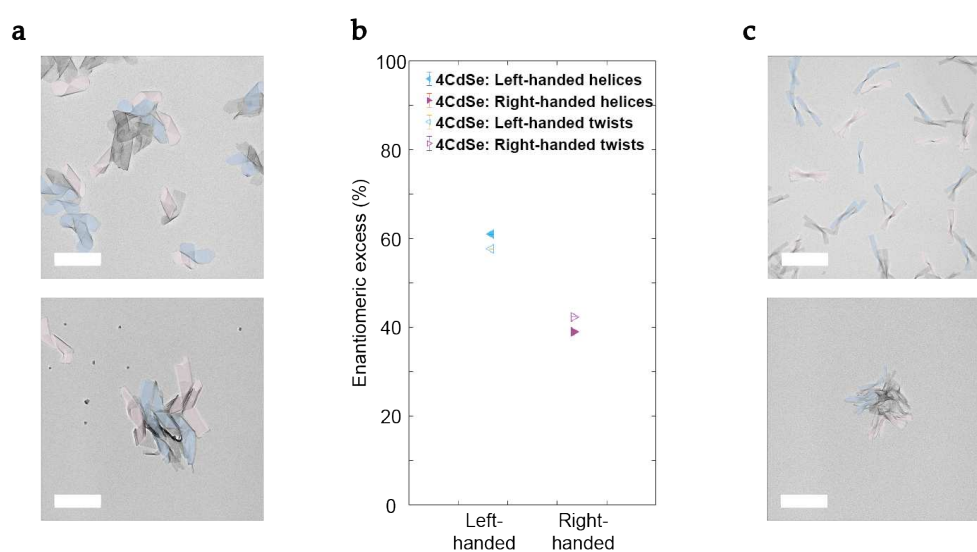


FIGURE 3.5: TEM images of separate batches of 4 MLs CdSe (a) nanohelices and (c) twists both capped by achiral carboxylates upon synthesis. The different enantiomers: left- and right-handed ones are respectively color-coded with blue and pink to ease evaluations of enantiomeric excess. Data plotted in (b) is accounted for a population of 100 objects and averaged over 3 batches of as-synthesized nanoparticles. Scale bar: 200 nm.

Therefore, a huge challenge remains at resolving an achiral system in order to leverage the chiroptical activity generated through the shape of the whole nanostructure. Herein, weak g -factors observed in the order of 10^{-5} are mainly attributed to the insignificant enantiomeric excess of the chiral entities (Fig. 3.5(b)). Carried out image analysis at high resolution allows a crude distinction of their handedness based on the objects' contrast and at first approximations, it appears that a weak enantiomeric excess is observed for three average batches of synthesized samples. This point however, would certainly require further exhaustive in-situ tomography techniques to reproduce significative statistical data [178].

We thus attempt to detail in **Chapter 4** a strategy of enantiomeric separation that could help to sort such systems of achiral mix. Nevertheless, this preliminary shape study done on NPLs of a given thickness enables at least, the determination of noise signals that are related to the optical alignment of the CD instrument itself. In which case, these latter ought to correspond to values found for 3 (resp. 4) MLs CdSe NPLs that are square-shaped which

equal 0.3 (resp. $1.7 \cdot 10^{-5}$). For the following discussions in the next sections, the average dissymmetry factor obtained for these most isotropic square samples is taken as absolute errors, in part to account for the contributions of lattice chirality and crystal defects, but also, surely the effect of light scattering and possible birefringence originating from these nanostructures [179, 180].

3.2 Direct ligation with chiral compounds

Among several evoked origins of inorganic chiral materials from **Chapter 1**, it is suggested that the presence of chiral stabilizers can enantiomerically distort the outermost atoms of a nanoparticle, in order to imprint symmetry-breaking behaviors onto this latter. Therefore, the stronger the binding of these chiral compounds onto the surface of an inorganic core, the greater the distortion of this underlying material would become and thus, leading to a more important chiroptical observation [181]. For these examples, similar molecules with either one single anchoring group or more like cysteine and *N*-isobutyrylcysteine were usually investigated. Thereby, surface ligands that carry two anchoring groups such as two oxygen atoms from two carboxylates or carboxylate groups combined with thiolates, have strong interactions with the inorganic core of the material and often, these latter cause inorganic lattice distortions more easily than those possessing only one single point of attachment.

3.2.1 Thiol functional groups

Concerning chiral semiconductor nanoparticles, the pioneer report on the use of cysteine molecules was done on the functionalization of CdTe synthesized through a direct organometallic route [84]. Moreover, a chiral memory effect was also found for these thiolates-capped nanoparticles [182]. After a second ligand exchange reaction with achiral thiols, these CdTe candidates still displayed a symmetrical mirror CD spectrum that was similar to that of the original chiral *L*-cysteinemethylester-hydrochloride-capped ones. This seems to point to a unique fact that in this case, the induced chirality is conserved and memorized directly onto the surface of these nanoparticles rather than being in interaction with the inorganic core.

In our present investigation, if one were to wonder about the structural effect of chiral molecules on the magnitude of resulting CD signals, in total four different chiral compounds of thiols and carboxylic acids have been looked into. This ought to enable g-factor comparisons between ligands that are either strongly or weakly bound to the surface cadmiums, since sulfurs exhibit in general a higher chemical affinity towards them compared to the oxygen atoms. Moving on, discussions related to the number of possessed stereocenters in a ligand and the CD dependence on the thicknesses of NPLs are also elaborated.

Cysteine molecules

Firstly, a phase-transfer ligand exchange procedure as detailed in the **Materials and Methods** section is carried out using *L*-cysteine molecules to substitute the relatively weakly bound carboxylates. As illustrated in Fig. 3.6(b), this molecule at the experimental pH of 13 presents three functional moieties: carboxylate (COO^-), amino (NH_2) and thiolate (S^-) as dictated by their respective pKa values. On the surface of a QD, all three groups can potentially be coordinated to the cadmium cations where the strongest affinity is demonstrated by the part of sulfides. Herein, as the six exposed facets of a NPL consist mainly of (1 0 0) family of planes and its equivalent, this eliminates preliminarily the possibility of a tridentate binding form of *L*-cysteine molecules. These 3 MLs CdSe NPLs that are initially

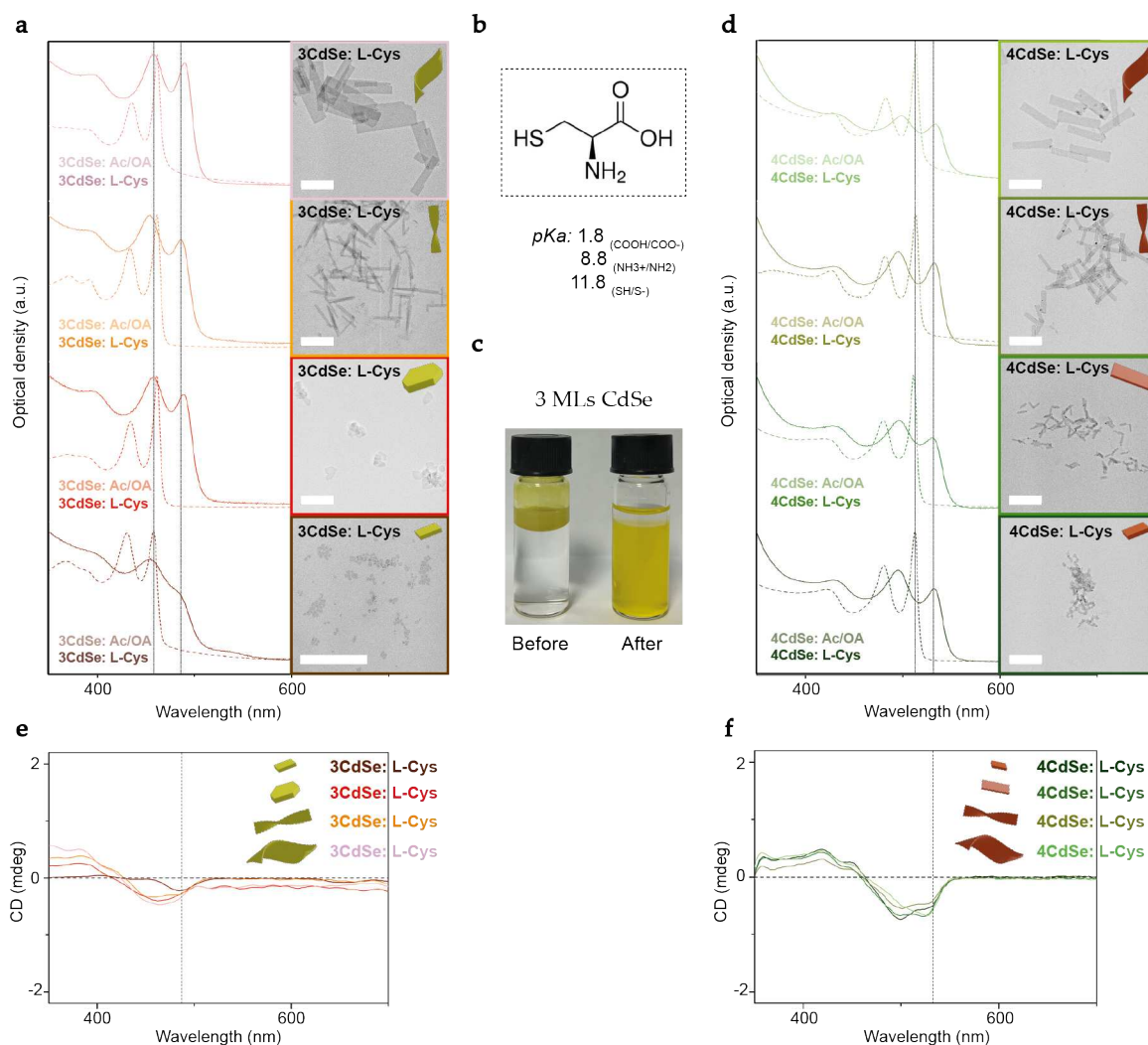


FIGURE 3.6: Absorption spectra of various shapes of 3 (resp. 4 MLs) CdSe NPLs subjected to a ligand exchange from a mix of acetates-oleates to *L*-cysteine molecules, displayed in (a) (resp. (d)). The chemical formula of this chiral compound is shown in (b) and the visual observation at bench of such chemical reaction before and after, is illustrated in (c) for the 3 MLs ones. The dashed lines indicate the shift of their first excitonic peak located near 490 (resp. 534 nm) after ligand exchange. The resulting CD signals for 3 (resp. 4 MLs) structures are displayed in (e) (resp. (f)), along with their TEM images at the final state. Scale bar: 200 nm.

suspended in hexane are clearly phase-transferred into the denser aqueous solution after a certain amount of reaction time, as shown visually in Fig. 3.6(c). During experiment, the reaction medium is followed by the absorption spectroscopy and the redshift of the e-hh transition peak stagnates around 490 (resp. 534 nm) upon a completion of ligand exchange independently of the 3 (resp. 4 MLs) particles' shape (Fig. 3.6(a,d)). This is most likely attributed to the partial delocalization of the carrier wave function from the inorganic core onto the surface stabilizers, as has already been observed in most cases of ligand exchange.

Under TEM, it is interesting to note that similarly to iodides, these particles are entirely unfolded upon a surface functionalization by *L*-cysteine molecules and lie flat on their wide facets. This constitutes therefore another strategy that can be used to better observe an

object's morphology and to deduce histograms of its size distribution. Via the elemental analysis data reported in Tab. 3.1, one can compute in each case, a cadmium-to-selenium ratio that is constantly close to 4:3 for 3 MLs CdSe NPLs and a sulfur-to-surface cadmiums ratio that varies around 50 %, given that one cysteine molecule binds to two surface cadmiums. According to several investigations on the binding mode of cysteine molecules, in particular on the surface of cadmium-based clusters and nanoparticles through multinuclear solid-state NMR techniques, Takegoshi and co-workers have demonstrated that the ligands bind to CdSe₃₄ magic clusters via coordination as S⁻-NH₂ bidentate and S⁻ monodentate ligations, in amounts of 43 % and 57 % respectively [183, 184]. These results also hinted at the effect of ligand mobility on the photoluminescence quantum yield of semiconductor clusters, since monodentate ones can undergo mobile intramolecular bond rotations in contrary to the rigid bidentate form [185].

Concerning NPLs, as the amino ligation is hindered due to the unfavorable binding between surface cadmiums and *L*-type stabilizers, one may assume a scenario where S⁻-COO⁻ bidentate is occurring. As revealed by the means of density functional theory calculations, as the concentration of *L*-cysteine molecules increases, the predominant binding mode of these latter on a QD's surface evolves from tridentate to bidentate [186]. Herein experimentally, at a ratio of entering ligands of 50 equivalences with respect to the amount of surface cadmiums that is initially present, one may consider a full surface coverage of chiral ligands if they were to passivate two cadmium sites per molecule. A prior observed sulfur-to-surface cadmiums ratio of 50 % hints indeed at this assumption, while the other moiety is anchored by the carboxylate coming from the exact single molecule and thus, enabling a complete surface passivation.

3 MLs CdSe NPLs	<i>L</i> -cysteine-capped					
	Number of planes	Atomic ratio in theory (%)	Result for squares (%)	Result for polygons (%)	Result for twists (%)	Result for helices (%)
Cd	4	50.0	46.1±1.2	49.5±0.1	49.4±0.6	48.9±0.1
Se	3	37.5	39.9±1.3	38.4±0.6	37.6±0.1	38.8±0.1
S	1	12.5	14.1±0.1	12.1±0.6	13.1±0.6	12.4±0.1

TABLE 3.1: Theoretical and experimental atomic ratios of cadmium, selenium and sulfur upon phase-transfer ligand exchange with *L*-cysteine molecules, carried out on various shapes of 3 MLs CdSe NPLs.

In comparison to previous cases, the resulting CD signals herein are as well directly related to the excitonic band structure of the semiconductor NPLs (Fig. 3.6(e,f)). The CD line shape follows exactly an identical pattern going from 3 MLs to thicker 4 MLs ones, separated by a redshift of 44 nm. This proves that these CD transitions arise from the coupling between the same chiral surface ligands and NPLs of different thicknesses themselves. In terms of *g*-factor values computed for the population of 3 MLs, these latter vary between (2.34 - 4.02 - 1.70 - 3.35) · 10⁻⁴ for squares, polygons, twists and helices. Whereas for the 4 MLs, values of (5.27 - 6.59 - 4.73 - 3.17) · 10⁻⁴ are rather obtained. Due to the absence of an absolute trend in these induced CD results, independently of the anisotropic shape of NPLs, it would be clearer to interpret these values in terms of their average. For these structures of different thicknesses capped by *L*-cysteine, this yields in fact 2.85 and 4.94 · 10⁻⁴. A previous report

4 MLs CdSe NPLs	<i>L</i> -cysteine-capped		
	Number of planes	Atomic ratio in theory (%)	Result for helices (%)
Cd	5	50.0	49.8±0.2
Se	4	40.0	42.0±0.2
S	1	10.0	8.1±0.3

TABLE 3.2: Theoretical and experimental atomic ratios of cadmium, selenium and sulfur upon phase-transfer ligand exchange with *L*-cysteine molecules, carried out on 4 MLs CdSe nanohelices.

of comparable ligand exchange with cysteine molecules showcased the highest band edge CD signal intensity of about $5 \cdot 10^{-4}$ with 5 MLs CdSe NPLs [89]. Thus, this leaves one to suspect about a possible increase of *g*-factor values with the thickness of an inorganic core, where the hole levels are localized, to enter in hybridization with the HOMO of the chiral ligands.

Dithiothreitol molecules

Secondly, another thiol-functionalized candidate called *L*-dithiothreitol, has been investigated with its chemical formula represented in Fig. 3.7(b). Visually speaking, the 4 MLs CdSe NPLs that are initially suspended in hexane are distinctly phase-transferred into the denser aqueous solution after an overnight reaction (Fig. 3.7(c)). These latter are monitored via absorption spectroscopy similarly to the case of *L*-cysteine and the position of the first excitonic transition peak stagnates around 500 (resp. 538 nm) upon a completion of ligand exchange independently of the 3 (resp. 4 MLs) particles' shape. Relating back to the strain exerted by surface adsorbed ligands, it seems in this case that the contractile stress is significant enough to curl the NPLs up in contrary to the former *L*-cysteine molecules (Fig. 3.7(a,d)). This is coherent with the occurrence of their $S^- - COO^-$ bidentate form that ought to compensate both the contractile and tensile strains respectively induced by these two components. Ultimately, it results in an energetically relaxed structure that is quasi-flat as confirmed via TEM imaging (Fig. 3.6(a,d)).

3 MLs CdSe NPLs	<i>L</i> -dithiothreitol-capped					
	Number of planes	Atomic ratio in theory (%)	Result for squares (%)	Result for polygons (%)	Result for twists (%)	Result for helices (%)
Cd	4	44.4	46.7±2.5	45.8±2.0	45.7±1.1	45.7±0.5
Se	3	33.3	36.0±0.6	37.3±1.2	36.1±1.0	35.9±0.1
S	2	22.2	17.5±1.8	16.9±0.7	18.2±0.1	18.5±0.4

TABLE 3.3: Theoretical and experimental atomic ratios of cadmium, selenium and sulfur upon phase-transfer ligand exchange with *L*-dithiothreitol molecules, carried out on various shapes of 3 MLs CdSe NPLs.

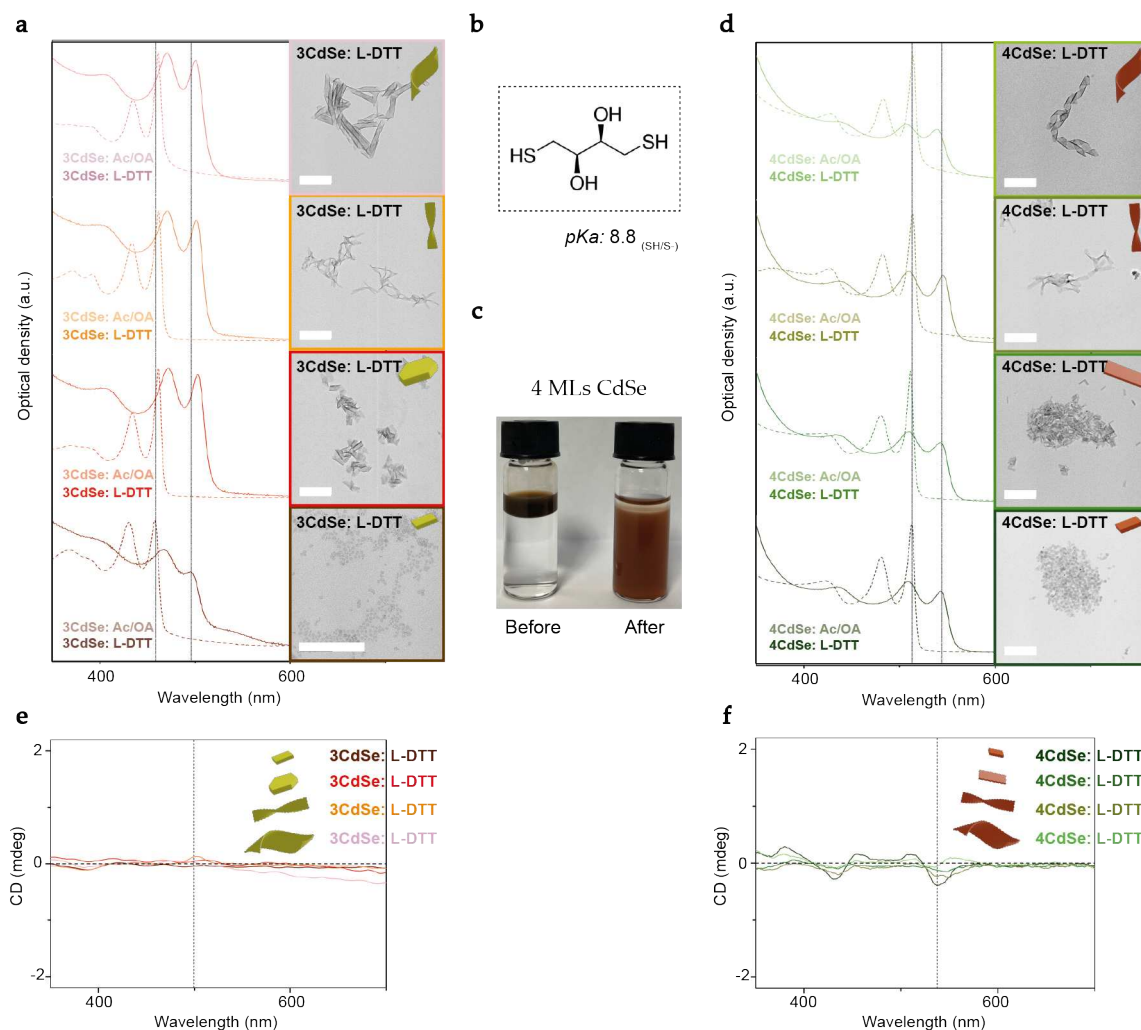


FIGURE 3.7: Absorption spectra of various shapes of 3 (resp. 4 MLs) CdSe NPLs subjected to a ligand exchange from a mix of acetates-oleates to *L*-dithiothreitol molecules, displayed in (a) (resp. (d)). The chemical formula of this chiral compound is shown in (b) and the visual observation at bench of such chemical reaction before and after, is illustrated in (c) for the 4 MLs ones. The dashed lines indicate the shift of their first excitonic peak that stagnates near 500 (resp. 538 nm) after ligand exchange. The resulting CD signals for 3 (resp. 4 MLs) structures are displayed in (e) (resp. (f)), along with their TEM images at the final state. Scale bar: 200 nm.

4 MLs CdSe NPLs	<i>L</i> -dithiothreitol-capped		
	Number of planes	Atomic ratio in theory (%)	Result for helices (%)
Cd	5	45.5	49.6±0.6
Se	4	36.4	38.6±0.6
S	2	18.2	11.8±0.1

TABLE 3.4: Theoretical and experimental atomic ratios of cadmium, selenium and sulfur upon phase-transfer ligand exchange with *L*-dithiothreitol molecules, carried out on 4 MLs CdSe nanohelices.

Herein, the elemental analysis once again reveals a good agreement between theoretical and experimental cadmium-to-selenium ratios that are constantly close to 4:3 and sulfur-to-surface cadmiums ratios that vary around 70 % (Tab. 3.3). Since the *L*-dithiothreitol molecules do not seem to induce any sort of interparticle cross-linking and assemblies as shown by Fig. 3.7, it is fair to assume that these latter bind to the CdSe NPLs via coordination as S^-S^- bidentate. One can also argue on this point by stressing out the amount of entering ligands introduced this time around, which is only of 5 equivalences with respect to the quantity of surface cadmiums that is initially present. An order of magnitude lesser in terms of chiral ligands is used, since tests that were previously carried out at 50 equivalences have all led to an etching of NPLs. In this case where a lower concentration of chiral compound is added, it should further favor the binding mode in its lowest energy configuration that corresponds to bidentate instead of being monodentate.

The average dissymmetry factor varies in the order of 0.69 and $1.10 \cdot 10^{-4}$ for *L*-dithiothreitol-capped 3 and 4 MLs CdSe NPLs (Fig. 3.7(e,f)). Surprisingly, the CD response of these *L*-dithiothreitol-capped NPLs turns out to be relatively weak, with a 4-fold decrease in direct comparison to the former *L*-cysteine-capped nanoparticles. Despite this unexpected dissymmetry gap, one can still extract the general trend where a greater average value is obtained in the case of thicker NPLs than the slightly thinner ones. This drop in terms of *g*-factor can only seemingly be due to the chemical structure of these two different thiol-functionalized chiral adsorbates, which plays a critical role at optimizing the chiroptical performance of colloidal nanoparticles.

3.2.2 Carboxylic functional groups

When both *L*-cysteine and *L*-dithiothreitol molecules bind to the CdSe NPLs via coordination as S^-COO^- and S^-S^- bidentates, although one remarks that the distance between the asymmetric carbon(s) and the anchoring group(s) seems comparable, this has still led to a puzzling difference in terms of dissymmetry factor. Two open questions remain on whether: (i) the amino chiral substituent in the case of cysteine molecules, is actually inducing a greater distortion than both the hydroxyls combined for dithiothreitol or (ii) the presence of carboxylate anchoring groups favors the inorganic core-ligands electronic coupling better.

Tartaric acid molecules

In order to enlighten these matters, a third chiral candidate called tartaric acid has been studied. As displayed in Fig. 3.8(b), this compound offers readily the availability to procure its different forms of enantiomers: *L*-(+), *meso* and *D*-(-) as color-coded in cyan, purple and magenta respectively. Its molecular structure preserves the dihydroxyl chiral feature that is localized in the middle of the carbon backbone, similarly to *L*-dithiothreitol. This thus allows a direct comparison of the nature of anchoring group between these two chiral stabilizers.

As demonstrated in prior sections on scenarios of phase-transferred *L*-cysteine- and *L*-dithiothreitol-capped CdSe NPLs, it seems rather that the resulting dissymmetry factors vary insignificantly with the lateral size of the inorganic substrates, in agreement with the reported study of Oron and co-workers [89]. Hence, this following paragraph focuses only on two main geometries: twists and helices, subjected to a ligand exchange with the different enantiomers of tartaric acid. A dependence of the computed *g*-factor values on

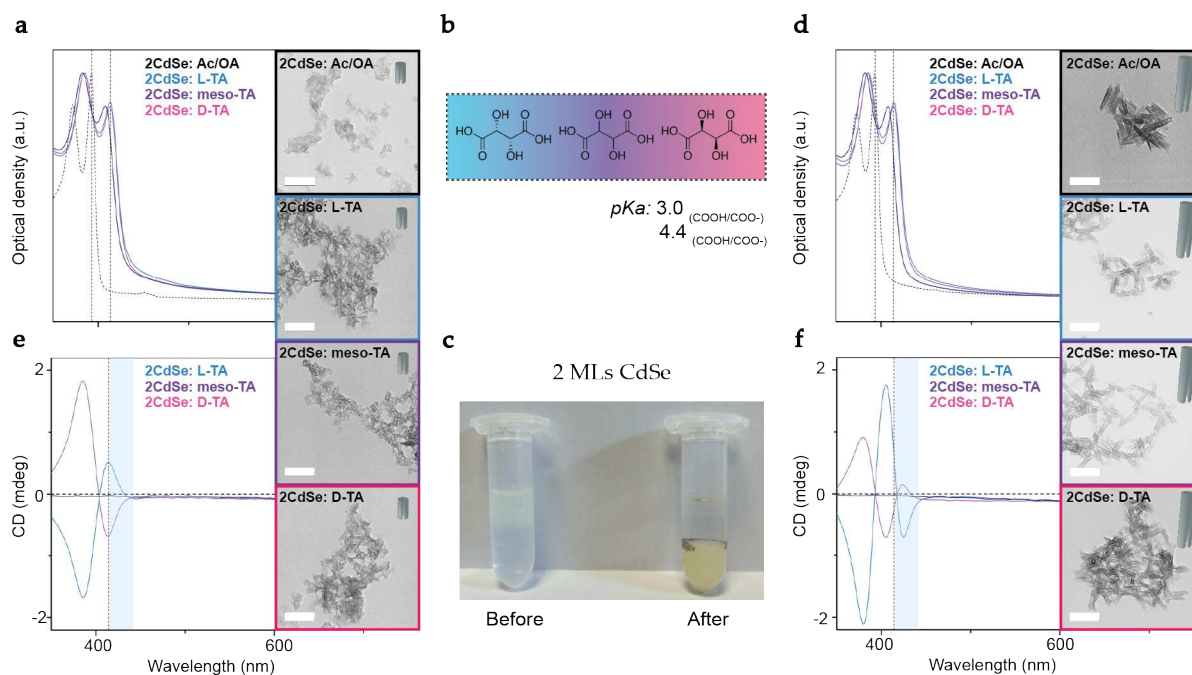


FIGURE 3.8: Optical spectra in terms of absorption and CD for two different lateral sizes of 2 MLs CdSe NPLs, that are subjected to a ligand exchange from a mix of acetates-oleates to *L*(+)-, *meso*- and *D*(-)-tartaric acid molecules, as displayed in (a) and (d). The chemical formula of these three enantiomeric forms is shown in (b) and the visual observation at bench of such chemical reaction before and after is illustrated in (c). The dashed lines indicate the shift of their first excitonic peak from 392 to 414 nm upon ligand exchange, while the highlighted region displays an additional sigmoid located at the first band edge transition of large particles. Their corresponding TEM images with these various surface alterations are shown. Scale bar: 200 nm.

the thicknesses of NPLs, passivated by both former chiral thiol molecules, is once again observed with this chiral carboxylic candidate. This has then motivated the synthesis of NPLs that are 2, 3, 4 and 5 MLs thick for the rest of the work in this part, to be post-synthetically surface-modified.

As displayed in Fig. 3.8(a,d), the as-synthesized carboxylates-capped 2 MLs CdSe NPLs exhibit excitonic transitions involving e-hh (resp. e-lh) states that are situated at 392 (resp. 372 nm). Initially, these nanoparticles present themselves as scrolls measuring (4140 ± 330) nm² before being laterally extended up to ten times greater. The protocol of phase-transfer ligand exchange as detailed in the **Materials and Methods** section is seemingly different from the previous one used for *L*-cysteine and *L*-dithiothreitol. It avoids the introduction of an alkaline agent to deprotonate the chiral compounds for an efficient functionalization, but instead, by leveraging the *Le Chatelier's* principle to overwrite equilibria of involved chemical mechanisms. As precedent, these latter are monitored via absorption spectroscopy during experiment and the position of the first excitonic transition peak shifts to 414 nm upon a completion of ligand exchange independently of the NPLs' lateral size and tartaric acids' enantiomeric form.

Under excitation by circularly polarized sources, these tartrate-capped nanoscrolls demonstrate CD signals that are perfectly mirrored along a spectrum, which is due to the

racemic mixture of *L*-(+)- and *D*-(-)-tartaric acids (Fig. 3.8(e,f)). This control experiment with the *meso*-form confirms the absence of preferential binding of one specific enantiomeric form of tartaric acid over another. Besides in Fig. 3.8, their corresponding TEM images do not picture any significant differences depending on the adsorbed molecules' chirality. The derivative line shape of CD signals associated to each exciton absorption feature is clearly evidenced, where it crosses zero and changes sign at peaks of the absorption response. This characteristic behavior better known as the Cotton effect reflects exactly which circular polarization is preferably absorbed [69]. Indeed, this bisignated pattern designates a splitting of the hole level to two sub-bands, during the wave function hybridization-type coupling between the HOMO of a ligand and valence band states in quantum particles. Cases for which this coupling is strong, leading to an efficient hybridization, shows that one of these two sub-bands is pushed higher than the original valence band edge and thus, modifying the optical properties of the inorganic core by narrowing the associated bandgap [187].

The comparison between CD spectra of objects possessing two different lateral sizes, reveals an additional sigmoid located at the first band edge transition. For a given enantiomeric form of tartaric acid, this hints somewhat at a supplementary split according to the angular momentum of states between the electron and hole, of the first exciton energy level. Furthermore, this observation of an additional sigmoid is slightly more pronounced on NPLs that possess a pair number of MLs than the odd ones. One can remark the presence of a supplementary CD dip at higher wavelengths than the absorbance maximum, much more easily on large 2 and 4 MLs CdSe compared to the 3 and 5 MLs ones (Fig. 3.8, 3.9). While recent reports on electron transmission through chiral molecules suggest an existing relationship between spin and chirality, however it cannot be concluded for the present work, in the absence of a theoretical model, whether this such similar mechanism applies for excitations in NPLs possessing exactly either a pair or odd number of MLs in terms of thickness along their one-dimensional quantum confinement direction [188, 189].

According to these surface modifications by chiral tartaric acid molecules on NPLs that are 2, 3, 4 and 5 MLs thick, several common aspects can be pointed out: (i) the position of the first excitonic peak redshifts respectively by (22 – 20 – 19 – 5) nm, independently of the nanoparticles' lateral size and enantiomeric form of ligands used and (ii) the two-dimensional objects' morphology is well preserved upon exchange with a ratio of entering ligands fixed at 5 equivalences with respect to the amount of surface cadmiums that is initially present (Fig. 3.8(a,d), 3.9(a-f)). Globally, the resulting CD signals consist of a similar line shape that is progressively migrating to the location of each NPL population's excitonic bands (Fig. 3.9(g-l)). As for their absolute dissymmetry factors, in average between nanoparticles of two different shapes, this gives (3.26 – 3.44 – 12.59 – 7.77) (resp. (2.06 – 1.93 – 2.65 – 7.00) · 10⁻⁴) for the *L*-(+)- (resp. *D*-(-)-) tartaric acid surface modifications.

By comparing dissymmetry factors obtained for dithiothreitol valued at 0.69 and 1.10 · 10⁻⁴ on 3 and 4 MLs CdSe NPLs, there is in average a 4-fold increase with tartaric acid. In both scenarios, independently of the dithiol or dicarboxylic acid functional groups, there is an observed decrease in the band-gap resulting from the delocalization of photogenerated exciton wave functions of the nanocrystals into their chiral ligand shell. According to the theory of hybridization, a hole created in the valence band of a semiconductor material renders it π -acceptor and interacts seemingly with the filled HOMO of the surface passivating ligand acting as π -donor [190, 191, 192]. This hybrid bonding orbital redshifts the lowest energy absorption peak due to an increase of the quantum confinement size and in particular under circularly polarized light, CD signal is produced from the coupling of electric dipole transition moments between considered chromophore parts [193]. Via this

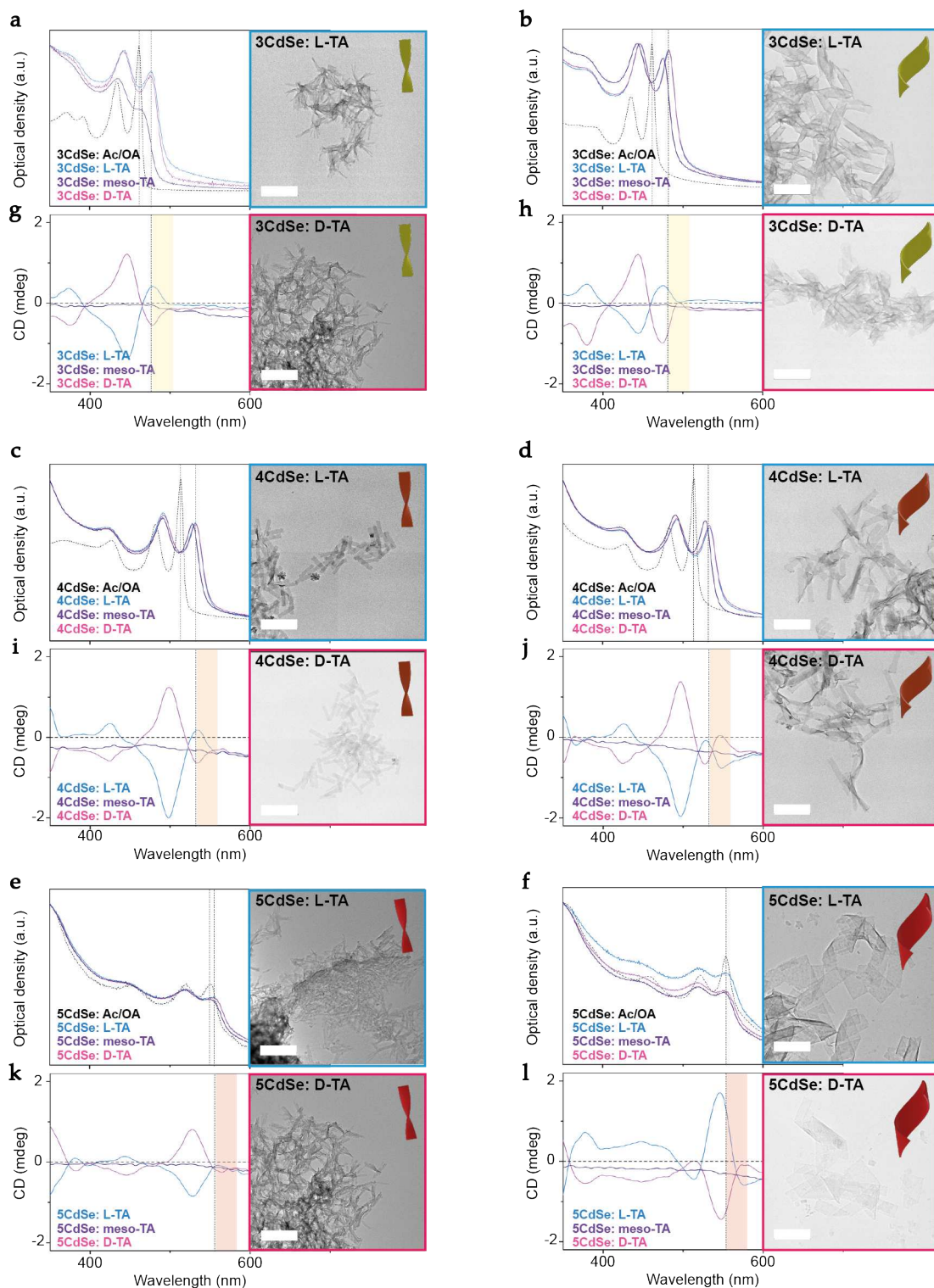


FIGURE 3.9: Optical spectra in terms of absorption and CD for two different sizes and shapes: twists and helices, of (a,b) 3, (c,d) 4 and (e,f) 5 MLs CdSe NPLs that are subjected to a ligand exchange from a mix of acetates-oleates to *L*(+)-, *meso*- and *D*(-)-tartaric acid molecules. The dashed lines indicate the shift of their first excitonic peak from 462 (resp. 512 and 555 nm) to 482 (resp. 531 and 560 nm) for structures that are 3 (resp. 4 and 5 MLs) thick. The highlighted region displays an additional sigmoid located at the first band edge transition, which is easily identified for large NPLs that possess a pair number of MLs. Their corresponding TEM images in the case of functionalization with *L*(+)- and *D*(-)-tartaric acid are shown. Scale bar: 200 nm.

reasoning, the mere difference between dithiol and dicarboxylic acid anchoring groups from the molecular structure itself hints strongly at distinct coupled polarization behaviors with the CdSe excitonic transitions.

In the visible region characteristic to the absorption of these cadmium-based NPLs, the HOMO originates from the selenium 4p orbital, while the cadmium 5s orbital contributes to the LUMO. Herein, it becomes essential to consider their band alignment with the chromophores of a surface ligand that are susceptible to induce any sort of polarizations, that was demonstrated to impact the global strength of CD signals [194, 195, 196]. CdSe nanotrapods possessing two various crystal structures: zinc blende core and wurtzite arms for instance, recorded such induced CD line shapes owing to intracrystal charge transfer and band alignment effect [197]. Similarly, chiral QD assemblies between CdSe and CdTe efficiently harvested their interparticle band engineering to result in varying electron-transfer rates that depended on the strength of the acceptor's CD spectrum [198]. These findings imply the consequence of bias orientation and selectivity of dipoles on a chiral absorbing medium. The resulting dipole screening properties of these chiral quantum particles could notably prove useful for creating spin selective conduction pathways toward sensitized photovoltaic devices [199].

Malic acid molecules

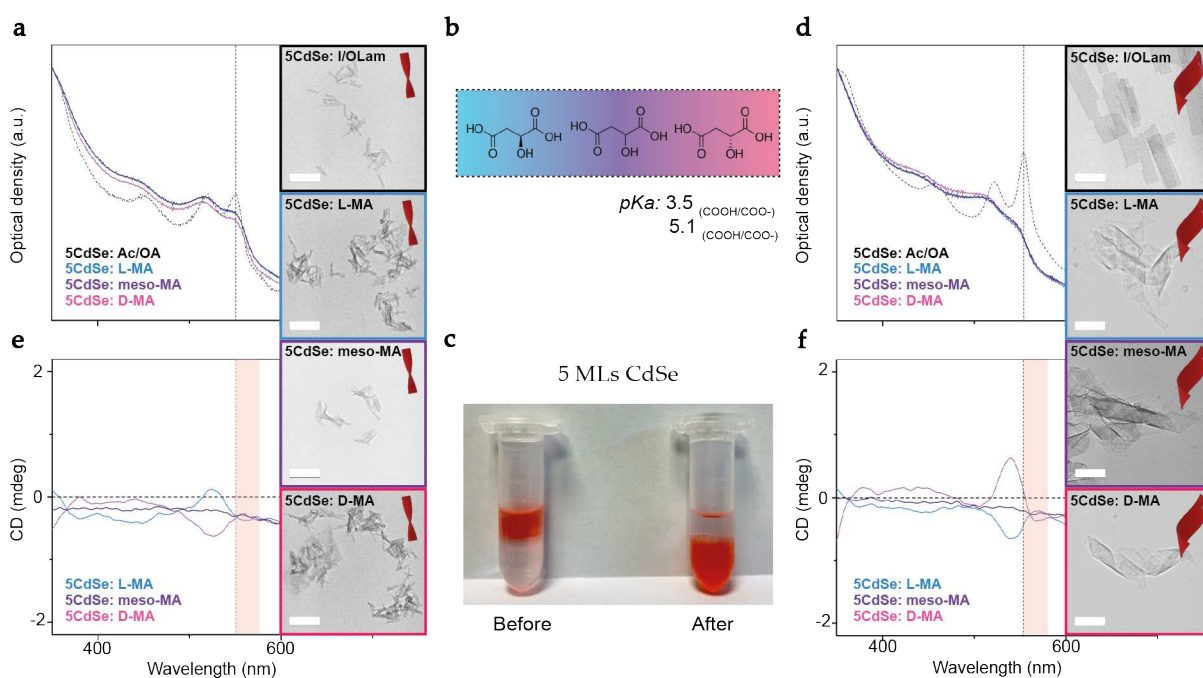


FIGURE 3.10: Optical spectra in terms of absorption and CD for two different shapes of 5 MLs CdSe NPLs, that are subjected to a ligand exchange from a mix of acetates-oleates to *L*-(-), *meso*- and *D*-(+)-malic acid molecules, as displayed in (a) and (d). The chemical formula of these three enantiomeric forms is shown in (b) and the visual observation at bench of such chemical reaction before and after is illustrated in (c). The dashed lines indicate the initial position of their first excitonic peak near 555 nm, while the highlighted region displays an additional sigmoid located at the first band edge transition of large particles. Their corresponding TEM images with these various surface alterations are shown. Scale bar: 200 nm.

Lastly, a fourth chiral candidate called malic acid has been investigated under a similar approach to tartaric acid. As displayed in Fig. 3.10(b), this compound offers as well the possibility to procure its different forms of enantiomers: *L*-(-), *meso* and *D*-(+) as color-coded in cyan, purple and magenta respectively. In contrary to the former carboxylic candidate, there is only a monohydroxyl chiral feature that is localized along the carbon backbone of this molecule. Hence, it enables a direct comparison of the effect of stereocenter number on the magnitude of CD signals, for an identical anchoring mode of these two carboxylic ligands.

These 5 MLs CdSe NPLs initially suspended in hexane, are phase-transferred into the denser methanol solution, upon a complete ligand exchange as depicted in Fig. 3.10(c). During experiment, these latter are monitored via absorption spectroscopy and the redshift of the first excitonic peak turns out to be less pronounced compared to tartaric acid (Fig. 3.10(a,d)). By summarizing the data of these chiral malate-capped NPLs of different thicknesses, there is a net difference by 4 nm in each case compared to the tartrate-capped ones (Fig. 3.11(a-f)). This yields peak positions that are respectively localized at (410 – 478 – 527 – 551) nm, while once again being independent of the NPLs' lateral size and enantiomeric form of adsorbed molecules.

Despite the similar carboxylic anchoring group existing between tartaric and malic acids, the difference in spectral shifts can be attributed to a crystalline deformation which alters the quantum well width of the CdSe inorganic core. XRD analysis of chiral carboxylates-capped 3 MLs nanohelices indicate that their respective in-plane lattice parameter differs by a fraction for the (220) family of planes as depicted in Fig. 3.12(a). There is an inclining trend towards greater 2θ values (shaded in purple) in the case of tartrates, compared to malates whose peak maxima are rather localized in the green zone. This lateral contraction of the crystal lattice leads then to a more important perpendicular expansion of their confinement direction as illustrated in Fig. 3.12(d) and therefore, displaying a slight redder optical feature in absorption [23].

Peng and co-workers have previously identified the various coordination modes between surface cationic sites and carboxylate ligands, based on a combination of FTIR, NMR and density functional theory (DFT) techniques to distinguish their molecular structure in a series of zinc blende CdSe nanocrystals presenting unique facets [200]. In particular for NPLs dominated with {1 0 0} basal planes, the chelating and bridging modes have been underlined as the dominant coordinations of carboxylates on these polar facets (Fig. 3.12(b)). Herein, each surface cadmium is coordinated to two selenium atoms from its lattice and thus, an ideal ligand coordination would be to provide two coordinating bonds for a complete tetrahedron environment of the exposed cations. Since tartaric and malic acids exhibit significant spectral redshifts than their initial case passivated by acetates-oleates, it is reasonable to believe that the cause of quantum well expansion originates from an important contractile factor such as bidentate ligation of a molecule onto one single lattice unit (Fig. 3.12(e)).

If these bicarboxylic structures were to passivate the {1 0 0} basal planes of NPLs under an optimal *cis*-configuration, the conformation of these latter alone have been generated using *molden* and minimized with the *AMBER* force field package, as depicted in Fig. 3.12(c). This yields end-to-end distances between oxygen atoms that are utmost (resp. at least) 0.443 (resp. 0.365 nm) for tartrates and in parallel, 0.442 and 0.378 nm for malates. A crude estimation of an average of these two values in each scenario, compared to the ideal zinc blende reduced lattice parameter a_c , gives a mismatch ratio of -5.6 and -4.2 % respectively

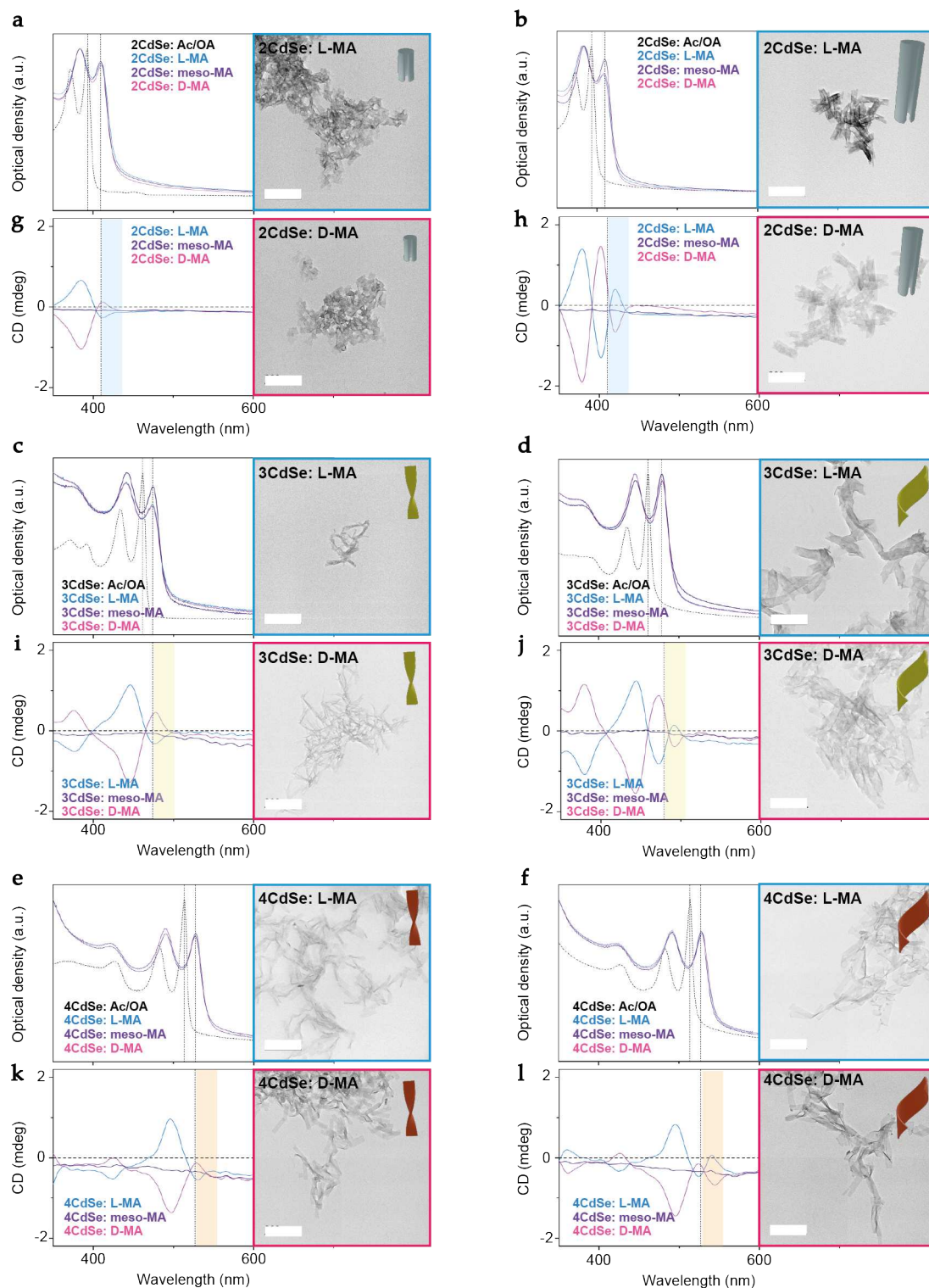


FIGURE 3.11: Optical spectra in terms of absorption and CD for two different sizes and shapes: twists and helices, of (a,b) 2, (c,d) 3 and (e,f) 4 MLs CdSe NPLs that are subjected to a ligand exchange from a mix of acetates-oleates to *L*-(-), *meso*- and *D*-(+)-tartaric acid molecules. The dashed lines indicate the shift of their first excitonic peak from 392 (resp. 462 and 512 nm) to 410 (resp. 478 and 527 nm) for structures that are 2 (resp. 3 and 4 MLs) thick. The highlighted region displays an additional sigmoid located at the first band edge transition, which is easily identified for large NPLs that possess a pair number of MLs. Their corresponding TEM images in the case of functionalization with *L*-(-) and *D*-(+)-tartaric acid are shown. Scale bar: 200 nm.

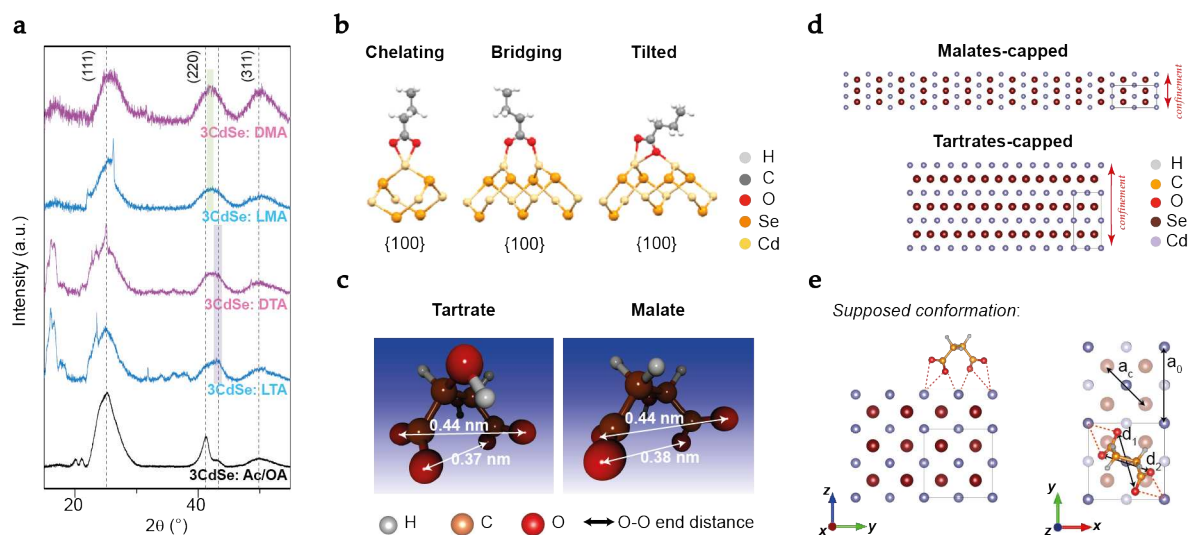


FIGURE 3.12: (a) Diffractogrammes of 3 MLs CdSe nanohelices functionalized with both chiral enantiomers of tartaric and malic acids, with respect to the initial achiral carboxylates-capped ones. The dashed lines in the region of (2 2 0) family of planes correspond to lattice parameter values of 6.19 and 5.90 Å, along with highlighted zones showing their peak maxima. (b) Illustration of three possible coordination modes for carboxylates on the {1 0 0} facet on a NPL. (c) Estimation of end-to-end distances between oxygen atoms for an optimal *cis*-configuration of both the chiral candidates, generated under *molden-AMBER* package. (d) Scheme of a supposed tetragonal CdSe lattice deformation during the adsorption of tartrates and malates onto a piece of 3 MLs NPL. (e) In average, one ligand binds in a bidentate fashion to two surface cadmium atoms, where $a_0 = 0.605$ nm, $a_c = 0.428$ nm, $d_1 = 0.443$ nm and $d_2 \sim 0.37$ nm. Adapted from [200].

for tartrates and malates. Thus, this finding points to an out-of-plane lattice expansion that is more important in the former case and agrees coherently with our absorption and XRD experiments.

It is curious to state that uniquely on 5 MLs CdSe nanohelices, the CD dip at its first excitonic transition evolves oppositely compared to all structures and even, its nanotwists counterpart of the same thickness. In the usual case of tartaric acid, the *L*-(+) (resp. *D*-(-)) form exhibits a CD dip that is of negative (resp. positive) sign. However, as one can observe in Fig. 3.9(l), this tendency becomes inverted at least in the zone of e-hh transition, while preserving the usual pattern at lower wavelengths. This confirms that the cyan curves correspond indeed to *L*-(+)-tartaric acid, as their CD signal in the near-UV region matches one another, while being mirror-image to the magenta plots for *D*-(-)-tartaric acid. Same goes with malic acid found in Fig. 3.10(d), where solely an inversion is noticed in the e-hh transition zone of these 5 MLs CdSe nanohelices. While on other structures, the *L*-(-) (resp. *D*-(+)) form exhibits a CD dip that is rather of positive (resp. negative) sign. This odd behavior might surely be related to the absence of significant redshift for ligand exchanges performed on these 5 MLs CdSe nanohelices. Seemingly, the angular momentum between electron and hole states is of opposite nature, when their absorption spectra either do not change or become blueshifted.

By weighing in the behavior of chiral tartaric and malic acids-capped CdSe NPLs,

several interesting trends can be extracted for all NPL populations of various thicknesses: (i) identical CD line shape can be found between the pair (*L*(+)-tartaric acid and *D*(+)-malic acid) and similarly, for the pair (*D*(-)-tartaric acid and *L*(-)-malic acid) in each single case of ligand exchange and (ii) greater *g*-factor values are demonstrated when anchored ligands possess two stereocenters instead of one. This first peculiar behavior of paired molecules between tartaric and malic acids falls back indeed to the fundamental definition of optical isomers, for structures that hold the same sequence of atoms and bonds, but are of different spatial arrangement. Enantiomers that are named dextrorotary (resp. levorotary) are assigned (+) (resp. (-)), which tend to rotate plane-polarized light in the positive clockwise (resp. negative anti-clockwise) direction [201]. Hence, all the above CD findings agree well between the two pairs of (*L*(+)-tartaric acid and *D*(+)-malic acid), along with (*D*(-)-tartaric acid and *L*(-)-malic acid).

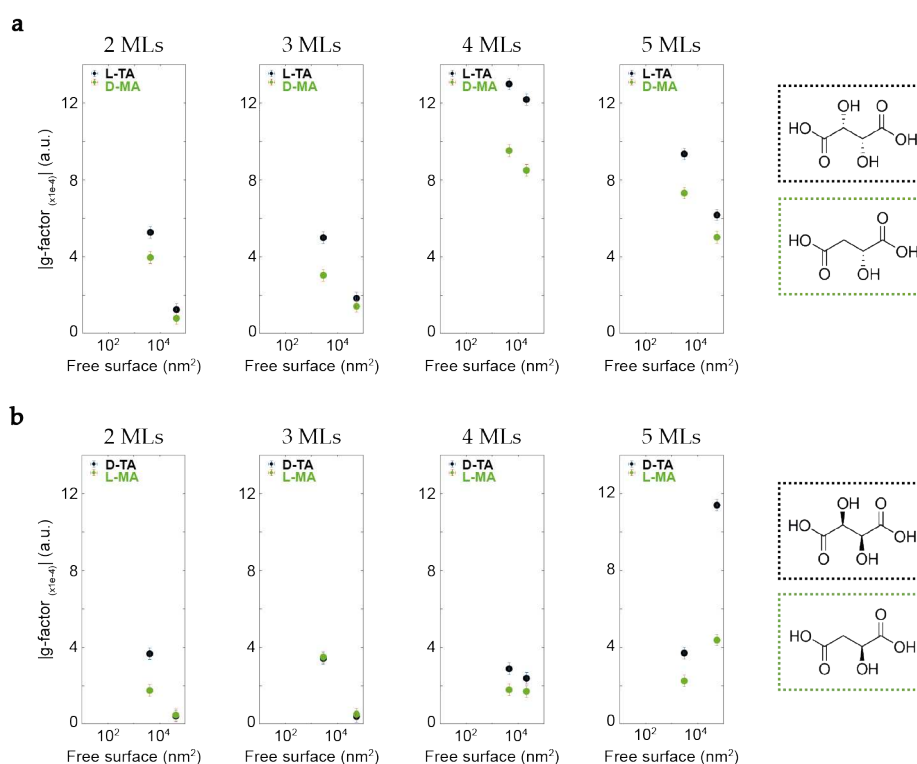


FIGURE 3.13: Absolute *g*-factor values of chiral carboxylates-capped 2, 3, 4 and 5 MLs CdSe NPLs of two different lateral sizes. In (a) (resp. (b)), the pair (*L*(+)-tartaric acid and *D*(+)-malic acid) (resp. (*D*(-)-tartaric acid and *L*(-)-malic acid)) is represented in order to compare the similar optical isomers from two different families of molecules.

In Fig. 3.13, the overall view of resulting *g*-factors is summarized for all 2, 3, 4 and 5 MLs thick NPLs that have undergone ligand exchanges with the chiral tartaric and malic acids. It is important to state that they are plotted as a function of free lateral surfaces composing every NPL structure. These latter are therefore given by the expression $2 \cdot (LW + LH + WH)$, for both investigated geometries of the same NPL population, where (*L*,*W*,*H*) each respectively indicates its length, width and thickness. As noticed beforehand by Ferry and co-workers, there was a near 2-fold increase in *g*-factor values between these two families of chiral carboxylates-bound CdSe QDs reaching up to $1.60 \cdot 10^{-4}$ [181]. Herein, a similar trend can be observed for studies carried out on NPLs, where malic acids are

constantly displaying dissymmetry values that are lower than tartaric acids. If one were to assume an average value of these two investigated shapes, it would have given the largest factor up to $12.59 \cdot 10^{-4}$ in the case of *L*-(+)-tartrate-capped 4 MLs nanoparticles.

Despite an absence of linearly increasing *g*-values with less confined NPLs, one can still observe an average growing trend in each horizontal panel of Fig. 3.13, going from 2 to 5 MLs. During considered hybridization between the hole level and surface ligand's HOMO, it was demonstrated that the splitting magnitude increased with QDs' size for the first band edge transition and underlined the importance of an energetic resonance between these two bands [202]. Via this reasoning, it was assumed that the HOMO level of cysteine molecules lies just above the valence band of CdSe and as the size of QDs was increased, this former will be pushed closer into resonance with the ligand's HOMO. On the other hand however with tiny CdS QDs, a decaying signal of induced CD was rather observed with their increasing size [203]. This was attributed to the decrease of spatial overlap between the hole level's wave function and that of the surface ligands. Thereby, these reports highlight the importance of band alignment of different considered materials if one were to predict an evolution of their chiroptical absorption behaviors.

Characterizations of exchanged surface ligands

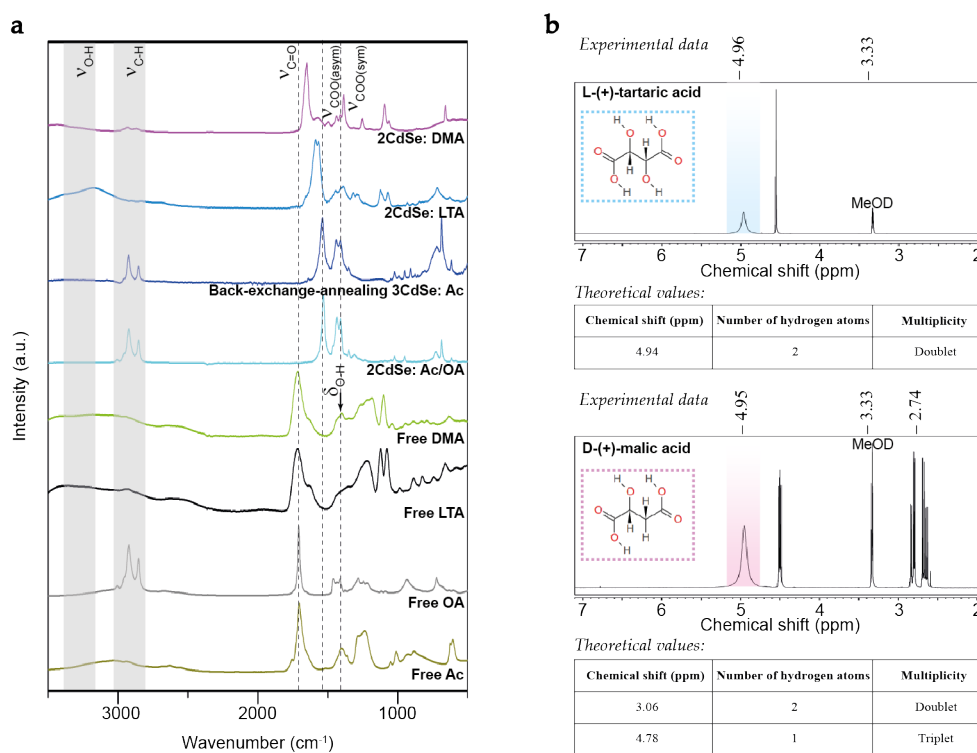


FIGURE 3.14: (a) FTIR spectra of free carboxylic acids and carboxylates-bound CdSe NPLs. (b) Experimental and theoretical ^1H NMR findings of *L*-(+)-tartaric and *D*-(+)-malic acids, where deuterated methanol is used as the solvent.

Nevertheless, these chiral carboxylates-capped NPLs are subjected to further characterizations that enable the information extraction of surface ligands' behavior such as their coverage and binding mode. In Fig. 3.14(a), the FTIR spectra of typical free suspending

carboxylic acid molecules like acetic, oleic, tartaric and malic have been recorded under similar experimental conditions as those used during ligand exchange. Unsurprisingly, these latter all exhibit common vibrational modes associated to the stretching and bending of hydroxyl and carbonyl bonds as indicated. During experiment, as the pH of reaction medium situates below 4, this gives indeed a partial protonation of functional groups according to their respective pKa values. Prior reports have confirmed that in order to efficiently substitute a bound carboxylate ligand with a free carboxylic acid, it is essential that this process be accompanied by a proton-transfer event [204, 205]. Herein, this criterion is well respected without employing any basic solutions, in contrary to the previous procedure of displacing bound carboxylates by free thiol molecules like cysteine and dithiothreitol, that was performed near a pH of 12.5.

Both large 2 MLs CdSe NPLs capped by a mix of acetates-oleates and those of 3 MLs, that are back-exchanged by acetic acids alone through the route of chlorides, display exactly similar spectra. It is as if these monodentate carboxylates bind in an identical fashion to the surface cadmiums of NPLs, leading to comparable values of asymmetrical and symmetrical carboxylate vibrational bonds. In order to ensure a complete ligand back-exchange towards acetates, an additional annealing procedure is carried out in parallel to verifications by absorption spectroscopy and elemental analysis (Appendix D).

Whereas for *L*-(+)-tartrate- and *D*-(+)-malate-capped ones, the peak corresponding to the asymmetrical stretching of carboxylate bonds becomes significantly shifted to higher energies as depicted in Fig. 3.14(a). This might potentially be due to the anchoring ligands via coordination as COO^- - COO^- bidentate, where the chemical environment seen by these two ends of carboxylate with respect to the molecular midpoint is dissymmetric. Notably in the case of malic acid, the presence of one single hydroxyl substituent accentuates its structural dissymmetry compared to the tartaric ones. Through binding as bidentate, not only the energy associated to their molecular conformation is shown to be favorable, this non-negligible shift of about 113 cm^{-1} compared to the conventional vibration of monodentate surface ligands hints at a change in binding mode from chelating to a tilted fashion as depicted in Fig. 3.12(b) [206, 186, 30]. Therefore, this further confirms the assumption of a bidentate ligation for tartrates and malates, under a *cis*-configuration.

Both experimentally and theoretically obtained ^1H NMR data performed on *L*-(+)-tartaric acid and *D*-(+)-malic acid molecules demonstrate a good agreement of their proton resonances in Fig. 3.14(b), with deuterated methanol used as the solvent. One can leverage the fact that these chiral acid molecules present a prominent peak situated around 4.8 ppm, to promptly differentiate from the ones of acetates and oleates. Via this method, a ratio of chiral-to-achiral acids both simultaneously present on the outer surface of a NPL can then be estimated, although it was assumed that the quantity of acetates-oleates left unexchanged ought to be infinitely small. As displayed in Fig. 3.15, indeed the initial signals that were assigned to the presence of acetates located at 2.0 ppm disappear entirely upon ligand exchange with both *L*-(+)-tartaric acid and *D*-(+)-malic acid molecules. Whereas, traces of methyl contribution from oleates can be determined at 0.9 ppm.

By performing these similar evaluations on NPLs of various thicknesses for the pair (*L*-(+)-tartaric acid and *D*-(+)-malic acid), the molecular ratio of chiral compounds-to-oleates can then be assessed, as plotted in Fig. 3.15(b). It is important to state that a primarily homogenous ligand distribution on each individual particle over the entire ensemble of analyzed NPLs is assumed. As expected at equilibrium, the relative number of exchanged chiral molecules varies quasi-independently with the thickness of the inorganic core. Despite

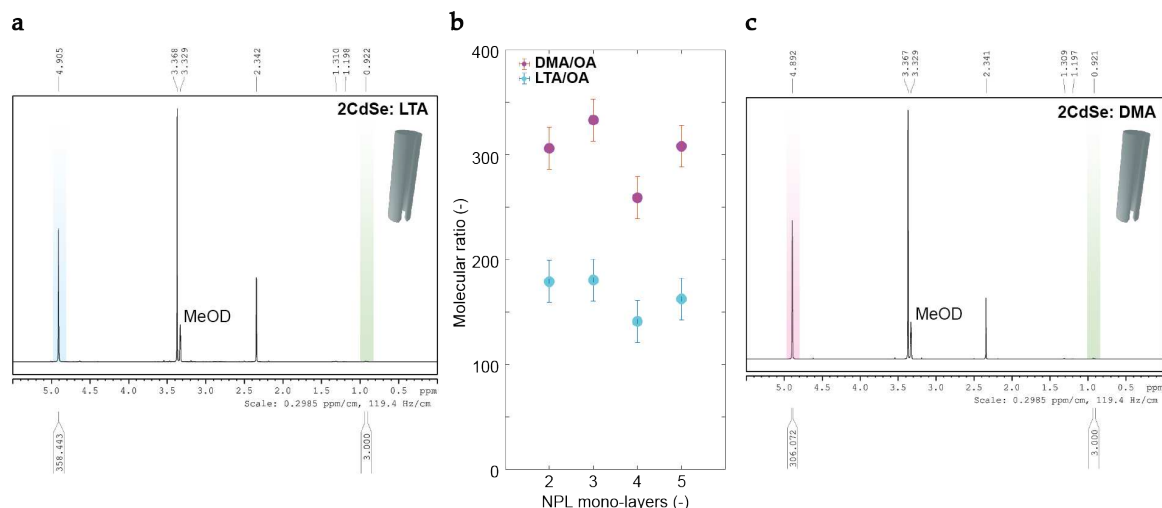


FIGURE 3.15: ^1H NMR spectra of *L*-(+)-tartrate- (resp. *D*-(+)-malate-) capped large 2 MLs CdSe nanoscrolls displayed in (a) (resp. (c)). Highlighted areas in cyan (resp. magenta) correspond to the characteristic resonance of *L*-(+)-tartaric acid (resp. *D*-(+)-malic acid), in conjunction with the data from Fig. 3.14(b). The green ones represent the methyl contribution from oleates that were previously found in Fig. 2.2 from Chapter 2. The resulting molecular ratio of chiral compounds-to-oleates is then deduced for one single population of NPLs: the largest ones, with various thicknesses in (b).

the fact that the ligand adsorption energies were generally shown to increase with the size of an inorganic core, this does not cause any major differences in terms of relative amount of exchanged-to-unexchanged molecules during the final state [207, 208]. This might be understood since the ligand desorption energies too, increase with the particles' size as entropy-related contributions to the free energy of displacement and hence, this yields a final constant ratio for the same CdSe material between NPLs of different thicknesses [209]. The order of magnitude of as-obtained molecular ratios hints at an efficient ligand exchange from an achiral mix of carboxylates to these two families of chiral agents, that convey colloidal stability overtime in polar solvents.

3.3 Surface modification with halides

Until recently, a clear distinction between the studies of ligand exchange carried out on NPLs exhibiting both the wurtzite and zinc blende structures has been published [210, 211]. The nonpolar facets of the wurtzite structure have in theory, equal numbers of atoms coming from the 12th and 16th columns of the periodic table of elements and are charge neutral. The polar facets of the zinc blende structure however, are terminated by positively charged cadmium atoms. Thereby, the previous one expresses in majority a preference with neutral *L*- or *Z*-type ligations unlike the latter one which tends only to anionic *X*-type ligations.

These changes in surface ligation are most often accompanied by observable bathochromic or hypsochromic shifts of the optical band gap of these semiconductor nanocrystals. Weiss and co-workers have initially demonstrated that the incorporation of phenyldithiocarbamate ligands onto the surfaces of II-VI QDs can result in modifications up to 1 eV of the lowest-energy absorption feature to a lower scale [187]. In these systems, holes

delocalized into the ligand shells, hence increasing the effective confinement dimension and decreasing the associated potential. Concurrently, ligand exchange of native carboxylates with aliphatic thiol or phosphonic acid performed on CdSe NPLs also implied a large shift of excitonic transition energy up to 240 meV [23]. In such cases, the electronic coupling between the inorganic core and surface ligands came in again to modify the initial crystal lattice, to result in either an increase or decrease of the quantum confinement as elucidated in Chapter 2.

3.3.1 Two-steps ligand exchange towards ibuprofen molecules

The starting point of this section began by selecting an uncommon chiral candidate that possessed an adequate molecular size, in order to minimize the consequence of steric hindrance and to ease the process of ligand exchange on pristine NPLs capped by achiral carboxylate ligands. Ideally, the chiral compound ought to exhibit one single functional group via which, it anchors onto the inorganic substrate. Herein, (*S*)-(+)-ibuprofen has been chosen where its chemical formula and the position of asymmetric carbon are shown in Fig. 3.16(a). According to the modeling made under *Gaussian*, it presents a dimension of (1.0 × 0.5 × 0.4) nm³ in its lowest energy configuration and a pKa value near 4.9 [212]. In comparison to linear carboxylates like acetates (resp. oleates), these latter are estimated in the order of (0.2 (resp. 1.8) × 0.5 × 0.5) nm³ [17, 18].

Characterizations on 3 and 4 MLs CdSe NPLs

A two-steps procedure has been carried out, where the native carboxylate ligands are first removed with halides before being redisplaced again by chiral ibuprofen molecules during the second time around. It has been demonstrated that halides are X-type ligands that are capable of redshifting the optical features of NPLs to approximately 80 meV for 4 MLs CdSe structures and simultaneously, increasing their photoluminescence quantum yield to an order of 70 % [147]. As detailed in the **Materials and Methods** section, the substitution of halide ligands onto 3 MLs CdSe nanohelices is performed at room temperature through the introduction of oleylamine and metal halides dissolved in ethanol, into a solution of nanoparticles suspended in hexane. This leads to a significant bathochromic shift of the optical band gap of these latter, in the order of 18 (resp. 35 and 34 nm) for ligand exchanges toward chlorides (resp. bromides and iodides).

Moreover, to ensure the colloidal stability of NPLs in nonpolar solvents, oleylamine is jointly added during ligand exchange. Interestingly enough, the introduction of oleylamine reduces the possibility of cadmium halide MLs' formation around the semiconductor's inorganic core and results in a final position of the absorption features close to those of the intermediate NPLs stabilized by amines through hydrogen bonding with the surface halides [211]. It is important to note that the ratio of entering ligands is fixed at 10 equivalences with respect to the amount of surface cadmiums that is present. After an overnight reaction and thorough washing steps to eliminate additional and unreacted cadmium halides, these zinc blende 3 MLs CdSe nanohelices are subjected to the reversibility test of X-to-X' ligand exchange (Fig. 3.17). For this purpose, 100 equivalences of (*S*)-(+)-ibuprofen dissolved in ethanol are introduced into a purified solution of halides-capped NPLs suspended in hexane. This back-exchange towards carboxylate ligations yields a hypsochromic shift of the lowest-energy spectral feature back to 474 nm, a position close to that of the initial acetates/oleates-capped nanohelices at 462 nm (Fig. 3.16(a)).

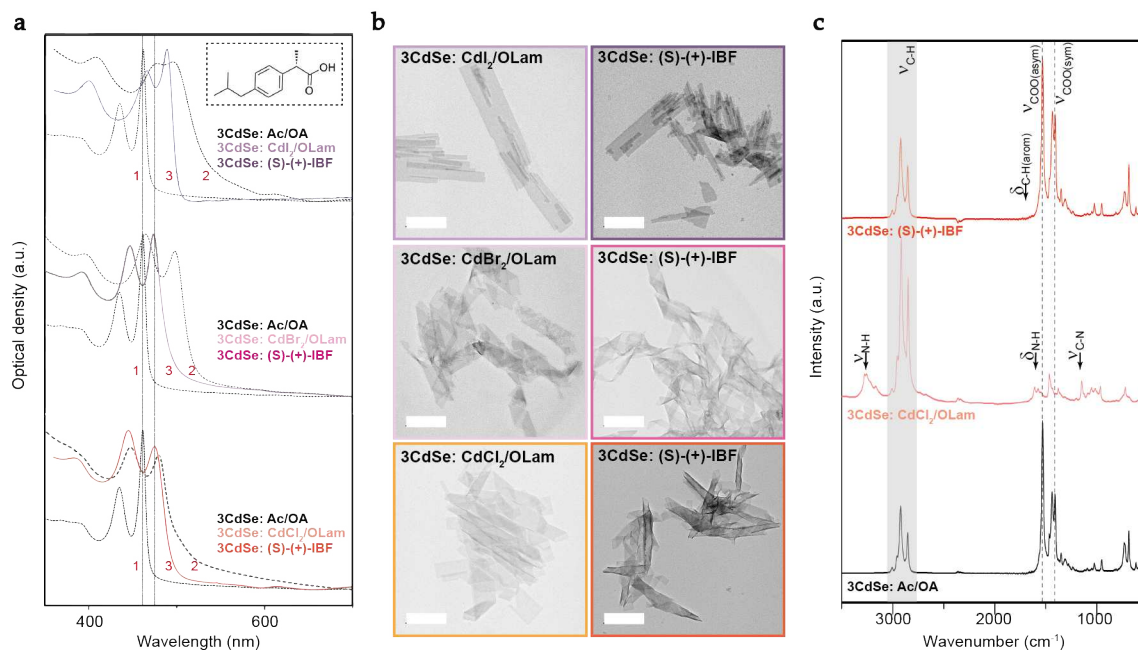


FIGURE 3.16: (a) Absorption spectra of subsequent steps (orders indexed in red) of ligand exchange starting from 3 MLs CdSe nanohelices capped by a mix of acetates-oleates (black dotted lines). Bottom (resp. middle and top) panel represents the case where cadmium chlorides (resp. bromides and iodides), along with oleylamine are first employed and plotted as colored dotted lines. Later on, these latter are back-exchanged by the chiral molecule displayed in the inlet, called (S)-(+)-ibuprofen according to the chemical pathway depicted in Fig. 3.17(b). Their corresponding TEM images are shown in (b). Scale bar: 200 nm. (c) In the case of NPLs treated with chlorides, these particles are monitored at each step with FTIR.

As shown in Fig. 3.16(a), the position of the associated first excitonic peaks after a back-exchange reverts indeed to 474 nm in the case of chlorides and bromides. For iodides however, its position seems to be retained at 488 nm. Their corresponding TEM images show that a first complete ligand exchange from achiral carboxylates to cadmium halides stabilized by oleylamine, gives NPLs which are less uniformly folded compared to their initial helical morphology. By referring to their associated XRD patterns presented in Fig. 3.18 for both 3 and 4 MLs structures, these latter are situated much closer to the bulk zinc blende CdSe possessing a lattice parameter of 6.05 Å, compared to the carboxylates-capped ones that are extended to 6.19 Å. Therefore, the induced strain is much lower in the case of halides which contributes to the eventual unfolding of the nanohelices [147].

The fact that the (2 2 0) peak is much sharper in the case of bromides compared to chlorides agrees well the previous finding elaborated in **Chapter 2**, where the full width at mid-height (FWMH) of peaks corresponding to the (2 2 0) family of planes related to the parameters a_0 and c , ought to decrease and becomes sharper as the helices radii increase. Indeed, this point matches well with the TEM images of chlorides- and bromides-capped nanohelices which are large in terms of diameter (Fig. 3.16(b)). For iodides however, since most of the objects lie flat on their wide facets, it is reasonable that the intensity ratio of (2 2 0) family of planes to the (1 1 1) ones diminishes, as the scattering probability of this former becomes slimmer. On the hand with those small rectangle-shaped 4 MLs, one can observe a presence of the sharp (2 2 0) peak independently of the chosen halide used during the

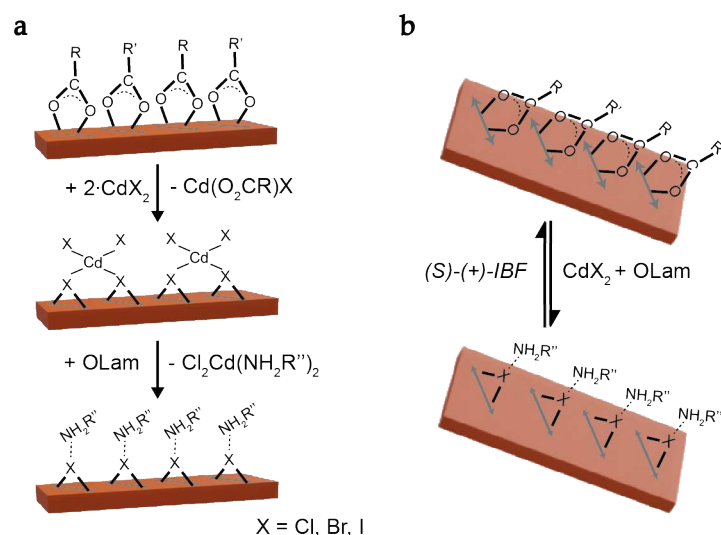


FIGURE 3.17: (a) Presumed pathway for the stages of ligand exchange carried out on zinc blende CdSe NPLs. R (resp. R' and R'') represents the rest of the carbon chains of acetates (resp. oleates and oleylamine). (b) Reversible back-exchange procedure, beginning from an achiral mix of carboxylates to halides co-stabilized by oleylamine, then reverting back to $(S)\text{-}(+)\text{-ibuprofen}$. Adapted from [211].

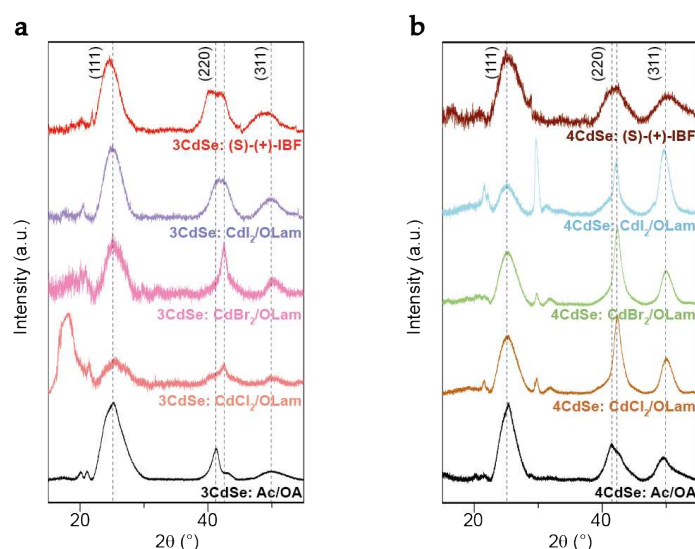


FIGURE 3.18: XRD patterns of 3 (resp. 4 MLs) CdSe NPLs displayed in (a) (resp. (b)) with various conditions of surface chemistry, from initially acetates-oleates-capped to halides co-stabilized by oleylamine and back-exchange to $(S)\text{-}(+)\text{-ibuprofen}$ via the route of chlorides. It is important to note that large nanohelices are employed in the case of 3 MLs ones, whereas small rectangle-shaped NPLs are screened for the 4 MLs ones. The two dotted lines in the region of (2 2 0) family of planes correspond to lattice parameter values of 6.19 and 6.01 Å.

first step of ligand exchange. This is mainly due to their tiny shape which renders them the ability to not only lie flat on their wide facets, but also to stack up along their narrow facets and thus, facilitating the diffraction of all contributions coming from the (2 2 0) family of

planes [213]. This highlights once again, the importance of NPLs' anisotropic orientation that is directly reflected onto their XRD patterns.

Besides, one can observe in Fig. 3.16(b) that the larger the atomic size of a halide, the more prominent the effect of unfolding goes from chlorides, bromides to iodides. Via this reasoning, upon a back-exchange with (S)-(+)-ibuprofen, the curvature of the NPLs is indeed slightly recovered in the case of chlorides and bromides. For iodides however, the nanoparticles stay globally flat. This is mainly attributed to the quantity of undisplaced halides by the incoming chiral compound, (S)-(+)-ibuprofen which in turn, hints at the reason why its excitonic peak's position was retained at 488 nm. In terms of their structural behavior under XRD, one can deduce that there is a global shift of peaks toward smaller Bragg angles according to Fig. 3.18. Indeed, by exchanging back the surface halides co-stabilized by oleylamine with (S)-(+)-ibuprofen, a tensile strain is once again exerted onto the inorganic core similarly to the initial acetates-oleates. Hence, this leads to an increase of the lattice parameter compared to the quasi bulk value that was previously due to the adsorption of different halides.

FTIR monitoring in Fig. 3.16(c) shows that upon surface alterations of 3 MLs CdSe NPLs with cadmium chlorides and oleylamine, the characteristic peaks of the carboxylates located near 1525 and 1420 cm^{-1} disappear. The appearance of new bands around 3250 and 1590 cm^{-1} confirms the presence of primary amines in the system, related to their different stretching and bending modes. Furthermore, the peak situated at 1145 cm^{-1} demonstrates the existence of carbon-nitrogen bonds. Subsequently following a back-exchange process, the initial features of the carboxylates are restored for both their asymmetrical and symmetrical stretching modes. Plus, one can also remark the importance of harmonics that are linked to the bending of carbon-hydrogen bonds in aromatic groups located around 1700 cm^{-1} . Elemental analysis on the other hand, indicates a chlorides- (resp. iodides-) to-surface cadmiums ratio of 75.0 (resp. 95.1 %) which underlines a lower exchange rate from iodides to chiral ibuprofen molecules (Tab. 3.5).

3 MLs CdSe NPLs	(S)-(+)-ibuprofen			
	Number of planes	Atomic ratio in theory (%)	Result via CdCl ₂ -OLam (%)	Result via CdI ₂ -OLam (%)
Cd	4	57.1	49.7±1.3	47.9±1.4
Se	3	42.9	33.5±1.3	31.9±1.7
Cl/I	0	0	16.7±0.9	20.2±1.4

TABLE 3.5: Theoretical and experimental atomic ratios of cadmium, selenium and halogens (resp. chlorine and iodine) upon a process of back-exchange with (S)-(+)-ibuprofen, carried out 3 MLs CdSe NPLs.

Fig. 3.19(a) displays the resulting CD signals of 3 MLs CdSe NPLs capped by (S)-(+)-ibuprofen obtained via back-exchange of halides co-stabilized by oleylamine. Significant chiroptical activity is only observed when chlorides are used as intermediates, in contrary to their counterparts: bromides and iodides, where their weak signals lead to an inconclusive judgement. This is presumably due to the existence of a threshold, dictating the minimal amount of chiral agents present in order to observe an efficient coupling between the surface ligands and inorganic substrate. The 20 % absolute excess of surface iodides in comparison to chlorides, which are still present after a back-exchange as shown by

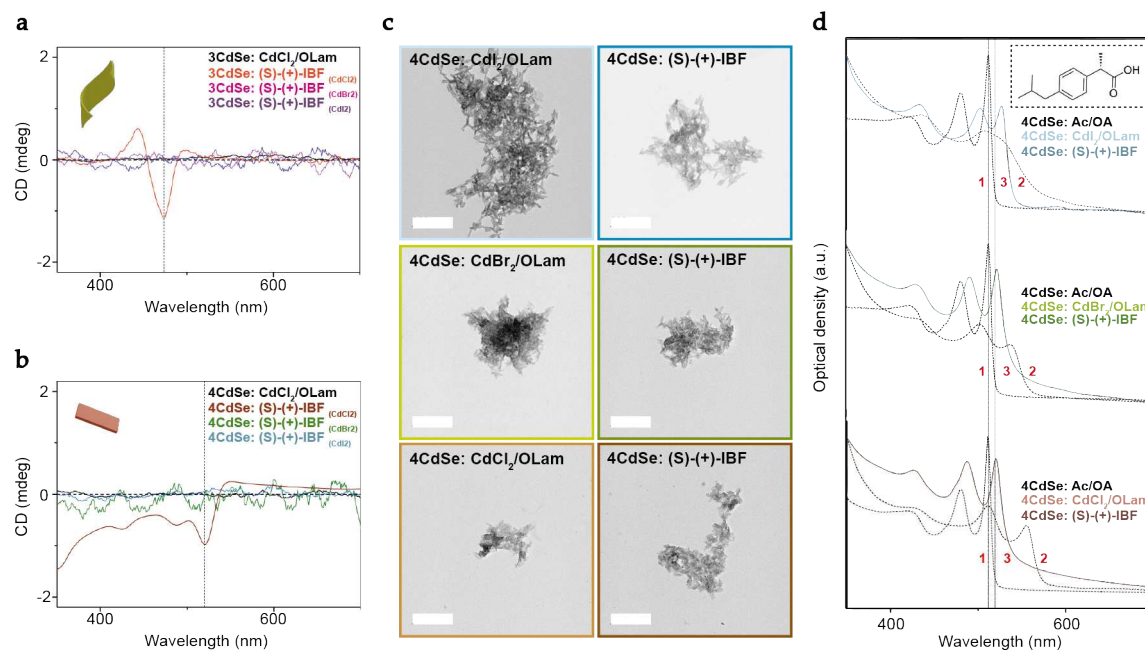


FIGURE 3.19: CD signals of back-exchanged (S)-(+)-ibuprofen-capped 3 (resp. 4) MLs CdSe NPLs displayed in (a) (resp. (b)). The dashed lines indicate the final shift of their first excitonic peak back to 474 (resp. 520 nm). TEM images of rectangle-shaped 4 MLs CdSe NPLs subjected to different stages of ligand exchange according to the chemical pathway depicted in Fig. 3.17(b), are shown in (c). Scale bar: 200 nm. (d) Absorption spectra of subsequent steps (orders indexed in red) of ligand exchange starting from 4 MLs CdSe NPLs capped by a mix of acetates-oleates-myristates (black dotted lines). Bottom (resp. middle and top) panel represents the case where cadmium chlorides (resp. bromides and iodides), along with oleylamine are first employed and plotted as colored dotted lines. Later on, these latter are back-exchanged by the chiral (S)-(+)-ibuprofen molecule, displayed in the inlet.

elemental analysis, might be significant enough to rule out any chance at obtaining active chiroptical nanomaterials (Tab. 3.5). It is important to state that none of these chiroptical behaviors is observed right upon the first step of ligand exchange with cadmium chlorides co-stabilized by oleylamine, as shown by the black control curves in Fig. 3.19(a,b).

A similar trend is once again observed on rectangle-shaped 4 MLs CdSe NPLs in Fig. 3.19(b). The only case that results in active chiroptical nanoobjects is via the route of back-exchanging chlorides co-stabilized by oleylamine, with (S)-(+)-ibuprofen in a ratio of entering ligands fixed at 100 equivalences with respect to the amount of surface cadmiums that is present. They each exhibit a g-factor of 1.44 (resp. $0.24 \cdot 10^{-4}$) for 3 (resp. 4) MLs CdSe NPLs and demonstrate maxima (resp. minima) of these sigmoids at (502 - 550) (resp. (474 - 519) nm). Upon the first step of ligand exchange towards chlorides (resp. bromides and iodides), this results in a significant bathochromic shift of the optical band gap of the 4 MLs CdSe NPLs, in the order of 45 (resp. 27 and 21 nm). Later on, the position of the associated first excitonic peaks after a back-exchange reverts to 520 nm for chlorides and bromides, compared to 527 nm in the case of iodides (Fig. 3.19(d)).

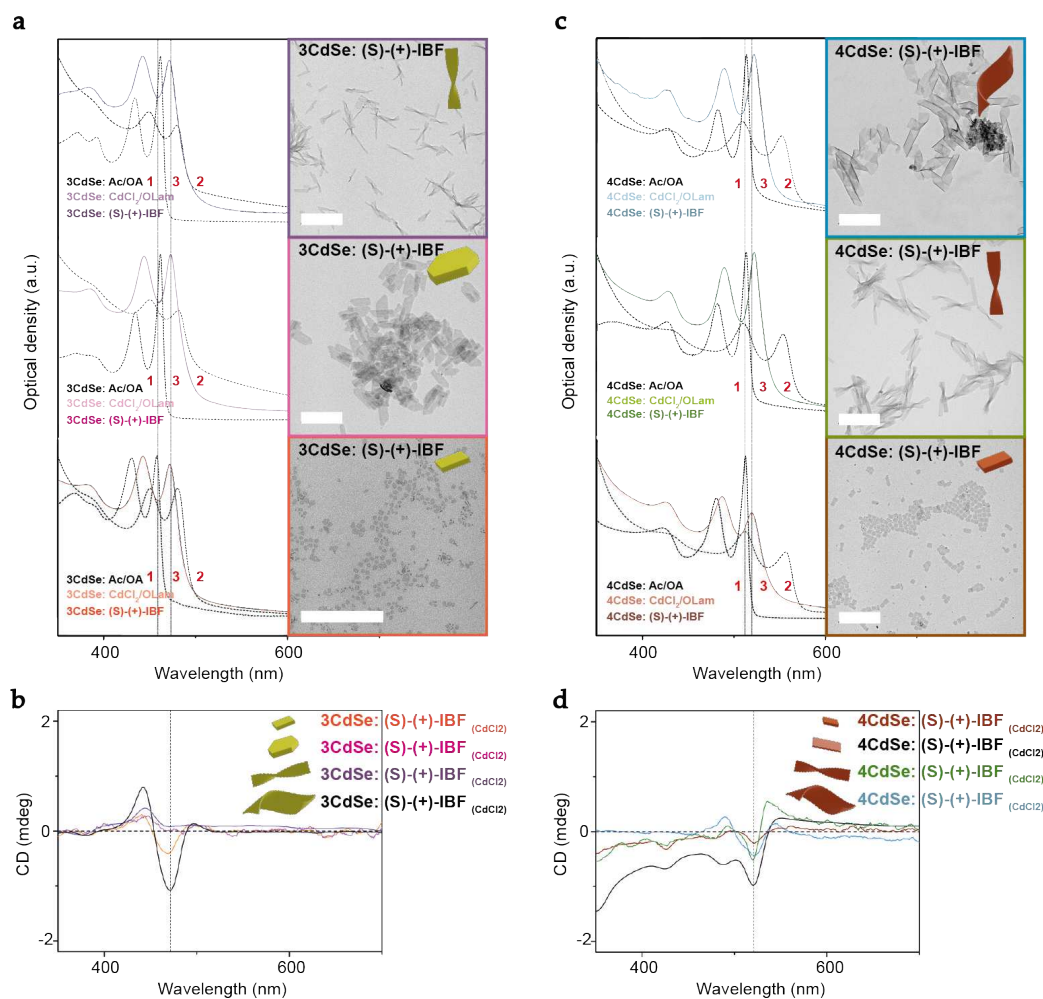


FIGURE 3.20: (a) Absorption spectra of subsequent steps (orders indexed in red) of ligand exchange starting from 3 MLs CdSe NPLs capped by a mix of acetates-oleates (black dotted lines). Bottom (resp. middle and top) panel represents the case where square-shaped (resp. polygons and twists), are first treated with cadmium chlorides-oleylamine and plotted as colored dotted lines. Later on, these latter are back-exchanged by (S)-(+)-ibuprofen according to the chemical pathway depicted in Fig. 3.17(b). Identical surface modifications done on 4 MLs CdSe NPLs (squares, twists and helices) are respectively shown in (c). The resulting CD signals for 3 (resp. 4 MLs) structures are displayed in (b) (resp. (d)), along with their TEM images at the final state. The dashed lines indicate the final shift of their first excitonic peak back to 474 (resp. 520 nm). Scale bar: 200 nm.

Extension onto different shapes of 3 and 4 MLs structures

This protocol of back-exchange has later been both extended onto 3 and 4 MLs CdSe NPLs that were previously synthesized in various shapes. One can observe that the hypsochromic shift upon the back-exchange with (S)-(+)-ibuprofen, yields a final position of the associated first excitonic peak near 473 ± 1 and 519 ± 1 nm independently of the morphology of the nanoparticles. It is important to note that these recorded values are close to those fore-mentioned in the case of 3 MLs nanohelices and 4 MLs rectangles. According to the TEM images displayed in Fig. 3.20(a,c), it is interesting to point out that despite multiple steps of surface alteration on these atomically thin nanosheets, their two-dimensional appearance is

well-preserved without suffering any major etching. During previous tests where higher ratios of entering ligands were introduced with respect to the present amount of surface cadmiums, it was shown that the NPLs may be damaged and lost their well-defined structure near the boundaries.

CD spectra in Fig. 3.20(b,d) give rise to dissymmetry values of (0.05 – 1.13 – 1.34 - 1.44) (resp. (0.02 - 0.24 – 0.26 – 0.25) · 10⁻⁴) for 3 MLs CdSe squares, polygons, twists and helices (resp. 4 MLs squares, rectangles, twists and helices). One of the first drawn conclusions is that independently of the number of MLs constituting the NPLs, seemingly for the square-shaped ones, their dissymmetry factor is weak below 10⁻⁵. This value situates in the same order of magnitude than those found in the beginning, for CD originating from achiral carboxylates-capped square NPLs. Oddly by adding chiral (*S*)-(+)-ibuprofen molecules onto these square objects, it does not seem to intensify their absorptive-like CD signals by much, in contrary to an intuitive thought.

Secondly, the evolution of dissymmetry values tends to a plateau for the rest of the studied geometries on 3 and 4 MLs CdSe NPLs capped by (*S*)-(+)-ibuprofen. This limit seems to be independent of the particles' anisotropic shape among rectangles, polygons, twists and helices. In another sense, this evolves independently of the lateral sizes of the inorganic substrate on which the chiral ligands are adsorbed. In conjunction with the work reported by Oron and co-workers, a similar *L*- and *D*-cysteine coverage found on different NPL populations whose lateral dimensions ranged from 43 to 650 nm², has led to hardly changing *g*-factors among them [89].

The redshift of the CD dip position at the NPLs' band edge transition with their thicknesses, display a global absorptive line shape in both Fig. 3.20(b,d). This qualitative observation associated to the e-hh excitonic transition state is in fact composed of two degenerate contributions of the two in-plane dipoles of a NPL [214]. If these latter were of opposite sign, this would have suggested a dispersive trend that is typically observed for a wurtzite crystal structure due to coupling of its two different crystal axes, as depicted in Fig. 3.21(a) [215].

Experimentally and theoretically, it has been shown that for an identical NPL thickness, chiral cysteine-capped wurtzite structures exhibited a stronger chiroptical response than their zinc blende counterparts [216]. These observations were attributed to: (i) a greater dipole moment in the former case along its crystal direction [1 1 $\bar{2}$ 0] and (ii) a polarization oriented along [0 0 0 1], in contrary to the isotropic in-plane contributions of the zinc blende ones as calculated by DFT (Fig. 3.21). These combined factors strongly influenced the perturbation term in dipole-dipole interaction between the NPL and chiral ligand, via a chromophoric way of separately analyzing distinct CD peaks present in one single spectrum from UV to visible (Fig. 3.21(c)).

This preliminary method of chiral activation by surface-imprinting chiral ibuprofen molecules onto CdSe NPLs is fairly authentic. In which sense, it differs from the heavily reported phase-transferred ligand exchanges that frequently concern compounds derived from cysteine. Despite the (*S*)-(+)-ibuprofen coverage remaining far from being complete with respect to the present amount of surface cadmiums, due to a fragment of unremoved chlorides at an order of 75.0 %, CD signals with a dissymmetry factor up to 10⁻⁴ are still observed on 3 MLs CdSe NPLs with large lateral sizes. This value falls in the range between the commonly reported results for cysteine-capped chiral QDs estimated near 10⁻⁵ and those for NPLs with the same surface chemistry, standing at about 5 · 10⁻⁴ [217, 89].

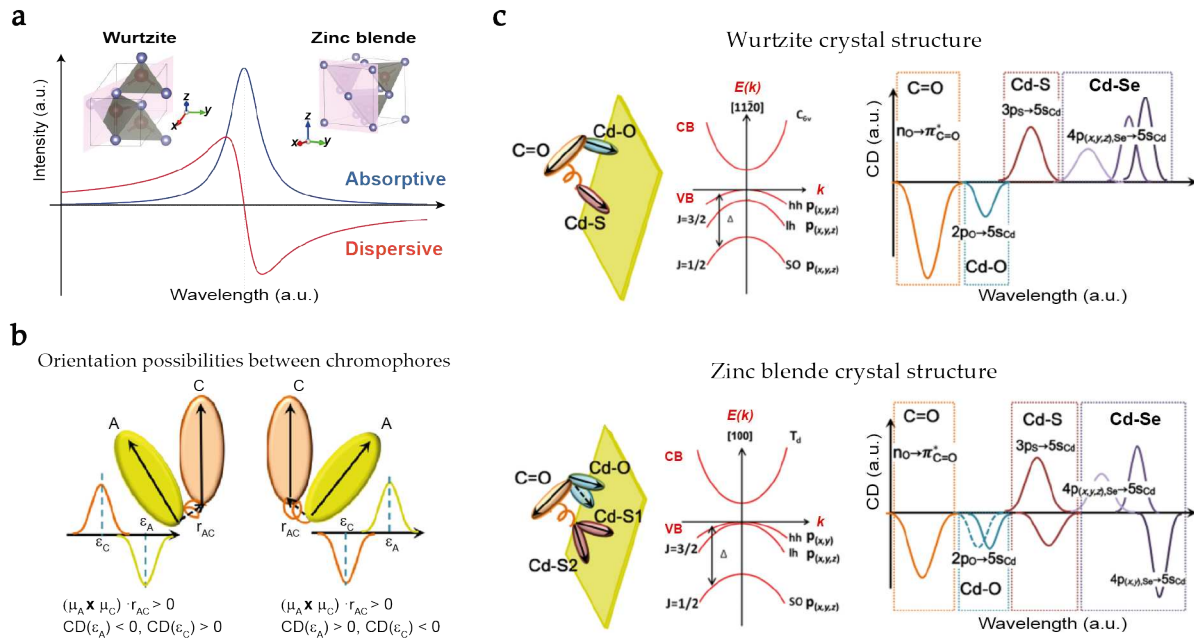


FIGURE 3.21: (a) Qualitative CD line shape, resulting from the sign of coupled dipoles localized in the core of an inorganic material. Crystal lattices of wurtzite and zinc blende are displayed, where their respective (1 1 -2 0) and (1 0 0) planes are color-coded in pink. (b) Schematic of two interacting chromophores noted as A and C, according to the nondegenerate coupled-oscillator model. These latter, distanced by r_{AC} possess transition energies noted as ϵ_A (resp. ϵ_C) and electric dipole transition moments μ_A (resp. μ_C). (c) CD interpretation of L-cysteine-capped wurtzite and zinc blende CdSe NPLs, attributed to different transitions between considered chromophores. A supposed binding through the carboxylic acid and thiol functional groups on these nanosubstrates is hypothesized, while the energy band structure is represented in each case along its [1 1 $\bar{2}$ 0] (resp. [1 0 0]) direction. Adapted from [216].

Thereafter, it would undoubtedly be interesting to work on strategies to achieve a higher chiral compound exchange rate, in order to investigate its influence on the resulting dissymmetry factor.

3.4 Conclusion

Several authentic strategies of attaining CD activity in semiconductor II-VI NPLs have been explored, thanks to the origin of their mirror-symmetry-breaking shapes and functionalization with chiral molecules on their outer surface. In short, Fig. 3.22 summarizes part of the tests that were detailed in this chapter.

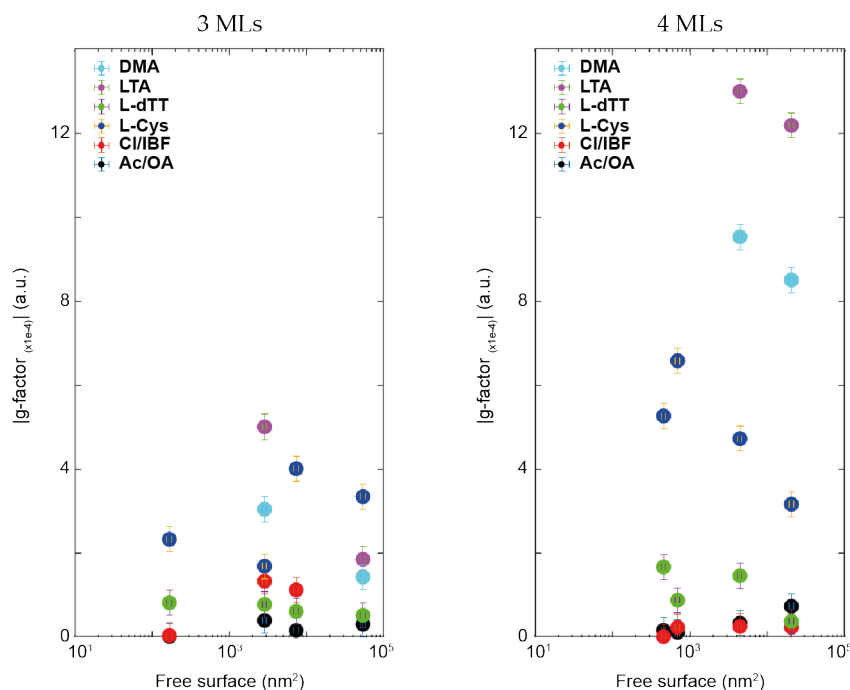


FIGURE 3.22: Absolute g-factor values of various shapes and sizes of 3 and 4 MLs CdSe NPLs presenting various surface chemistries. It recalls part of the experiments that was elaborated earlier, based-on acetates/oleates-, L-cysteine-, L-dithiothreitol-, L-(+)-tartrate-, D-(+)-malate- and (S)-(+)-ibuprofen via the route of chlorides-capped nanoparticles.

A clear trend is rather distinguished in the case of 4 MLs CdSe NPLs, where one would expect: (i) lowest dissymmetry values for achiral ligands-capped objects with random handedness (black dots), (ii) second to the last, (S)-(+)-ibuprofen-modified in presence of chlorides due to a partial exchange process (red dots), (iii) supposed stronger electronic interactions via coordination as S^- - COO^- bidentate demonstrated by L-cysteine compared to S^- - S^- bidentate in the case of L-dithiothreitol (blue and green dots) and lastly, (iv) enhancement of CD strength with the number of stereocenters going from D-(+)-malic acid to L-(+)-tartaric acid (cyan and magenta dots). Concerning the 3 MLs ones, vague yet similar evolutions can be deduced. Since the exciton splitting magnitude during hybridization with the surface ligands is anticipated to increase with the thickness of the CdSe core and a decrease of its energy gap, indeed the former pointed out aspects would be more noticeable on thicker nanostructures.

Among various spectroscopic tools available to characterize such chiroptical effects, the standard extinction-based electronic UV-visible CD has been chosen. In addition to controlling the nanomaterials' size, shape and composition at a sub-wavelength scale, the magnitude of such activities can be influenced by their surface chemistry play. A righteous

choice in terms of ligands employed to stabilize these colloidal nanoparticles in solution, reveals the origin of a hybridized coupling that could be leveraged as means to tune their induced CD strength.

On this note, chiral zinc blende CdSe NPLs display absorptive-like CD responses in contrary to conventional QDs and wurtzite cadmium-based materials. For a given surface functionalization, there is a progressive shift of the CD line shape towards greater wavelengths with the increase in NPLs' thickness, associated to their respective excitonic transitions. Two interesting aspects are however underlined: (i) an additional splitting of the e-hh corresponding CD peak observed for helical structures compared to the twisted ones, which leads to a belief that the dipoles' coupling correlates strongly to the local deformation degree of the crystal lattices and (ii) the CD line shape's dependence on the surface coverage of exchanged chiral ligands.

This latter is preliminarily noticed for 4 MLs CdSe NPLs passivated by enantiomers of tartaric and malic acids. As this investigation still constitutes an on-going work, grounded conclusions can yet be fully deduced. According to our comprehension, it appears that the induced CD line shape is highly sensitive to both, the NPLs' morphology and the chiral ligands' coverage, for its lowest energy absorption peak at least as depicted by the Cd-Se encircled region in Fig. 3.21(c). Further elucidations would be required to justify the deformation matrices between various crystal shapes and the kinetic evolution of their CD spectra during a process of ligand exchange for instance.

Chapter 4

Tribrid silica-based chiral helices

Until now, large helical semiconductor CdSe NPLs are synthesized with random handedness and a slight enantiomeric excess, as elucidated previously by microscope image analysis. Indeed, if one were to achieve an efficient enantiomeric synthesis that favors the growth of one handedness compared to the other, undoubtedly higher dissymmetry values are to be expected. By once again inspiring from what holds the nature, one realizes that many living organisms contain biominerals and composites with finely tuned properties, which reflect a remarkable level of control over the nucleation, growth and shape of these constituent crystals [218, 219, 220]. Among which, peptides play a key role in achieving this control [221]. The general thought is that organic molecules will affect mineralization through stereochemical recognition, where geometrical and chemical constraints dictate their binding to selectively express specific crystal facets.

As cited, the pioneer report of chiral semiconductor II-VI nanoparticles involved the addition of the penicillamine amino acid with other precursors under the method of microwave induced heating [84]. This result emphasized that the mechanism underlying crystal modification through organic molecules is best understood by the effects of binding and distortion on the interface of the growing crystal. In the same vein, the consequence of introducing separate enantiomers of aspartic acid, into a solution from which calcite is formed has also been reported [222]. This has typically yielded hillocks that are mirror images of one another, observed under SEM micrographs. This site-specific binding of amino acid leading to surface steps, changes the step-edge free energies and gives rise to direction-specific growth that is unique to individual amino acid enantiomers.

Speaking of these chiral modifications that propagate from atomic to macroscopic length scales, ordered chiral mesoporous silica can also be synthesized through a surfactant-templated method [223]. Among the anionic surfactants tested in previous works, *N*-acyl-*L*-alanine is a chiral organic molecule that can form a chiral nematic phase in the presence of small amounts of decanol [224]. This phenomenon has been attributed to the change in effective cross-sectional area at the interface of aggregates. Plus, the presence of chiral anionic surfactants induces changes in the conformation of the amphiphile in the micelle and distorts the micellar shape, leading to chiral micelles. Upon calcination, both the anionic surfactant and the organics of the aminosilane as co-structure-directing agent are removed, giving uniform mesopores of 2.2 nm in diameter.

In fact, the formation of twisted ribbons consisting of surfactant bilayers was first demonstrated by MacKintosh and co-workers [225]. Therein, gemini surfactants that are defined as a molecule consisting of two identical (twin) surfactants joined by a hydrocarbon spacer of variable length, have been shown to display unusual properties compared to those of simple surfactants and lipids [226]. Cationic gemini surfactants having chiral counterions form gels in both water and some organic solvents by creating extended networks

of the multi-lamellar twisted ribbons. In this reported system, the chirality originates from the counterion rather than from the amphiphile itself, which allows both the tuning of the pitch and the enantiomeric excess of these chiral twisted structures [227]. This degree of control has then been leveraged in the following part of our work to be employed as helical templates for the crystallization and functionalization of inorganic materials.

4.1 Synthesis of surfactant-silica helices

As reported by Oda and co-workers, the synthesis of a new series of dimeric surfactants coupled with chiral tartrate counter anions yielded helical objects, whose curvature can be tuned by an enantiomeric excess of the introduced reagents such as chiral tartaric acids [227]. Later, thanks to the feasible sol-gel polycondensation of silanes onto organic templates, a hybrid silica-surfactant system can be built [100]. These structures have attracted a considerable amount of attention for their outer and inner confined environment's functionalization, underlining their application potentials for adsorbance and catalysis over thousands of nm² on a single-particle level.

Herein, we report a complementary strategy to finely tune the morphology of chiral silica helices, whose synthesis is done in the presence of malic acids as the counter anions. This route yields objects in the micrometer range in contrast to the formerly obtained nanometric structures. By beginning with the as-synthesized gemini surfactants possessing the formula $(\text{H}_{2m+1}\text{C}_m \text{Me}_2\text{N}^+) - \text{C}_x\text{H}_{2x} - (\text{N}^+\text{Me}_2 \text{C}_m\text{H}_{2m+1})$, described as *m-x-m*, these achiral amphiphiles adapt only chiral properties when they are complexed with enantiomers of malate counterions. The sol-gel transcription onto these self-assembled *18-2-18*:malate structures has been successful to reproduce an individual hybrid helices system, with a homogenous silica coating and monodisperse diameter in the order of 0.2 μm and 1.2 μm in length (Appendix E).

4.1.1 Self-assembly of gemini surfactants

According to the protocol detailed in **Materials and Methods** section, bromooctadecane and ethylenediamine molecules have been promptly reacted together under a two-steps synthesis, to produce the *18-2-18* gemini surfactant compound. ¹H NMR analysis demonstrates added proton resonances from the diamine molecule that are associated to: (i) their methyls located near 3.5 ppm and (ii) their carbonyl parts near 4.8 ppm, compared to the spectrum of the bromooctadecane compound alone (Fig. 4.1(a)). This depicts a proportional increase in the proton counting with the introduction of two bromooctadecane chains into the diamine molecule. Each peak has been identified with the chemical shift induced on each proton location and labeled accordingly.

Secondly, the present complexing anions that are bromides have been substituted by chiral *L*-(-)-malate enantiomers via a process of salt precipitation by silver atoms. ¹H NMR analysis evidences the appearance of a new peak situated around 4.5 ppm (Fig. 4.1(b)). This latter labeled η , is assigned to the two protons located at the β -position of the hydroxyl group of malic acids. Fine integration of the other corresponding resonances displays a close matching number of protons that are expected in a single *18-2-18* gemini surfactant molecule.

Additionally, the substitution of initial bromide counterions by other forms of malate enantiomers: *D*-(+), and *meso*, along with *D*-(-)-tartrate is also carried out (Appendix E).

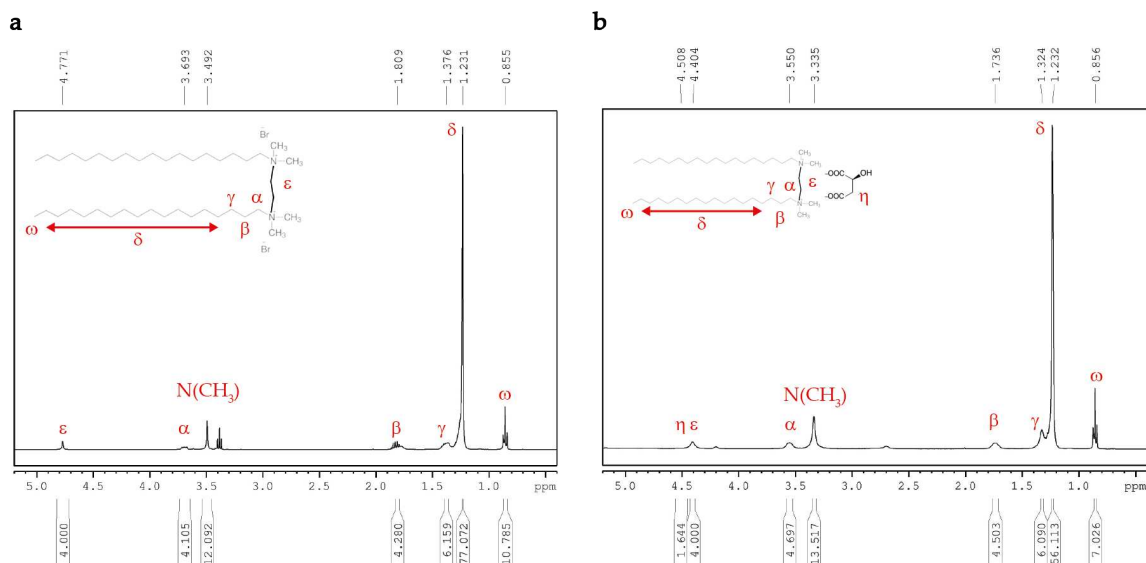


FIGURE 4.1: ^1H NMR analysis of (a) the as-synthesized *18-2-18*:bromide gemini surfactant molecule and (b) *18-2-18*:(*L*)malate after counterion exchanges. Estimated values for the proton assessment: 0.9 ppm (6H, $\text{CH}_3 \times 2$); 1.2 ppm (56H, $(\text{CH}_2)_{14} \times 2$); 1.3 ppm (4H, $\text{CH}_2 \times 2$); 1.7 ppm (4H, $\text{CH}_2 \times 2$); 3.3 ppm (12H, $\text{N}^+(\text{CH}_3)_2 \times 2$); 3.6 ppm (4H, $\text{CH}_2 \times 2$); 4.3 ppm (4H, $\text{N}^+(\text{CH}_2)_2\text{N}^+$); 4.5 ppm (2H, $\text{CH} \times 2$).

This confirms the non-specific binding of the counterions independent of their handedness to the polar head of *18-2-18* gemini surfactants. In each ^1H NMR analysis, there is a good agreement in terms of number of protons present that can be distinctly attributed to the individual molecules.

In order to control the morphology of the self-assembled objects, *18-2-18*:malate gemini surfactants are incubated overtime under aqueous conditions. Right before TEM imaging, a thin silica shell coating has been applied onto them. Fig. 4.2 shows a panel of various forms obtained as a function of incubation period. Remarkably a shape-transitioning phenomenon is noticed, ranging from vesicles to flat membranes, then to curved helicoids and hollow cylindrical objects. This result is analogous to those well-documented phase diagrams on the emulsification of surfactants and polymer molecules depending on their formulation [228, 229, 230, 231]. Here instead, at a fixed amount of chemical reactants, the only factor contributing to the kinetic arrangement of gemini molecules is time. The substitution of bromides by a racemic mix of malate ions leads uniquely to flat membranes without induced curvature, whose lateral size only increases overtime.

Similarly to the results from Oda and co-workers, a shift from twisted to coiled objects are also reported on *16-2-16*:tartrate systems. In terms of helices radii however, the ones synthesized from our *18-2-18*:malate are an order of magnitude higher than theirs, which were estimated at 10 nm [232]. One can then wonder about the obvious difference in helices radii between these two systems. Therefore, identical substitutions on *18-2-18* gemini surfactants complexed with chiral tartrate have been performed and imaged under TEM. These latter turn out to exhibit identical helices radii to the prior case of *16-2-16*:tartrate (Fig. 4.3). This hints that certainly, the chiral complexing anions are most responsible for the observed increase in final helices radii by an order of magnitude, rather than the difference in surfactant chain length.

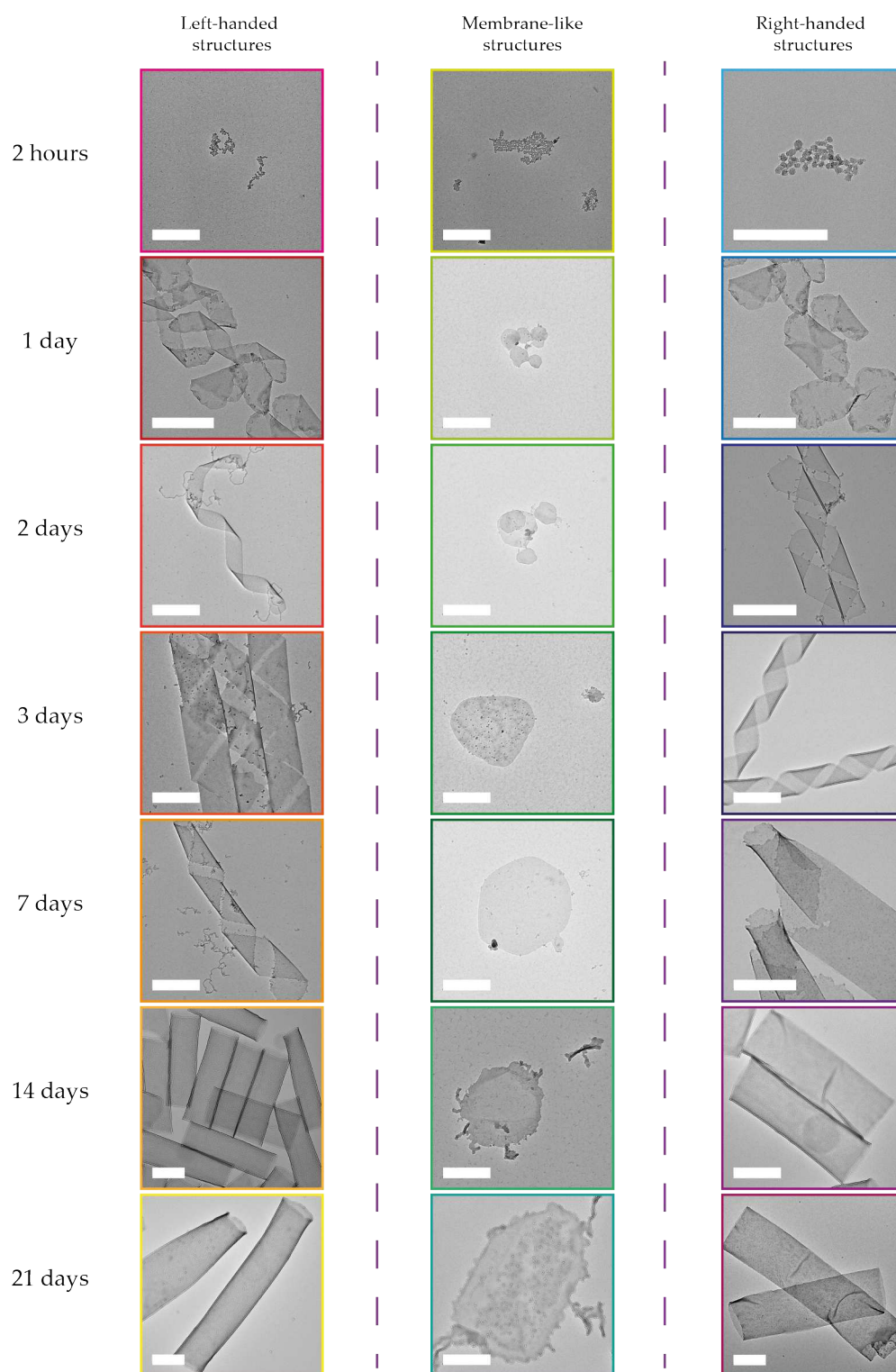


FIGURE 4.2: TEM images of the kinetic shape transition of gemini surfactant assemblies upon silica coating, where the molecules are beforehand complexed by (left column) *D*-(+)-, (middle column) *DL*- and (right column) *L*-(-)-malate ions. Scale bar: 500 nm.

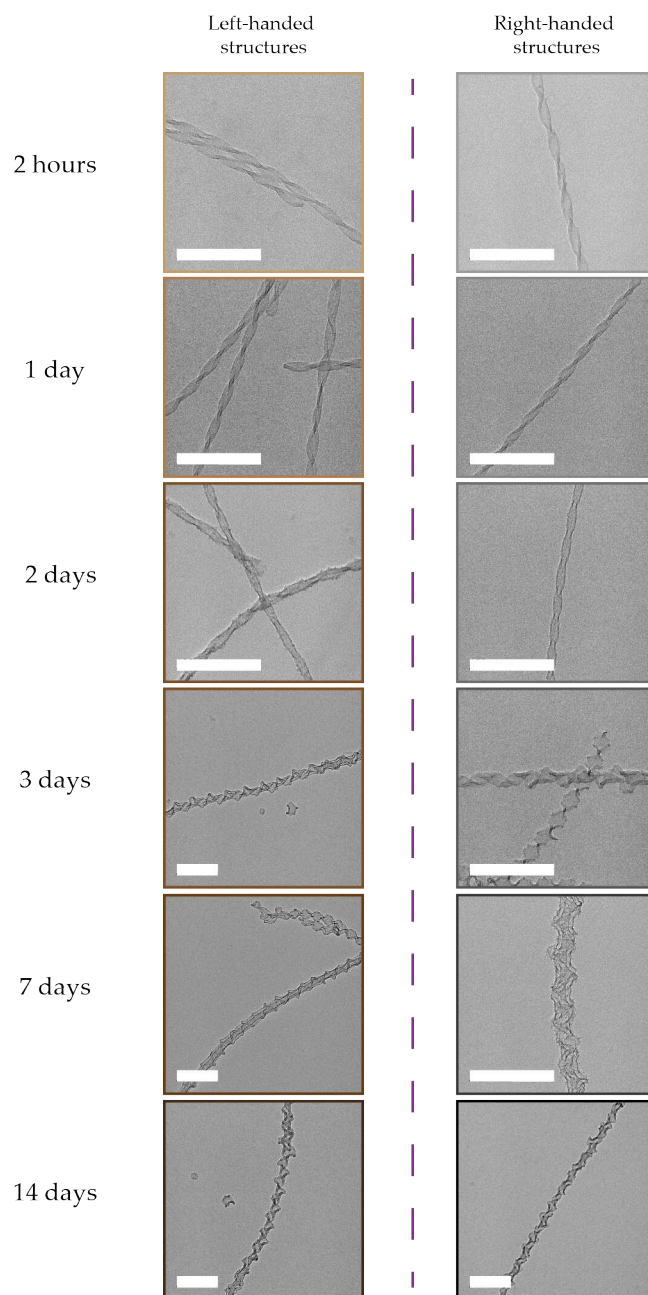


FIGURE 4.3: TEM images of the kinetic shape transition of gemini surfactant assemblies upon silica coating, where the molecules are beforehand complexed by (left column) *D*-(-)- and (right column) *L*-(+)-tartrate ions. Scale bar: 200 nm.

In order to obtain uniformly defined helical structures, the self-assembly process of *18-2-18*:malate gemini surfactants have been stopped exactly after three days of incubation. Upon which, the alkoxy silane sites are condensed to form the silica framework. The particles are thoroughly washed with ethanol to remove any subsequent secondary nucleation of unwanted spherical silica objects. Fig. 4.4 illustrates the formation of left- (resp. right-) handed structures when the complexation to *18-2-18* gemini surfactants is done with *D*-(+)- (resp. *L*-(-)-malate) counterions. The spacing between silica walls of a helix is estimated to

equal 6.5 nm, which corresponds to the thickness of two bilayers of interpenetrated gemini surfactant membranes [100].

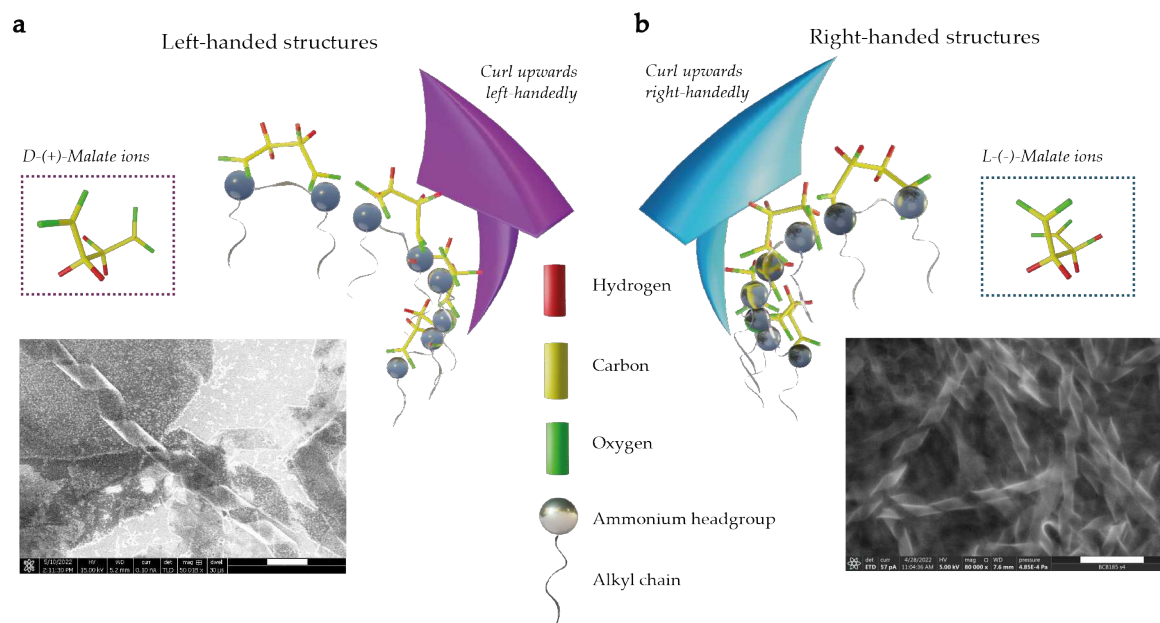


FIGURE 4.4: (a) The use of *D*-(+)-malate to substitute bromide as complexing counterions to *18-2-18* gemini surfactants, yielded microhelices with left-handedness. Images taken under SEM enable a certain distinction of their curling direction. Scale bar: 1 μm . The scheme depicts the self-assembly of a layer of surfactants with a thickness of around 1.6 nm, winding toward the left direction as pointed out by the magenta-colored arrow. (b) Respectively, replacing the initial achiral anions with the counterpart of the prior chiral molecule *L*-(-)-malate, resulted in microhelices with right-handedness. Data recorded with high contrast and resolution SEM displayed net images, that allow to determine their sense of chirality. Scale bar: 1 μm . This time around, the cartoon shows an ordered arrangement of gemini surfactant molecules, curling toward the right direction as pointed out by the cyan-colored arrow.

4.1.2 Surface patterning with CdSe NPLs

The versatile yet robust synthetic availability of silica particles has been leveraged in the following section to modify their surface silanols. Upon obtaining a hybrid silica-surfactant helical system, the helices are treated with a thiol-based silane called 3-mercaptopropyl trimethoxysilane (MPTMS), according to the scheme shown in Fig. 4.5(a). EDX analysis enables the determination of sulfur atoms present in the thio-modified system while omitting the oxygen, which later hosts the grafting of CdSe nanoparticles (Tab. 4.1). Taking into account the high affinity of sulfur atoms toward cadmium ones, a series of as-synthesized carboxylates-capped CdSe NPLs of various forms (square, needle-like and rectangular) have been immobilized onto the helical matrices, as shown in Fig. 4.5(c). Therefore, the previously non-absorbing *18-2-18*:(*D/L*)malate particles in the visible region suspended in toluene, exhibit now optical features thanks to the incoming CdSe guests. Fig. 4.5(b) indicates the absorption and emission spectra of the resulting tribrid systems. The first excitonic peak located at 512 nm corresponds to the heavy hole to conduction band (e-hh) transition of this class of semiconductor II-VI NPLs as mentioned in previous chapters and their narrow emission properties with low Stokes shift centered around 516 nm.

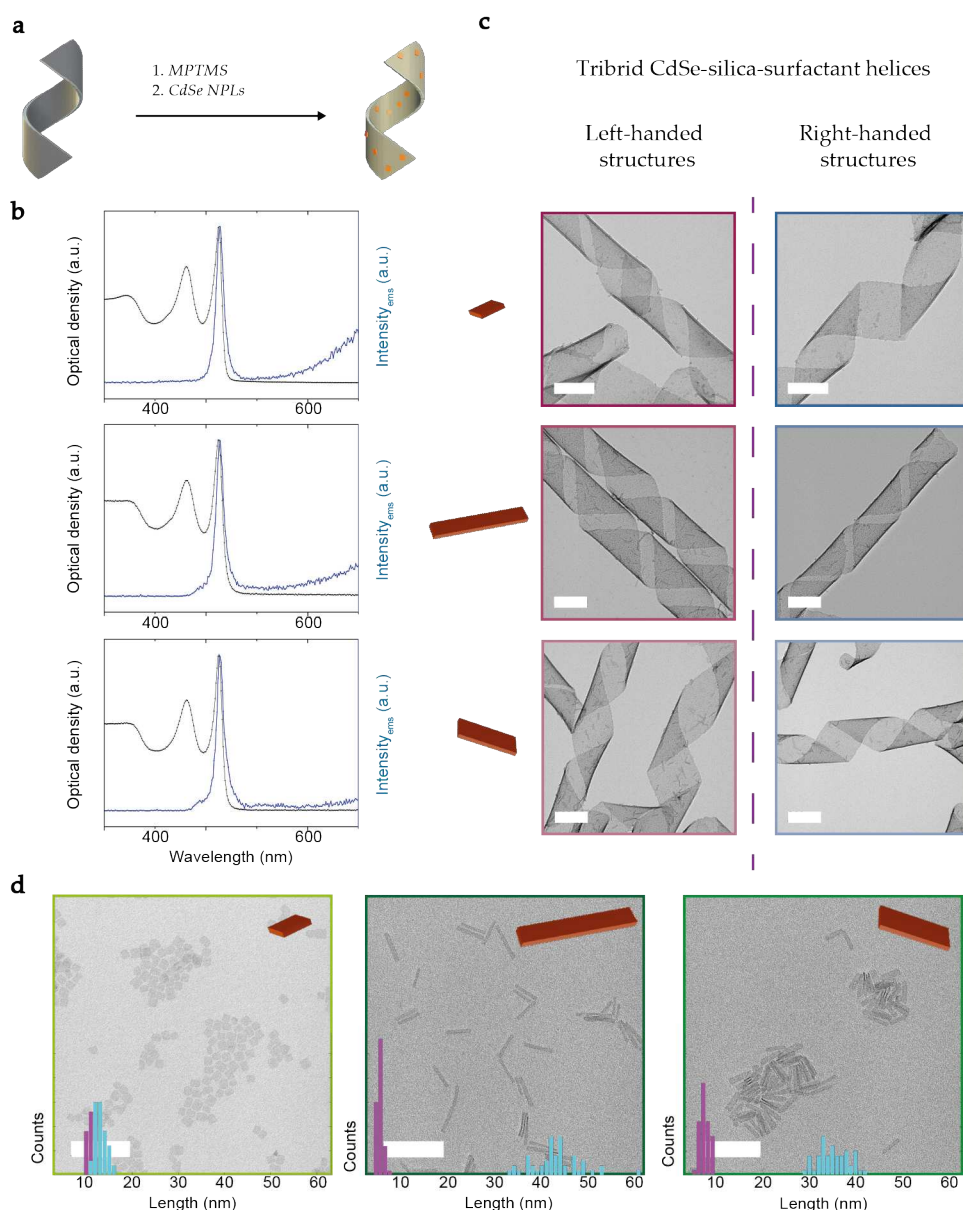


FIGURE 4.5: (a) The as-synthesized hybrid microhelices, possessing in average $0.2 \mu\text{m}$ in diameter and $1.2 \mu\text{m}$ in length, undergo a functionalization with MPTMS for a thio-modified system. It enables the grafting of carboxylates-capped CdSe NPLs owing to the high affinity of sulfur atoms toward cadmium ones, which are present on the outer surface of these zinc-blende crystals. (b) The associated optical spectra in the visible region for absorption and emission are shown for *18-2-18:(D)malate@CdSe* (resp. square, needle-like and rectangular), in the case of left-handed helices. (c) Their corresponding TEM images are shown both on microhelices of opposite handedness. Owing to the robust and facile synthesis of these quantum particles with well-defined lateral dimensions, an evaluation of the number of grafted objects enables the determination of the initial quantity of silica helices present in solution. Scale bar: 200 nm. (d) TEM images of as-synthesized carboxylates-capped 4 MLs CdSe NPLs of various forms (square, needle-like and rectangle). Image analysis for a population of 100 particles at least under *ImageJ* shows that, their lateral dimensions are (160 ± 10) , (270 ± 20) and $(260 \pm 20) \text{ nm}^2$. Scale: 100 nm.

Element	Composition (%)
Si	92±1
S	8±0.1

TABLE 4.1: Elemental analysis by EDX on thio-modified *18-2-18:(D/L)malate* silica helices while omitting the oxygen contributions.

These quantum particles present an upper-hand of globally well-controlled synthesized geometries, where the squared ones (resp. needle-like and rectangular) are (13x13) (resp. (45x6) and (32x7) nm²) as displayed in Fig. 4.5(d). Through a careful calculation of the introduced number of NPLs, together with TEM images analysis, an estimation of the CdSe grafting density is valued to the order of 10² per silica particle. Thus, in relative to the initially introduced quantity of guest nanoparticles, the concentration of individual hybrid helices' number is approximately 10¹⁰ per mL of solution after an error of estimation by 10 %, due to chemical losses for instance (Tab. 4.2).

4 MLs CdSe NPLs	Lateral dimensions (nm ²)	Lattice units, where $a=0.605$ nm	Number of surface Cd ions per wide facet per NPL	Number of surface Cd ions per wide facet per 20 μ L of introduced NPLs	Number of silica helices estimated from a number of grafted NPLs
Square	13x13	21x21	925	$2.4 \cdot 10^{16}$	$2.2 \cdot 10^{11}$
Needle-like	45x6	74x9	1416	$2.4 \cdot 10^{16}$	$1.4 \cdot 10^{11}$
Rectangle	32x7	52x11	1208	$2.4 \cdot 10^{16}$	$1.7 \cdot 10^{11}$

TABLE 4.2: Method used to estimate the concentration of *18-2-18:(D/L)malate* silica helices in solution, via the exact grafting of particles with known dimensions onto individual host matrices. The number of grafted NPLs estimated on each single silica structure is evaluated to scale to the order of 10².

However, these solutions of *18-2-18:malate@CdSe* systems do not demonstrate any chiroptical properties in absorption. Oda and co-workers have previously demonstrated that perovskite nanocrystals and CdSe nanorods functionalized *16-2-16:tartrate* chiral silica helices exhibited clear CD signals only at dried state [233, 97]. Solutions of these similar tribid systems were drop-casted onto a quartz plate and left to dry for CD measurements at 0 and 90 ° to eliminate any linear dichroism effects. The authors reported that both solvated and dried TEM images of silica helices showed densely attached nanocrystals on their surface. However in the solvated case, grafted objects displayed a thick and swollen layer around the silica substrate without notable helical organization with strongly solvated ligands. In contrast at dried state, the nanocrystals were closer bound due to ligands collapse, leading towards a greater interaction for the dipolar coupling.

4.1.3 Functionalization with gold nanoparticles

As our main interest relies on colloidal systems in solution, we have taken a step back by functionalizing another family of materials, the gold ones onto our *18-2-18:malate* chiral

silica helices. As the order of interaction in plasmonic couplings is much higher than the local excitons, indeed there would be a higher chance at expecting CD behavior in gold functionalized systems compared to CdSe. Previously, it has been shown that chiroptical activity with an anisotropy factor in the order of 10^{-4} can be achieved by direct grafting of various sizes of gold nanoparticles onto 16-2-16:tartrate chiral silica helices [102]. Hence, this has driven our next investigation into a similar direction to the former case, but with a distinct approach of synthesizing these tribrid materials that ultimately exhibit slight higher g-factor values than the reported literature.

In contrary to the previous chemical alteration by a thiol-based silane to efficiently couple the silica helices to surface cadmium atoms of CdSe NPLs thanks to a high reaction affinity, one can also imagine doing so by an amino-based molecule called 3-aminopropyl triethoxysilane (APTES). FTIR spectroscopy is employed to confirm the surface immobilization of these introduced silane groups. Among the pre-existing peaks before selective chemistry modification, there are huge bands corresponding respectively to the asymmetric and symmetric strong Si-O-Si absorptions around 1070 and 800 cm^{-1} (Fig. 4.6). The hydroxyl groups are themselves revealed by the stretching bands located around 3400 and 965 cm^{-1} , while the methyl ones are visible in the region of 2880 cm^{-1} . After an amino-modification, it appears that bands resulting from the asymmetric and symmetric stretchings of primary amine groups are barely visible due to the masking by -OH vibrations.

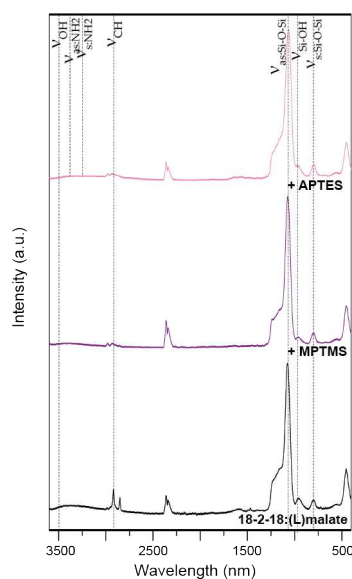


FIGURE 4.6: FTIR spectra of (black) the resulted 18-2-18:(L)malate silica helices prior to any surface chemical alterations, then either (violet) thiol-modified with MPTMS or (pink) amino-modified with APTES.

Herein, a method by depositing and in-situ growth is used to prepare gold-decorated silica helices. The aim is to yield a tribrid surfactant-silica-plasmonic system that is optically responsive to CD in solution. This preliminary approach relies notably on the grafting of pre-synthesized gold seeds onto a silica helical substrate and later on, growing them in-situ with a plating solution (Fig. 4.7). Via this route, one is able to separately tune the final size of gold nanoparticles, as well as their surface coverage which play a crucial role at determining the magnitude of observed CD effect. Unlike previous reports, the chemical

pathways that were used to yield similar systems are different than ours [102]. The authors have instead adopted a direct grafting method, by first synthesizing different batches of gold nanoparticles of various sizes ranging from 4 to 10 nm before immobilizing them onto either bare or amino-modified 16-2-16:(*D/L*)tartrate silica helices.

CD properties of tribid surfactant-silica-gold structures

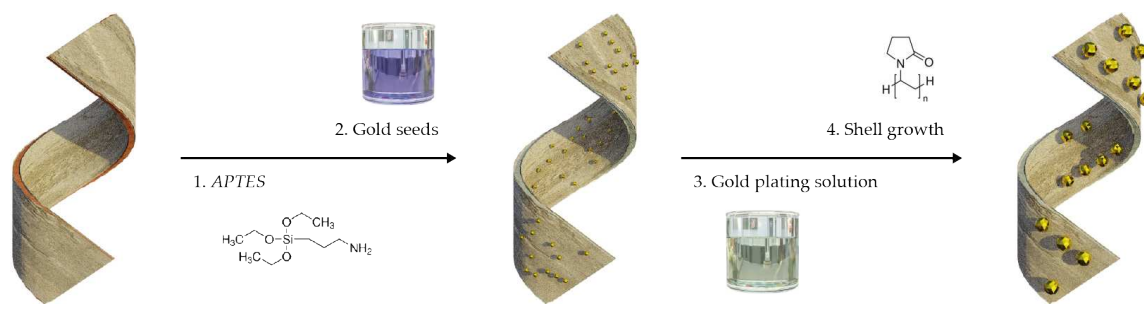


FIGURE 4.7: Pathways for depositing and in-situ growth of gold nanoparticles on hybrid surfactant-silica helices. First step consists of modifying the surface chemistry of as-synthesized and purified 18-2-18:(*D/L*)malate suspended in ethanol with APTES. Then, an aqueous solution of pre-prepared gold seeds by reduction of hydrogen tetrachloroaurate (III) is added. Separately, an aqueous gold plating solution is set by mixing gold precursors and potassium carbonate together. Once the silica helices functionalized with gold seeds are washed, a mixture of growth solution, PVP and formaldehyde is introduced and left under stirring. Over the course, the solution turns from light purple to blue which is characteristic of the gold nanoshell's growth.

As depicted by the left part of the scheme in Fig. 4.7, a solution of gold seeds is first prepared by a borohydride reduction of citrate-stabilized gold ions in water under ambient conditions [234]. As the color of the solution turns rapidly ruby red, the size of these gold seeds stays consistently smaller than 4 nm. A certain amount of this starting solution preserved in the refrigerator is later added into the amino-modified silica helices in ethanol and left to react overnight.

The precedent non-absorbing amino-modified 18-2-18:(*L*)malate particles in the visible region suspended in ethanol, possess now an optical feature thanks to the incoming gold seeds (Fig. 4.8(a)). It presents a resonance peak located at 513 nm. Upon depositing these plasmonic nanoparticles onto the silica substrate, its helical morphology and structure are much well preserved (Fig. 4.8(b)). In terms of CD, one can observe in Fig. 4.8(c) that a distinct signal is obtained after functionalization with the seeds. It demonstrates a chirality transfer from the helices to the gold seeds when they arrange in a helical manner instead of being randomly suspended in solution. This confers them a greater chance to interact with their neighboring gold nanoparticles and gives rise to complex features. The Cotton effect is noted at the position of resonance peak and records a *g*-factor value of 10^{-5} , where the maximum (resp. minimum) of the sigmoid situates at 537 (resp. 490 nm).

After several purification steps to remove the unreacted excess gold seeds, an aqueous growth solution is added alongside a weak reducing agent, formaldehyde and left under overnight stirring. Additionally, a molecule called polyvinyl pyrrolidone (PVP) with a mean molecular weight of (8000-12000) is added during the gold nanoshell growth [235]. It avoids notably the formation of secondary nucleation of unwanted gold particles other

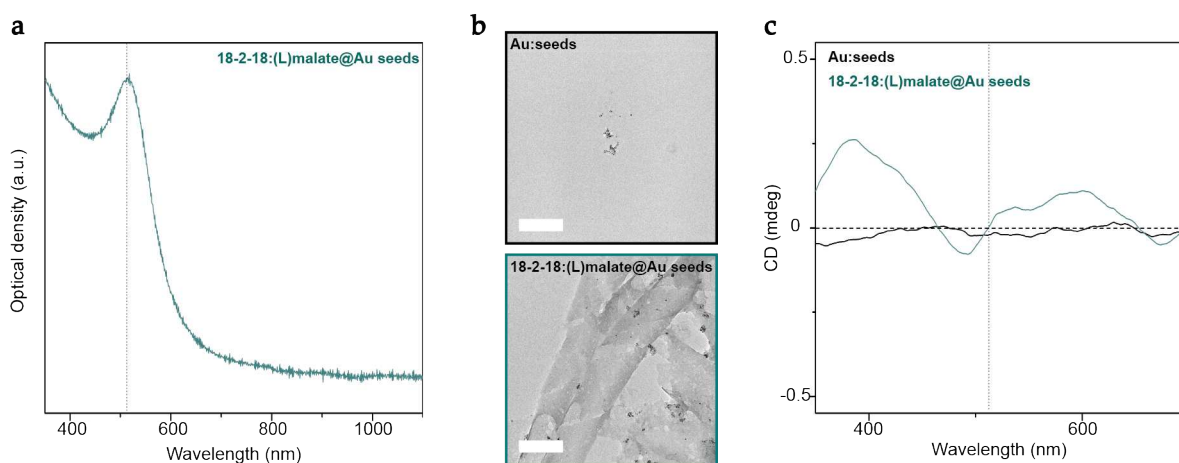


FIGURE 4.8: (a) Absorption spectra of $18-2-18:(L)malate@Au$ seeds in distilled water. (b) TEM images of the (top) pre-prepared gold seeds and (bottom) tribrid surfactant-silica-gold seeds structures. Scale bar: 200 nm. (c) CD spectra of these two corresponding solutions in distilled water. The dashed lines indicate the peak of plasmonic resonance at 513 nm.

than on the already pre-existing grafted seeds by slowing down the overall reaction's kinetic [236, 237]. However, an over-addition of PVP has been shown to lead to the possible formation of spikes and star-shaped gold-coating around silica nanoparticles [238]. Therefore, the added amount of various compounds has been preliminarily optimized to ensure a functional procedure.

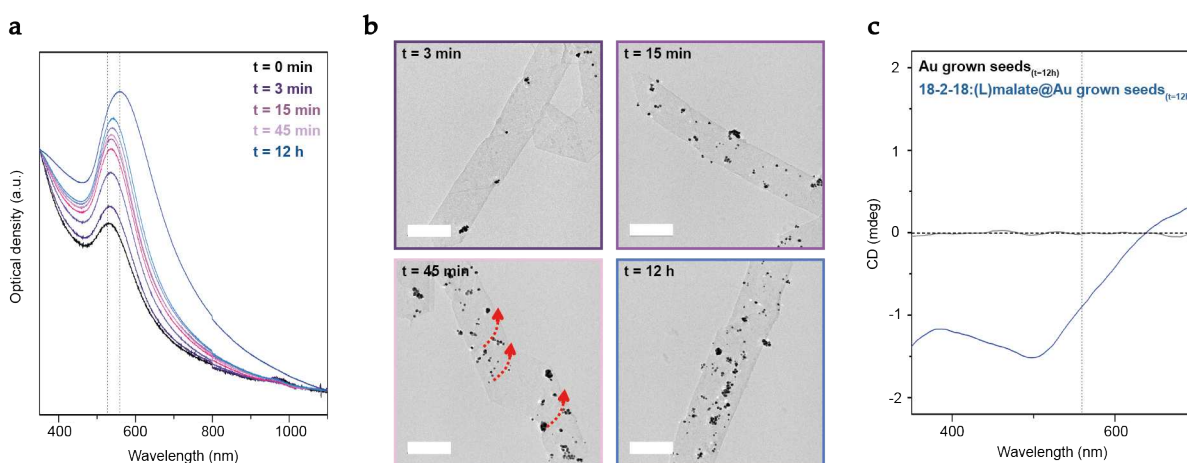


FIGURE 4.9: (a) Absorption spectra of $18-2-18:(L)malate@Au$ seeds under growth conditions in distilled water overtime. (b) TEM images of the aliquots at different time scales. Red arrows indicate the deposition of gold nanoparticles in a right-handed helical manner. Scale bar: 200 nm. (c) CD spectra of the purified particles at final state, $18-2-18:(L)malate@Au$ grown seeds_(t=12h) in distilled water, compared to a control experiment of Au grown seeds_(t=12h) in absence of the silica helices. The dashed lines indicate the shift of the resonance peak gradually to 558 nm.

As the gold nanoshell grows on the pre-deposited seeds, visually the solution turns blue which reflects a redshift in terms of absorption of about 45 nm, going from 513 to 558

nm (Fig. 4.9(a)). The resonance peak becomes as well larger and stronger in intensity, as the seeds are grown to be more polydispersed in size. TEM images confirm that overtime, the particles have indeed gained an increase in size to about 12 nm (Fig. 4.9(b)). On certain structures, one can notice the alignment of these gold deposits in a helical manner that is dictated by the initial handedness of the hybrid surfactant-silica objects. Two orders of magnitude increase in terms of g-factor is even recorded at $6 \cdot 10^{-3}$ in Fig. 4.9(c), where the maximum (resp. minimum) of the sigmoid situates at 556 (resp. 477 nm).

Preliminary tests have shown that some of the key parameters that can influence the growth of gold nanoshell include the quantities of: (i) 18-2-18:(L)malate@Au seeds, (ii) gold plating solution and (iii) PVP that are respectively introduced. Tab. 4.3 recapitulates several data sets that consist of modifying these parameters and their effect on the final state of tribrid surfactant-silica-plasmonic system.

Parameters and their introduced quantity (mL)	Test A	Test B	Test C	Test D
18-2-18:(L)malate@Au seeds solution	0.50	0.50	1.00	0.50
Gold-plating solution at 20mM	0.20	0.02	0.02	0.20
PVP solution at 1 mM	0.10	0.10	0.10	1.00

TABLE 4.3: Four various sets of growth conditions for 18-2-18:(L)malate@Au seeds in distilled water.

According to Fig. 4.10, one can deduce by comparing tests A and B that an insufficiency in gold plating solution does not lead to a favorable growth of grafted seeds, at a fixed amount of 18-2-18:(L)malate@Au seeds present in solution. Between tests B and C, it appears that a more diluted solution of 18-2-18:(L)malate@Au seeds suffers a severe etching. This is probably due to the constant amount of other added compounds like formaldehyde and carbonate salts that could potentially degrade the structure. A twice more concentrated solution in test C seems to better retain the silica helical shape, but again, due to the lack of growth precursors, the redshift of resonance peak is hardly noticed even after 18 hours of reaction. By increasing the quantity of introduced PVP, it does not appear that the resonance peak is further redshifted by comparing the values of final state in both tests A and D, which equal 558 and 549 nm. However, the polydispersity of grown gold nanoshells is more significant, given its broader absorption spectrum and this tends to agree with previous findings where the anisotropy of coating becomes more important with the addition of PVP [239, 240, 241].

In terms of CD, test B yields the weakest signal which fluctuates around zero due to the absence of an evident helical substrate (Fig. 4.11(a)). Whereas, test D exhibits the highest dissymmetry factor among them, reaching a value of $5 \cdot 10^{-4}$. Herein, the most optimal growth procedure is found for these amounts of chemical compounds: 0.5 mL of 18-2-18:(D/L)malate@Au seeds solution, 1 mL of gold plating solution and 0.1 mL of PVP

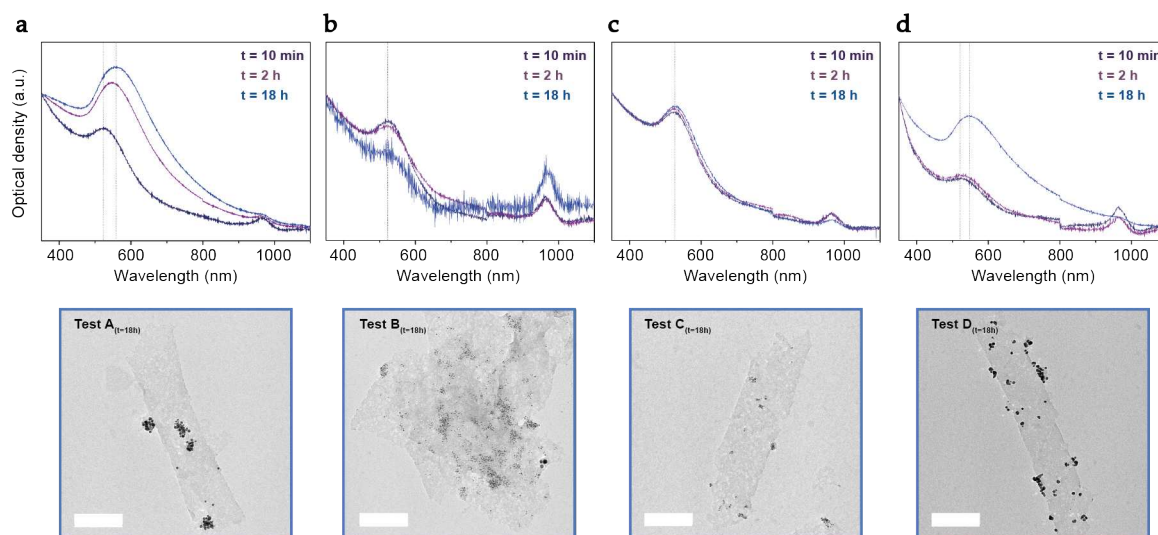


FIGURE 4.10: Absorption spectra (top panel) and TEM images (bottom panel) of the associated $18-2-18:(L)$ malate@Au grown seeds, under the conditions presented in Tab. 4.3. The dashed lines indicate the shift of the resonance peak gradually to 558 and 549 nm in cases of tests A and D respectively, while being stuck at 513 nm in both tests B and C. Scale bar: 200 nm.

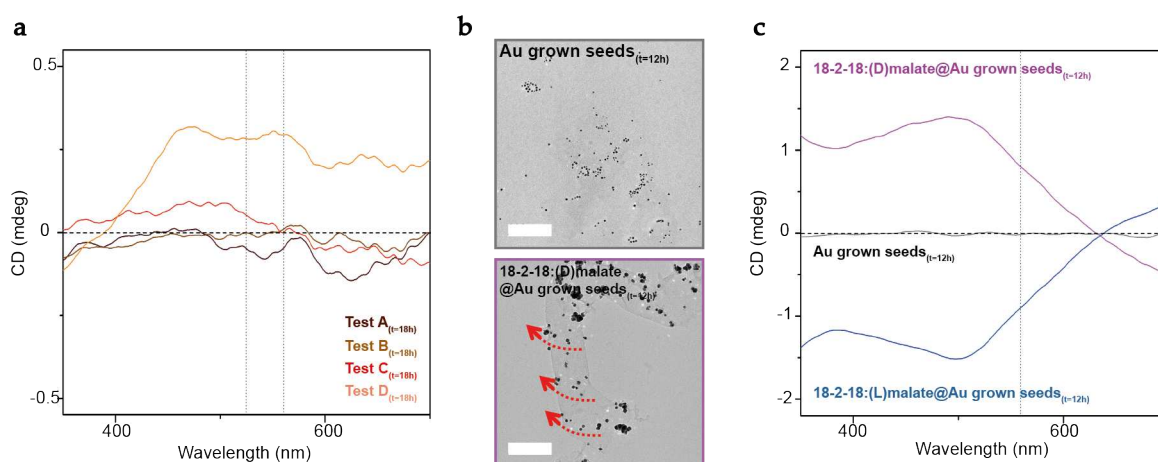


FIGURE 4.11: (a) CD spectra of the associated $18-2-18:(L)$ malate@Au grown seeds, synthesized under the conditions presented in Tab. 4.3. The two black dotted lines correspond respectively to the resonance wavelengths, situated at 513 and 558 nm. (b) TEM images of a control experiment of Au grown seeds ($t=12h$) in absence of the silica helices and similar gold nanoshell's growth carried out on $18-2-18:(D)$ malate@Au seeds in distilled water. Scale bar: 200 nm. Their corresponding CD spectra are plotted in (c) with a dashed line indicating their resonance peak position near 558 nm.

solution. Via this formulation, tribrid $18-2-18:(D/L)$ malate@Au grown seeds structures are obtained with a well preserved helical substrate and demonstrate CD signals that are mirror images of one another as shown in Fig. 4.11(c).

Going further, it appears interesting to synthesize a homogeneous coating of gold shell

around the silica helices, as this might boost the local interaction between gold nanoparticles and perhaps increase the resulting polarization signals. At first approximations, it is challenging to create a single domain of gold uniform shell via this two-step depositing and in-situ growth method. At best, one can first tackle by densely packing the initial gold seeds on a silica substrate. Then, under a well-chosen growth condition, these latter might possibly fuse by oriented attachment in spite of an imperfect crystalline domain. Hence this time around, the introduced quantity of gold seeds to be grafted onto amino-modified *18-2-18:(D/DL/L)malate* during the first step is varied.

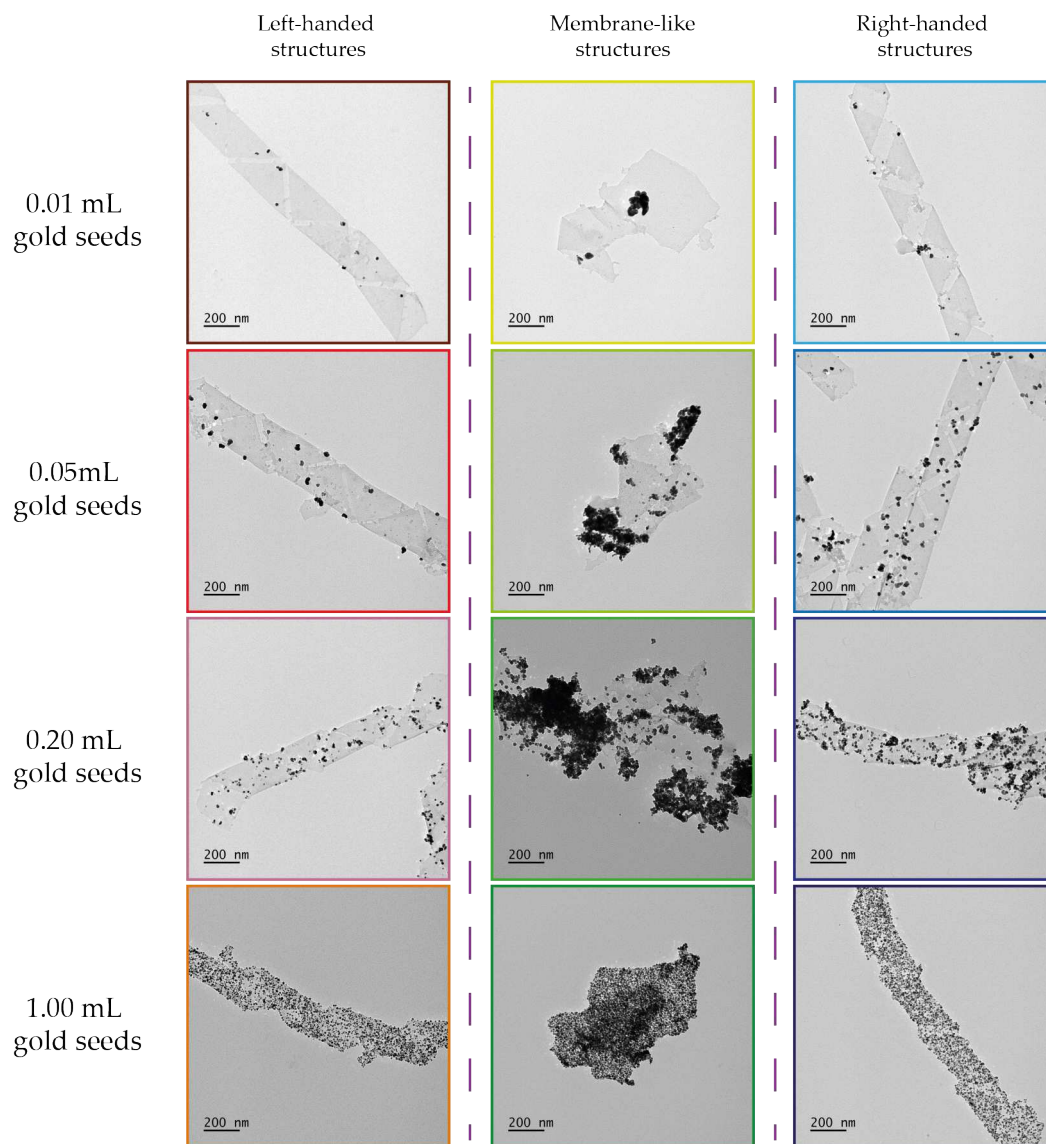


FIGURE 4.12: TEM images of *18-2-18:(D/DL/L)malate@Au* grown seeds upon overnight reaction and purification steps, where the hybrid surfactant-silica helices are beforehand synthesized in the presence of (left column) *D*-(+)-malate, (middle column) *DL*-malate and (right column) *L*-(-)-malate ions. The quantity of functionalized gold seeds between each row is varied by introducing different volumes of an identical stock solution, prepared at 0.27 mM. Scale bar: 200 nm.

Fig. 4.12 displays a series of *18-2-18:(D/DL/L)malate@Au* grown seeds synthesized

with varying amounts of grafted gold seeds during the first step of the chemical pathway pictured in Fig. 4.7. Later, the growth procedure that is used consists of 1 mL of 18-2-18:(D/DL/L) malate@Au seeds solution, 1 mL of gold plating solution and 0.15 mL of PVP solution. As one can point out, at the upper limit of gold seeds added, the silica surface coverage is well-saturated with an absence of secondary nucleation. The resonance peak in each scenario remains unmodified compared to the previous cases, reaching 558 nm after an overnight reaction and an average gold nanoparticles' size of 12 nm.

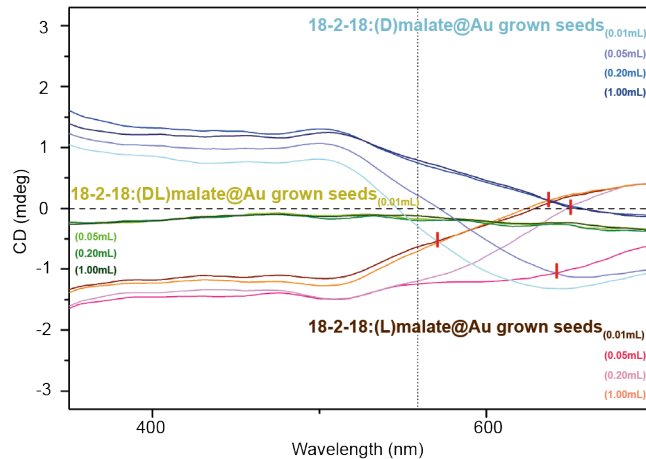


FIGURE 4.13: CD spectra of the associated 18-2-18:(D/DL/L)malate@Au grown seeds, synthesized under the conditions presented in Fig. 4.12. Red marks indicate the crossing wavelength for each pair of bisignated patterns, where the same amount of gold seeds is employed. The dashed lines indicate the peak of plasmonic resonance at 558 nm.

g-factor ($\cdot 10^{-4}$ a.u.)	18-2-18:(D)malate@Au grown seeds	18-2-18:(L)malate@Au grown seeds	Crossing of bisignated patterns (nm)
0.01 mL gold seeds	-3.86	-8.03	571
0.05 mL gold seeds	+2.43	-10.95	642
0.20 mL gold seeds	+6.63	-10.95	650
1.00 mL gold seeds	+22.33	-12.86	637

TABLE 4.4: Dissymmetry values for 18-2-18:(D/L)malate@Au grown seeds that are obtained under various amounts of grafted gold seeds, taken at a wavelength of 558 nm.

Similarly to the result acquired in Fig. 4.11(c), 18-2-18:(D)malate@Au grown seeds (resp. (L)malate) exhibit a CD signal that polarizes positively (resp. negatively) at lower wavelengths (Fig. 4.13). As expected, the series of control experiment carried out on the *meso*-form yield global curves that fluctuate around zero. Between each pair of bisignated patterns, where the same exact amount of gold seeds is used, it appears that their respective crossing wavelength is located around 640 nm except for the case of 0.01 mL introduced solution. It is curious to notice that this least populated configuration gives rise to this observed shift, where each grown gold nanostructure is located further from one another as punctual points. It is then less possible to create multiple aggregates. In which case, each gold spot grows to be more uniform in size distribution as evidenced under TEM. Therefore, the resulting polarization resembles more of a spectrum obtained for an array of

identically-sized objects. In other words, their assimilated Cotton effect should occur at the exact resonance peak's position situated near 558 nm, being less redshifted compared to the other three cases.

By increasing the surface coverage of gold nanoparticles on silica helices, Tab. 4.4 records an increasing trend of absolute g-factor values for both chiral structures of opposite handedness. However, diffusion was fairly present when measuring the CD spectra of these tribid surfactant-silica-gold helices in solution, that has led to their non-zero tails toward higher wavelengths (Fig. 4.13). Each single plasmonic crystal domain can in fact, be treated as an array of polarizable dipoles. If their individual size were to increase, the total electric field does too which gives rise to a higher polarizability of these objects in agreement with the work reported by Oda and co-workers [102]. In the following section, simulation performed with the discrete dipole approximation enables to typically deduce the optical properties of plasmonic materials such as absorption, extinction and scattering, as a function of their composition, geometry, arrangement etc. [242, 243, 244]. Thanks to which, the CD behavior of an ensemble of aligned particles can also be coded, to run several simple studies from a theoretical point of view.

Simulation of plasmonic CD under discrete dipole approximation

Herein, the volume integral-based method and more specifically, the discrete dipole approximation is looked into to generate theoretical CD predictions for our studied system. In other words, it is also called the coupled dipole method or coupled dipole approximation. This formalism was introduced by Purcell and Pennypacker to study the scattering and absorption of light by non-spherical dielectric grains, with dimensions comparable to the wavelength of illumination [245]. This electromagnetic model describes a frequency domain approach, in which a particle is discretized into N cubic array of polarizable elements. Each voxel is then treated as an individual dipole and its optical response is due to the summation of the incident light electric field and its $(N-1)$ neighboring elements [246].

The primary objective of this approximation is to compute each dipole's polarization in order to simulate the optical properties of the nanoparticles, which requires solving $3N$ linear equations [247]. Calculating linearly $3N$ elements of a polarization vector can be computationally costly, along with a computing time and memory that increase significantly with increasing N [248]. Therefore, among certain backdoor solutions, is by implementing the complex conjugate gradient and the Fast Fourier Transform techniques reported in literature [249, 250]. This helps to reduce the computational time from the order of N^3 to $N \log(N)$ and the required memory from the order of N^2 to N .

The polarization of each dipole is expressed by:

$$P_i = \alpha_i E_{loc}(r_i) \quad (4.1)$$

where α_i is the polarizability and $E_{loc}(r_i)$ the total electric field given at a location r_i .

Since isotropic materials are considered in this work, their corresponding polarizability is direction independent. This term can be expressed by the lattice dispersion relation and written as:

$$\alpha_i = \frac{\frac{3d^3}{4\pi} \left(\frac{\epsilon_i - 1}{\epsilon_i + 2} \right)}{1 + \frac{3}{4\pi} \left(\frac{\epsilon_i - 1}{\epsilon_i + 2} \right) [(b_1 + m^2 b_2 + m^2 b^3 S)(kd)^2 - \frac{2}{3} i(kd)^3]} \quad (4.2)$$

where d , k and λ_m are the size of the cubical voxel, wavenumber and wavelength of the incident light coming in from the medium, respectively. Along with [251],

$$b_1 = -1.891531, b_2 = 0.1648469, b_3 = -1.7700004, S = \sum_{j=1}^3 (\vec{a}_j \vec{e}_j) \quad (4.3)$$

where \vec{a}_j and \vec{e}_j are the unit vectors representing the propagation and the polarization direction of the incident light.

On the other hand, the total electric field of a dipole at a location r_i is given by:

$$E_{loc}(r_i) = E_{incident}(r_i) + E_{other}(r_i) = E_0 \exp(ikr_i - i\omega t) - \sum_{j \neq i}^N A_{ij} P_j \quad (4.4)$$

where N is the number of dipoles, A_{ij} a complex matrix that represents the interaction between a receiving dipole at r_i and the radiating dipole at r_j , and P_j represents the polarization of radiating dipole at r_j .

The expression of the interaction matrix A_{ij} between two coupled dipoles is written as:

$$A_{ij} = \frac{\exp(ikr_{ij})}{r_{ij}} [k^2 (\vec{r}_{ij} \vec{r}_{ij} - \mathbf{1}_3) + \frac{(ikr_{ij} - 1)}{r_{ij}^2} (3\vec{r}_{ij} \vec{r}_{ij} - \mathbf{1}_3)] \quad (4.5)$$

where r_{ij} is the distance from dipole i to j , \vec{r}_{ij} is a unit vector in the direction from dipole i to j , and $\mathbf{1}_3$ indicates the (3×3) identity matrix. The diagonal elements of the interaction matrix are essentially defined as $A_{ii} = \alpha_i^{-1}$, which leads to a simplified form of the polarization equation as:

$$\sum_{i=1}^N A_{ij} P_j = E_{incident}(r_i) \quad (4.6)$$

These equations can be resumed in a matrix-vector format as below:

$$\begin{bmatrix} A_{xx} & A_{xy} & A_{xz} \\ A_{yx} & A_{yy} & A_{yz} \\ A_{zx} & A_{zy} & A_{zz} \end{bmatrix} \begin{bmatrix} P_x \\ P_y \\ P_z \end{bmatrix} = \begin{bmatrix} E_{incident,x} \\ E_{incident,y} \\ E_{incident,z} \end{bmatrix} \quad (4.7)$$

where $A_{\beta\gamma}$ (β and $\gamma = x, y$ or z) is a ($N \times N$) matrix that represents the interaction matrix between β^{th} and γ^{th} components of the dipoles. P_β and $E_{incident,\beta}$ are ($N \times 1$) arrays representing the β^{th} components of the polarization vector and the incident electric field, respectively. Since the nine blocks of the interaction matrix are symmetric regarding the change of indices in calculating this term, at the end only six independent blocks of A (A_{xx} , A_{xy} , A_{xz} , A_{yy} , A_{yz} and A_{zz}) are required.

By computing this matrix-vector format to obtain the polarization vector of each dipole at different wavelengths, the absorption, extinction and scattering cross-sections of a nanoparticle can be written as:

$$C_{abs} = \frac{4\pi |k|}{|E_0|^2} \sum_{i=1}^N \left[\text{Im} \left(\frac{P_i \cdot P_i^*}{\alpha_i^*} \right) - \frac{2}{3} |k^3| |P_i|^2 \right] \quad (4.8)$$

$$C_{ext} = \frac{4\pi |k|}{|E_0|^2} \sum_{i=1}^N \left[\text{Im} (E_{incident}^*(r_i)) \cdot P_i \right] \quad (4.9)$$

$$C_{scat} = C_{ext} - C_{abs} \quad (4.10)$$

where Im and $*$ indicate the imaginary part and the complex conjugate, respectively. The absorption, extinction, and scattering efficiencies σ are expressed by dividing the corresponding optical cross-sections by the nanoparticle's geometrical one (πr_{eff}^2). Herein, r_{eff} is defined as the radius of a sphere possessing an equal volume of the studied nanoparticle with an arbitrary shape.

Finally, the CD trend of the plasmonic structures can be expressed as the difference between the average extinction efficiencies calculated for left- and right-handed circularly polarized light [174, 252]:

$$CD = C_{NPs}(\sigma_{ext,LCPL} - \sigma_{ext,RCPL}) \quad (4.11)$$

where C_{NPs} represents the concentration of plasmonic structures in solution [102].

Validation on a single and aligned particle(s)

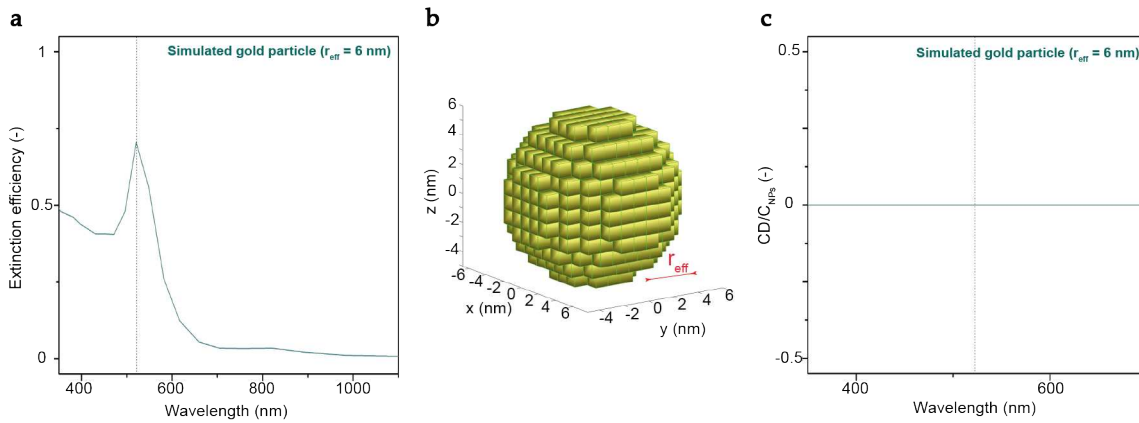


FIGURE 4.14: (a) Simulated extinction spectrum of a single isolated gold nanoparticle, with a radius $r_{eff} = 6$ nm suspended in water. (b) Schematic of a spherical object generated under discrete dipole approximation. (c) Computed CD trend as the extinction difference under left- and right-handed circularly polarized light excitations.

Firstly, this home-coded model has been tested out on a single isolated gold nanoparticle suspended in water. The dielectric constant of the medium is then taken as a function of its refractive index, determined at $n = 1.333$. Whereas for gold materials, assuming that only the free electrons are affected by confinement effects, their dielectric function can be expressed in the following way:

$$\epsilon_{NPs}(r_{eff}) = \epsilon_{NPs}(\infty) - \frac{\omega_p^2}{\omega(\omega + i\Gamma_0)} + \frac{\omega_p^2}{\omega(\omega + i(\Gamma_0 + \frac{V_f}{r_{eff}}))} \quad (4.12)$$

where $\epsilon_{NPs}(\infty)$ reflects the tabulated dielectric function of bulk gold, $\omega_p = 8.8$ eV, $V_f = 1.4 \cdot 10^6$ ms⁻¹ and $\Gamma_0 = 0.081$ eV are the plasma frequency, the Fermi velocity of free electrons and the electron damping of gold, respectively.

In order to construct a spherical geometry of radius $r_{eff} = 6$ nm, the size of each individual cubical voxel is chosen to be 1 nm^3 which leads to a total of 216 generated dipoles to be computed as illustrated in Fig. 4.14(b). Under a linear excitation source along \vec{z} -direction, its extinction spectrum is simulated with a resonance peak located at 522 nm (Fig. 4.14(a)). This value, which assumes an individual size without the presence of aggregation, appears to be close to the experimental result obtained around 558 nm. An absence of CD behavior as depicted in Fig. 4.14(c), is expected for a perfect isotropic nanocrystal and agrees coherently with the experimental findings plotted in Fig. 4.8(c).

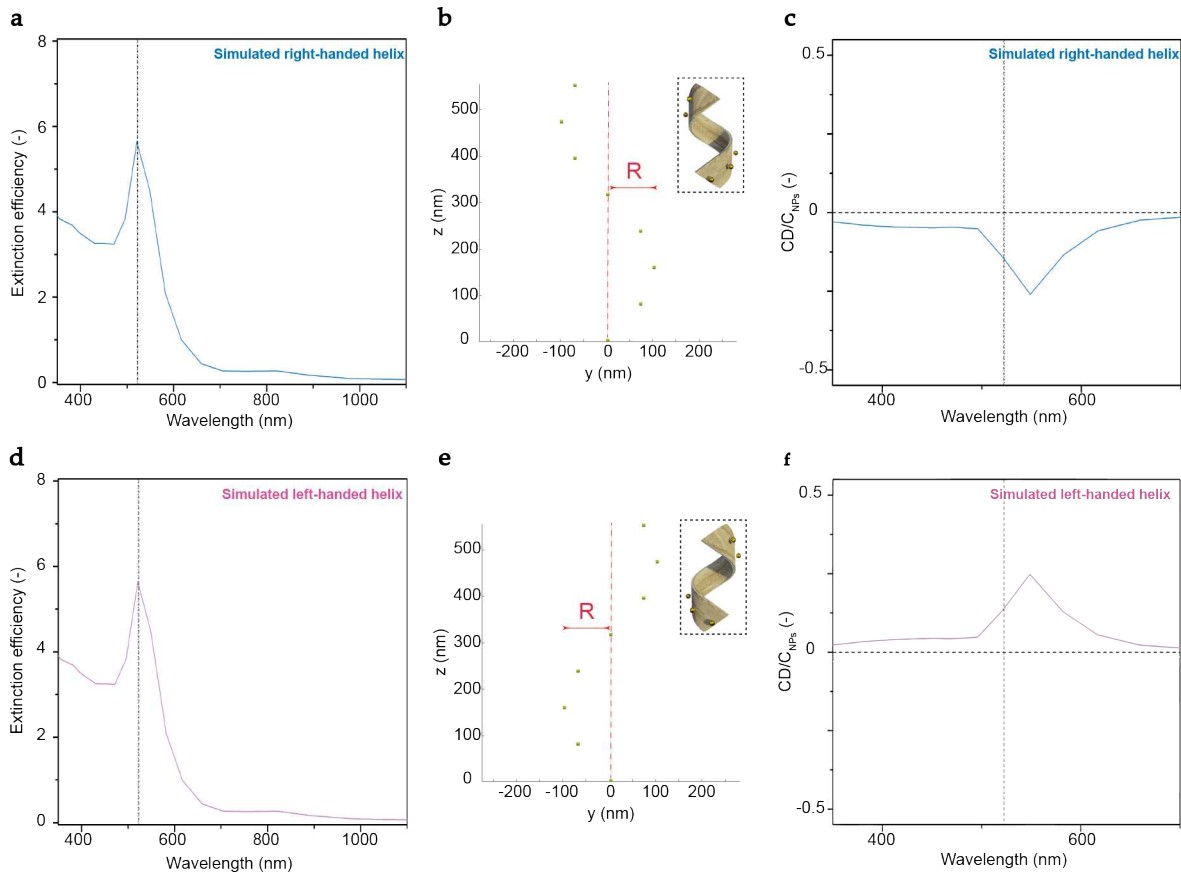


FIGURE 4.15: (a) Simulated extinction spectrum of an array of 8 gold nanoparticles arranged in a right-handed helical manner, with a radius $r_{eff} = 6$ nm of each individual object suspended in water. The ensemble mimics the experimental deposition of grown gold seeds around a silica helix that possesses a radius $R = 100$ nm. (b) Schematic of these aligned nanospheres generated under discrete dipole approximation, projected onto the yz -plane. Inset shows a cartoon of the pictured right-handed helix in three-dimensional space. (c) Computed CD trend as the extinction difference under left- and right-handed circularly polarized light excitations. While identical data for the other chiral moiety corresponding to the left-handed ones are plotted in (d-f).

As eight nanoparticles are simultaneously generated this time around to constitute a full helix, the resulting optical properties in terms of absorption and CD are shown in Fig. 4.15. These latter are equally spaced along a helical angle that equals 45° , around a cylindrical envelope that possesses a radius $R = 100$ nm. The associated pitch can then be calculated in the order of 550 nm. This mimics identically the as-mentioned experimental deposition of grown gold seeds on a hybrid surfactant-silica helix, except that the presence of silica

substrate is not taken into account during simulations. Absorption-wise, the addition of supplementary gold nanoparticles in the system increases linearly the optical density without shifting the initial resonance peak situated at 522 nm. However, CD trend displays a notable negative (resp. positive) dip in this region for right- (resp. left-handed) helical structure. According to Liedl and co-workers who studied both experimentally and theoretically the potential of DNA templates for the programmable design of helical plasmonic nanostructures, it was suggested that the chirality arose from collective plasmon-plasmon interactions between gold nanoparticles [253]. The splitting between the longitudinal and transversal modes of the incident light was due to their plasmonic dipole interactions within the helix, resulting in either positive-negative or negative-positive line shape of a CD spectrum.

As one can expect, the CD trends demonstrate mirror images between these two chiral objects. The magnitude of this chiroptical activity depends in theory, on the intensity of the plasmon resonance and also, on the strength of the interparticle plasmonic coupling [254]. This explains the bisignated CD signals obtained both through experiment and simulation, via a chiral helical arrangement of these individual gold nanoparticles. It enables notably the propagation of a plasmonic coupling wave along both helical directions to result in an enhanced absorption of the incident light, dictated by the handedness of the silica substrate.

Effect of gold nanoparticles' size with respect to the helical substrate

In order to better comprehend the prior experimental analysis represented in Fig. 4.13 and Tab. 4.4, two series of simulated studies have been performed, where (i) the individual size of gold nanoparticles r_{eff} , and (ii) the radius of cylindrical envelope R , are both separately varied. This captures essentially several experimental consequences, where the amplitude of CD signals is increased and exhibits longer tails toward higher wavelengths, as the density of grafted objects increases. The grafted interparticle distance in other words, also becomes smaller. Therefore, by solely varying r_{eff} or R while keeping the position and number of particles constant in view of computational costs, these two scenarios assimilate indeed a global modification of the grafted interparticle distance.

A change in terms of the individual size of gold nanoparticles r_{eff} , which takes up values of (2 – 4 – 6 – 8) nm indicates an interparticle distance that is equally spaced by (107 – 103 – 99 – 95) nm, respectively. This is applied to an array of eight nanoparticles arranged in a right-handed helical manner, which forms a complete turn on a cylindrical envelope of radius $R = 100$ nm as pictured by Fig. 4.16(b). An increase in magnitude for both extinction cross-section and CD is observed with an increase in r_{eff} and hence, a decrease in interparticle distance (Fig. 4.16(a,c)). These simulated right-handed helices exhibit expected negative signals with a dip at 549 nm, in the vicinity of the experimental plasmon resonance frequency obtained at 558 nm. In comparison to the plots from Fig. 4.13, identical trends are observed, but the experimental CD dips appear to be blueshifted and situate at 511 nm. This is most probably due to the uneven size distribution of grown gold nanoparticles that is not perfectly centered around 12 nm.

On the other hand, a change in terms of the radius of cylindrical envelope R , which takes up values of (25 – 50 – 75 – 100) nm reflects an interparticle distance that is equally spaced by (16 – 44 – 71 – 99) nm, respectively. This scenario is simulated for an array of eight nanoparticles possessing individually a size $r_{eff} = 6$ nm, arranged in a right-handed helical manner to form a complete turn (Fig. 4.17). Interestingly, one remarks that the optical density remains similar for all cases since the intensity of the plasmon resonance

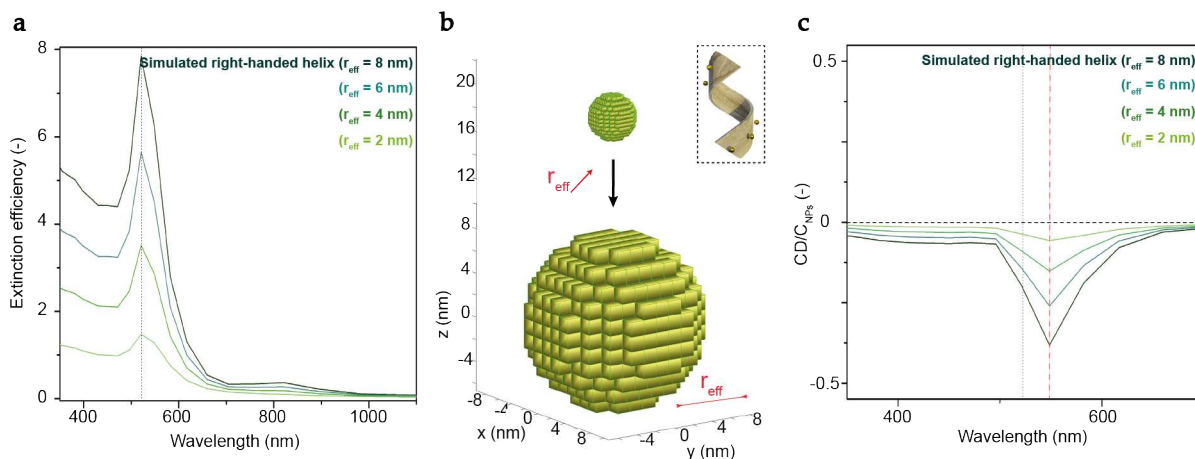


FIGURE 4.16: (a) Simulated extinction spectrum of an array of eight gold nanoparticles arranged in a right-handed helical manner, with a variable radius r_{eff} suspended in water. (b) Schematic of the spherical objects generated under discrete dipole approximation. Inset shows a cartoon of the pictured right-handed helix in three-dimensional space. (c) Computed CD trends as the extinction difference under left- and right-handed circularly polarized light excitations. Black dotted (resp. red dashed) line serves as eye-guide for the plasmon resonance frequency located at 522 (resp. 549 nm).

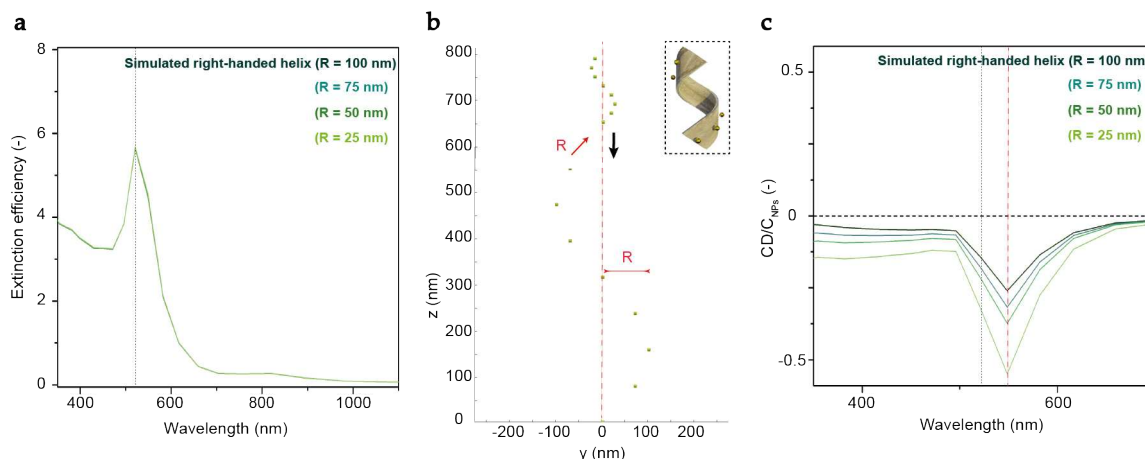


FIGURE 4.17: (a) Simulated extinction spectrum of an array of eight gold nanoparticles arranged in a right-handed helical manner, with a variable radius R suspended in water. (b) Schematic of the spherical objects generated under discrete dipole approximation. Inset shows a cartoon of the pictured right-handed helix in three-dimensional space. (c) Computed CD trends as the extinction difference under left- and right-handed circularly polarized light excitations. Black dotted (resp. red dashed) line serves as eye-guide for the plasmon resonance frequency located at 522 (resp. 549 nm).

was not modified. However, their associated CD spectra demonstrate an increasing trend with a decrease in R and hence, once again a decrease in the interparticle distance. This agrees well with the g -factor findings listed in Tab. 4.4, which display greater values with the increasing strength of the interparticle plasmonic coupling.

Herein, an alternative way to design three-dimensional helical nanostructures with

strong and controllable chiroptical properties is carried out by using hybrid surfactant-silica nanohelices as chiral templates, along with gold nanoparticles as plasmonic active units. It appears that a homogenous gold nanoshell coating is not fully achieved, with still a certain spacing between individual domains of in-situ grown nanoparticles. The highest g-factor is unsurprisingly obtained in the case of a densely packed structure, reaching an order of $20 \cdot 10^{-4}$. It is interesting to note that this value is around two-fold larger than the greatest value obtained in previous chapter, for *L*-(+)-tartrate-capped 4 MLs CdSe nanohelices and ten-fold higher than the reported result by direct grafting of gold nanoparticles onto 16-2-16:(*D/L*)tartrate silica helices [102]. This might originate from two factors, mainly because (i) the average number of grafted objects on an individual helix is more important for our synthesized 18-2-18:(*D/L*)malate silica structures, since their initial size is of an order of magnitude higher than 16-2-16:(*D/L*)tartrate, enabling them to host more incoming guests and to attain a larger plasmon resonance intensity for a given interparticle distance in both cases and (ii) the final average size of plasmonic active units is slightly bigger in the present case ($r_{eff} = 6$ nm) compared to the reported value that situates around 5 nm.

Curiously a side-to-side comparison between the two synthesized systems in this section: 18-2-18:(*D/L*)malate@CdSe and 18-2-18:(*D/L*)malate@Au grown seeds, only the latter tribrid plasmonic case displays an active CD behavior for colloidal particles suspended in solution. This is coherent to the former findings, where CdSe nanocrystals grafted onto chiral silica nanoribbons only exhibited chiroptical properties when the measurements were taken under a dried film state [97]. The supposed close contact and densely packed self-organization of these tribrid semiconductor nanostructures appeared to play a key role, since their interaction order was of shorter range than the coupled plasmonic ones [81, 255]. Nevertheless, it would still be interesting enough to subject these candidates for eventual experiments of circularly polarized luminescence which have yet been reported.

4.2 Manipulating fluorescently-labelled silica objects

As mentioned in the beginning of Chapter 3 about inorganic CdSe nanohelices, these as-synthesized objects with two opposite handedness presented a weak enantiomeric excess. In order to obtain a population of pure chiral objects, one of the post-synthetic ways that one could think of, is by a physical separation method occurring under hydrodynamics effect. To achieve so, it is important to demonstrate that indeed, the migration speed of the different chiral counter-parties ought to be significant enough and under a rightly designed fluidic channel, a separation chamber can be made possible [137, 256, 142]. Additional mechanisms such as by introducing non-linear flows or by generating a propeller effect with a rotating external field coupled to the dipole moment of enantiomers have also been derived [257, 108].

Herein, our motivation is to apply a new concept called opto-acoustophoresis as a potential chiral resolution technique. This describes the coupling between acoustics first realized in a fluidic resonator and under the perturbation of optical excitations, it reveals a separating action that is able to control the aggregation process of microparticles [136]. As preliminary proof-of-concept studies, as-synthesized hybrid surfactant-silica helices that are either purely left- or right-handed structures, have been chosen as the main candidate. This is because first of all, (i) silica material presents a relatively high acoustic contrast factor that reacts promptly to acoustic waves, (ii) the overall micrometric size of silica helices allows an efficient response to opto- and acousto-perturbations and a facile observation under built-in

optical microscopes and (iii) the versatility of silica's surface modification. As seen previously, they can be functionalized by nanoparticles and different fluorescent markers such that it is possible to manually differentiate the helices' handedness.

4.2.1 Setting up samples and opto-acousto resonator

In collaboration with researchers from the group of Physique et Mécanique des Milieux Hétérogènes (PMMH), post-synthetic manipulations of these fluorescently labeled chiral objects under acoustic levitation have been carried out. The chosen fluorophore in our work is called fluorescein and in particular, the isothiocyanate one (FITC). Upon previous amino-modification of the hybrid surfactant-silica helices with APTES and owing to the covalent coupling via thiourea bonds, these molecules are incorporated onto the silica surface. Under FTIR, the appearance of a slight band around 3250 cm^{-1} is attributed to the stretching of secondary amine groups as shown by Fig. 4.18(c). Besides, the conjugated alkene bonds that form harmonics also contribute to the band intensity around 1580 cm^{-1} . This chemically post-modified system is then abbreviated as *18-2-18:(D/L)malate@FITC*.

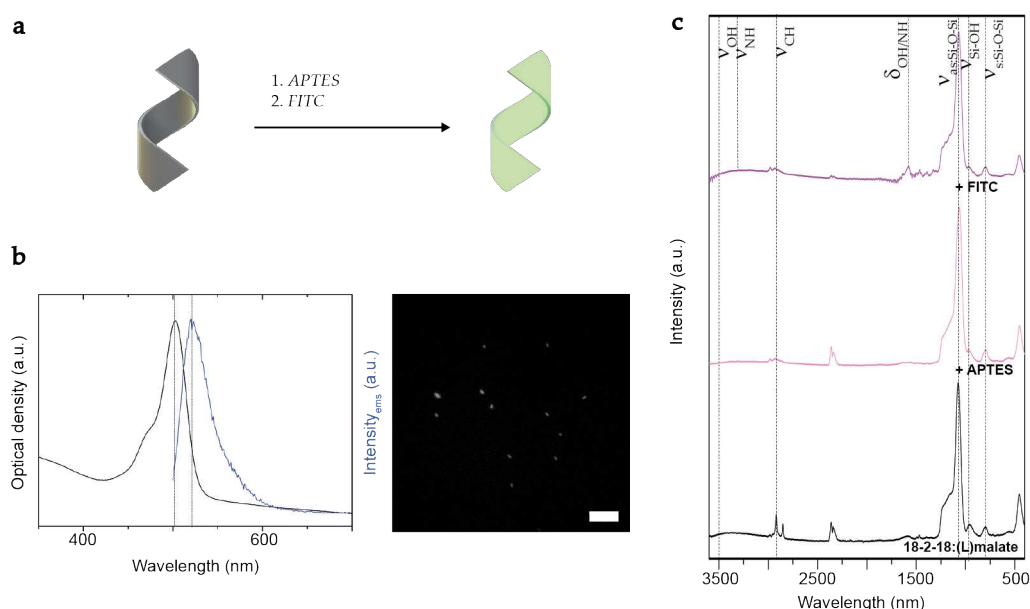


FIGURE 4.18: (a) The as-synthesized hybrid microhelices, possessing in average $0.2\ \mu\text{m}$ in diameter and $1.2\ \mu\text{m}$ in length, undergo a functionalization with APTES for an amino-modified system. This enables to host thiourea bonds with FITC molecules, for the purpose of fluorescent labeling. (b) Optical spectra of *18-2-18:(L)malate@FITC* system and the associated fluorescence microscopy image. The resulted grafting density is estimated to be 10^8 fluorescent molecules per silica helix, which absorbs and emits respectively, around 500 and 525 nm. Scale bar: $10\ \mu\text{m}$. (c) FTIR spectra of (black) *18-2-18:(L)malate* silica helices prior to any surface chemical alterations, then (pink) amino-modified with APTES and (magenta) coupled to FITC.

Once these fluorescent helices have been synthesized, their motion is studied under opto- and acousto-perturbations in the group of Jean-Luc Aider et Mauricio Hoyos. Typically, a resonant cavity in which an ultrasonic standing wave is generated, contains a suspension of particles to be observed and tracked under optical dark-field microscope (Fig. 4.19). This allows for the creation of an ARF field with an acoustic pressure node,

located at mid-height of the cavity. The axial component of the ARF drives the particles to migrate toward the pressure node, where they can be maintained in acoustic levitation as shown in Fig. 4.19(b). While its transverse component forces the particles to gather toward the local maximum of acoustic energy, where objects such as passive particles or cells can ultimately form aggregates [258, 259, 117]. Finally when the distance between objects becomes sufficiently small, they are attracted by each other due to a secondary acoustic force called the Bjerknes force, which renders the aggregates strongly cohesive [127].

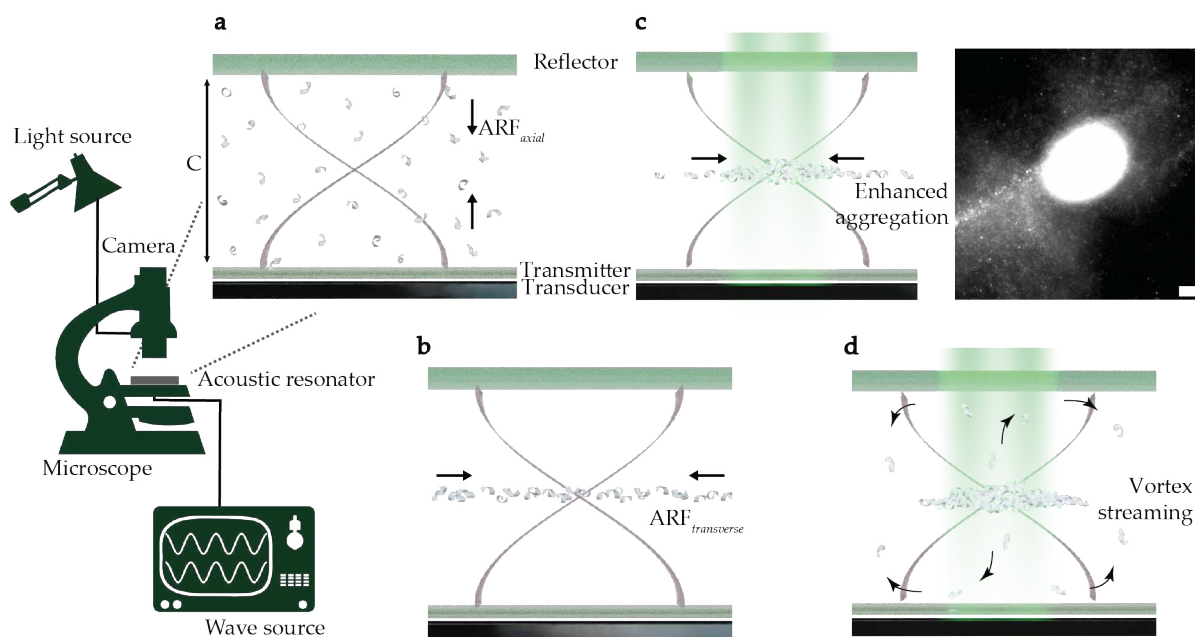


FIGURE 4.19: (a) Side-view of an acoustic resonator, inside which contains a suspension of particles subjected to a full period λ_{ac} , of ultrasonic standing wave. The height of the acoustic cavity C , measures $330 \mu\text{m}$ and by tuning the acoustic frequency, it enables the modification of the nodal plane's position along z -axis. (b) When the acoustic is switched on, it leads to the creation of trapped particles in the mid-plane. This acoustic levitation phenomenon owes firstly to the axial component of the acoustic resonance force acting on the objects. The transverse component on the other hand comes into play, which allows the formation of local aggregates. (c) Under specific light illumination at 488 nm , enhanced particles' aggregation is observed. The hence associated migration behavior of these fluorescent probes is tracked and analyzed in a quantitative manner. Inset shows a fluorescent image viewed from above, of a growing aggregate during experiment. Scale bar: $30 \mu\text{m}$. (d) Acoustic streaming effect is recorded overtime, where certain particles due to their small length scale, display vortex-like displacements to reconcentrate into local aggregates.

Dense materials such as silica, have large acoustic contrast factor which makes them highly responsive to the ARF, whose typical expression experienced by spherical particles suspended in a liquid subjected to an ultrasonic standing wave acoustic field can be written as:

$$\mathbf{F}_{ac}(z) = \frac{\pi}{2} \langle E_{ac} \rangle k d_p^3 F_Y \sin(2kz) \cdot \mathbf{e}_z \quad (4.13)$$

along with,

$$F_Y = \frac{1 + \frac{2}{3} \left(1 - \frac{\rho_f}{\rho_p}\right)}{2 + \frac{\rho_f}{\rho_p}} - \frac{\rho_f c_f^2}{3\rho_p c_p^2} \quad (4.14)$$

where $\langle E_{ac} \rangle$ depicts the time-averaged acoustic energy density in a channel, $k = \frac{2\pi}{\lambda_{ac}} = \frac{2\pi f_{ac}}{c}$ the wave number of an acoustic plane wave of frequency f_{ac} , d_p the diameter of a particle and z the axial position of a particle which starts off from 0 at the bottom of a channel and ends with C at its top. Indeed, the acoustic contrast factor represented by F_Y can be defined as the difference in density ρ and propagation speed of acoustic waves c between an object noted with subscript p and its surrounding medium with f , according to Eqn. 4.14. In general, an object with a density greater than the medium will migrate to the pressure node, whereas lipid drops in an aqueous medium for instance, will move to the antinode.

Peculiar phenomena can also be observed depending on the shape and materials of the objects in suspension. For example, gold cylindrical nanorods which are 2 μm long with a diameter of 0.3 μm , behave differently than spherical particles under the presence of an ARF. Instead of forming stable aggregates, they spontaneously start moving upon reaching the levitation plane. This phenomenon is called self-acoustophoresis and the nanorods can be considered as an artificial active matter [105]. It has also been demonstrated that the above system can be used as an acoustic trap for these active particles or even micro-organisms like bacteria [260]. In this case, the population of self-propelled objects is indeed confined in the acoustic resonance force field, which translates into a trapped environment in which collective motions can be observed. Another captivating sight is recently found, when simultaneously illuminating trapped particle aggregates under a specific optical wavelength. Aider and co-workers observed that the objects can be ejected from the illuminated area, while being kept in acoustic levitation. This phenomenon is named opto-acoustophoresis and depends strongly on a set of acoustic and optical parameters [136].

During experiment, once the acoustics is turned on, 18-2-18:(D/L)malate@FITC helices start moving toward the levitation plane. Then, a monochromatic illumination at 488 nm is switched on as pictured by Fig. 4.19(c). One can observe an acceleration of the particles' migration, in order to form an aggregate with increasing light intensity. This intriguing behavior is found to be dependent on a properly selected illumination wavelength, which corresponds to the objects' absorption spectrum located around 500 nm. This process of enhanced aggregation occurs while maintaining the particles in levitation, at cavity's mid-height under a constant ARF. In the following section, the as-tracked and plotted average in-plane particles' velocities correspond to this enhanced aggregation phenomenon, observed under a simultaneous opto- and acousto-coupling that has yet been reported in literature.

4.2.2 Tracking of particles under migration

In order to produce quantitative data, video recordings with high resolution are carried out. A good surrounding contrast is needed and an adequate amount of light intensity is employed during the recordings. The snapshots time-series are then analyzed. A tracking algorithm developed under *Matlab*, is used to measure the particles' velocities. This allows a quick and automated evaluation of a statistical value of average migration speeds for a large population of detected fluorescent particles.

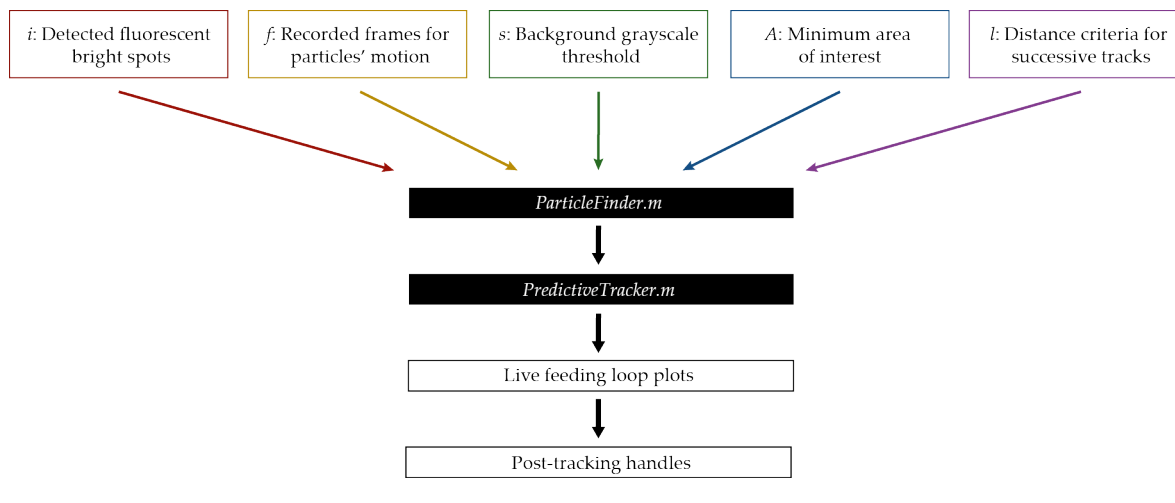


FIGURE 4.20: Flowchart according to which the tracking code is written under *Matlab*.

Fig. 4.20 displays the scheme of this home-built tracking algorithm. Five major inputs are required to initiate a tracking process of a recording that is saved under the .avi format. It includes two numerating parameters such as labels for the different detected spots located in each frame i and indications to cross-over between successive frames in order to define their individual motion f . At the same time, it is necessary to denote certain criteria about the definition of a fluorescent bright spot for the algorithm's recognition. To do so, three determining parameters such as the background grayscale threshold s , minimum area of interest A and distance above which tracks break between successive frames l , have been entered.

The first code called *ParticleFinder.m* applies these inputs onto the video recording with a certain frame rate, in order to identify the positions, durations and hence, the computed velocities of bright spots projected onto an orthonormal basis (\vec{u}, \vec{v}) . These data are compiled into a .mat file and later, serves again as raw inputs for the following code called *PredictiveTracker.m*. This latter produces Lagrangian particle tracks by using a predictive three-frames best-estimate algorithm [261, 262, 263, 264]. It allows the differentiation of each trajectory in time by convolution with a Gaussian smoothing and a differentiating kernel, to yield time-series of positions and velocities for each tracked particle. The total number of tracks, along with the mean and root-mean-square of track lengths are also returned to enable an estimation of associated errors.

On the user's interface, loop plots are constantly updated to show the progress of particles' tracking of a recording. For instance, Fig. 4.21 illustrates the evolution of track lengths traced in various color codes from a time stamp $t = 1$ s, forwards to 5 and 9 s. Once the analysis is finished, post-tracking tools are used to extract useful quantitative information like the average in-plane velocity of tracked particles and their distribution. This step enables also the unit conversion from pixels and frames, to actual scales expressed in meter and second.

Influence of illuminated light intensity

Fig. 4.22(a) illustrates the influence of illuminated light intensity on the resulting average particles' velocity, under several conditions of acoustic amplitude and a fixed frequency

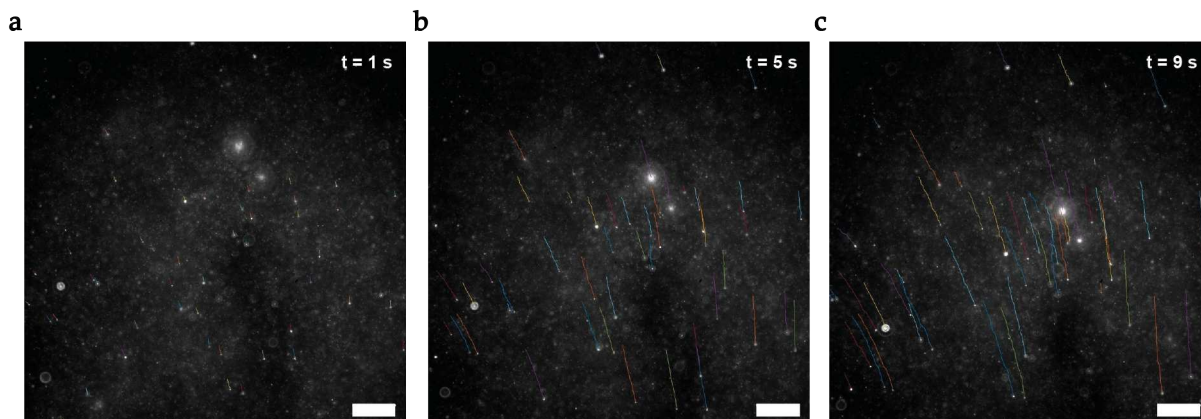


FIGURE 4.21: Tracked migration of *18-2-18:(D)malate@FITC* left-handed helices at different time stamps, upon a stabilized system that corresponds to the scenario depicted in Fig. 4.19(d). Fluorescence microscopy image in (a) (resp. (b) and (c)) is captured right after 1 (resp. 5 and 9 s). The applied acoustic amplitude is fixed at 8 V with a frequency of 1.88 MHz. A full strength of light illumination at 488 nm is switched on and the recorded video frame rate is of 20 images per second under the observation of a 20x objective lens. Scale bar: 30 μm .

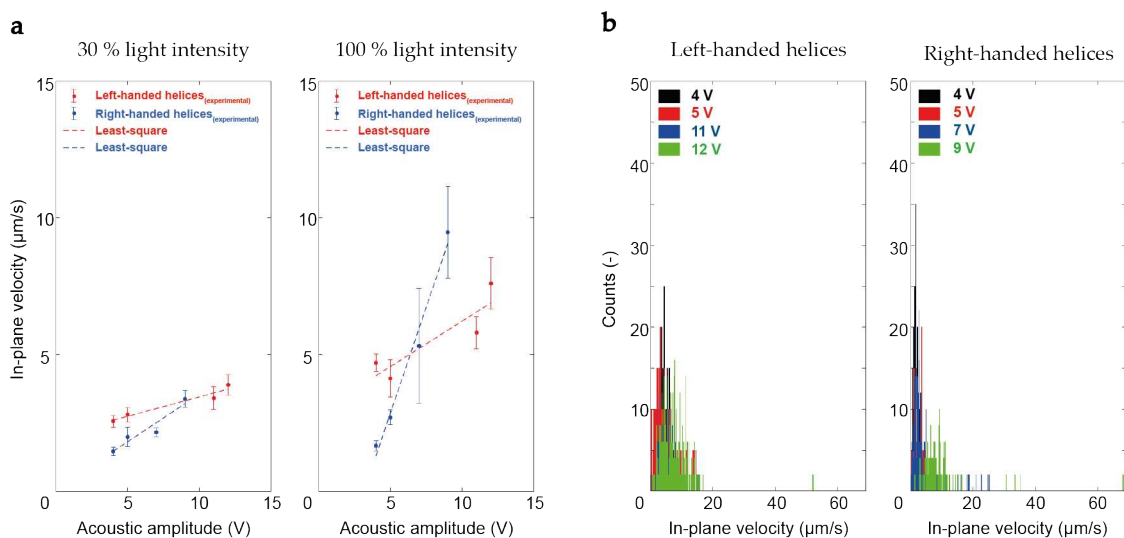


FIGURE 4.22: (a) Average in-plane velocity of *18-2-18:(D/L)malate@FITC* left- and right-handed silica helices as a function of acoustic amplitudes, under two different illuminated light intensities at 488 nm. During experiment, the acoustic frequency is set at 1.88 MHz. (b) Histogram plots for the tracked fluorescent particles of opposite handedness, illuminated at 100 % of light intensity. In each case, a total number of more than 50 particles is accounted for. Bin: $0.2 \mu\text{m}\cdot\text{s}^{-1}$.

of 1.88 MHz, for both chiral helices. The velocity increases with the light intensity and suggests that the *18-2-18:(D/L)malate@FITC* silica helices travel indeed at a higher speed, with an increase in both the opto- and acousto-excitations. A transition point appears around 7 V below which (resp. above which), left-handed (resp. right-handed) helices demonstrate dominant migration speeds.

In comparison to reports where artificial helical swimmers are showcased, their average velocities scale generally to $1 \text{ mm}\cdot\text{s}^{-1}$ for a tail length of 1.5 mm, placed in a cylindrical channel of 1.6 mm under an imposed shear rate of $0.62 \text{ mm}\cdot\text{s}^{-1}$ [265]. Taking into account the dimensions of each respective system, their angular velocities seem to vary coherently in the order of unity Hz. As for chiral particles under hydrodynamics shear flow where the Péclet number is large, Doi and co-workers have demonstrated that an object of 10 nm migrates with a sign determined by their chirality, in a Taylor-Couette cell set-up rotating at 100 rpm, over a distance of 1 mm in several minutes [266].

Herein, neither kind of external shear rate is applied during experiment. But seemingly, by choosing the right working conditions in terms of acoustic and optical parameters, one is able to promote a faster migration of either population of chiral silica helices. It is once again important to stress that the self-propulsion of these particles is only analyzed at the mid-height of the cavity, while neglecting its third velocity component along the z-axis. Indeed, under the presence of the axial component of the ARF, most objects are confined in the plane of acoustic pressure node as mentioned beforehand. Moving on, in order to consequently achieve an efficient enantiomeric separation of these systems, opto-acoustofluidics would be interesting to either play on the design of microchannels or by applying various continuous flow systems to further differentiate the migration speeds of these chiral moieties upon reaching a collection outlet.

Influence of dilution

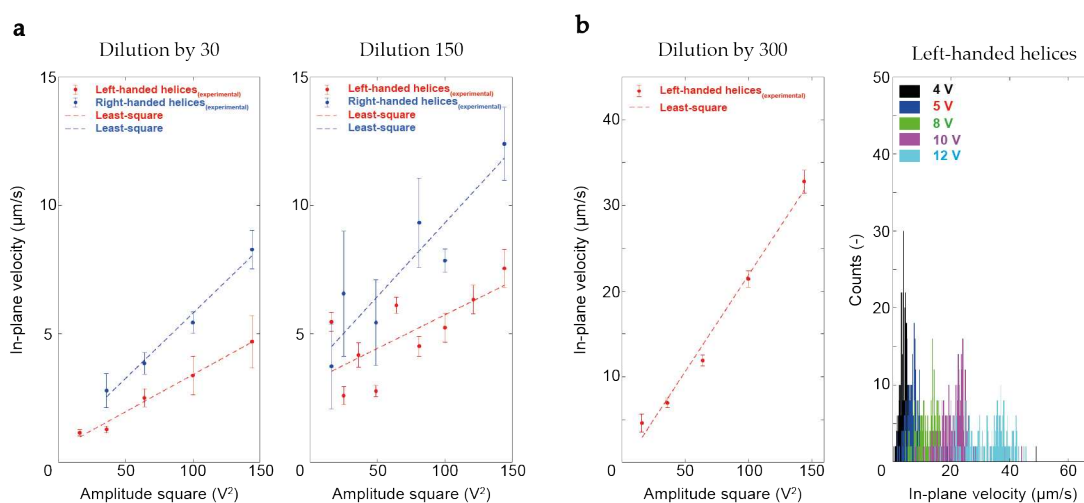


FIGURE 4.23: (a) Average in-plane velocity of 18-2-18:(D/L)malate@FITC left- and right-handed silica helices due to the effect of dilution. The result is plotted as a function of square of acoustic amplitudes, which scales to an energy input. The intensity of illuminated light at 488 nm is set at 30 % with a frequency of 1.88 MHz. (b) Video analysis of highly diluted left-handed structures, under similar working conditions as in (a). Left panel shows their moving speed as a function of square of acoustic amplitudes, while the right panel represents histogram plots for the associated analysis. A total number of more than 50 particles is accounted for in each case. Bin: $0.2 \text{ }\mu\text{m}\cdot\text{s}^{-1}$.

Often, moving objects in a directed manner display varying behaviors either as an effect of a collective phenomenon or in a diluted regime. Fig. 4.23 plots the evolution of the silica particles' moving speed as a function of square of acoustic amplitudes, as the acoustic energy is proportional to the square of signal amplitudes applied to the transducer, under distinct dilutions. The analysis shows that the velocity of the objects is increased in less concentrated suspensions. These results are curiously comparable to those of collective cell migration in tissues which slows down as the cell density rises [267, 268]. Undeniably, collective movements are inter-correlated instead of being independent, which explains their behavior that is locally more elastic than viscous. In both factors of dilution (resp. 30 and 150), right-handed silica helices show much important migration speeds than their mirrored selves, the left-handed ones. Going further by diluting to an order of magnitude higher, two-fold values are even obtained for these Gaussian-distributed 18-2-18:(D)malate@FITC silica helices as shown by Fig. 4.23(b).

Influence of particles' shape

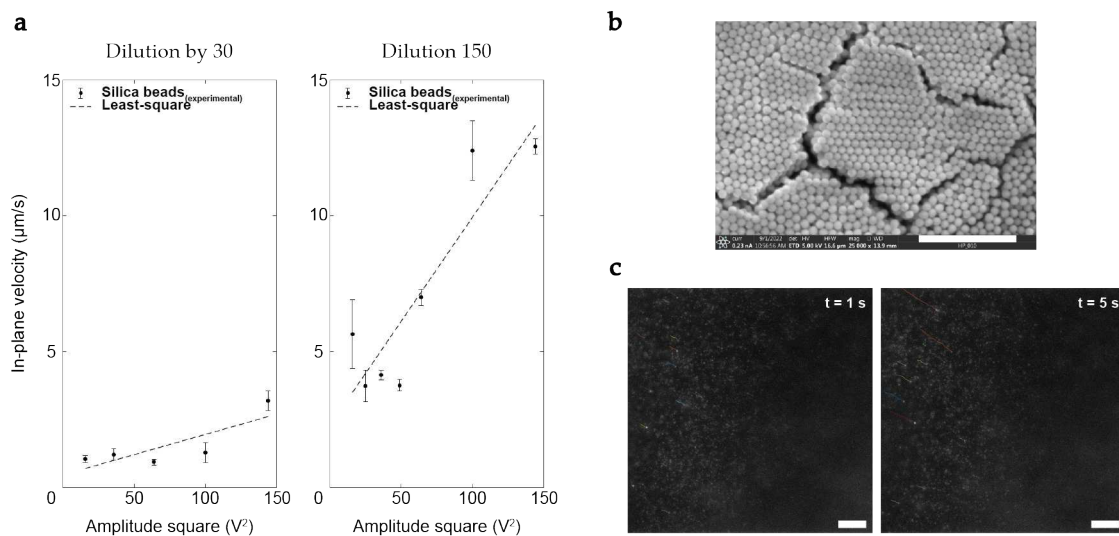


FIGURE 4.24: (a) Average in-plane velocity of fluorescently labeled silica beads with FITC due to the effect of dilution. The result is plotted as a function of square of acoustic amplitudes, which scales to an energy input. Under similar working conditions as in Fig. 4.23, the intensity of illuminated light at 488 nm is set at 30 % with a frequency of 1.88 MHz. (b) SEM image of these beads synthesized through classical Stöber method. Scale: 5 μm . The number of particles is calculated from the weighed mass of dried silica beads, using the formula: $N \sim \frac{m}{\rho \frac{4}{3} \pi r^3}$. For instance, 10 mg of as-synthesized dried silica beads with a density of 2 $\text{g}\cdot\text{cm}^{-3}$ and a diameter of 0.44 μm , yield a number in the order of 10^{12} . (c) Their migration behaviors at a factor of dilution 150 are tracked at different time stamps $t = 1$ (resp. 5 s). The applied acoustic amplitude is fixed at 8 V with a frequency of 1.88 MHz. A full strength of light illumination at 488 nm is switched on and the recorded video frame rate is of 20 images per second under the observation of a 50x objective lens. Scale bar: 30 μm .

In addition, the effect of nanoparticles' shape has been investigated by synthesizing silica spherical beads whose diameter is narrowly distributed in the order of 0.4 μm (Fig. 4.24(b)). This is achieved by using the well documented classical Stöber method

[269]. These silica beads have been subjected to identical chemical modifications as in the case of 18-2-18:(D/L)malate@FITC silica helices, to be labeled fluorescently. Fig. 4.24(a) reveals that these spherical particles present similar migration speeds as compared to the 18-2-18:(L)malate@FITC right-handed helices in diluted suspensions by a factor of 150, but exhibit much lower velocities at a dilution factor of 30. It is interesting to underline that the increase in velocity for spherical particles occurs at a steeper rate, as compared to the helical particles in general.

A simple scaling law of the volumic ratio between hard spheres and fine strips of helices shows a dependence on $\sim \frac{r^3}{hWH}$. Herein, $r = 0.2 \mu\text{m}$ represents the radius of an individual silica bead, $h = 6.5 \text{ nm}$ the spacing between silica walls of a helix, which corresponds to the thickness of two bilayers of interpenetrated gemini surfactant membranes, while W and H are the width and length of an individual silica helix, estimated to be in average 0.2 and 1.2 μm [232]. This points in fact, to values that are much greater in the case of spherical than helical objects. According to the work of Yosioka and Whitworth, as the primary and secondary acoustic forces scale to the volume of a targeted particle, this ought to generate greater acoustic confinement effect on the spherical structures at first thought [123, 126].

However in the presence of an additional light coupling to our experiment, the spherical particles' migration speeds resulting from the enhanced aggregation phenomenon as illustrated in Fig. 4.19(d), do not seem to entirely obey the previous theories established solely on acoustics. In further diluted suspensions at a factor of 150 for instance, one can imagine how the migration of particles could be less compact compared to a more concentrated situation at a factor of 30. Visually speaking, as evidenced under fluorescence microscopy, one can remark that the close packing of either dense or hollow objects like hard silica beads compared to cylindrical helices, implies a non-negligible effect on their collective movement.

Upon an aggregation of a flock of silica beads, a still configuration that does not self-rearrange much is observed over time (Fig. 4.25(a)). The identified fluorescent particle encircled in red located at its initial position $t = 1 \text{ s}$, does not move by an inch over time. However, when it comes to helices, individual particles that make up an aggregate are constantly self-rearranging and recirculating within the border of this latter. Therefore, the aggregate itself does not freeze as a whole, but adapts frequently multiple changing internal conformations. Fig. 4.25(b) displays once again, an identified fluorescent particle encircled in red situated at its initial position $t = 1 \text{ s}$ and over the course of 9 s, it is traveling as illustrated by the yellow label and moving away from its initial location in red. On the other hand, the aggregate composed of right-handed silica helices in Fig. 4.25(c), demonstrates a conformational change that is observed in the encircled green zone.

This might hold the reason why in more concentrated suspensions, an inversed trend where spherical particles display in average a lower migration speed than the helices was observed in Fig. 4.24(a), due to the jamming of short-range and dense interparticles' close packing. This goes to underline the objects' compressibility resulting from their shape factor, can indeed have an effect on their collective movement at a given mass concentration. In the same vein, a much alike acoustic experiment on the culture of mesenchymal cells also spontaneously reorganized into spheroids under levitation [117]. This work demonstrates that the materials' compressibility does play a major part on the resulting pattern of self-assembled active matters [270, 271].

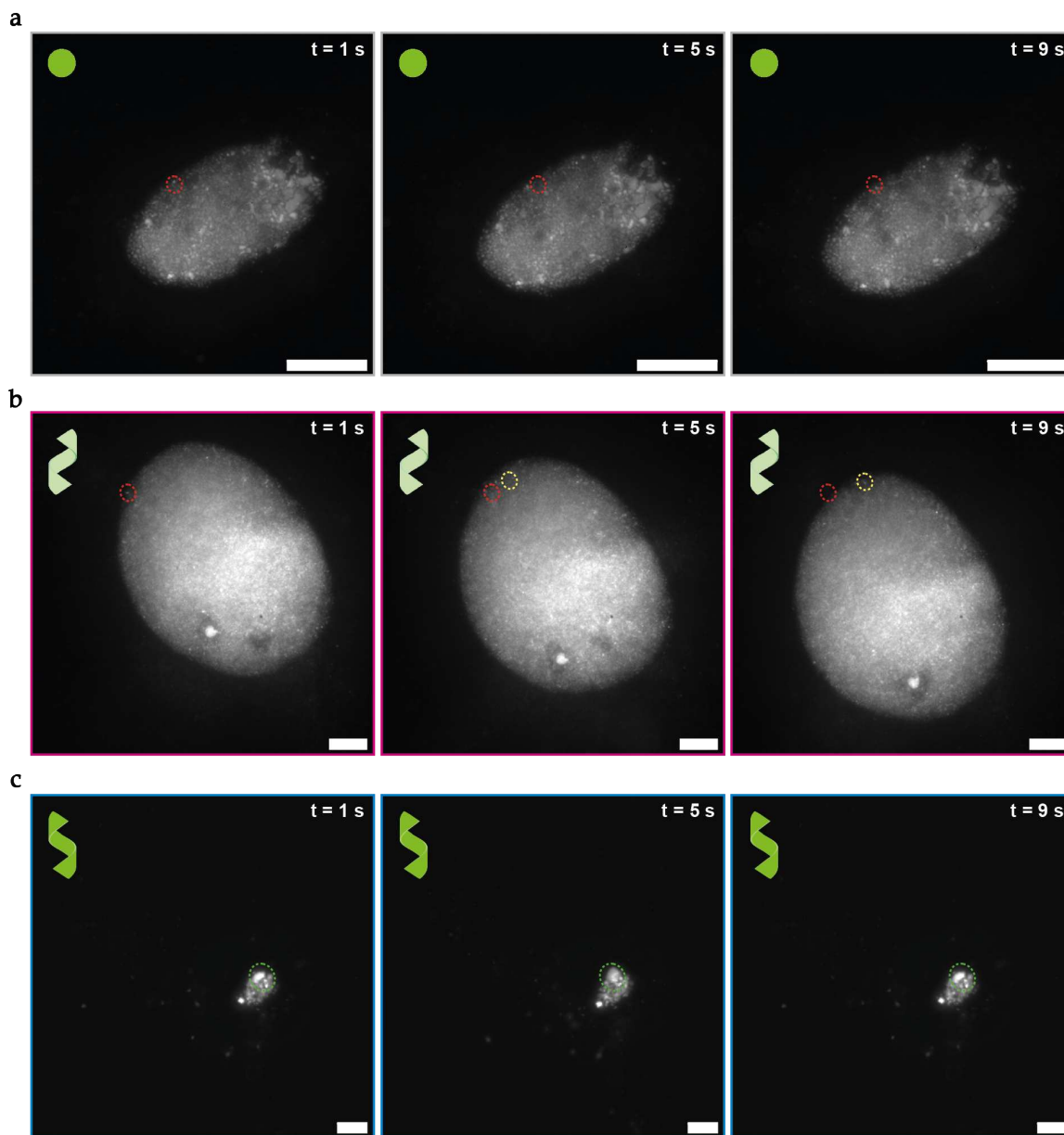


FIGURE 4.25: Tracked behavior of fluorescently labeled silica particles at different time stamps, upon an aggregated system that corresponds to the scenario depicted in Fig. 4.19(d). Fluorescence microscopy images in (a) (resp. (b) and (c)) represent the case of silica beads (resp. $18\text{-}2\text{-}18\text{:}(D)\text{malate@FITC}$ left-handed helices and $18\text{-}2\text{-}18\text{:}(L)\text{malate@FITC}$ right-handed helices), captured at 1, 5 and 9 s during experiment. The applied acoustic amplitude is fixed at 12 V with a frequency of 2.06 MHz. The mass concentration of different studied samples is set to be constant. A full strength of light illumination at 488 nm is switched on and the recorded video frame rate is of 20 images per second under the observation of either a 20x or a 50x objective lens. Scale bar: 30 μm .

4.3 Enhanced-aggregation phenomenon under opto- and acousto-coupling

Previous reports on coupled experiments between opto- and acousto-excitations have shown breakups of aggregates confined at the nodal plane of a cavity [136]. Plausible explanation of this phenomenon has been primarily attributed to the creation of a thermal boundary layer around an individually heated particle, during illumination by an optical wave. The hence generated fluid density gradients then lead to the particles' motion induced by the ARF and applied to the fluid layers. This has led to a competition between the transverse component of the acoustic force and the resulting viscous drag [272].

Relying on a thermofluidic instability model, the former report hinted at a potential thermally induced fluid density gradient as drag source for the observed ejection of fluorescently labeled polystyrene particles, when these latter are subjected to the identical fore-mentioned opto- and acousto-perturbations. Experiment and numerical simulation both pointed out that the introduction of fluid density gradients through the heating of an aggregate can trigger lateral jets of its own constituting particles. If a fluid is locally heated and simultaneously undergoes an ARF, then a large scale flow similarly to Rayleigh-Bénard convection motions, but with an inversed rotating direction can be generated [273, 274, 275].

Thereby, it has been documented that the particles were dragged away by the induced flow, along a direction which satisfies both the decreasing temperature and particles' concentration gradients. In other words, this ejection phenomenon, where particles were laterally splurged out from the centered zone of an aggregate while still being confined at the acoustic pressure node, demonstrates an opposing observation to our findings. In the present case, it is rather an enhanced-aggregation phenomenon that leads to the increased local concentration of particles to ultimately form a stabilized and cohesive self-rearranging blob.

4.3.1 Electric field and heat transfer simulations

By carrying out a similar reasoning on the heating of fluid around an object that is subjected to simultaneous opto- and acousto-perturbations, numerical simulations have been performed to evaluate the induced electric field. It models the heating of its surrounding, embedded in a medium that is analog to a potential difference, as power dissipation Joule effect. The calculation in this following section is performed with *FEATool Multiphysics* run under *Matlab* to essentially compare: (i) the effect of materials between silica and polystyrene, and (ii) the geometry of objects like spherical and helical, could imply on the resulting thermal boundary layer.

According to the particles-in-a-box approach, a cuboid whose dimension along the z-axis ($c = 6.6 \mu\text{m}$) scales 50 times smaller than our experimental acoustic cavity ($C = 330 \mu\text{m}$) is built (Fig. 4.26). Then for the particles, a sphere (resp. a helix) measuring 0.5 (resp. $0.3 \mu\text{m}$) in diameter is also generated, where both of these structures are centered around the identical origin $(-1,0,0)$. Subsequently, a finite-element mesh algorithm is performed to generate grid cells whose mean volume is similar in both cases and equals $10^{-4} \mu\text{m}^3$.

In the as-generated scheme, a simulation environment is built with the Poisson's equation:

$$-\nabla \cdot (\epsilon_r \nabla V - \mathbf{P}) = \rho \quad (4.15)$$

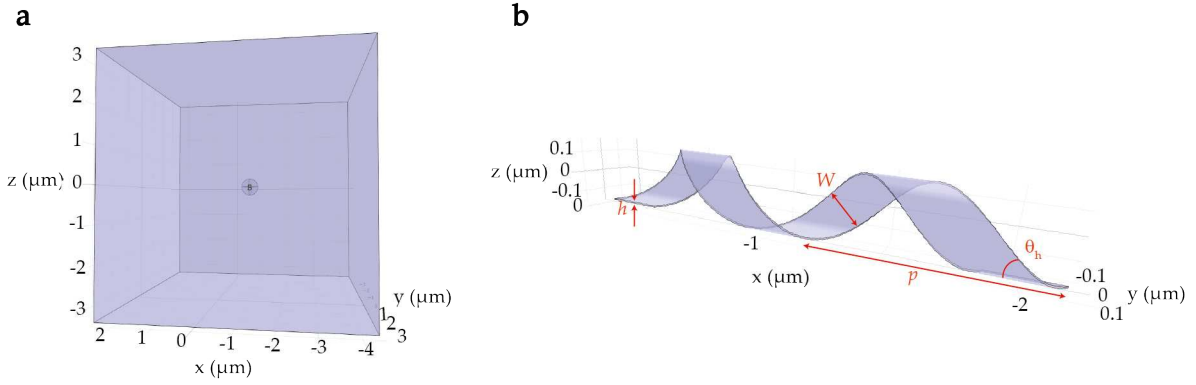


FIGURE 4.26: The as-built particles-in-a-box simulation environment to model experimental objects embedded in a medium. The cuboid represents a size that has been reduced 50 times in comparison to an actual acoustic cavity, to avoid time-consuming mesh generation and vector calculation. The schemes display both (a) a spherical object, whose diameter is 0.5 nm and (b) a piece of helix, which is described by an ensemble of parameters (h, W, p, θ_h) . This latter constitutes its thickness, width, pitch and helical angle, respectively.

where ϵ_r is the relative permittivity of a medium, V the applied potential difference, \mathbf{P} the polarization vector and ρ the density of charge.

In order to approximate the experimental scenario of an applied voltage of 10 V in our down-scaled cuboid, the value of V is fixed at 0.2 V across its top and bottom facets. While the boundary condition of the others is set to a symmetric insulation geometry that satisfies the Neumann postulate:

$$\mathbf{n} \cdot (-\epsilon_r \nabla V + \mathbf{P}) = 0 \quad (4.16)$$

where several values of relative permittivity for different media are taken to be: $\epsilon_{water} = 80.2$, $\epsilon_{ethanol} = 24.3$, $\epsilon_{polystyrene} = 3$ and $\epsilon_{silica} = 3.9$.

The hence associated electric field is injected as a source to be dissipated according to the following equation:

$$\rho C_p T' + \nabla \cdot (-\kappa \nabla T) + \rho C_p \mathbf{u} \cdot \nabla T = Q \quad (4.17)$$

where ρ is the density of a medium, C_p the heat capacity, κ the thermal conductivity, \mathbf{u} the convection velocity vector and Q the heat source. This latter is derived as a function of the material's conductivity σ , in order to efficiently couple the gradient of the electrical potential to the temperature field. It is essential to note that the initial condition of the surrounding T_0 , is set to be 273.15 K.

4.3.2 Choice of materials and geometry of objects

By numerically solving the electrostatic coupled to heat transfer law to approximate either polystyrene beads embedded in an aqueous solution or silica objects in ethanol, the top panel in Fig. 4.27 displays the distribution of electric field around the particles along their cross-section in xz -plane. As one could expect, the induced electric field is much important in the case of spherical objects, owing to their larger cross-sectional size compared to helices. A numerical evaluation of the ratio between their cross-sectional sizes yields a

Materials	ρ ($\text{kg}\cdot\text{m}^{-3}$)	C_p ($\text{J}\cdot\text{kg}^{-1}\cdot\text{K}^{-1}$)	κ ($\text{W}\cdot\text{m}^{-1}\cdot\text{K}^{-1}$)	σ ($\Omega^{-1}\cdot\text{m}^{-1}$)
Water	997	4182	0.598	$\frac{1}{1.8\cdot 10^5}$
Ethanol	789	244	0.166	$\frac{1}{19.5\cdot 10^4}$
Polystyrene	1050	1400	0.150	$\frac{1}{1.6\cdot 10^{14}}$
Silica	2410	705	1.4	$\frac{1}{10^{17}}$

TABLE 4.5: Values of input parameter for the various considered materials adapted from the *COMSOL Material Library*.

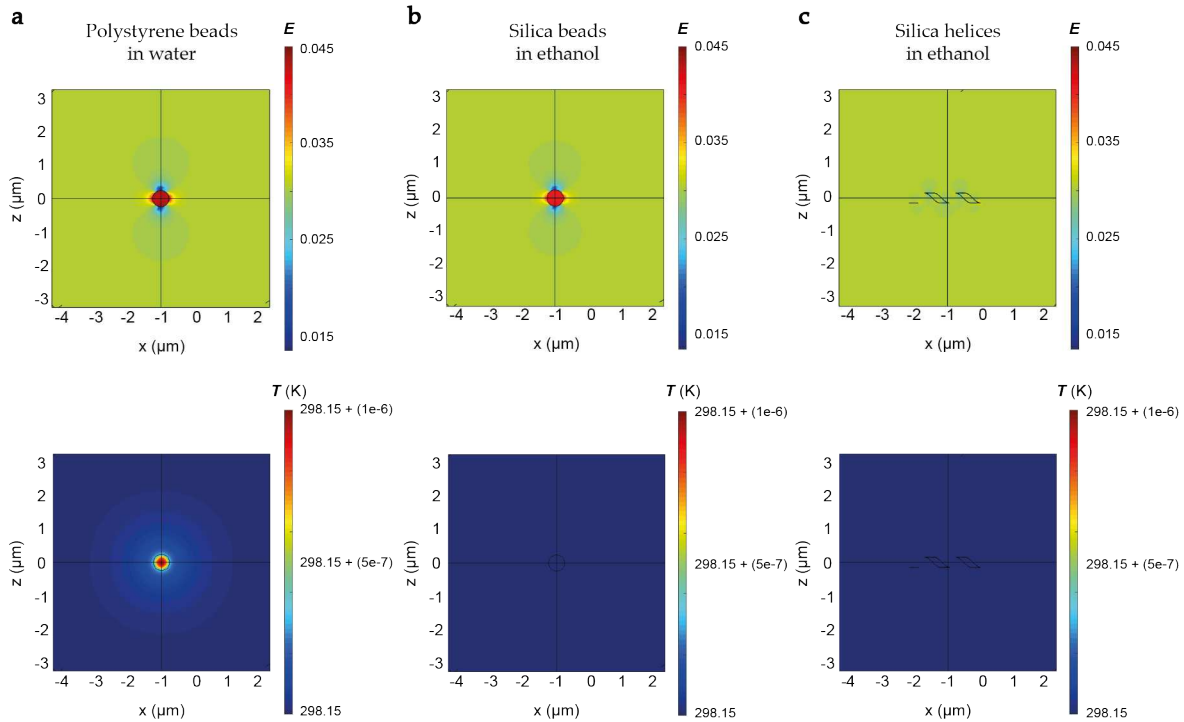


FIGURE 4.27: Electric field and heat transfer simulations performed on an individual (a) polystyrene bead suspended in water, (b) silica bead in ethanol and (c) silica helix in ethanol. In top panel, the induced electric fields across the xz -plane are plotted when a potential difference of 0.2 V is applied to the simulation box along the z -axis. Color code shows absolute values ranging from 0.0135 to 0.0450 in each case. In bottom panel, the associated power dissipations as heat loss to surrounding are displayed. Color code shows values ranging from 298.15 to $(298.15 + 10^{-6})$ K in each case.

value around 20, with an expression that scales to $\sim \frac{r^2}{hW}$ as depicted by Fig. 4.26(b).

When this term dissipates by radiative heat loss through defined boundaries, an equilibrium state is reached, where the associated temperature maps are plotted in the bottom panel of Fig. 4.27. On a scale of 10^{-6} K change in temperature, an isolated polystyrene bead suspended in water exhibits a uniform heating which is centered around its core. The thickness of thermal boundary layer that is heated up to $5\cdot 10^{-7}$ K can be estimated in the order of several hundreds of nm, from the outer surface of the free particle. This agrees well with the scaling law of a typical thermal boundary layer which occurs when there is a heated surface and a flow past it, given by the expression: $\delta_T \sim \left(\frac{\kappa L}{\rho C_p V_\infty}\right)^{1/2}$ [276, 277,

278]. Therein, (κ, ρ, C_p) is the thermal conductivity, density and heat capacity of the medium, respectively, L the local length scale of an object and V_∞ the fluid velocity at far-field. The value of this latter is taken in the order of $10^{-4} \text{ m}\cdot\text{s}^{-1}$, adapted from the work of Aider and co-workers, upon monitoring the flow around an aggregate of five polystyrene beads (similar in size to ours) under the presence of both buoyant and acoustic forces [272]. This crude numerical evaluation yields an utmost value of $1 \text{ }\mu\text{m}$, which is close to our simulation finding.

Surprisingly, when the material is switched from polystyrene to silica, the computation indicates a close-to-zero modification in terms of the bead's surrounding temperature as shown by Fig. 4.27(b). This drastic difference can be mainly attributed to the higher thermal capacity property of polystyrene compared to silica. At first approximations, it is assumed that the energy conversion from the optical power has been fully dedicated to the eventual heating of the surrounding fluid layer by the particle itself, without any secondary source. In the absence of thermal boundary layer in this case, indeed zero ejection phenomenon is observed experimentally and this agrees well with the thermo-acoustofluidic simulations previously reported by our collaborators.

If one were to modify the geometry of objects this time around, by switching from a sphere ($r = 0.25 \text{ }\mu\text{m}$) to a helix ($r = 0.15 \text{ }\mu\text{m}$) presenting two pitches and hence, a length of about $1.9 \text{ }\mu\text{m}$ as pictured by Fig. 4.27(c), once again an absence of thermal boundary layer is noticed on a scale of 10^{-6} K . It appears through this preliminary study that, the choice of materials plays a frontal role at ultimately determining the emergence of particles' ejection phenomenon due to the induced fluid density gradient as drag source away from the central aggregate, rather than the geometry itself. As a result, the opposing observation (enhanced-aggregation of particles toward the central aggregate) found in our present work, occurs under a mechanism that ought to be different than the balance of forces due purely to acoustic radiation and Stokes drag.

4.3.3 Influence of individual particle's size and number

Higher exhaustive calculations are performed under identical postulates, to model objects at a larger scale and an assembly of aligned particles (Fig. 4.28). In terms of finite-element mesh generation, a mean volume of $10^{-4} \text{ }\mu\text{m}^3$ similar to former cases is conserved. From a physical point of view, it is crucial that this chosen parameter be smaller than the two typical length scales that are in play: thermal and viscous penetration depths. Their respective scaling law is written: $\delta_{ther} \sim (\frac{D_{th}}{\omega})^{1/2}$ and $\delta_{visc} \sim (\frac{\nu}{\omega})^{1/2}$, as a function of D_{th} the thermal diffusivity of medium, ν its kinematic viscosity and ω the applied acoustic frequency at 298.15 K [279, 280]. A numerical evaluation of these two length scales in water yields values in the order of 0.28 and $0.73 \text{ }\mu\text{m}$, respectively. Hence, the size of the smallest element of the mesh used during simulation that equals $0.05 \text{ }\mu\text{m}$, well satisfies these boundary conditions.

A two-fold increase in size of the polystyrene bead in Fig. 4.28(a) demonstrates that the resulting power dissipation as heat loss to surrounding increases too, as this term scales to the volume of an object. The represented individual polystyrene bead suspended in water exhibits a uniform heating, with a thermal boundary layer heated up to $5 \cdot 10^{-7} \text{ K}$ that can be estimated to exceed $1 \text{ }\mu\text{m}$. Whereas, neither an increase in particles' size, nor an assembly of aligned objects seem to be able to modify the previous observations made for silica. Once again, a homogeneity in terms of temperature distribution is recorded, which leads to a low probability that the particles' migration originates from the drag along fluid layers, as reported by the work based on polystyrene beads that respond promptly to the creation of

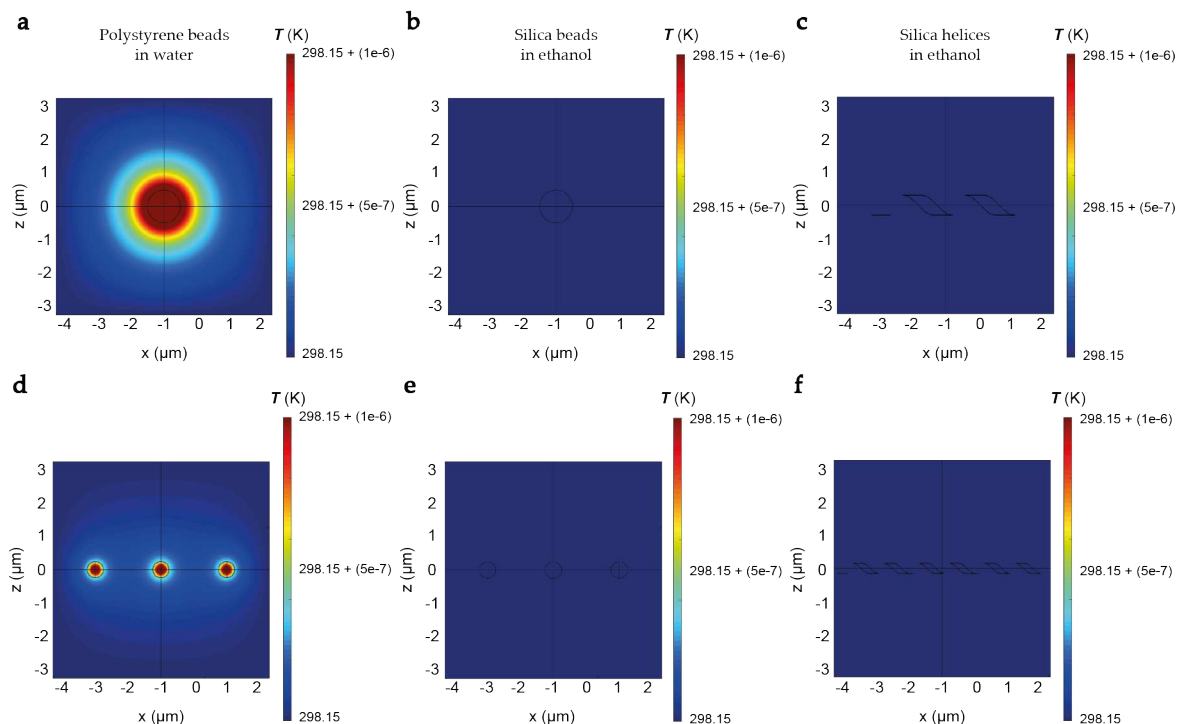


FIGURE 4.28: Heat transfer simulation performed on an individual (a) polystyrene bead suspended in water, (b) silica bead in ethanol and (c) silica helix in ethanol. In comparison to Fig. 4.27, all the mentioned particles have been scaled up twice. This represents an isolated (a) polystyrene bead ($r = 0.5 \mu\text{m}$) (b) silica bead ($r = 0.5 \mu\text{m}$) and (c) silica helix ($r = 0.3 \mu\text{m}$) that is around $3.8 \mu\text{m}$ long. In bottom panel, results for an alignment of three (d) polystyrene beads suspended in water, (e) silica beads in ethanol and (f) silica helices in ethanol are shown. This time around, the size of particles remains identical but its number has been tripled. This represents an array of objects, where the mid-point of each individual one is placed in a $2\text{-}\mu\text{m}$ -spaced fashion compared to its neighbors. Color code shows values ranging from 298.15 to $(298.15 + 10^{-6})$ K in each case.

thermal boundary layer [136].

Herein, an enhanced-aggregation phenomenon is rather documented for fluorescein-capped silica particles under both increasing opto- and acousto-excitations. For objects whose dimension is comparable to $1 \mu\text{m}$, it has been reported that their movement could be dictated by acoustic streaming to end up forming vortex-like patterns in a microfluidic chamber [132]. As the synthesized silica particles in our work revolve around this length scale, unquestionably this former neglected force might contribute to the local concentration of particles confined at the acoustic pressure node. Therefore, another type of multi-nodes acoustic cavity that allows a viewing direction from the side (instead of an upper-view), has been implemented with a home-designed polydimethylsiloxane device in order to verify our preliminary assumptions (Fig. 4.29).

By finely tuning the wave resonance frequency, a number of pressure nodes can be simultaneously generated along the cavity's height as illustrated in Fig. 4.29(b). Preliminary

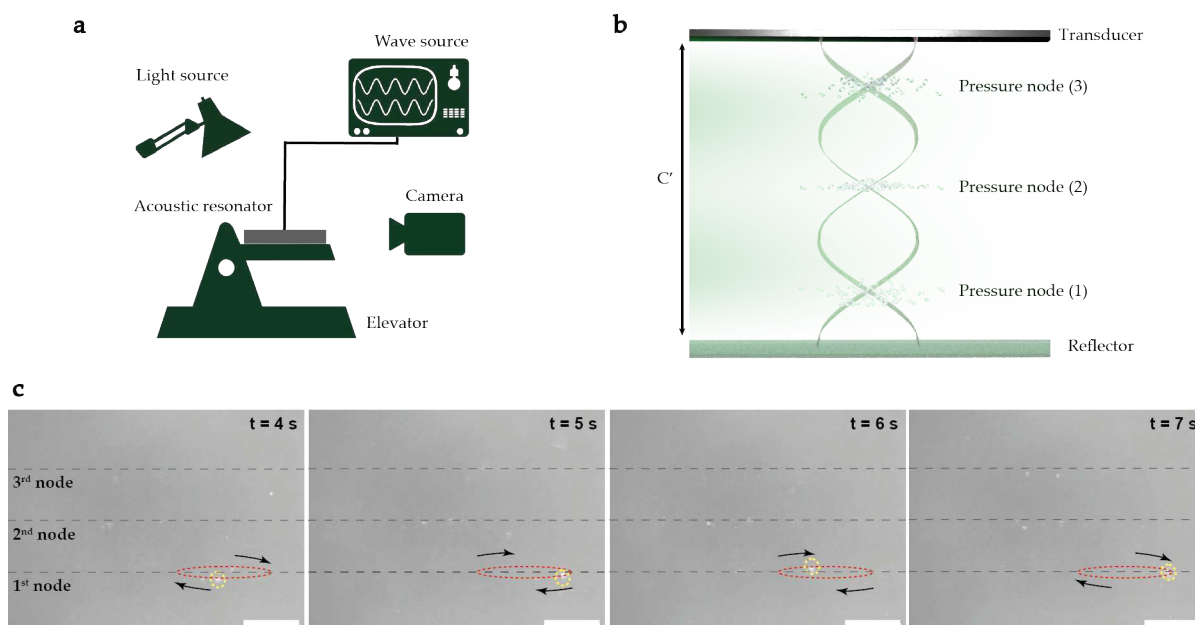


FIGURE 4.29: (a) Schematic of the optical imaging set-up for a multi-nodes acoustic field. (b) An example of a 3-nodes pressure profile generated in such acoustic cavities. By adapting the right frequency to the height of the PDMS device C' , multiple periods of standing ultrasonic wave can be simultaneously created. (c) Vortex-like displacements displayed by *18-2-18:(D)malate@FITC* left-handed helices that are confined in the first nodal plane, at different time stamps $t = 4$ (resp. 5, 6, 7 s). Red dotted line represents their global elliptical trajectory with particles that are encircled in yellow and black arrows to indicate their moving direction. The applied acoustic amplitude is fixed at 11 V with a frequency of 2.11 MHz. A 50 % strength of light illumination at 488 nm is switched on and the recorded video frame rate is of 20 images per second under the observation of a 50x objective lens. Scale bar: 30 μm .

tests display a series of recording where the suspended *18-2-18:(D)malate@FITC* silica helices are trapped in multiple disk-like layers under acoustic levitation. As soon as the acoustics is switched on, an important amount of particles are confined as monolayers and remain stable over the entire period of recording time, whose duration is less than an hour long. Thanks to this technique, vortex-like displacements of free-suspending objects are evidenced not only along the z -axis, but as well as in the xy -plane. It is interesting to point out the capacity of certain particles to even hop and travel in between pressure nodes. It appears that handling these relatively tiny particles from an acoustics and optical point of view, the focusing force along the axial direction no longer stays predominant and acoustic streaming might have to be accounted for, to fully capture their motion. Moving forward with this novel acoustofluidic set-up, it would be highly interesting to further leverage this enhanced-aggregation phenomenon that is yet to be entirely comprehended, onto building an eventual chiral resolution method based on the evidenced difference in migration speed existing between objects of opposite handedness.

4.4 Conclusion

An alternative approach of synthesizing chiral tribid organic-inorganic structures, with finely controlled handedness has been suggested. This benefits from the self-assembly of gemini surfactants complexed with chiral counterions like malic acids, doted by their robust capacity to be functionalized by silica. This constitutes a wide degree of freedom in surface chemistry play, where three systems abbreviated as *18-2-18@CdSe*, *18-2-18@Au* and *18-2-18@FITC* have been explored.

These hereby yielded helices of left- and right-handedness, measuring in average 0.2 μm in diameter and 1.2 μm in length, serve as substrate to host incoming guests. In the first case of grafting semiconductor NPLs with well-defined shape and dimensions, it enables an evaluation of the silica helices' number concentration which is crucial thereafter, to precisely determine their added quantity for controlled synthesis of gold nanoparticles for example. This leads then to the second part of this work about depositing and in-situ growth of gold-decorated silica helices. Such colloidal plasmonic system exhibits chiroptical behavior as CD that increases in magnitude with the strength of the interparticle plasmonic coupling in its resonance region. From a simulation point of view performed under discrete dipole approximation, similar evolution of CD signals is obtained, underlining the significant effect of interparticle distance. Despite the as-predicted absence of CD phenomenon on colloidal silica structures coupled to semiconductor nanoparticles in solution, this class of material still holds the potential for circularly polarized light emission studies, as hinted by the process of chirality transfer that is worth investigating [281, 99].

On the other hand, as silica material reacts positively to confinement under acoustic levitation experiments, the as-synthesized chiral helices have been fluorescently labeled for observation under dark-field microscopy. Moreover, at a specific illumination wavelength, the particles' average in-plane migration speed in the order of several tens of $\mu\text{m}\cdot\text{s}^{-1}$, is demonstrated to increase with both opto- and acousto-excitations, as well as higher factors of dilution. As a function of the helices' handedness, it is noticed that their traveling velocity may differ depending on the chosen working conditions and hence, one is able to promote a faster migration of either population of chiral objects.

Side-to-side comparisons of identical materials, but of different morphologies, reveal that the enhanced-aggregation phenomenon occurs in a fashion that depends largely on the concentration of suspended particles. Another distinguishable point lies also on the formation of an internally self-rearranging aggregate that is recorded in the case of helical objects, similarly to active matters like bacteria and mesenchymal cells. Numerically computed heat transfer simulations and multi-nodes acoustic techniques hint towards the end, at a qualitative reasoning for the origin of particles' enhanced-aggregation phenomenon that requires further proofs in view of acoustic streaming [282, 283].

Indeed, if the postulated heating mechanism is confirmed, then any optically absorbing materials set under an ultrasonic wave field without the creation of thermal boundary layer could be transformed into a local in-plane particles trap, during illumination with an adequate wavelength. This constitutes thereby a contactless way to selectively manipulate objects in suspension, in addition to the initial idea of this chapter, which is to elaborate a proof-of-concept for the separation of chiral moieties based on their respective migration speed.

Chapter 5

Conclusions et perspectives

5.1 Conclusions

General understanding and characterizations of helical objects constituted a major part of this body of work, towards obtaining chiroptically active materials in the visible range with semiconductor CdSe NPLs. The underlining correlation between their surface functionalization with adsorbed molecules and the modification of their crystal lattices, documented a shape-transitioning effect on these atomically thin nanosheets. Their rich capacity to host a panel of chiral functional ligands has been harvested, for an efficient electronic coupling of transition states between these chromophores. One of the goals was to extend the current availability of chiroptically active materials onto II-VI semiconductors in view of their large tunable spectral range.

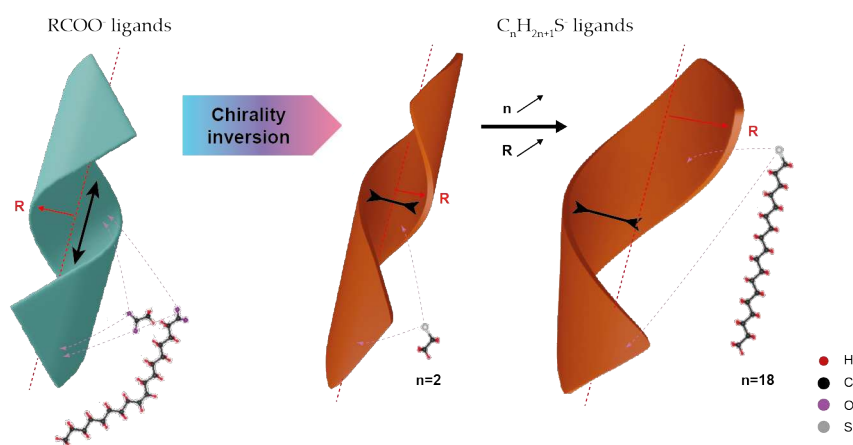


FIGURE 5.1: Tuning the handedness and helices radii of CdSe NPLs via modifications of surface chemistry. The above cartoon illustrates the chirality inversion of a piece of carboxylates-capped right-handed helix into a left-handed one, when the surface ligands are substituted by linear alkanethiolates with varying chain lengths.

In **Chapter 2**, the curling of NPLs has been tuned by righteously choosing the length of organic ligands grafted onto the surface of these inorganic nanoparticles, via a specific anchoring group (Fig. 5.1). This approach relied on the mismatch between the inorganic crystal lattice and layer of anchoring atoms, in addition to the steric repulsion brought by their aliphatic chains. Quantitative mechanical analysis captured these three components as separate acting contributions in a three-layers misfit strain model, valid for homo- and hetero-structured CdSe-CdS NPLs with varying thicknesses. As assumed strong in-plane deformations ($\sim 20\%$) of each inorganic stacking layer resulted in the internal energy minimization of residually stressed bodies into an optimal helical configuration, while

considering a layer of packed organic chains in lateral compression close to 1 GPa. This method well depicted the physical conditions for the formation of nanohelices and in predicting their associated radii.

Despite the important surface stress induced by thiolate headgroups, the average in-plane lattice parameter of CdSe nanohelices remained however, equal to that of zinc blende bulk. XRD studies revealed the significant role of specific orientations when it comes to investigating anisotropic distorted objects. In which case under anisotropic scattering, certain contributions can be either unscreened or broadened due to the object's alignment with the incident beam and the local dispersion of discrete distances between paired atoms. As helices' radii increase with a surface passivation by longer and sterically occupying ligands, their XRD pattern smoothens out since the presence of distortions due to high surface curvature is less prominent compared to helices with smaller radii.

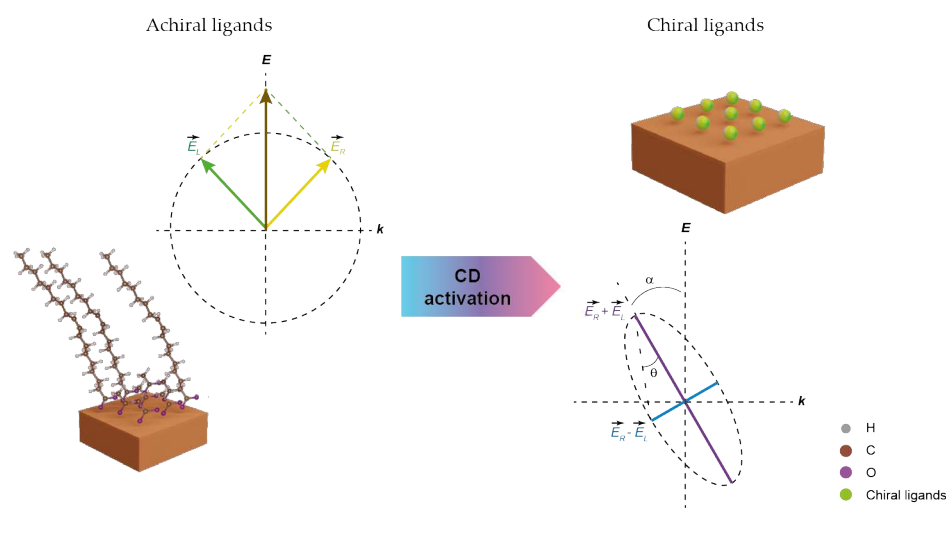


FIGURE 5.2: Synthesizing chiroptically active CdSe NPLs in absorption via alterations of surface functionalization. The above cartoon depicts the rotation of the circularly polarized components' major axis due to a difference in refractive indices of a chiral absorbing medium, which gives rise to measured CD signals.

In **Chapter 3**, numerous strategies were implemented to synthesize CdSe NPLs that exhibited circular dichroism properties (Fig. 5.2). The most promising route, consisted in exchanging their native surface achiral carboxylates by chiral compounds such as tartaric acid, gave rise to dissymmetry values in the order of 10^{-3} . This factor was demonstrated to increase with the number of stereocenters and the reducing distance between the considered chromophores. Chiral molecules presenting carboxylate anchoring group rather than thiolate, was found to yield greater g-factor values upon coupled onto CdSe NPLs, by comparing the scenarios between *L*-tartaric acid, *L*-dithiothreitol and *L*-cysteine. This was hypothesized to be related to their respective HOMO band alignment during hybridization with the hole level of CdSe.

Post-modified chiral zinc blende NPLs displayed absorptive-like CD signals in contrary to conventional QDs and wurtzite cadmium-based materials. For a given surface chemistry of NPLs with various thicknesses, a progressive shift of the CD line shape towards greater wavelengths corresponding exactly to their respective excitonic transitions was recorded. This resulted in a slight increase of g-factor values with the thickness of inorganic core and a

decrease of its energy gap. Seemingly, this observation was attributed to an increase in resonance for an electronic coupling between CdSe and the presence of chiral surface ligands.

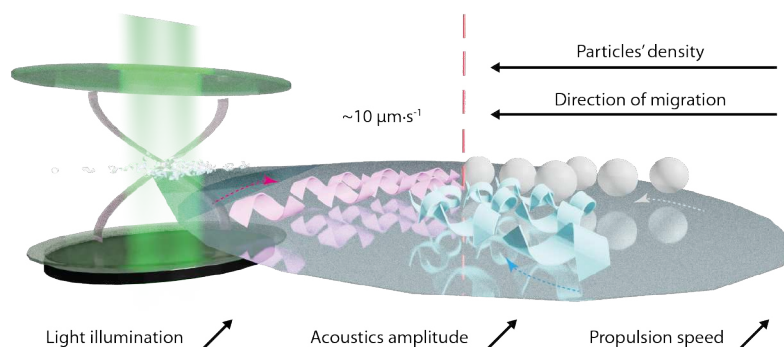


FIGURE 5.3: Manipulating fluorescently labeled silica objects under simultaneous opto- and acousto-perturbations. The above cartoon displays the enhanced-aggregation phenomenon of particles in a cavity's mid-plane, at an average in-plane velocity that increases with both the magnitude of light and acoustic excitations.

In **Chapter 4**, an alternative approach of fabricating helical structures with finely controlled handedness was introduced, that benefited strongly from the self-assembly of gemini surfactants complexed with chiral counterions like malic acids. Among three studied systems, silica helices functionalized with gold nanoparticles in particular, showed increasing CD responses in their plasmon resonance region with the strength of the interparticle plasmonic coupling, in agreement with simulations performed under discrete dipole approximation. Experimentally, this was achieved by modifying the grafting density of pre-prepared gold seeds before an in-situ growth, to underline the significant effect of interparticle distancing.

The other captivating route, where fluorescently marked chiral silica helices were subjected to experiments in acoustic levitation, displayed distinct migration behaviors between objects of opposite handedness tracked under dark-field microscope (Fig. 5.3). Depending on the chosen opto-acousto working conditions, a faster migration of an either population of left- or right-handed helices can be promoted. This enhanced-aggregation phenomenon occurring under an optimal light excitation, was evidenced to depend as well on the concentration and nature of suspended particles. Numerical heat transfer simulations and multi-nodes acoustic recordings hinted towards the end, at a qualitative reasoning for the origin of this observation which might require further proofs in view of acoustic streaming.

5.2 Perspectives

The formation of cadmium chalcogenide nanohelices has been elucidated due to the adsorption of surface ligands and resulting stress contributions, leading toward an energy-favored configuration. This yielded a quasi-racemic system composed of chiral helices from both handedness. Efforts have been dedicated into synthesizing either population of enantiomers rather than a mix of both, via addition of chiral chemical compounds during their two-dimensional lateral growth. Two principal struggles were: (i) the preservation of an atomically scaled quantum well structure with defined morphologies and (ii) the meticulous choice of a suitable chiral compound capable of driving an enantio-selective

synthesis of CdSe NPLs.

In the first point, it is noticed that an average steric hindrance brought by the carboxylate aliphatic chains is necessary for the growth of two-dimensional objects with well defined borders and edges. Despite single introduced chains alone like octanoates were able to yield NPLs, it appears that a dynamic mix of acetates and oleates better preserves their uniformity. After several attempts, it is also found that a combination of hexanoic and ibuprofene acid molecules gave rise to NPLs possessing irregular cloud-like shapes. To some extent during lateral extensions of small-sized objects, it occurs that certain edges can result into finger-like projections that we primarily, relate to a mechanical instability phenomenon. Due to the important tensile strain exerted by the carboxylate anchoring groups onto CdSe crystal lattices, this might generate starting points of local defects that could over time during synthesis, be amplified into breaking an object's symmetry in a periodic manner. Thus, a slight addition of halogenides for instance, that will in part help reducing the lattice mismatch could be imagined to promote the lateral growth of NPLs, as was demonstrated in the case of their axial growth favored by chlorides.

The second listed point can in fact be understood as a way to induce a preferential growth along a certain facet, of a strain-induced crystal. Essentially, chosen chiral ligands were sterically occupying and comparable to that of long aliphatic chains like oleic acids, in hope that these latter would passivate in majority the top and bottom wide facets of a NPL. The side narrow facets that were either more exposed or capped by shorter achiral ligands, would then grow under a strain-induced environment brought by the adsorption of chiral molecules, mainly on the basal planes of a NPL. This assumed strongly that the order of magnitude of induced mechanical strain onto crystal lattices would be sufficient to overwrite its crystallization under standard thermodynamic conditions. Further experimental and theoretical confirmations would be much required to justify claims made in such studies.

Chiroptical properties in absorption were demonstrated in CdSe NPLs via an efficient coupling of these latter to chiral functional surface ligands. This owed greatly to a righteous choice of molecule, in regard of a favorable hybridization through its anchoring group and the description of chiral stereocenters. Two interesting points were underlined, where: (i) an additional splitting of the e-hh corresponding CD peak with the shape of CdSe NPLs and (ii) a dependence of CD line shapes on the surface coverage of exchanged chiral ligands. Since the symmetry of selenium 4p orbital of the hh band revolved around $p_{(x,y)}$ in contrary to the $p_{(x,y,z)}$ experienced by the lh and so bands, it seemed curious that this might give rise to a curvature-dependent phenomenon that affected only the e-hh excitonic transition. Experimentally, a prominent trend of intensified peak splitting has been noticed, going from the tiniest flat square-shaped CdSe NPLs to the rectangular, twisted and finally, the helical ones. It would be interesting to estimate for each geometry, how the neighboring dipoles are coupled to one another and indeed, if it correlates to a sort of local curvatures and degrees of deformation in inorganic crystal lattices. As the induced CD line shapes were highly sensitive to the excitonic transition wavelength, it would be reasonable to follow the kinetic evolution of these CD signals during ligand exchanges, to shed light onto their bisignated pattern and indeed, if a shape-transitioning effect were in play.

As proof-of-concept to a crystal sorting method, distinct average in-plane migration speeds between separate chiral objects were shown. This varied mainly as a function of the acoustics and optical working conditions, while the effect of particles' shape and concentration in solution revealed self-organizing behaviors similarly to certain biological systems.

With these information in hand, it would be intriguing to build actual opto-acoustofluidic devices. One of the challenges relies on the design optimization of such microcavities with respect to an optimal separation time, at a given input shear flow. In terms of chemical point of view, it was possible to fluorescently label hybrid surfactant-silica helices with two different markers like fluorescein and rhodamine for instance. This can then help to differentiate the two enantiomers from one another post-separation with the use of a spectrophotometer, since they would absorb and emit light at distinct wavelengths: 490 and 520 nm for fluorescein, while in the case of rhodamine, 540 and 570 nm. Via this approach, aliquots could be collected at the outlets of a microchannel and subsequently analyzed, based on their retention and flow time.

Appendix A

Publications and communications

Publications

Surface modification of CdE (E: S, Se and Te) nanoplatelets to reach thicker nanoplatelets and homostructures with confinement-induced intraparticle type I energy level alignment

Nicolas Moghaddam, Corentin Dabard, Marion Dufour, Hong Po, Xiangzhen Xu, Thomas Pons, Emmanuel Lhuillier and Sandrine Ithurria

Journal of the American Chemical Society **2021** 143, 1863–1872

Optimized cation exchange for mercury chalcogenide 2D nanoplatelets and its application for alloys

Corentin Dabard, Josep Planelles, Hong Po, Eva Izquierdo, Lina Makke, Charlie Gréboval, Nicolas Moghaddam, Adrien Khalili, Tung Huu Dang, Audrey Chu, Stefano Pierini, Claire Abadie, Mariarosa Cavallo, Erwan Bossavit, Xiang Zhen Xu, Philippe Hollander, Mathieu Silly, Emmanuel Lhuillier, Juan I. Climente and Sandrine Ithurria

Chemistry of Materials **2021** 33, 9252–9261

Chiral helices formation by self-assembled molecules on semiconductor flexible substrates

Hong Po, Corentin Dabard, Benoit Roman, Etienne Reyssat, José Bico, Benoit Baptiste, Emmanuel Lhuillier and Sandrine Ithurria

ACS Nano **2022** 16, 2901–2909

Double-crowned 2D semiconductor nanoplatelets with bicolor power-tunable emission

Corentin Dabard, Victor Guilloux, Charlie Gréboval, Hong Po, Lina Makke, Ningyuan Fu, Xiang Zhen Xu, Mathieu G. Silly, Gilles Patriarche, Emmanuel Lhuillier, Thierry Barisien, Juan I. Climente, Benjamin T. Diroll and Sandrine Ithurria

Nature Communications **2022** 13, 5094

2D II–VI semiconductor nanoplatelets: from material synthesis to optoelectronic integration

Benjamin T. Diroll, Burak Guzelturk, Hong Po, Corentin Dabard, Ningyuan Fu, Lina Makke, Emmanuel Lhuillier and Sandrine Ithurria

Chemical Reviews **2023** 123, 3543–3624

Communications

- ESPCI Paris PC Focus Day 2020 on science vulgarization
- Bad Honnef Physics School 2021 on exciting nanostructures: characterizing advanced confined systems
- nanoGe Spring Meeting 2022 on semiconductor nanocrystals basic science (synthesis, spectroscopy, electronic structure, device and application)
- Doctoral School (ED 397) Days 2022
- Workshop on colloidal nanocrystals 2023
- Materials Research Society Spring Meeting 2023 on advanced manufacturing of 2D materials at the atomic scale

Prizes

- Poster award at Bad Honnef Physics School 2021

Appendix B

Materials and Methods

Chemicals and precursors

Purchased products

Octadecene (ODE) (Sigma-Aldrich, 90 %), cadmium acetate dihydrate ($\text{Cd}(\text{Ac})_2 \cdot 2\text{H}_2\text{O}$) (Sigma-Aldrich, 99.995 %), cadmium oxide (CdO) (Strem Chemicals, 99.99 %), myristic acid (Sigma-Aldrich, 99 %), selenium powder (Se) (Strem Chemicals, 99.99 %), sulfur powder (S) (Sigma-Aldrich, 99.99 %), oleic acid (Sigma-Aldrich, 90 %), acetic acid (Sigma-Aldrich, 99.8 %), ethanethiol (Fluka, >98 %), butanethiol (Aldrich-Chemistry, 99 %), octanethiol (Fluka, >97 %), dodecanethiol (Aldrich-Chemistry, >98 %), octadecanethiol (Aldrich-Chemistry, 98 %), tributylphosphine (TBP) (Sigma-Aldrich, 97 %), trioctylphosphine (TOP) (Alfa Aesar, 90 %), cadmium chloride hydrate ($\text{CdCl}_2 \cdot x\text{H}_2\text{O}$) (Sigma-Aldrich, 99.995 %), cadmium bromide tetrahydrate ($\text{CdBr}_2 \cdot 4\text{H}_2\text{O}$) (Sigma-Aldrich, 98 %), cadmium iodide (CdI_2) (Sigma-Aldrich, 99 %), sodium tetrahydroborate (NaBH_4) (Sigma-Aldrich, 99 %), sodium sulfide nonahydrate ($\text{Na}_2\text{S} \cdot 9\text{H}_2\text{O}$) (Aldrich-Chemistry, 99.99 %), toluene (VWR, 99.5 %), *n*-hexane (VWR, 99 %), ethanol (VWR, 96 %), methanol (VWR, 99.8 %), *N*-methylformamide (NMF) (Thermo Scientific, 99 %), acetonitrile (VWR, 99.95 %), diethyl ether (VWR, 99 %), ethyl acetate (VWR, 99 %), chloroform (VWR, 99 %), acetone (VWR, 99 %), tetrahydrofuran (THF) (VWR, 99 %), *N,N,N',N'*-tetramethyl ethylenediamine (Sigma-Aldrich, 99.5 %), 1-bromooctadecane (Sigma-Aldrich, 98 %), *D*-(+)-malic acid (Sigma-Aldrich, 97 %), *L*-(-)-malic acid (Sigma-Aldrich, 99 %), *DL*-malic acid (Sigma-Aldrich, 99 %), *D*-(+)-tartaric acid (Sigma-Aldrich, 99 %), *L*-(-)-tartaric acid (Sigma-Aldrich, 99.5 %), silver carbonate (Ag_2CO_3) (Sigma-Aldrich, 99 %), ammonia solution (Sigma-Aldrich, 32 %), tetraethyl orthosilicate (TEOS) (Sigma-Aldrich, 99 %), 3-aminopropyl triethoxysilane (APTES) (Sigma-Aldrich, 97 %), 3-mercaptopropyl trimethoxysilane (MPTMS) (Sigma-Aldrich, 95 %), fluorescein isothiocyanate (FITC) (Sigma-Aldrich, 90 %), rhodamine B (Sigma-Aldrich, 90 %), polyvinyl pyrrolidone K15 (PVP) (Sigma-Aldrich), formaldehyde methanol solution (Sigma-Aldrich, 37 wt.%), hydrogen tetrachloroaurate trihydrate ($\text{HAuCl}_4 \cdot 3\text{H}_2\text{O}$) (Sigma-Aldrich, 99.9 %), potassium carbonate (K_2CO_3) (Sigma-Aldrich, 99 %) and trisodium citrate dihydrate (Sigma-Aldrich, 99 %) were used as received.

Synthesized compounds

Cadmium carboxylate ($\text{Cd}(\text{OOCR})_2$)

Similarly to the report of Moreels and co-workers by using a three-neck flask, 2.56 g (20 mmol) of CdO and 11 g (50 mmol) of carboxylic acid are mixed and degazed at 70 °C during 30 min [284]. Next, the heating temperature is increased to 200 °C for 20 min, under argon flow until the solution turns colorless. At the end during cooling, 30 mL of methanol are added to solubilize the excess of myristic acid at 60 °C. The final product is precipitated

with methanol and the washing process is repeated three times before being left to dry under vacuum at 70 °C overnight.

Cadmium dithiolate (Cd(SR)₂)

In a centrifuge tube, 1.83 g (10 mmol) of CdCl₂·xH₂O is dissolved in a 30 mL solution consisting of an equal volume mix of Milli-Q H₂O and ethanol. Approximately 10 mL of ammonia solution is added dropwise under constant stirring until the solution turns colorless. For each linear carbon chain ($n = 2, 4, 8, 12, 18$), 20 mmol of thiol solutions is introduced dropwise with the formation of white precipitates. At the end of addition, the mixture is stirred for 2 h before being washed twice with an equal amount of Milli-Q H₂O and ethanol. The final product is dried under vacuum at 70 °C overnight.

Trioctylphosphine selenide at 1 M (TOPSe)

In a glovebox, 20 mL of trioctylphosphine and 1.58 g (20 mmol) of selenium powder are stirred overnight until a colorless solution is obtained. This final product is later stored in the glovebox to prevent oxidation.

Bi(stearoyl) selenide (Se(OCC₁₇)₂)

Adapted from the report of Norris and co-workers in a 50 mL flask, 0.076 g (2 mmol) of LiAlH₄ are added into a mixture of 0.192 g (2.4 mmol) of elemental selenium and 20 mL of dry THF cooled to -10 °C under argon flow [42, 285]. The mixture is stirred for 30 min to form the aluminium hydride hydrogen selenide compound (LiAlHSeH), which presents itself as a greyish dispersion to be further reacted with carboxylic acid chlorides without purification. After 30 min, 0.68 mL (2 mmol) of stearoyl chloride are added into the mixture over the course of 2 min and again left under stirring. This addition of stearoyl chloride is repeated for another three times at the 60, 90 and 120 min marks. Finally after 150 min of reaction time, 5 mL of distilled water are added to quench the unreacted reagents. The organic reaction mixture is then diluted with 25 mL of diethyl ether after removing the ice bath and washed five times with 20 mL of brine solution at a mass concentration of 25 %. The final organic phase is collected and heated to 50 °C to form a clear brownish solution, before being left to crystallize overnight. The crystals are later filtered and dried at 30 °C under vacuum overnight.

Sulfide octadecene at 0.1 M (SODE)

In a three-neck flask, 100 mL of ODE is degassed at 70 °C during 30 min. Later under argon, 480 mg (15 mmol) of sulfur powder is added and the mixture is heated at 140 °C up to a point where it turns slightly yellowish and clear. This solution is then cooled and stored at room temperature.

Gemini surfactants (18-2-18:bromide)

Adapted from the report of Huc and co-workers, a two-steps method is employed to yield *m,m*-dimeric surfactants, where *m* is the carbon number of alkyl chains that is to be introduced onto the initial diamine [286]. 15 mL of diamine compound (0.1 mol) are placed in a three-neck flask, into which 27 mL of 1-bromooctadecane (0.08 mol) and 50 mL of acetonitrile are added. The mixture is then kept at 40 °C during 3 days, after which the solvent is evaporated. 50 mL of diethyl ether are added and the medium is left to crystallize overnight, before filtering and drying under vacuum. A quarter of the previously obtained compound

(20 mmol) are again placed in a three-neck flask, into which 27 mL of 1-bromooctadecane (80 mmol) and 50 mL of ethyl acetate are introduced. The mixture is heated under reflux for 2 days, after which the solvent is again evaporated. A chloroform-acetone mix in the volume ratio of 1:1 is introduced for crystallization. The final product, so called *18-2-18*:bromide, is later filtered and dried under vacuum.

Complexation with chiral acids (*18-2-18*:malate/tartrate)

Adapted from the work of Oda and co-workers, 5 mmol of malic (resp. tartaric acid) and 1.38 g of silver carbonate (5 mmol) are placed in a three-neck flask, into which 7 mL of methanol are introduced. The mixture is then stirred under vacuum for 1 hour, before heated to 45 °C. A *18-2-18*:bromide solution pre-prepared by weighing 2.25 g of dried precursor and dissolving them in 10 mL of hot methanol, is swiftly injected into the reaction medium. The mixture is then kept at 45 °C for 30 min, before filtering to obtain a colorless solution. The solvent is later evaporated, before adding in a chloroform-methanol mix in the volume ratio of 9:1 for crystallization. The final product, so called *18-2-18*:malate (resp. *18-2-18*:tartrate), is filtered and dried under vacuum.

Gold seeds measuring ~4 nm

90 mL of an aqueous solution of hydrogen tetrachloroaurate is prepared at 0.27 mM with Milli-Q purified water. Into which are added 2 mL of an aqueous solution of sodium citrate at 1 wt.%. The mixture is stirred for 1 min before the addition of 0.075 wt.% NaBH₄ dissolved in 1 mL of the formerly prepared sodium citrate aqueous solution at 1 wt.%. The medium stays continuously under stirring for another 5 min before being stored at 4 °C. The solution appears ruby red in the end.

Gold plating solution at 20 mM

Adapted from the work of Goharshadi and co-workers, 50 mg (0.36 mmol) of K₂CO₃ are dissolved in 197 mL of Milli-Q aqueous solution under vigorous stirring [235]. Then, 3.75 mL of an aqueous solution of hydrogen tetrachloroaurate prepared at 20 mM with Milli-Q purified water are added dropwise. The mixture is stirred over the course of 30 min before being stored at 4 °C. The solution appears slight yellow in the end.

Synthesis of nanoparticles

Cadmium-based nanoplatelets

2 MLs CdSe

- Scrolls measuring ~(35 x 60) nm²

Adapted from the report of Vasiliev and co-workers, 0.16 mL of oleic acid and 260 mg (1 mmol) of cadmium acetate dihydrate are placed into a three-neck flask containing 20 mL of ODE, before being degazed at 70 °C for 30 min prior to the synthesis [59]. The reaction mixture is heated to 100 °C) under argon. Once the temperature is reached, 0.25 mL of TOPSe at 1 M diluted to 0.5 mL by ODE, are swiftly injected into the reaction mixture under vigorous stirring to initiate the particles' nucleation. Later, the reaction is left under stirring for 4 h for the particles' growth, forming an opalescent pale white solution. Finally, the reaction is quenched by rapid injection of 2 mL of oleic acid during cooling at 60 °C. CdSe nanoscrolls are precipitated by adding an equal volume of acetone and separated by centrifugation at 5000 rpm for 10 min. This washing step

is repeated twice and the pale white precipitate is redispersed in 10 mL of hexane for further growth into larger NPLs.

3 MLs CdSe

- Squares measuring $\sim(7 \times 10) \text{ nm}^2$
Adapted from the report of Cuniberti and co-workers, 68 mg (0.15 mmol) of cadmium decanoate, 46 mg (0.075 mmol) of bis(stearoyl)selenide, 107 mg (0.4 mmol) of cadmium acetate dihydrate and 15 mL of ODE are degazed in a three-neck flask for 1 h at room temperature [287]. Under argon, the system is heated to 150 °C and kept for 6 h for the NPL growth. Then, the flask is cooled to room temperature and the resulting NPLs are precipitated by adding isopropanol with subsequent centrifugation. The precipitate is dissolved in 3 mL of CHCl_3 and acetonitrile is added dropwise until the system becomes slightly turbid. The NPLs are precipitated by centrifugation while the QDs impurities remain in the supernatant. The washing procedure is repeated until the precipitate consists solely of 3 MLs NPLs.
- Polygons measuring $\sim(50 \times 95) \text{ nm}^2$
In a three-neck flask, 240 mg (0.9 mmol) of cadmium acetate dihydrate are weighed before adding in 15 mL of ODE and 0.15 mL of oleic acid. The mixture is degazed at 70 °C under vacuum for 30 min. The temperature of the mixture is then increased to 190 °C under argon. At 185 °C, 0.14 mL (0.14 mmol) of TOPSe at 1 M are swiftly injected and the reactive medium is left under stirring for 10 min. At the end of the reaction during cooling to room temperature, 1 mL of oleic acid are added. The NPLs are precipitated with ethanol and suspended in 10 mL of hexane.
- Twists measuring $\sim(11 \times 122) \text{ nm}^2$
In a three-neck flask, 240 mg (0.9 mmol) of cadmium acetate dihydrate are weighed before adding in 15 mL of ODE and 0.45 mL of oleic acid. The mixture is degazed at 70 °C under vacuum for 30 min. The temperature of the mixture is then increased to 190 °C under argon. At 185 °C, 0.14 mL (0.14 mmol) of TOPSe at 1 M are swiftly injected and the reactive medium is left under stirring for 10 min. At the end of the reaction during cooling to room temperature, 1 mL of oleic acid are added. The NPLs are precipitated with ethanol and suspended in 10 mL of hexane.
- Helices measuring $\sim(88 \times 302) \text{ nm}^2$
In a three-neck flask, 260 mg (1.1 mmol) of cadmium acetate dihydrate are introduced before adding in 10 mL of ODE and 0.25 mL of oleic acid. The mixture is heated at 70 °C under vacuum for 30 min. In a syringe, 0.6 mL (0.6 mmol) of TOPSe at 1 M diluted in 4.4 mL of ODE is prepared. Under argon, the heating temperature is then increased to 190 °C, and the selenium precursor is injected over the course of 40 min. The solution gets more tainted in yellow as time goes on. At the end of the injection, the heating mantle is removed to allow complete cooling of the reaction medium to room temperature. To precipitate the NPLs, equal amounts of ethanol and hexane are introduced during washing. At the end, the pellet of NPLs is suspended in 10 mL of hexane for further use.

4 MLs CdSe

- Squares measuring $\sim(14 \times 14) \text{ nm}^2$
Into a three-neck flask are introduced 24 mg (0.3 mmol) of Se powder and 340 mg (0.6 mmol) of $\text{Cd}(\text{Myr})_2$. 15 mL of ODE are then added before heating the mixture to 70 °C

under vacuum for 30 min. The temperature is later increased to 240 °C under argon and when the mixture turns orange around 200 °C, 200 mg (0.75 mmol) of cadmium acetate dihydrate are rapidly added. The reaction is continued under constant stirring during 10 min. At the end during cooling, 0.5 mL of oleic acid are added. Washing steps with ethanol and hexane are performed to separate synthesized NPLs from QDs. The pellet is redispersed in 10 mL of hexane.

- Rectangles measuring $\sim(7 \times 32) \text{ nm}^2$
Into a three-neck flask are introduced 24 mg (0.3 mmol) of Se powder and 340 mg (0.6 mmol) of Cd(Myristate)₂. 15 mL of ODE are then added before heating the mixture to 70 °C under vacuum for 30 min. The temperature is later increased to 240 °C under argon and when the mixture turns orange around 200 °C, 110 mg (0.5 mmol) of cadmium acetate anhydrous are rapidly added. The reaction is continued under constant stirring during 10 min. At the end during cooling, 0.5 mL of oleic acid are added. Similar washing steps with ethanol and hexane are used to separate synthesized NPLs from QDs. The pellet is redispersed in 10 mL of hexane for further growth into larger NPLs.
- Needles measuring $\sim(6 \times 45) \text{ nm}^2$
Into a three-neck flask are introduced 24 mg (0.3 mmol) of Se powder and 340 mg (0.6 mmol) of Cd(Myristate)₂. 15 mL of ODE are then added before heating the mixture to 70 °C under vacuum for 30 min. The temperature is later increased to 240 °C under argon and when the temperature reaches 180 °C, 110 mg (0.5 mmol) of cadmium acetate anhydrous are rapidly added. The reaction is continued under constant stirring during 10 min. At the end during cooling, 0.5 mL of oleic acid are added. Similar washing steps with ethanol and hexane are used to separate synthesized NPLs from QDs. The pellet is redispersed in 10 mL of hexane for further growth into larger NPLs.

Lateral growth towards NPLs with large dimensions

In a three-neck flask, cadmium acetate dihydrate are introduced to increase the surface area of the initial NPLs. 10 % of previously synthesized small CdSe NPLs can be precipitated in a mixture of ethanol and hexane, then being suspended in 6 mL of ODE. This latter is added into the flask, in addition to 0.3 mL of oleic acid and heated at 70 °C under vacuum for 15 min. A growth solution consisting of TOPSe at 1 M diluted in ODE is prepared in a syringe. The heating temperature is then increased to 150 (resp. 235 °C) under argon in the case of 2 (resp. 4 MLs) NPLs, at which the injection of growth solution begins over the course of 40 min. The solution turns turbid as time goes on, which actually indicates light diffusion by large particles. After cooling, equal amounts of ethanol and hexane are used during purification and the pellet is redispersed in 10 mL of hexane. The quantity of cadmium and selenium precursors used are calculated as a proportional increase in terms of lateral size of the initial particles.

Growth by c-ALD towards thicker 5, 6 and 7 MLs CdSe

Adapted from the work of Talapin and co-workers, the precursors of selenium are prepared by reducing their mesh form in a solution of NMF and ethanol in the presence of NaBH₄ [57]. To grow 5 MLs CdSe NPLs for instance, 10 % of as-synthesized 3 MLs CdSe NPLs are taken as starting materials. The introduction of selenium ions onto the surface of existing NPLs in the presence of TBP induces their precipitation in hexane. This latter is then resuspended in NMF and washed in toluene before the surface addition of cadmium precursors. These NPLs are finally annealed in the presence of 25 mg (0.1 mmol) of cadmium acetate dihydrate, 35 μL of oleic acid, 45 μL of TBP and 4 mL of ODE at 235 °C. At the end of the reaction, the

particles are purified in a mixture of ethanol and hexane, before being suspended in 10 mL of hexane. Essentially, this method enables the growth of particles along their thickness direction without modifying much their lateral size.

Growth by c-ALD towards CdSe/CdS core-shell NPLs

10 % of as-synthesized 3 MLs CdSe NPLs suspended in hexane are withdrawn and the precursors of sulfur are added. The addition of Na₂S dissolved in a solution of NMF and ethanol induces the transfer of nanoparticles into the polar solvent. These NPLs are then washed and resuspended in NMF. The layer of cadmium atoms is grown through the addition of cadmium acetate dihydrate, before transferring them back to the apolar solvent by adding oleic acid. These steps could be repeated a certain amount of time to grow thicker CdS shells onto existing CdSe core structures.

4 MLs CdS

In a three-neck flask, 240 mg (0.9 mmol) of cadmium acetate dihydrate are placed before adding in 10 mL of ODE and 0.2 mL of oleic acid. The mixture is degazed at 70 °C under vacuum for 15 min. The heating temperature is then increased to 210 °C under argon, at which the injection of 6 mL (0.6 mmol) of SODE at 0.1 M occurs over the course of 4 h. At the end of the injection, heating is removed to enable complete cooling of the reaction medium down to room temperature, before washing the nanoparticles in a mixture of ethanol and hexane. The pellet is redispersed in 10 mL of hexane.

Silica particles

Spherical beads

Adapted from the work of Giorgis and co-workers, two solutions are prepared where one contains a mixture of ammonia–water in a molar ratio of 0.46:2.89 and the other contains a mixture of ethanol-TEOS in a molar ratio of 2.15:0.05 [269]. These two solutions are rapidly mixed together in a thermostatically controlled water bath around 30 °C. After 180 min, the resulting spheres are washed three times with ethanol before being left to dry under vacuum overnight.

Self-assembly of surfactants and silica wall coating

Adapted from the report of Oda and co-workers, 7.2 mg of 18-2-18:malate are placed in a glass vial, into which 10 mL of distilled water are introduced [97]. The mixture is first kept in an incubator at 60 °C for 20 min, before being transferred to another incubator at 20 °C for 3 days. A 50 mL aqueous solution of respective malic acid enantiomer is prepared at a concentration of 0.1 mM, into which 2.5 mL of TEOS are introduced. This latter is then left under mixing overnight. At the end of the surfactants' incubation period, 10 mL of hydrolyzed silicate solution are added into the glass vial and continued to be kept at 20 °C overnight. The reaction medium is then washed once with methanol under centrifugation at 15000 rpm during 10 min and twice with ethanol, before resuspending the final precipitate in 10 mL of ethanol.

Surface chemistry modification of silica helices

Into previously purified 18-2-18:malate silica helices solution in ethanol, 20 μL of MPTMS (resp. APTES) are added. The mixture is then sonicated for 10 min and kept at 70 °C

overnight, before washing with ethanol under centrifugation at 15000 rpm during 10 min. This surface modification step is once again repeated overnight, before washing the reaction medium twice with toluene (resp. ethanol). The final product is resuspended in 10 mL of toluene (resp. ethanol).

Grafting of NPLs onto mercapto-modified silica helices

Into 1 mL of former purified and mercapto-modified 18-2-18:malate silica helices solution in toluene, 20 μ L of as-synthesized 4 MLs CdSe NPLs solution in hexane of various shapes are introduced. The mixture is sonicated for 10 min and kept at 3 μ C for 3 days. This latter is then washed twice with toluene under centrifugation at 6000 rpm during 10 min, until absorption signals are no longer detected in the supernatant related to the presence of free NPLs. The final compound is resuspended in 1 mL of toluene.

Grafting of gold seeds onto amino-modified silica helices

Into 1 mL of previously purified and amino-modified 18-2-18:malate silica helices solution in ethanol, a certain amount of gold seeds solution is introduced. The mixture is vigorously stirred at room temperature overnight. This latter is then washed three times with distilled water under centrifugation at 6000 rpm during 10 min, until absorption signals are no longer detected in the supernatant related to the presence of free gold seeds. The final compound is resuspended in 1 mL of distilled water.

In-situ growth of grafted gold nanoparticles

Into former purified 18-2-18:malate@Au seeds aqueous solution, a certain amount of gold plating and PVP solution, respectively pre-prepared at 20 and 1 mM is simultaneously introduced. The mixture is stirred at room temperature for 2 min before the addition of formaldehyde. This latter is then followed by absorption spectroscopy over the course of one full day. In the end, the particles are washed three times with ethanol under centrifugation at 6000 rpm during 10 min, before being redispersed in distilled water.

Fluorescent labeling of amino-modified silica helices

Into 1 mL of previously purified and amino-modified 18-2-18:malate silica helices solution in ethanol, 400 μ L of pre-prepared fluorescein isothiocyanate dye solution in ethanol at a concentration of 2.5 μ M are introduced. The mixture is left under vigorous stirring overnight at room temperature under dark conditions. This latter is then washed four times under centrifugation at 15000 rpm during 10 min, until absorption signals are no longer detected in the supernatant related to the presence of free dye molecules. The final sample is resuspended in 1 mL of ethanol.

Characterization techniques

Absorption spectroscopy

Absorption spectra are recorded at room temperature on a Cary-5000 spectrophotometer with a scanning speed of 600 nm \cdot min⁻¹. During measurements, small fractions are withdrawn from initial colloidal solutions of nanoparticles to be diluted to an optical density <3. Either glass test tubes or quartz cuvettes with a 1 cm optical path length are used.

Emission spectroscopy

Emission spectra are recorded at room temperature on a Edinburgh spectrophotometer illuminated by a Xenon lamp source. During measurements, small fractions are withdrawn from initial colloidal solutions of nanoparticles to be diluted to a count-per-second $<2 \cdot 10^4$ in order to avoid phenomenon of reabsorption. Quantum yield measurements are performed via an integrating sphere, consisting of a cavity with a high reflection rate. A first measurement of solvent emission alone is conducted to serve as the reference value. Subsequently, a second measurement is done on a solution containing the nanoparticles. Using the F900 application, the difference between the amount of absorbed and emitted photons by the sample is measured, thus enabling an evaluation of its quantum yield.

Fourier transform infrared spectroscopy

Data is recorded on a Bruker Vertex 70 spectrometer at room temperature, in a wavenumber range between $(400-4000) \text{ cm}^{-1}$. During measurements, concentrated nanoparticles colloidal solutions are drop-cast onto the detection zone and signals are recorded after solvent evaporation.

Nuclear magnetic resonance spectroscopy

Data is acquired with respect to hydrogen-1 and carbon-13 nuclei within the molecules of a substance, in order to determine the structure of its molecules. Deuterated chloroform is used as the solvent in all measurements at a working condition of 400 MHz. Raw data saved is then exported and treated with Bruker TopSpin application.

X-ray diffraction analysis

Signals from thin films of nanoparticles drop-cast on a (311)-cutted mono-crystalline silicon substrate are recorded on a Phillips X'Pert diffractometer with a $\text{Cu-K}\alpha$ radiation. Measurements are performed at a working condition of 40 kV in voltage and 40 mA in current. Scattering patterns are obtained under the θ - 2θ reflection mode, in a 2θ range between $(10-60)^\circ$ with a step size of 0.016° . Raw data saved under the format of XRDML is later treated with HighScore application.

Transmission electron microscope

Images are recorded on a JEOL 2010 transmission electron microscope at a working voltage of 200 kV. The data is later analyzed under *ImageJ* and information on their dimensions' distribution is obtained over a population of 50 samples at least.

Scanning electron microscope and energy dispersive X-ray analysis

Images are recorded on a Thermo Fisher Quattro environmental scanning electron microscope at a working condition of 15 kV in voltage and 50 pA in current. The data is later analyzed under *ImageJ* and information on their dimensions' distribution is obtained over a population of 50 samples at least. The energy-dispersive X-ray spectroscopy signals are obtained through an Oxford Instrument detector mounted onto the microscope.

Wide-field fluorescence microscope

Fluorescent images of 18-2-18:FITC silica helices are observed under Olympus IX-71 microscope equipped with a white lamp source, 100x numerical aperture, 1.45 objective, Quantem 512SC CCD camera and a filter cube adapted to the fluorescent probe (excitation: 475-35, dichroic: MD499, emission: 530-43).

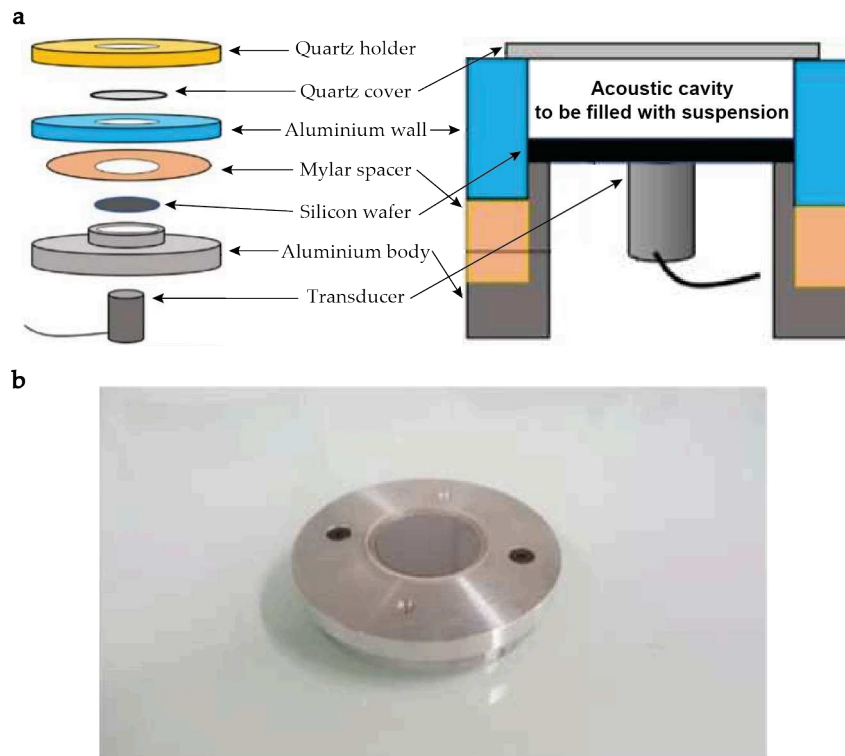


FIGURE B.1: (a) Dissected and side views of an acoustic resonator used to monitor the focusing dynamics of particles during opto-acousto experiments. The cylindrical cavity has a diameter of 25 mm and a thickness of 330 μm , resulting in a total volume of $\sim 200 \mu\text{L}$. (b) Photographed image of the acoustic resonator made of aluminium. The schematics are not drawn to scale. Adapted from [288].

Acoustic resonator

According to Aider and co-workers, a homebuilt aluminium circular cavity of diameter $D = 25 \text{ mm}$ and height $C = 330 \mu\text{m}$ is built as pictured in Appendix Fig. B.1 [136, 272]. Its bottom is made of a silica wafer, whose diameter equals 25 mm and possesses a thickness of 500 μm . On the other hand, its top part is enclosed by a round quartz plate, whose diameter is 30 mm and 1 mm thick. The removable cover plate is built in a way that it allows easy and practical changes of observed medium, which represents around 200 μL of solution. A 2 MHz piezoelectric transducer is then glued onto the silica wafer and powered by a wave generator. The sinusoidal signal frequency is tuned to maximize the ARF, which corresponds to the resonance condition: $\lambda_{ac} = 2h$. In practice, this is done through monitoring the reflected electric signal displayed by an oscilloscope and minimizing the amplitude of this latter. In most cases, the optimal frequency is located around 1.9 MHz with fluctuations in the order of several kHz.

Optical set-ups

The as-described acoustic cavity is placed on the moving stage of a fluorescence microscope (Olympus BX-2), where observations are made under objectives of different magnifications. The employed light source (CoolLED pE-300-W, Andover, UK) enables a fine control of the illumination wavelength in the visible region. The intensity of light excitation is simultaneously controlled by a probe (ThorLabs PM16-130) connected to the computer, possessing an optical power range from 5 pW to 500 mW. All recordings are made using a high resolution camera (PCO Panda 4.2bi) and are later post-treated under *ImageJ* for particles' tracking purposes.

Appendix C

Folding of nanoplatelets

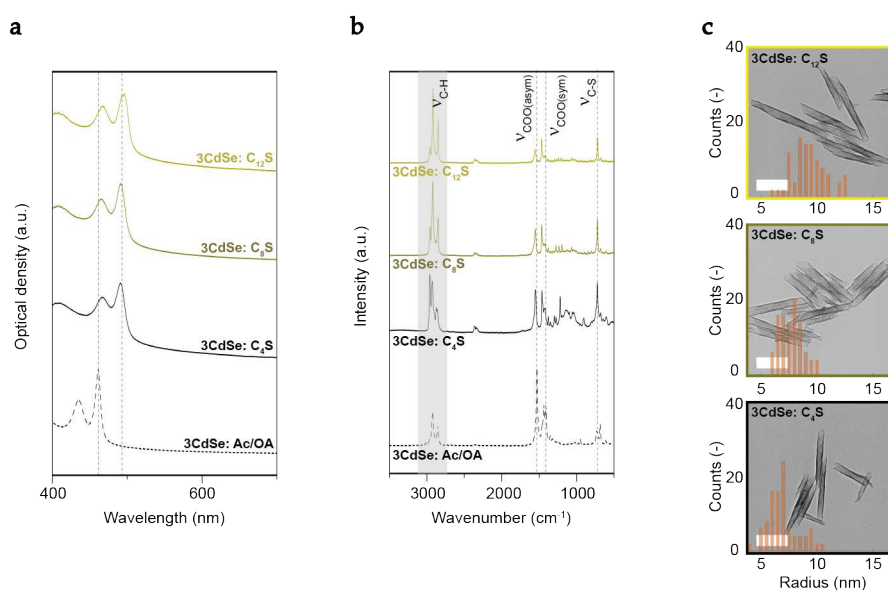


FIGURE C.1: (a) Absorption spectra of 3 MLs CdSe nanohelices before and after surface ligands modification, from initially acetates/oleates-capped to linear alkanethiolates-capped, where $n = 4, 8, 12$. Their corresponding FTIR spectra (resp. TEM images) are shown in (b) (resp. (c)). Scale bar: 200 nm.

3 MLs CdSe NPLs	Carboxylates-capped			Thiolates-capped				
	Number of planes	Atomic ratio in theory (%)	Result (%)	Number of planes	Atomic ratio in theory (%)	Result for C_4S (%)	Result for C_8S (%)	Result for $C_{12}S$ (%)
Cd	4	57.1	58.0 ± 2.0	4	44.4	43.5 ± 1.5	45.5 ± 2.5	43.5 ± 3.5
Se	3	42.9	42.0 ± 2.0	3	33.3	35.5 ± 3.5	31.5 ± 2.5	31.5 ± 2.5
S	-	-	-	2	22.3	21.0 ± 2.0	23.0 ± 1.0	25.0 ± 1.0

TABLE C.1: Theoretical and experimental atomic ratios of cadmium, selenium and sulfur for carboxylates- and thiolates-capped 3 MLs CdSe NPLs.

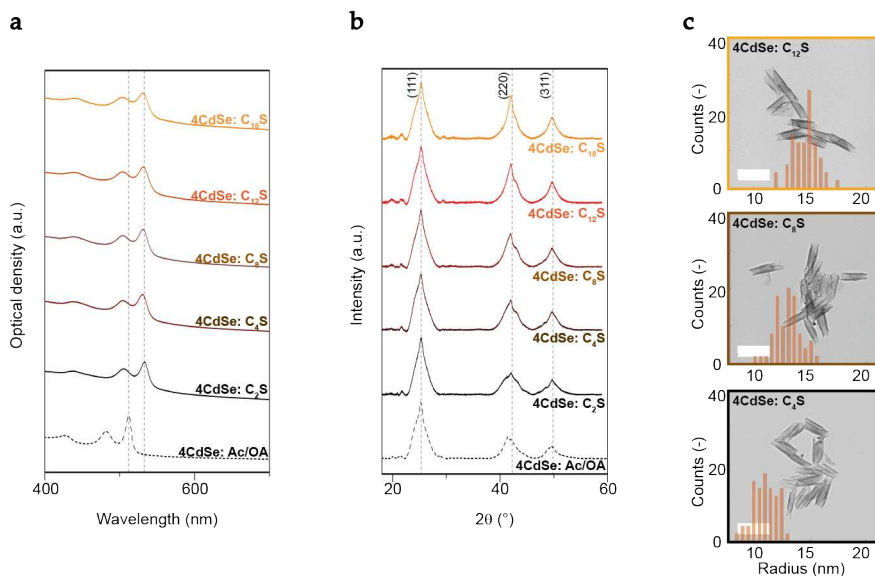


FIGURE C.2: (a) Absorption spectra of 4 MLs CdSe nanohelices before and after surface ligands modification, from initially acetates/oleates-capped to linear alkanethiolates-capped, where $n = 2, 4, 8, 12, 18$. Their corresponding X-ray diffractogrammes (resp. TEM images) are shown in (b) (resp. (c)). Scale bar: 200 nm.

4 MLs CdSe NPLs	Carboxylates-capped	Thiolates-capped				
	Result (%)	Result for C ₂ S (%)	Result for C ₄ S (%)	Result for C ₈ S (%)	Result for C ₁₂ S (%)	Result for C ₁₈ S (%)
Cd	52.5±1.5	46.5±2.5	42.5±1.5	44.5±2.0	44.0±3.0	49.5±2.0
Se	47.5±1.5	38.0±3.0	39.0±2.0	38.5±2.0	37.5±3.5	36.0±1.5
S	-	15.5±1.0	18.5±2.0	17.0±0.5	18.5±2.0	14.5±1.0

TABLE C.2: Theoretical and experimental atomic ratios of cadmium, selenium and sulfur for carboxylates- and thiolates-capped 4 MLs CdSe NPLs.

5 MLs CdSe NPLs	Carboxylates-capped	Thiolates-capped				
	Result (%)	Result for C ₂ S (%)	Result for C ₄ S (%)	Result for C ₈ S (%)	Result for C ₁₂ S (%)	Result for C ₁₈ S (%)
Cd	55.5±1.0	46.5±1.5	45.5±2.0	46.5±5.0	46.0±5.0	44.0±2.5
Se	44.5±1.0	40.0±5.5	41.0±2.0	38.0±4.5	37.5±4.0	40.5±2.5
S	-	13.5±5.0	13.5±1.5	15.5±1.0	16.5±1.5	15.5±1.0

TABLE C.3: Theoretical and experimental atomic ratios of cadmium, selenium and sulfur for carboxylates- and thiolates-capped 5 MLs CdSe NPLs.

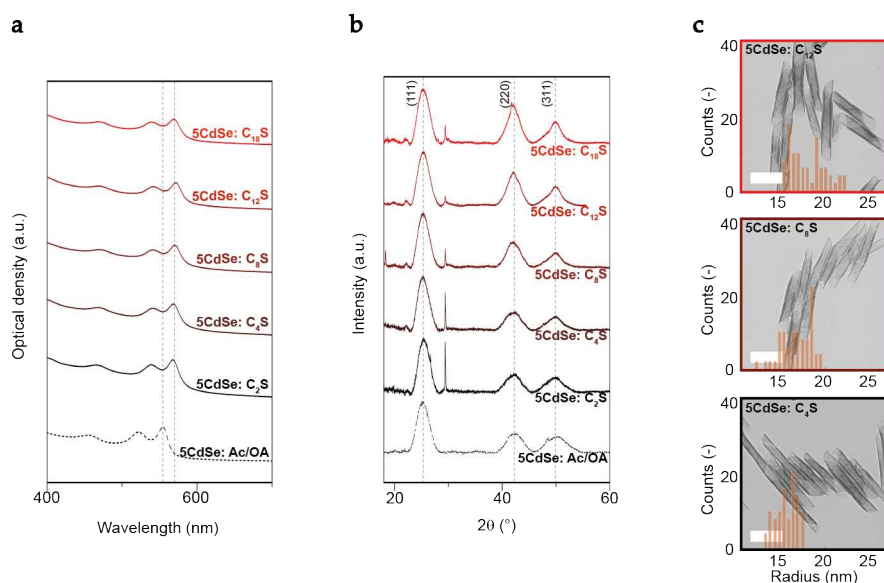


FIGURE C.3: (a) Absorption spectra of 5 MLs CdSe nanohelices before and after surface ligands modification, from initially acetates/oleates-capped to linear alkanethiolates-capped, where $n = 2, 4, 8, 12, 18$. Their corresponding X-ray diffractogrammes (resp. TEM images) are shown in (b) (resp. (c)). Scale bar: 200 nm.

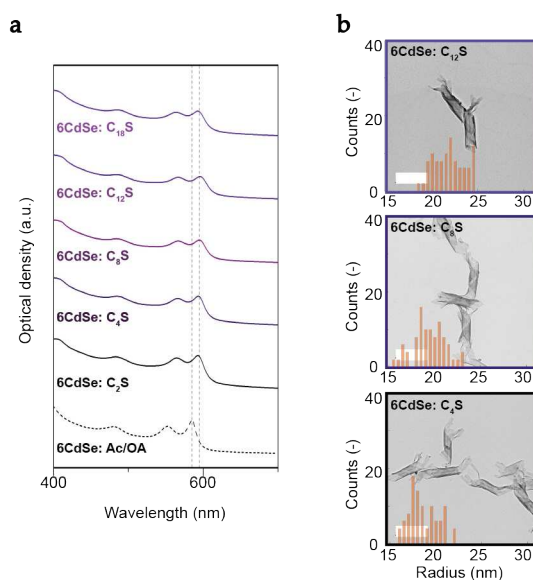


FIGURE C.4: (a) Absorption spectra of 6 MLs CdSe nanohelices before and after surface ligands modification, from initially acetates/oleates-capped to linear alkanethiolates-capped, where $n = 2, 4, 8, 12, 18$. Their corresponding TEM images are shown in (b). Scale bar: 200 nm.

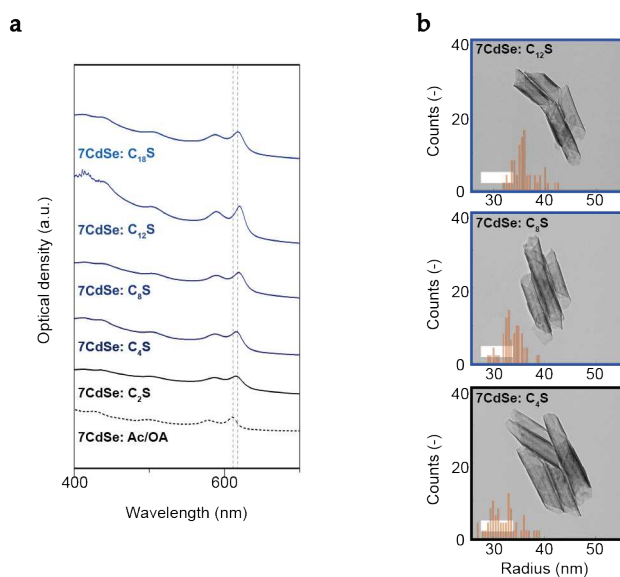


FIGURE C.5: (a) Absorption spectra of 7 MLs CdSe nanohelices before and after surface ligands modification, from initially acetates/oleates-capped to linear alkanethiolates-capped, where $n = 2, 4, 8, 12, 18$. Their corresponding TEM images are shown in (b). Scale bar: 200 nm.

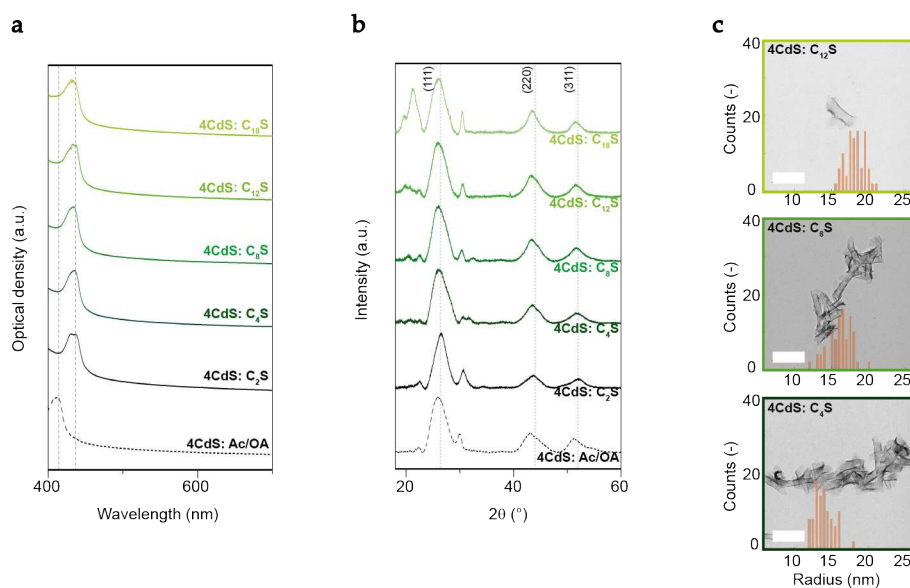


FIGURE C.6: (a) Absorption spectra of 4 MLs CdS nanohelices before and after exchanges of surface ligands, from initially acetates/oleates-capped to linear alkanethiolates-capped, where $n = 2, 4, 8, 12, 18$. Their corresponding X-ray diffractogrammes (resp. TEM images) are shown in (b) (resp. (c)). In contrary to the interplane distances of CdSe respectively associated to the (1 1 1), (2 2 0) and (3 1 1) families that equal 25.5° , 42.2° and 49.9° , the dashed lines in (b) represent those of CdS for which $2\theta = 26.5^\circ$, 44.0° and 52.1° . Scale bar: 200 nm.

4 MLs CdS NPLs	Carboxylates-capped	Thiolates-capped				
	Result (%)	Result for C ₂ S (%)	Result for C ₄ S (%)	Result for C ₈ S (%)	Result for C ₁₂ S (%)	Result for C ₁₈ S (%)
Cd	55.5±1.5	47.5±1.0	46.5±1.0	46.5±1.0	46.0±1.0	46.0±1.0
Se	-	-	-	-	-	-
S	44.5±1.5	52.5±1.0	53.5±1.0	53.5±1.0	54.0±1.0	54.0±1.0

TABLE C.4: Theoretical and experimental atomic ratios of cadmium, selenium and sulfur for carboxylates- and thiolates-capped 4 MLs CdS NPLs.

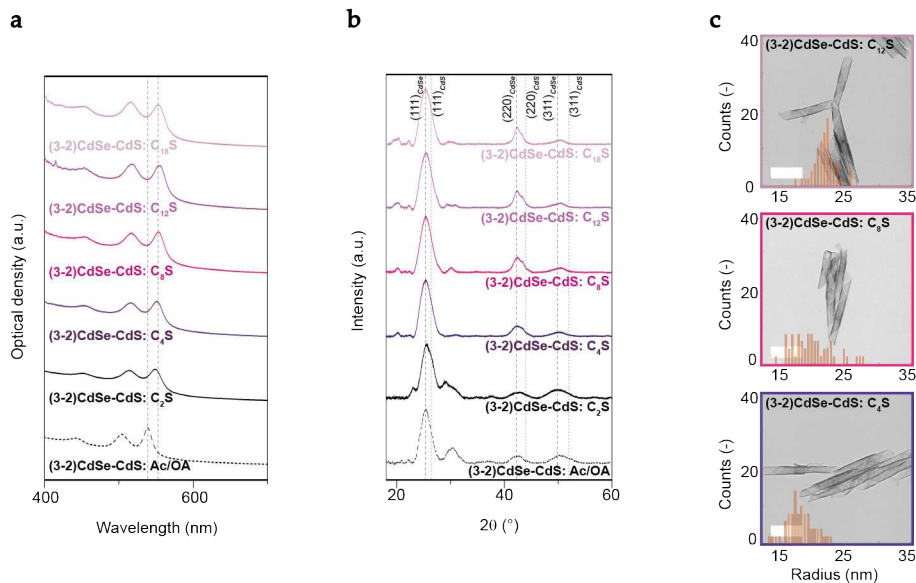


FIGURE C.7: (a) Absorption spectra of (3-2) MLs CdSe-CdS nanohelices before and after exchanges of surface ligands, from initially acetates/oleates-capped to linear alkanethiolates-capped, where $n = 2, 4, 8, 12, 18$. Their corresponding X-ray diffraction diagrams (resp. TEM images) are shown in (b) (resp. (c)). The interplane distances of CdSe (resp. CdS) that are associated to the (1 1 1), (2 2 0) and (3 1 1) families which equal 25.5° , 42.2° and 49.9° (resp. 26.5° , 44.0° and 52.1°), are plotted as dashed (resp. dotted) lines for eye-guides in (b). Scale bar: 200 nm.

(3-2) MLs CdSe- CdS NPLs	Carboxylates-capped		Thiolates-capped			
	Result (%)	Result for C ₂ S (%)	Result for C ₄ S (%)	Result for C ₈ S (%)	Result for C ₁₂ S (%)	Result for C ₁₈ S (%)
Cd	51.5±1.0	48.0±1.0	47.0±1.0	46.0±1.0	46.5±1.0	46.5±1.0
Se	28.5±1.0	21.0±1.0	21.0±1.0	23.0±1.0	21.5±1.0	22.5±1.0
S	20.0±1.0	31.0±1.0	32.0±1.0	31.0±1.0	32.0±1.0	31.0±1.0

TABLE C.5: Theoretical and experimental atomic ratios of cadmium, selenium and sulfur for carboxylates- and thiolates-capped (3-2) MLs CdSe-CdS NPLs.

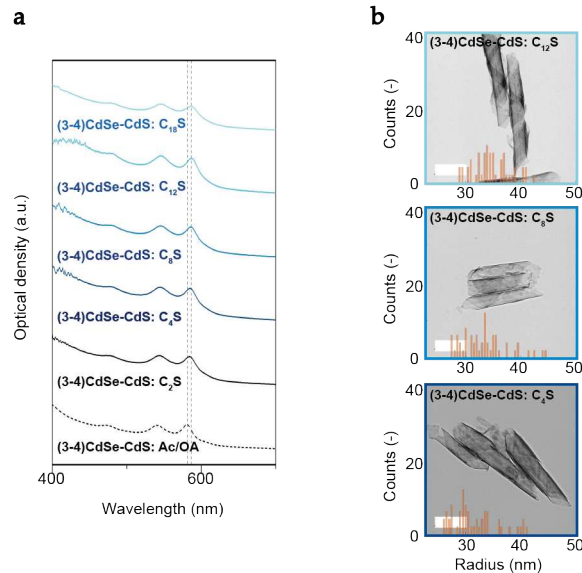


FIGURE C.8: (a) Absorption spectra of (3-4) MLs CdSe-CdS nanohelices before and after exchanges of surface ligands, from initially acetates/oleates-capped to linear alkanethiolates-capped, where $n = 2, 4, 8, 12, 18$. Their corresponding TEM images are shown in (b). Scale bar: 200 nm.

Appendix D

Chiral imprints on nanoplatelets

3 MLs CdSe NPLs	g-factor ($\cdot 10^{-5}$ a.u.)	λ_{CD} (nm)
Squares	+2.2	465
	-1.7	449
Polygons	-0.8	473
	-2.5	456
Twists	-3.5	463
	-4.6	452
Helices	-2.6	469
	-3.7	455

TABLE D.1: CD optical properties for achiral carboxylates-capped 3 MLs CdSe NPLs of various shapes.

4 MLs CdSe NPLs	g-factor ($\cdot 10^{-5}$ a.u.)	λ_{CD} (nm)
Squares	+0.7	517
	-4.1	502
Polygons	+1.6	520
	-4.0	501
Twists	+6.8	524
	0	503
Helices	+11.1	526
	+3.7	506

TABLE D.2: CD optical properties for achiral carboxylates-capped 4 MLs CdSe NPLs of various shapes.

3 MLs CdSe NPLs	g-factor ($\cdot 10^{-4}$ a.u.)	λ_{CD} (nm)
Squares	-0.86	523
	-3.81	492
Polygons	-2.84	500
	-5.19	469
Twists	+0.33	525
	-3.72	466
Helices	-2.09	498
	-4.61	469

TABLE D.3: CD optical properties for *L*-cysteine-capped 3 MLs CdSe NPLs of various shapes.

4 MLs CdSe NPLs	g-factor ($\cdot 10^{-4}$ a.u.)	λ_{CD} (nm)
Squares	-2.07	556
	-8.47	509
Polygons	-5.22	551
	-7.95	521
Twists	-1.61	556
	-7.85	511
Helices	+0.09	555
	-6.43	525

TABLE D.4: CD optical properties for *L*-cysteine-capped 4 MLs CdSe NPLs of various shapes.

3 MLs CdSe NPLs	g-factor ($\cdot 10^{-4}$ a.u.)	λ_{CD} (nm)
Squares	-0.64	506
	-1.01	490
Polygons	+2.16	503
	-0.92	491
Twists	+1.30	516
	+0.27	488
Helices	+0.46	500
	+0.59	488

TABLE D.5: CD optical properties for *L*-dithiothreitol-capped 3 MLs CdSe NPLs of various shapes.

4 MLs CdSe NPLs	g-factor ($\cdot 10^{-4}$ a.u.)	λ_{CD} (nm)
Squares	-1.17	556
	-2.18	537
Polygons	-0.84	556
	-0.93	538
Twists	-1.48	553
	-1.45	536
Helices	+1.20	560
	-0.44	534

TABLE D.6: CD optical properties for *L*-dithiothreitol-capped 4 MLs CdSe NPLs of various shapes.

2 MLs CdSe NPLs	g-factor ($\cdot 10^{-4}$ a.u.)	λ_{CD} (nm)
Small scrolls capped by <i>L</i> (+)-tartaric acid	+6.24	415
	-16.78	387
Small scrolls capped by <i>D</i> (-)-tartaric acid	-7.63	415
	+14.99	386
Large scrolls capped by <i>L</i> (+)-tartaric acid	+18.03	405
	-20.53	378
Large scrolls capped by <i>D</i> (-)-tartaric acid	-9.11	405
	+9.99	378

TABLE D.7: CD optical properties for chiral tartrate-capped 2 MLs CdSe NPLs of various sizes.

3 MLs CdSe NPLs	g-factor ($\cdot 10^{-4}$ a.u.)	λ_{CD} (nm)
	+5.74	478
Twists capped by <i>L</i> (+)-tartaric acid	-15.76	447
	-9.97	479
Twists capped by <i>D</i> (-)-tartaric acid	+16.84	447
	+6.93	474
Helices capped by <i>L</i> (+)-tartaric acid	-10.65	444
	-13.21	473
Helices capped by <i>D</i> (-)-tartaric acid	+12.38	443

TABLE D.8: CD optical properties for chiral tartrate-capped 3 MLs CdSe NPLs of various shapes.

4 MLs CdSe NPLs	g-factor ($\cdot 10^{-4}$ a.u.)	λ_{CD} (nm)
	+2.70	532
Twists capped by <i>L</i> (+)-tartaric acid	-28.69	500
	-9.48	532
Twists capped by <i>D</i> (-)-tartaric acid	+15.27	501
	-0.91	528
Helices capped by <i>L</i> (+)-tartaric acid	-23.46	498
	-7.41	527
Helices capped by <i>D</i> (-)-tartaric acid	+12.21	498

TABLE D.9: CD optical properties for chiral tartrate-capped 4 MLs CdSe NPLs of various shapes.

5 MLs CdSe NPLs	g-factor ($\cdot 10^{-4}$ a.u.)	λ_{CD} (nm)
	-1.94	558
Twists capped by <i>L</i> (+)-tartaric acid	-16.78	530
	-3.20	557
Twists capped by <i>D</i> (-)-tartaric acid	+10.63	529
	+16.08	548
Helices capped by <i>L</i> (+)-tartaric acid	-3.71	513
	-22.90	548
Helices capped by <i>D</i> (-)-tartaric acid	+0.10	513

TABLE D.10: CD optical properties for chiral tartrate-capped 5 MLs CdSe NPLs of various shapes.

2 MLs CdSe NPLs	g-factor ($\cdot 10^{-4}$ a.u.)	λ_{CD} (nm)
	-3.25	412
Small scrolls capped by <i>L</i> (-)-malic acid	+6.78	385
	+1.55	412
Small scrolls capped by <i>D</i> (+)-malic acid	-9.48	386
	-8.54	402
Large scrolls capped by <i>L</i> (-)-malic acid	+7.55	377
	+7.72	402
Large scrolls capped by <i>D</i> (+)-malic acid	-9.31	376

TABLE D.11: CD optical properties for chiral malate-capped 2 MLs CdSe NPLs of various sizes.

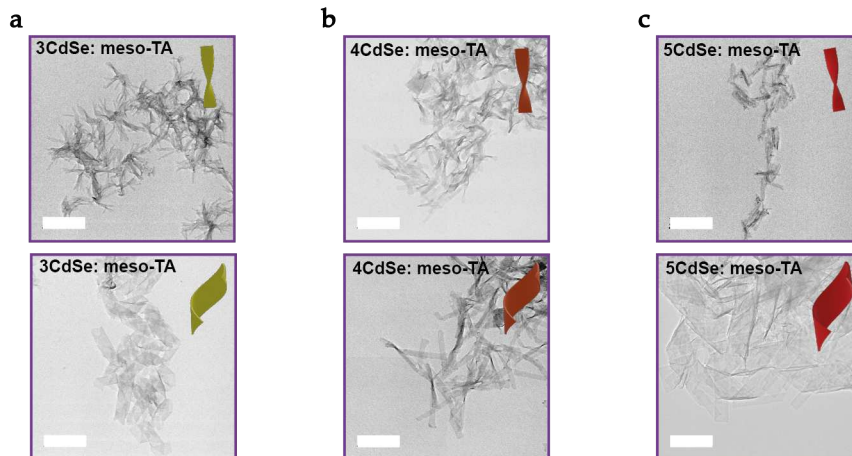


FIGURE D.1: TEM images of two different lateral sizes of 3 (resp. 4 and 5 MLs) CdSe NPLs capped by *meso*-tartaric acid molecules, as displayed in (a) (resp. (b) and (c)). Scale bar: 200 nm.

3 MLs CdSe NPLs	g-factor ($\cdot 10^{-4}$ a.u.)	λ_{CD} (nm)
	-5.20	479
Twists capped by <i>L</i> (-)-malic acid	+12.21	447
	+5.91	479
Twists capped by <i>D</i> (+)-malic acid	-12.01	447
	-8.09	471
Helices capped by <i>L</i> (-)-malic acid	+9.15	444
	+6.59	471
Helices capped by <i>D</i> (+)-malic acid	-9.46	442

TABLE D.12: CD optical properties for chiral malate-capped 3 MLs CdSe NPLs of various shapes.

4 MLs CdSe NPLs	g-factor ($\cdot 10^{-4}$ a.u.)	λ_{CD} (nm)
	-6.90	528
Twists capped by <i>L</i> (-)-malic acid	+10.51	497
	-1.59	529
Twists capped by <i>D</i> (+)-malic acid	-17.47	499
	-6.73	524
Helices capped by <i>L</i> (-)-malic acid	+10.17	496
	-1.59	524
Helices capped by <i>D</i> (+)-malic acid	-15.42	496

TABLE D.13: CD optical properties for chiral malate-capped 4 MLs CdSe NPLs of various shapes.

5 MLs CdSe NPLs	g-factor ($\cdot 10^{-4}$ a.u.)	λ_{CD} (nm)
Twists capped by <i>L</i> (-)-malic acid	-5.99	556
	+1.46	524
Twists capped by <i>D</i> (+)-malic acid	-5.27	557
	-9.38	529
Helices capped by <i>L</i> (-)-malic acid	-7.27	547
	-1.50	499
Helices capped by <i>D</i> (+)-malic acid	+12.31	542
	-2.25	505

TABLE D.14: CD optical properties for chiral malate-capped 5 MLs CdSe NPLs of various shapes.

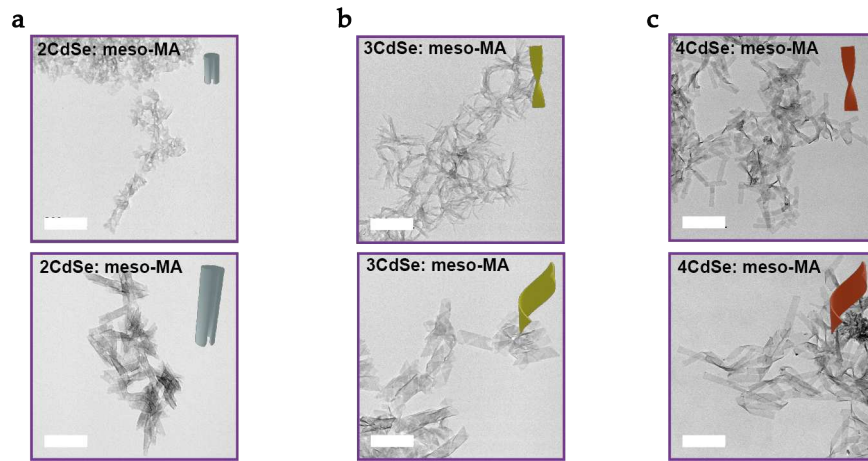


FIGURE D.2: TEM images of two different lateral sizes of 2 (resp. 3 and 4 MLs) CdSe NPLs capped by *meso*-malic acid molecules, as displayed in (a) (resp. (b) and (c)). Scale bar: 200 nm.

3 MLs CdSe NPLs	g-factor ($\cdot 10^{-4}$ a.u.)	λ_{CD} (nm)
Route of chlorides co-stabilized by oleylamine	+3.40	502
	-6.28	474
Route of bromides co-stabilized by oleylamine	-	-
Route of iodides co-stabilized by oleylamine	-	-

TABLE D.15: CD optical properties for (*S*)-(+)-ibuprofen-capped 3 MLs CdSe nanohelices.

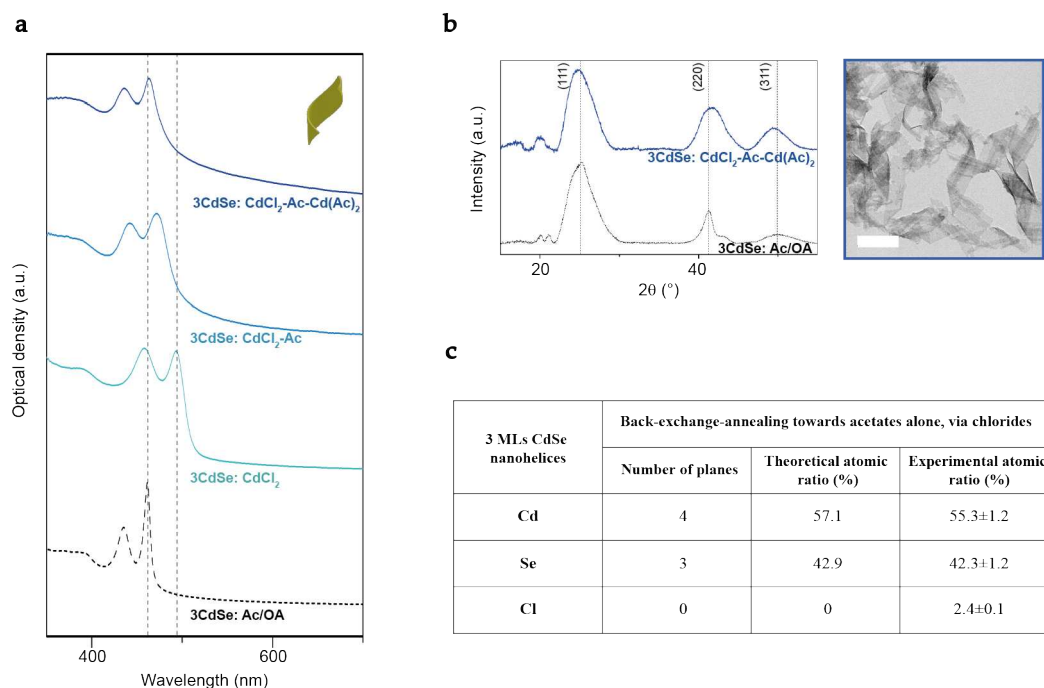


FIGURE D.3: (a) Absorption spectra of subsequent chemically surface-modified 3 MLs CdSe nanohelices. Beginning from a mix of acetates-oleates, these nanoparticles are subjected to ligand exchanges by cadmium chlorides, then acetic acids and finally, an annealing in the presence of cadmium acetates. (b) The X-ray diffractogramme and TEM image of these latter are displayed. Scale bar: 200 nm. (c) Theoretical and experimental atomic ratios of cadmium, selenium and chlorine upon a process of back-exchange-annealing towards acetates alone. It represents a ratio of 8.4 % in terms of chlorides-to-surface cadmiums, left unremoved in the end of the reaction.

4 MLs CdSe NPLs	g-factor ($\cdot 10^{-4}$ a.u.)	λ_{CD} (nm)
Route of chlorides co-stabilized by oleylamine	+1.09	550
	-1.57	519
Route of bromides co-stabilized by oleylamine	-	-
Route of iodides co-stabilized by oleylamine	-	-

TABLE D.16: CD optical properties for (S)-(+)-ibuprofen-capped 4 MLs rectangle-shaped CdSe NPLs.

3 MLs CdSe NPLs	g-factor ($\cdot 10^{-4}$ a.u.)	λ_{CD} (nm)
Squares	+2.48	508
	-2.57	466
Polygons	+2.44	504
	+0.02	470
Twists	+2.27	506
	+0.41	471

TABLE D.17: CD optical properties for (S)-(+)-ibuprofen-capped 3 MLs CdSe NPLs.

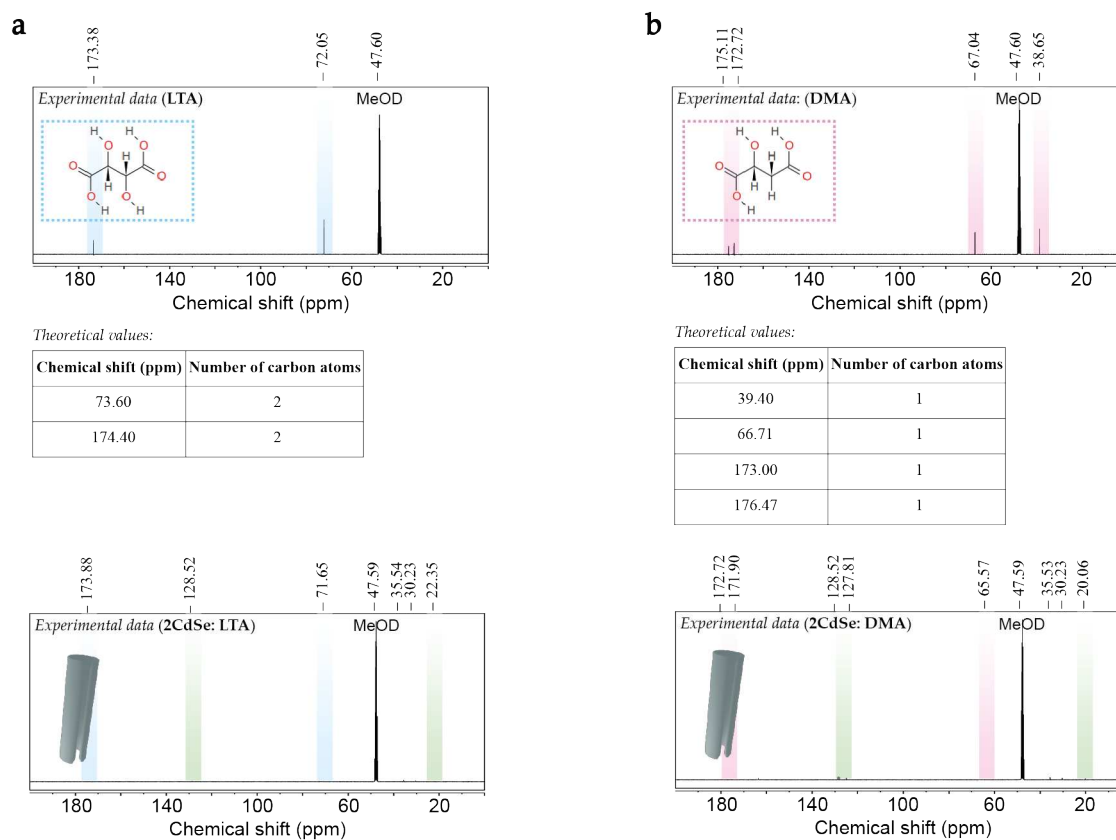


FIGURE D.4: (a) Experimental and theoretical ^{13}C NMR findings of *L*-(+)-tartaric and *D*-(+)-malic acids, where deuterated methanol is used as the solvent. Bottom panel displays the experimental spectra of large 2 MLs CdSe nanoscrolls that have been subjected to these ligand exchanges, with slight traces (color-coded in green) from oleic acid.

4 MLs CdSe NPLs	g -factor ($\cdot 10^{-4}$ a.u.)	λ_{CD} (nm)
Squares	+0.10	549
	-0.14	524
Twists	+0.75	549
	-1.27	516
Helices	+0.94	547
	-0.45	519

TABLE D.18: CD optical properties for (*S*)-(+)-ibuprofen-capped 4 MLs CdSe NPLs.

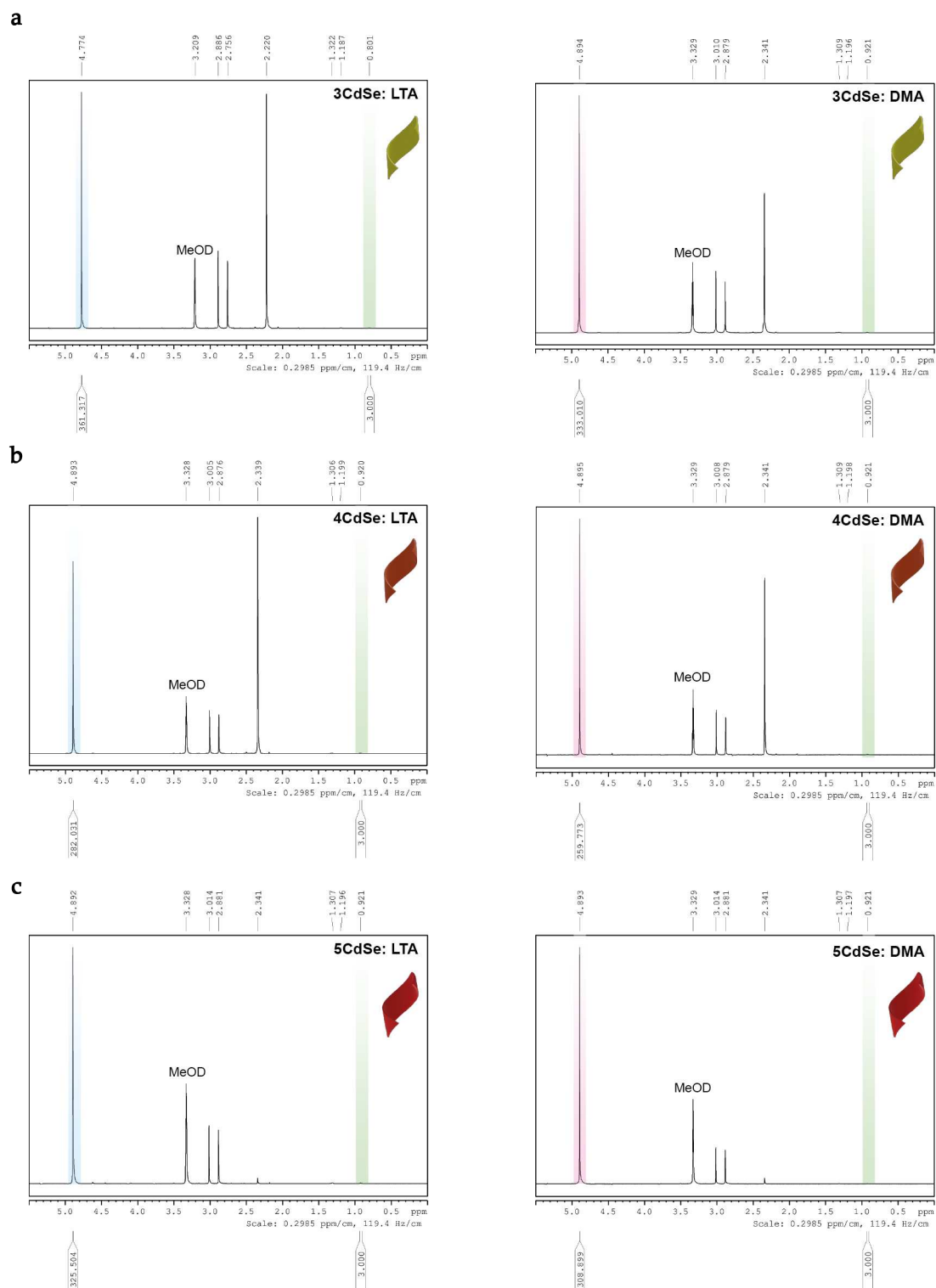


FIGURE D.5: ^1H NMR spectra of *L*-(+)-tartrate (resp. *D*-(+)-malate) functionalization displayed in left (resp. right) panel, for NPLs that are (a) 3, (b) 4 and (c) 5 MLs thick. Highlighted areas in cyan (resp. magenta) correspond to the characteristic resonance of *L*-(+)-tartaric acid (resp. *D*-(+)-malic acid), while the green ones represent the methyl contribution from oleates.

Appendix E

Tribrid silica-based chiral helices

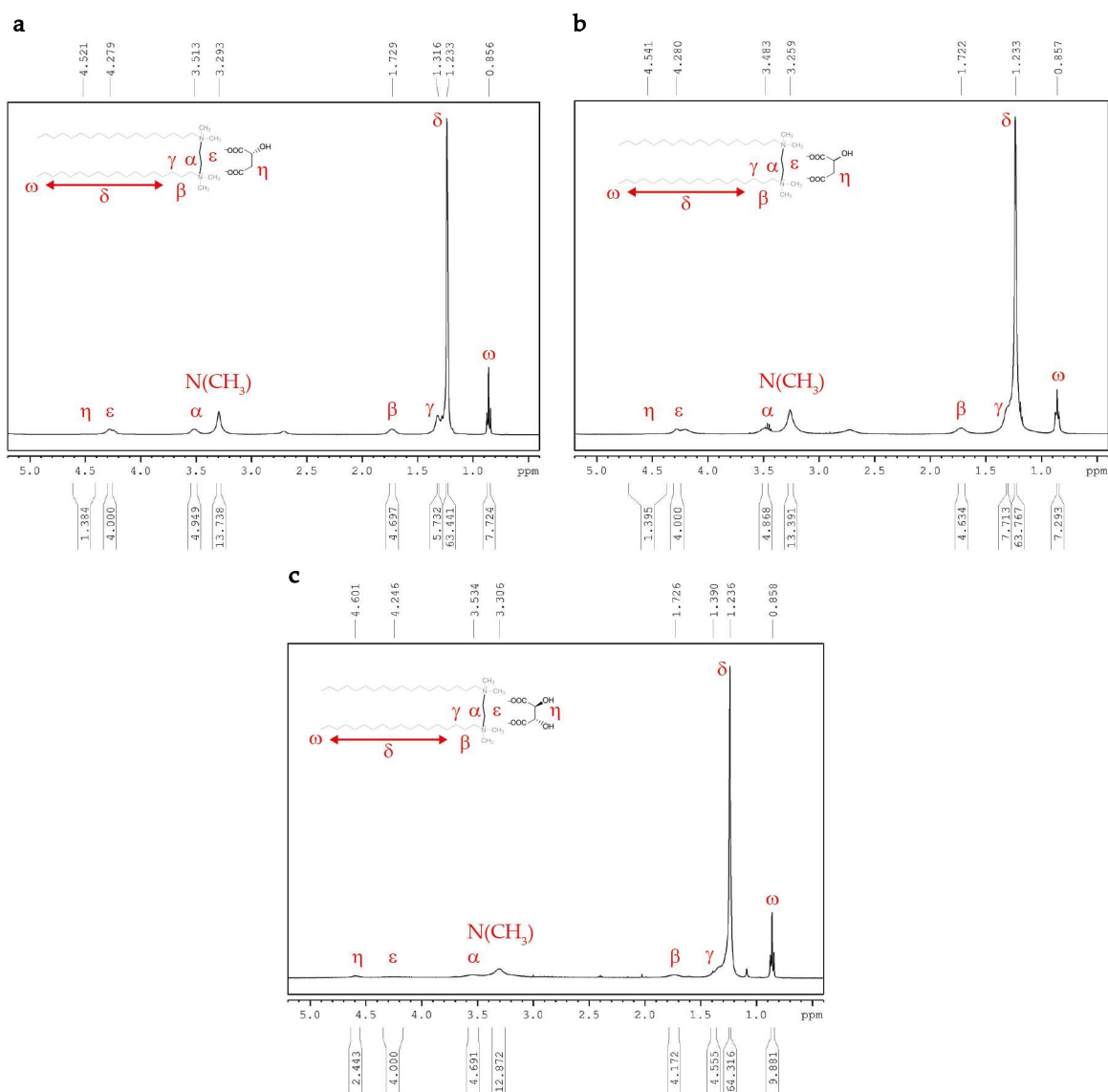


FIGURE E.1: ^1H NMR analysis of (a) the resulted 18-2-18:(D)malate, (b) 18-2-18:(DL)malate and (c) 18-2-18:(D)tartrate after bromide substitutions. Estimated values for the proton assessment: 0.9 ppm (6H, $\text{CH}_3 \times 2$); 1.2 ppm (56H, $(\text{CH}_2)_{14} \times 2$); 1.3 ppm (4H, $\text{CH}_2 \times 2$); 1.7 ppm (4H, $\text{CH}_2 \times 2$); 3.3 ppm (12H, $\text{N}^+(\text{CH}_2)_2 \times 2$); 3.6 ppm (4H, $\text{CH}_2 \times 2$); 4.3 ppm (4H, $\text{N}^+(\text{CH}_2)_2\text{N}^+$); 4.5 ppm (2H, $\text{CH} \times 2$).

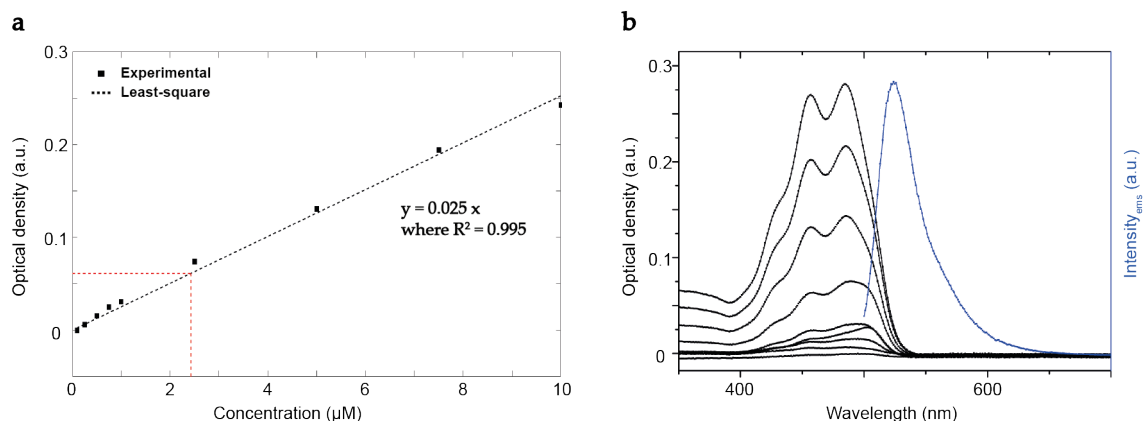


FIGURE E.2: (a) Calibration curve obtained from plotting the absorbance of FITC solutions in ethanol at 490 nm against their molar concentrations, where (b) their optical spectra are shown. Red dotted line represents the optical density of 1 mL purified fluorescently labeled silica helices in ethanol, reported onto the calibration curve. The number of fluorescent molecules grafted in average onto each individual helix (10^{10} per mL of solution) is estimated in the order of 10^8 .

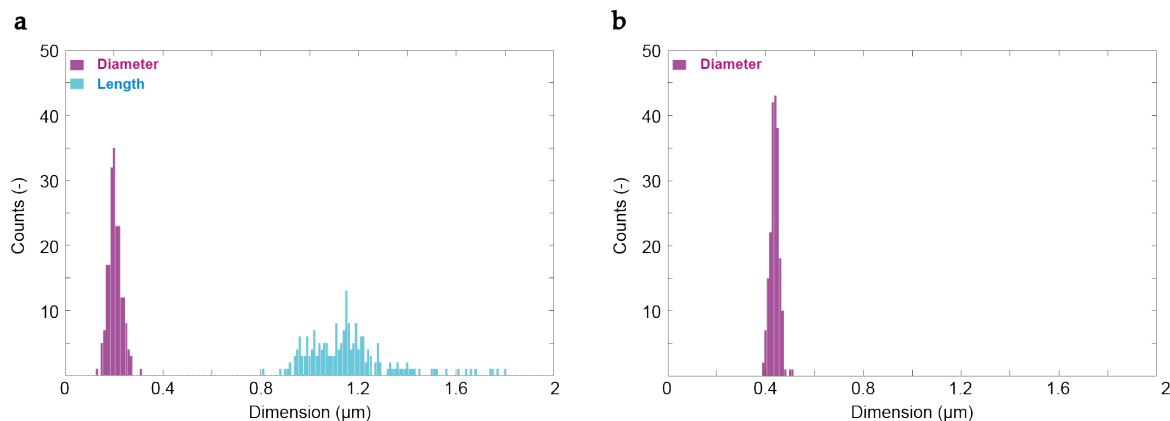


FIGURE E.3: Analysis of SEM images of (a) *18-2-18:(L)malate@FITC* right-handed silica helices and (b) fluorescently labeled silica beads. This shows in the first case, an average value of $(0.204 \pm 0.003) \mu\text{m}$ (resp. $(1.159 \pm 0.020) \mu\text{m}$) in terms of helices' diameter (resp. length) and in the second case, an average value of $(0.438 \pm 0.002) \mu\text{m}$ for the beads' diameter. A total number of 300 particles has been taken into account in both distributions and a two-tails Student-test with a confidence level of 97.5 % has been performed.

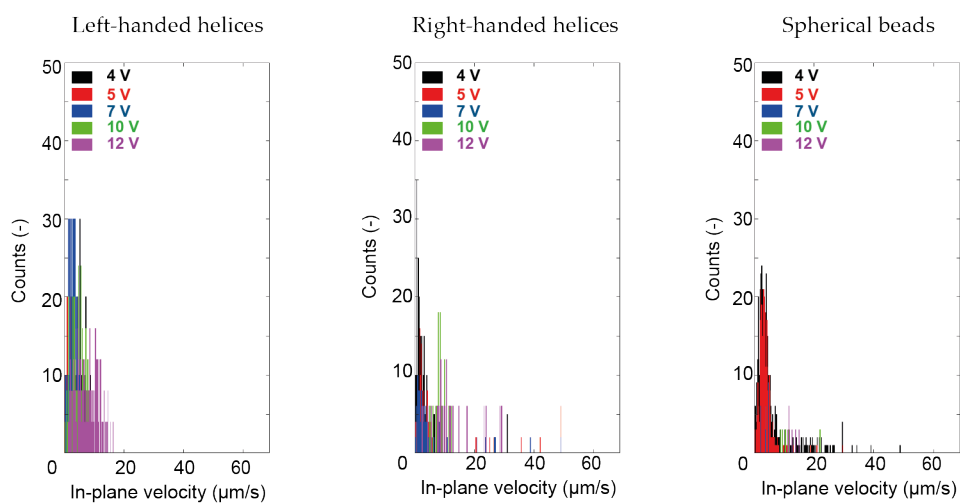


FIGURE E.4: Histogram plots for different tracked objects that are diluted to a factor of 150. Various acoustic amplitudes are applied during experiment, while the intensity of illuminated light at 488 nm is set at 30 % with a frequency of 1.88 MHz. In each case, a total number of more than 50 particles is accounted for. Bin: $0.2 \mu\text{m}\cdot\text{s}^{-1}$.

Bibliography

- [1] Junling Qu et al. "Nanoplatelet-Based Light-Emitting Diode and Its Use in All-Nanocrystal LiFi-like Communication". In: *ACS Applied Materials & Interfaces* 12.19 (2020). PMID: 32292032, pp. 22058–22065. DOI: [10.1021/acsami.0c05264](https://doi.org/10.1021/acsami.0c05264).
- [2] Benjamin T. Diroll. "Colloidal quantum wells for optoelectronic devices". In: *J. Mater. Chem. C* 8 (31 2020), pp. 10628–10640. DOI: [10.1039/D0TC01164A](https://doi.org/10.1039/D0TC01164A).
- [3] Manoj Sharma et al. "Near-Unity Emitting Copper-Doped Colloidal Semiconductor Quantum Wells for Luminescent Solar Concentrators". In: *Advanced Materials* 29.30 (2017), p. 1700821. DOI: [10.1002/adma.201700821](https://doi.org/10.1002/adma.201700821).
- [4] D. L. Dexter, R. S. Knox, and Joseph L. Katz. "Excitons". In: *Physics Today* 18.10 (Oct. 1965), pp. 62–64. DOI: [10.1063/1.3046951](https://doi.org/10.1063/1.3046951).
- [5] Volodya A Harutyunyan. *Effect of Static Electric Fields on The Electronic And Optical Properties of Layered Semiconductor Nanostructures: PART I: "Effect of Static Electric Fields on The Electronic Properties of Layered Semiconductor Nanostructures*. Bentham Science Publishers, 2015.
- [6] A. I. Ekimov and A. A. Onushchenko. "Quantum size effect in three-dimensional microscopic semiconductor crystals". In: *Soviet Journal of Experimental and Theoretical Physics Letters* 34 (Sept. 1981), p. 345.
- [7] Alexander Efros and Al Efros. "Interband Light Absorption in Semiconductor Spheres". In: *Soviet physics. Semiconductors* 16 (July 1982), pp. 772–775.
- [8] C. B. Murray, D. J. Norris, and M. G. Bawendi. "Synthesis and characterization of nearly monodisperse CdE (E = sulfur, selenium, tellurium) semiconductor nanocrystallites". In: *Journal of the American Chemical Society* 115.19 (1993), pp. 8706–8715. DOI: [10.1021/ja00072a025](https://doi.org/10.1021/ja00072a025).
- [9] Xiaogang Peng et al. "Shape control of CdSe nanocrystals". In: *Nature* 404.6773 (2000), pp. 59–61. DOI: [10.1038/35003535](https://doi.org/10.1038/35003535).
- [10] Jin Joo et al. "Low-Temperature Solution-Phase Synthesis of Quantum Well Structured CdSe Nanoribbons". In: *Journal of the American Chemical Society* 128.17 (2006), pp. 5632–5633. DOI: [10.1021/ja0601686](https://doi.org/10.1021/ja0601686).
- [11] Sandrine Ithurria and Benoit Dubertret. "Quasi 2D Colloidal CdSe Platelets with Thicknesses Controlled at the Atomic Level". In: *Journal of the American Chemical Society* 130.49 (2008), pp. 16504–16505. DOI: [10.1021/ja807724e](https://doi.org/10.1021/ja807724e).
- [12] Louis Brus. "Electronic wave functions in semiconductor clusters: experiment and theory". In: *The Journal of Physical Chemistry* 90.12 (1986), pp. 2555–2560. DOI: [10.1021/j100403a003](https://doi.org/10.1021/j100403a003).
- [13] Y. D. Kim et al. "Optical properties of zinc-blende CdSe and Zn_xCd_{1-x}Se films grown on GaAs". In: *Phys. Rev. B* 49 (11 1994), pp. 7262–7270. DOI: [10.1103/PhysRevB.49.7262](https://doi.org/10.1103/PhysRevB.49.7262).
- [14] M.L.H. Green. "A new approach to the formal classification of covalent compounds of the elements". In: *Journal of Organometallic Chemistry* 500.1 (1995), pp. 127–148. DOI: [10.1016/0022-328X\(95\)00508-N](https://doi.org/10.1016/0022-328X(95)00508-N).

- [15] Nicholas C. Anderson et al. "Ligand Exchange and the Stoichiometry of Metal Chalcogenide Nanocrystals: Spectroscopic Observation of Facile Metal-Carboxylate Displacement and Binding". In: *Journal of the American Chemical Society* 135.49 (2013), pp. 18536–18548. DOI: [10.1021/ja4086758](https://doi.org/10.1021/ja4086758).
- [16] Jonathan Owen. "The coordination chemistry of nanocrystal surfaces". In: *Science* 347.6222 (2015), pp. 615–616. DOI: [10.1126/science.1259924](https://doi.org/10.1126/science.1259924).
- [17] Danylo Zherebetsky et al. "Hydroxylation of the surface of PbS nanocrystals passivated with oleic acid". In: *Science* 344.6190 (2014), pp. 1380–1384. DOI: [10.1126/science.1252727](https://doi.org/10.1126/science.1252727).
- [18] Michael A. Boles et al. "The surface science of nanocrystals". In: *Nature Materials* 15.2 (2016), pp. 141–153. DOI: [10.1038/nmat4526](https://doi.org/10.1038/nmat4526).
- [19] Silvia Pedetti et al. "Optimized Synthesis of CdTe Nanoplatelets and Photoresponse of CdTe Nanoplatelets Films". In: *Chemistry of Materials* 25.12 (2013), pp. 2455–2462. DOI: [10.1021/cm4006844](https://doi.org/10.1021/cm4006844).
- [20] Roman B. Vasiliev et al. "Spontaneous Folding of CdTe Nanosheets Induced by Ligand Exchange". In: *Chemistry of Materials* 30.5 (2018), pp. 1710–1717. DOI: [10.1021/acs.chemmater.7b05324](https://doi.org/10.1021/acs.chemmater.7b05324).
- [21] Zheng Li and Xiaogang Peng. "Size/Shape-Controlled Synthesis of Colloidal CdSe Quantum Disks: Ligand and Temperature Effects". In: *Journal of the American Chemical Society* 133.17 (2011), pp. 6578–6586. DOI: [10.1021/ja108145c](https://doi.org/10.1021/ja108145c).
- [22] Dongdong Chen et al. "Structure Identification of Two-Dimensional Colloidal Semiconductor Nanocrystals with Atomic Flat Basal Planes". In: *Nano Letters* 15.7 (2015), pp. 4477–4482. DOI: [10.1021/acs.nanolett.5b00940](https://doi.org/10.1021/acs.nanolett.5b00940).
- [23] A. Antanovich et al. "A strain-induced exciton transition energy shift in CdSe nanoplatelets: the impact of an organic ligand shell". In: *Nanoscale* 9 (45 2017), pp. 18042–18053. DOI: [10.1039/C7NR05065H](https://doi.org/10.1039/C7NR05065H).
- [24] Arin R. Greenwood et al. "Determining the Structure–Property Relationships of Quasi-Two-Dimensional Semiconductor Nanoplatelets". In: *The Journal of Physical Chemistry C* 125.8 (2021), pp. 4820–4827. DOI: [10.1021/acs.jpcc.0c10559](https://doi.org/10.1021/acs.jpcc.0c10559).
- [25] Jörg Rockenberger et al. "The contribution of particle core and surface to strain, disorder and vibrations in thiolcapped CdTe nanocrystals". In: *The Journal of Chemical Physics* 108.18 (May 1998), pp. 7807–7815. DOI: [10.1063/1.476216](https://doi.org/10.1063/1.476216).
- [26] Shahaf Armon et al. "Geometry and Mechanics in the Opening of Chiral Seed Pods". In: *Science* 333.6050 (2011), pp. 1726–1730. DOI: [10.1126/science.1203874](https://doi.org/10.1126/science.1203874).
- [27] Yoel Forterre and Jacques Dumais. "Generating Helices in Nature". In: *Science* 333.6050 (2011), pp. 1715–1716. DOI: [10.1126/science.1210734](https://doi.org/10.1126/science.1210734).
- [28] C.-C. Wang. "On the geometric structures of simple bodies, a mathematical foundation for the theory of continuous distributions of dislocations". In: *Archive for Rational Mechanics and Analysis* 27.1 (1967), pp. 33–94. DOI: [10.1007/BF00276434](https://doi.org/10.1007/BF00276434).
- [29] E. Efrati, E. Sharon, and R. Kupferman. "Elastic theory of unconstrained non-Euclidean plates". In: *Journal of the Mechanics and Physics of Solids* 57.4 (2009), pp. 762–775.
- [30] Mingming Zhang et al. "Shape and fluctuations of frustrated self-assembled nano ribbons". In: *Nature Communications* 10.1 (2019), p. 3565. DOI: [10.1038/s41467-019-11473-6](https://doi.org/10.1038/s41467-019-11473-6).

- [31] Cécile Bouet et al. "Two-Dimensional Growth of CdSe Nanocrystals, from Nanoplatelets to Nanosheets". In: *Chemistry of Materials* 25.4 (2013), pp. 639–645. DOI: [10.1021/cm304080q](https://doi.org/10.1021/cm304080q).
- [32] Eline M. Hutter et al. "Conformal and Atomic Characterization of Ultrathin CdSe Platelets with a Helical Shape". In: *Nano Letters* 14.11 (2014), pp. 6257–6262. DOI: [10.1021/nl5025744](https://doi.org/10.1021/nl5025744).
- [33] M. Volmer and . Weber. "Keimbildung in übersättigten Gebilden". In: *Zeitschrift für Physikalische Chemie* 119U.1 (1926), pp. 277–301. DOI: [doi:10.1515/zpch-1926-11927](https://doi.org/10.1515/zpch-1926-11927).
- [34] Victor K. LaMer and Robert H. Dinegar. "Theory, Production and Mechanism of Formation of Monodispersed Hydrosols". In: *Journal of the American Chemical Society* 72.11 (1950), pp. 4847–4854. DOI: [10.1021/ja01167a001](https://doi.org/10.1021/ja01167a001).
- [35] Josiah Willard Gibbs. "A method of geometrical representation of the thermodynamic properties of substances by means of surfaces". In: vol. 2. Transactions of the Connecticut Academy of Arts and Sciences. 1873, pp. 382–404.
- [36] "Intermolecular and Surface Forces". In: *Intermolecular and Surface Forces (Third Edition)*. Ed. by Jacob N. Israelachvili. Third Edition. Boston: Academic Press, 2011, p. iii. ISBN: 978-0-12-391927-4. DOI: [10.1016/B978-0-12-391927-4.10024-6](https://doi.org/10.1016/B978-0-12-391927-4.10024-6).
- [37] Ronald Reifenberger. *Fundamentals of Atomic Force Microscopy*. WORLD SCIENTIFIC, 2015. DOI: [10.1142/9343](https://doi.org/10.1142/9343).
- [38] S. Ithurria et al. "Colloidal nanoplatelets with two-dimensional electronic structure". In: *Nature Materials* 10.12 (2011), pp. 936–941. DOI: [10.1038/nmat3145](https://doi.org/10.1038/nmat3145).
- [39] Alina Lyashchova et al. "Optical absorption, induced bleaching, and photoluminescence of CdSe nanoplatelets grown in cadmium octanoate matrix". In: *Nanoscale Research Letters* 9.1 (2014), p. 88. DOI: [10.1186/1556-276X-9-88](https://doi.org/10.1186/1556-276X-9-88).
- [40] Andreas Riedinger et al. "An intrinsic growth instability in isotropic materials leads to quasi-two-dimensional nanoplatelets". In: *Nature Materials* 16.7 (2017), pp. 743–748. DOI: [10.1038/nmat4889](https://doi.org/10.1038/nmat4889).
- [41] Ye Jiang et al. "Synthesis of CdSe Nanoplatelets without Short-Chain Ligands: Implication for Their Growth Mechanisms". In: *ACS Omega* 3.6 (2018), pp. 6199–6205. DOI: [10.1021/acsomega.8b01006](https://doi.org/10.1021/acsomega.8b01006).
- [42] Andreas Riedinger et al. "Identifying reactive organo-selenium precursors in the synthesis of CdSe nanoplatelets". In: *Chem. Commun.* 54 (83 2018), pp. 11789–11792. DOI: [10.1039/C8CC06326E](https://doi.org/10.1039/C8CC06326E).
- [43] Yongan Andrew Yang et al. "Synthesis of CdSe and CdTe Nanocrystals without Precursor Injection". In: *Angewandte Chemie International Edition* 44.41 (2005), pp. 6712–6715. DOI: [10.1002/anie.200502279](https://doi.org/10.1002/anie.200502279).
- [44] Nicolo Castro et al. "Insights into the Formation Mechanism of CdSe Nanoplatelets Using in Situ X-ray Scattering". In: *Nano Letters* 19.9 (2019), pp. 6466–6474. DOI: [10.1021/acs.nanolett.9b02687](https://doi.org/10.1021/acs.nanolett.9b02687).
- [45] Michael A. Lovette et al. "Crystal Shape Engineering". In: *Industrial & Engineering Chemistry Research* 47.24 (2008), pp. 9812–9833. DOI: [10.1021/ie800900f](https://doi.org/10.1021/ie800900f).
- [46] R.L. Parker. "Modeling crystal growth rates from solution: by M. Ohara and R.C. Reid (Prentice Hall, New Jersey, 1973) 272 pages, 19.95". In: *Journal of Crystal Growth* 22.4 (1974), pp. 335–338. DOI: [10.1016/0022-0248\(74\)90183-3](https://doi.org/10.1016/0022-0248(74)90183-3).
- [47] Florian D. Ott et al. "Ripening of Semiconductor Nanoplatelets". In: *Nano Letters* 17.11 (2017), pp. 6870–6877. DOI: [10.1021/acs.nanolett.7b03191](https://doi.org/10.1021/acs.nanolett.7b03191).

- [48] Philippe N. Knüsel et al. "Experimental Evidence for Two-Dimensional Ostwald Ripening in Semiconductor Nanoplatelets". In: *Chemistry of Materials* 32.7 (2020), pp. 3312–3319. DOI: [10.1021/acs.chemmater.0c01238](https://doi.org/10.1021/acs.chemmater.0c01238).
- [49] Dongdong Chen et al. "Epitaxial Integration of Multiple CdSe Quantum Dots in a Colloidal CdS Nanoplatelet". In: *Journal of the American Chemical Society* 144.19 (2022), pp. 8444–8448. DOI: [10.1021/jacs.2c01498](https://doi.org/10.1021/jacs.2c01498).
- [50] Yiya Chen et al. "Symmetry-Breaking for Formation of Rectangular CdSe Two-Dimensional Nanocrystals in Zinc-Blende Structure". In: *Journal of the American Chemical Society* 139.29 (2017), pp. 10009–10019. DOI: [10.1021/jacs.7b04855](https://doi.org/10.1021/jacs.7b04855).
- [51] S. Ithurria, G. Bousquet, and B. Dubertret. "Continuous Transition from 3D to 1D Confinement Observed during the Formation of CdSe Nanoplatelets". In: *Journal of the American Chemical Society* 133.9 (2011), pp. 3070–3077. DOI: [10.1021/ja110046d](https://doi.org/10.1021/ja110046d).
- [52] Murat Olutas et al. "Lateral Size-Dependent Spontaneous and Stimulated Emission Properties in Colloidal CdSe Nanoplatelets". In: *ACS Nano* 9.5 (2015), pp. 5041–5050. DOI: [10.1021/acs.nano.5b01927](https://doi.org/10.1021/acs.nano.5b01927).
- [53] Wooje Cho et al. "Direct Synthesis of Six-Monolayer (1.9 nm) Thick Zinc-Blende CdSe Nanoplatelets Emitting at 585 nm". In: *Chemistry of Materials* 30.20 (2018), pp. 6957–6960. DOI: [10.1021/acs.chemmater.8b02489](https://doi.org/10.1021/acs.chemmater.8b02489).
- [54] Nicolas Moghaddam et al. "Surface Modification of CdE (E: S, Se, and Te) Nanoplatelets to Reach Thicker Nanoplatelets and Homostructures with Confinement-Induced Intraparticle Type I Energy Level Alignment". In: *Journal of the American Chemical Society* 143.4 (2021), pp. 1863–1872. DOI: [10.1021/jacs.0c10336](https://doi.org/10.1021/jacs.0c10336).
- [55] Anatol Prudnikau, Andrey Chuvilin, and Mikhail Artemyev. "CdSe–CdS Nanoheteroplatelets with Efficient Photoexcitation of Central CdSe Region through Epitaxially Grown CdS Wings". In: *Journal of the American Chemical Society* 135.39 (2013), pp. 14476–14479. DOI: [10.1021/ja401737z](https://doi.org/10.1021/ja401737z).
- [56] Mickaël D. Tessier et al. "Efficient Exciton Concentrators Built from Colloidal Core/Crown CdSe/CdS Semiconductor Nanoplatelets". In: *Nano Letters* 14.1 (2014), pp. 207–213. DOI: [10.1021/nl403746p](https://doi.org/10.1021/nl403746p).
- [57] Sandrine Ithurria and Dmitri V. Talapin. "Colloidal Atomic Layer Deposition (c-ALD) using Self-Limiting Reactions at Nanocrystal Surface Coupled to Phase Transfer between Polar and Nonpolar Media". In: *Journal of the American Chemical Society* 134.45 (2012), pp. 18585–18590. DOI: [10.1021/ja308088d](https://doi.org/10.1021/ja308088d).
- [58] Benoit Mahler et al. "Core/Shell Colloidal Semiconductor Nanoplatelets". In: *Journal of the American Chemical Society* 134.45 (2012), pp. 18591–18598. DOI: [10.1021/ja307944d](https://doi.org/10.1021/ja307944d).
- [59] Daria A. Kurtina et al. "Atomically Thin Population of Colloidal CdSe Nanoplatelets: Growth of Rolled-up Nanosheets and Strong Circular Dichroism Induced by Ligand Exchange". In: *Chemistry of Materials* 31.23 (2019), pp. 9652–9663. DOI: [10.1021/acs.chemmater.9b02927](https://doi.org/10.1021/acs.chemmater.9b02927).
- [60] Y.F. Nicolau. "Solution deposition of thin solid compound films by a successive ionic-layer adsorption and reaction process". In: *Applications of Surface Science* 22-23 (1985), pp. 1061–1074. DOI: [10.1016/0378-5963\(85\)90241-7](https://doi.org/10.1016/0378-5963(85)90241-7).
- [61] Mika P Valkonen et al. "Growth of ZnS, CdS and multilayer ZnS/CdS thin films by SILAR technique". In: *Applied Surface Science* 115.4 (1997), pp. 386–392. DOI: [10.1016/S0169-4332\(97\)00008-1](https://doi.org/10.1016/S0169-4332(97)00008-1).

- [62] Laura Piveteau et al. "Colloidal-ALD-Grown Core/Shell CdSe/CdS Nanoplatelets as Seen by DNP Enhanced PASS-PIETA NMR Spectroscopy". In: *Nano Letters* 20.5 (2020), pp. 3003–3018. DOI: [10.1021/acs.nanolett.9b04870](https://doi.org/10.1021/acs.nanolett.9b04870).
- [63] Bastiaan B. V. Salzman et al. "From CdSe Nanoplatelets to Quantum Rings by Thermochemical Edge Reconfiguration". In: *Chemistry of Materials* 33.17 (2021), pp. 6853–6859. DOI: [10.1021/acs.chemmater.1c01618](https://doi.org/10.1021/acs.chemmater.1c01618).
- [64] John A. Schellman. "Circular dichroism and optical rotation". In: *Chemical Reviews* 75.3 (1975), pp. 323–331. DOI: [10.1021/cr60295a004](https://doi.org/10.1021/cr60295a004).
- [65] J.D. Jackson. *Classical Electrodynamics*. Wiley, 1962. ISBN: 9780471431312.
- [66] Thomas Martin Lowry. *Optical rotatory power*. Dover publications, 1964.
- [67] Jochen Autschbach. "Computing chiroptical properties with first-principles theoretical methods: Background and illustrative examples". In: *Chirality* 21.1E (2009), E116–E152. DOI: [10.1002/chir.20789](https://doi.org/10.1002/chir.20789).
- [68] A. Rodger and B. Nordén. *Circular Dichroism and Linear Dichroism*. Oxford Classical Monographs. Oxford University Press, 1997. ISBN: 9780198558972.
- [69] Nina Berova, Koji Nakanishi, and Robert Woody. *Circular Dichroism. Principles and Applications 2nd Edition*. Jan. 2000.
- [70] H. G. Kuball. "L. Velluz, M. Legrand and M. Grosjean: Optical Circular Dichroism (Principles, Measurements and Applications). Verlag Chemie GmbH, Weinheim/Bergstr.; Academic Press New York, London 1965. 247 Seiten, 149 Abbildungen, 10 Tabellen. Preis: DM 40,-." In: *Berichte der Bunsengesellschaft für physikalische Chemie* 69.5 (1965), pp. 442–442. DOI: [10.1002/bbpc.19650690516](https://doi.org/10.1002/bbpc.19650690516).
- [71] Bonnie Wallace and Robert Janes. *Modern techniques for circular dichroism and synchrotron radiation circular dichroism spectroscopy: 1*. Jan. 2009.
- [72] Kohsuke Mori, Yuichi Kondo, and Hiromi Yamashita. "Synthesis and characterization of FePd magnetic nanoparticles modified with chiral BINAP ligand as a recoverable catalyst vehicle for the asymmetric coupling reaction". In: *Phys. Chem. Chem. Phys.* 11 (39 2009), pp. 8949–8954. DOI: [10.1039/B910069E](https://doi.org/10.1039/B910069E).
- [73] Jiangfeng Zhou et al. "Negative refractive index due to chirality". In: *Phys. Rev. B* 79 (12 2009), p. 121104. DOI: [10.1103/PhysRevB.79.121104](https://doi.org/10.1103/PhysRevB.79.121104).
- [74] Zhou Xu et al. "Sensitive Detection of Silver Ions Based on Chiroplasmonic Assemblies of Nanoparticles". In: *Advanced Optical Materials* 1 (Sept. 2013). DOI: [10.1002/adom.201300148](https://doi.org/10.1002/adom.201300148).
- [75] Assaf Ben-Moshe, Alexander O. Govorov, and Gil Markovich. "Enantioselective Synthesis of Intrinsically Chiral Mercury Sulfide Nanocrystals". In: *Angewandte Chemie International Edition* 52.4 (2013), pp. 1275–1279. DOI: [10.1002/anie.201207489](https://doi.org/10.1002/anie.201207489).
- [76] Anvar S. Baimuratov et al. "Giant Optical Activity of Quantum Dots, Rods and Disks with Screw Dislocations". In: *Scientific Reports* 5.1 (2015), p. 14712. DOI: [10.1038/srep14712](https://doi.org/10.1038/srep14712).
- [77] Maria V. Mukhina et al. "Intrinsic Chirality of CdSe/ZnS Quantum Dots and Quantum Rods". In: *Nano Letters* 15.5 (2015), pp. 2844–2851. DOI: [10.1021/nl504439w](https://doi.org/10.1021/nl504439w).
- [78] Anvar S. Baimuratov et al. "Dislocation-Induced Chirality of Semiconductor Nanocrystals". In: *Nano Letters* 15.3 (2015), pp. 1710–1715. DOI: [10.1021/nl504369x](https://doi.org/10.1021/nl504369x).
- [79] Assaf Ben-Moshe et al. "Enantioselective control of lattice and shape chirality in inorganic nanostructures using chiral biomolecules". In: *Nature Communications* 5.1 (2014), p. 4302. DOI: [10.1038/ncomms5302](https://doi.org/10.1038/ncomms5302).

- [80] Jihyeon Yeom et al. "Chiral templating of self-assembling nanostructures by circularly polarized light". In: *Nature Materials* 14.1 (2015), pp. 66–72. DOI: [10.1038/nmat4125](https://doi.org/10.1038/nmat4125).
- [81] Wenchun Feng et al. "Assembly of mesoscale helices with near-unity enantiomeric excess and light-matter interactions for chiral semiconductors". In: *Science Advances* 3.3 (2017), e1601159. DOI: [10.1126/sciadv.1601159](https://doi.org/10.1126/sciadv.1601159).
- [82] Bimalendu Adhikari, Jayanta Nanda, and Arindam Banerjee. "Multicomponent hydrogels from enantiomeric amino acid derivatives: Helical nanofibers, handedness and self-sorting". In: *Soft Matter* 7 (Sept. 2011). DOI: [10.1039/C1SM05907F](https://doi.org/10.1039/C1SM05907F).
- [83] Cécile Roche et al. "Homochiral Columns Constructed by Chiral Self-Sorting During Supramolecular Helical Organization of Hat-Shaped Molecules". In: *Journal of the American Chemical Society* 136.19 (2014), pp. 7169–7185. DOI: [10.1021/ja5035107](https://doi.org/10.1021/ja5035107).
- [84] Mícheál P. Moloney, Yurii K. Gun'ko, and John M. Kelly. "Chiral highly luminescent CdS quantum dots". In: *Chem. Commun.* (38 2007), pp. 3900–3902. DOI: [10.1039/B704636G](https://doi.org/10.1039/B704636G).
- [85] Yunlong Zhou et al. "Optical Coupling Between Chiral Biomolecules and Semiconductor Nanoparticles: Size-Dependent Circular Dichroism Absorption". In: *Angewandte Chemie International Edition* 50.48 (2011), pp. 11456–11459. DOI: [10.1002/anie.201103762](https://doi.org/10.1002/anie.201103762).
- [86] Simon D. Elliott, Mícheál P. Moloney, and Yurii K. Gun'ko. "Chiral Shells and Achiral Cores in CdS Quantum Dots". In: *Nano Letters* 8.8 (2008), pp. 2452–2457. DOI: [10.1021/nl801453g](https://doi.org/10.1021/nl801453g).
- [87] Yunlong Zhou et al. "Similar Topological Origin of Chiral Centers in Organic and Nanoscale Inorganic Structures: Effect of Stabilizer Chirality on Optical Isomerism and Growth of CdTe Nanocrystals". In: *Journal of the American Chemical Society* 132.17 (2010), pp. 6006–6013. DOI: [10.1021/ja906894r](https://doi.org/10.1021/ja906894r).
- [88] Urice Tohgha et al. "Ligand Induced Circular Dichroism and Circularly Polarized Luminescence in CdSe Quantum Dots". In: *ACS Nano* 7.12 (2013), pp. 11094–11102. DOI: [10.1021/nn404832f](https://doi.org/10.1021/nn404832f).
- [89] Gaoling Yang, Miri Kazes, and Dan Oron. "Chiral 2D Colloidal Semiconductor Quantum Wells". In: *Advanced Functional Materials* 28.28 (2018), p. 1802012. DOI: [10.1002/adfm.201802012](https://doi.org/10.1002/adfm.201802012).
- [90] Anvar S. Baimuratov et al. "Optical Activity of Chiral Nanoscrolls". In: *Advanced Optical Materials* 5.16 (2017), p. 1600982. DOI: [10.1002/adom.201600982](https://doi.org/10.1002/adom.201600982).
- [91] Nikita V. Tepliakov et al. "Chiral Optical Properties of Tapered Semiconductor Nanoscrolls". In: *ACS Nano* 11.7 (2017), pp. 7508–7515. DOI: [10.1021/acsnano.7b04032](https://doi.org/10.1021/acsnano.7b04032).
- [92] Finn Purcell-Milton et al. "Induction of Chirality in Two-Dimensional Nanomaterials: Chiral 2D MoS₂ Nanostructures". In: *ACS Nano* 12.2 (2018), pp. 954–964. DOI: [10.1021/acsnano.7b06691](https://doi.org/10.1021/acsnano.7b06691).
- [93] Nilashis Nandi and Dieter Vollhardt. "Effect of Molecular Chirality on the Morphology of Biomimetic Langmuir Monolayers". In: *Chemical Reviews* 103.10 (2003), pp. 4033–4076. DOI: [10.1021/cr0006674](https://doi.org/10.1021/cr0006674).
- [94] Yong Wang et al. "Emerging chirality in nanoscience". In: *Chem. Soc. Rev.* 42 (7 2013), pp. 2930–2962. DOI: [10.1039/C2CS35332F](https://doi.org/10.1039/C2CS35332F).
- [95] Wenjing Yan et al. "Self-Assembly of Chiral Nanoparticle Pyramids with Strong R/S Optical Activity". In: *Journal of the American Chemical Society* 134.36 (2012), pp. 15114–15121. DOI: [10.1021/ja3066336](https://doi.org/10.1021/ja3066336).

- [96] Tao Hu et al. "Self-Organization of Plasmonic and Excitonic Nanoparticles into Resonant Chiral Supraparticle Assemblies". In: *Nano Letters* 14.12 (2014), pp. 6799–6810. DOI: [10.1021/nl502237f](https://doi.org/10.1021/nl502237f).
- [97] Peizhao Liu et al. "Chirality Induction to CdSe Nanocrystals Self-Organized on Silica Nanohelices: Tuning Chiroptical Properties". In: *ACS Nano* 15.10 (2021), pp. 16411–16421. DOI: [10.1021/acsnano.1c05819](https://doi.org/10.1021/acsnano.1c05819).
- [98] Yuan Wang et al. "Bamboo-like π -Nanotubes with Tunable Helicity and Circularly Polarized Luminescence". In: *Angewandte Chemie* 133.30 (2021), pp. 16751–16757.
- [99] Sylwia Parzyszek et al. "Tunable Circularly Polarized Luminescence via Chirality Induction and Energy Transfer from Organic Films to Semiconductor Nanocrystals". In: *ACS Nano* 16.11 (2022), pp. 18472–18482. DOI: [10.1021/acsnano.2c06623](https://doi.org/10.1021/acsnano.2c06623).
- [100] Thomas Delclos et al. "Individualized Silica Nanohelices and Nanotubes: Tuning Inorganic Nanostructures Using Lipidic Self-Assemblies". In: *Nano Letters* 8.7 (2008), pp. 1929–1935. DOI: [10.1021/nl080664n](https://doi.org/10.1021/nl080664n).
- [101] Jie Gao et al. "Slow kinetic evolution of nanohelices based on gemini surfactant self-assemblies with various enantiomeric excess; chiral segregation towards a racemic mixture". In: *Mater. Chem. Front.* 5 (7 2021), pp. 3021–3028. DOI: [10.1039/D0QM00989J](https://doi.org/10.1039/D0QM00989J).
- [102] Jiaji Cheng et al. "GoldHelix: Gold Nanoparticles Forming 3D Helical Superstructures with Controlled Morphology and Strong Chiroptical Property". In: *ACS Nano* 11.4 (2017), pp. 3806–3818. DOI: [10.1021/acsnano.6b08723](https://doi.org/10.1021/acsnano.6b08723).
- [103] Jie Gao et al. "Tuning the Chiroptical Properties of Elongated Nano-objects via Hierarchical Organization". In: *ACS Nano* 14.4 (2020), pp. 4111–4121. DOI: [10.1021/acsnano.9b08823](https://doi.org/10.1021/acsnano.9b08823).
- [104] Gerald Gübitz and Martin G. Schmid. "Chiral separation principles in capillary electrophoresis". In: *Journal of Chromatography A* 792.1 (1997), pp. 179–225. DOI: [10.1016/S0021-9673\(97\)00871-6](https://doi.org/10.1016/S0021-9673(97)00871-6).
- [105] Wei Wang et al. "Enantiomeric Separation and Determination of the Enantiomeric Impurity of Armodafinil by Capillary Electrophoresis with Sulfobutyl Ether-cyclodextrin as Chiral Selector". In: *Molecules* 17.1 (2012), pp. 303–314. DOI: [10.3390/molecules17010303](https://doi.org/10.3390/molecules17010303).
- [106] Marina Ciriani, Rudi Oliveira, and Carlos A. M. Afonso. "Semi-continuous and continuous processes for enantiomeric separation". In: *Green Chem.* 24 (11 2022), pp. 4328–4362. DOI: [10.1039/D1GC03668H](https://doi.org/10.1039/D1GC03668H).
- [107] Carina Lee et al. "Chirality in Organic and Mineral Systems: A Review of Reactivity and Alteration Processes Relevant to Prebiotic Chemistry and Life Detection Missions". In: *Symmetry* 14.3 (2022). DOI: [10.3390/sym14030460](https://doi.org/10.3390/sym14030460).
- [108] Thomas M. Hermans et al. "Vortex flows impart chirality-specific lift forces". In: *Nature Communications* 6.1 (2015), p. 5640. DOI: [10.1038/ncomms6640](https://doi.org/10.1038/ncomms6640).
- [109] Sunghan Ro, Juyeon Yi, and Yong Woon Kim. "Chiral Separation by Flows: The Role of Flow Symmetry and Dimensionality". In: *Scientific Reports* 6.1 (2016), p. 35144. DOI: [10.1038/srep35144](https://doi.org/10.1038/srep35144).
- [110] Michal Tencer and Roman Bielski. "Mechanical resolution of chiral objects in achiral media: Where is the size limit?" In: *Chirality* 23.2 (2011), pp. 144–147. DOI: [10.1002/chir.20892](https://doi.org/10.1002/chir.20892).
- [111] Gabriella Cipparrone et al. "Chiral Self-Assembled Solid Microspheres: A Novel Multifunctional Microphotonic Device". In: *Advanced Materials* 23.48 (2011), pp. 5773–5778. DOI: [10.1002/adma.201102828](https://doi.org/10.1002/adma.201102828).

- [112] Georgiy Tkachenko and Etienne Brasselet. "Optofluidic sorting of material chirality by chiral light". In: *Nature Communications* 5.1 (2014), p. 3577. DOI: [10.1038/ncomms4577](https://doi.org/10.1038/ncomms4577).
- [113] Nina Kravets et al. "Optical Enantioseparation of Racemic Emulsions of Chiral Microparticles". In: *Phys. Rev. Appl.* 11 (4 2019), p. 044025. DOI: [10.1103/PhysRevApplied.11.044025](https://doi.org/10.1103/PhysRevApplied.11.044025).
- [114] Ivo Leibacher, Sebastian Schatzer, and Jürg Dual. "Impedance matched channel walls in acoustofluidic systems". In: *Lab Chip* 14 (3 2014), pp. 463–470. DOI: [10.1039/C3LC51109J](https://doi.org/10.1039/C3LC51109J).
- [115] Alexander Garbin et al. "Acoustophoresis of disk-shaped microparticles: A numerical and experimental study of acoustic radiation forces and torques". In: *The Journal of the Acoustical Society of America* 138.5 (Nov. 2015), pp. 2759–2769. DOI: [10.1121/1.4932589](https://doi.org/10.1121/1.4932589).
- [116] Kelley A. Garvin et al. "Spatial patterning of endothelial cells and vascular network formation using ultrasound standing wave fields". In: *The Journal of the Acoustical Society of America* 134.2 (Aug. 2013), pp. 1483–1490. DOI: [10.1121/1.4812867](https://doi.org/10.1121/1.4812867).
- [117] Nathan Jeger-Madiot et al. "Self-organization and culture of Mesenchymal Stem Cell spheroids in acoustic levitation". In: *Scientific Reports* 11.1 (2021), p. 8355. DOI: [10.1038/s41598-021-87459-6](https://doi.org/10.1038/s41598-021-87459-6).
- [118] Jinjie Shi et al. "Continuous particle separation in a microfluidic channel via standing surface acoustic waves (SSAW)". In: *Lab Chip* 9 (23 2009), pp. 3354–3359. DOI: [10.1039/B915113C](https://doi.org/10.1039/B915113C).
- [119] M. Duquenooy et al. In: (Apr. 2012).
- [120] Olivier Dron et al. "ACOUSTIC FOCUSING OF PARTICLES IN A MICROCHANNEL. APPLICATION TO MICRO-PIV". In: Dec. 2008.
- [121] Philip Stephen Williams, Michel Martin, and Mauricio Hoyos. "Acoustophoretic Mobility and Its Role in Optimizing Acoustofluidic Separations". In: *Analytical Chemistry* 89.12 (2017), pp. 6543–6550. DOI: [10.1021/acs.analchem.7b00685](https://doi.org/10.1021/acs.analchem.7b00685).
- [122] John William Strutt Rayleigh. *The theory of sound*. eng. 2d ed., rev. and enl. London: Macmillan, 1894.
- [123] Katuya Yosioka. "Acoustic radiation pressure on a compressible sphere". In: *Acustica* 5 (1955), pp. 167–173.
- [124] Steven M. Woodside, Bruce D. Bowen, and James M. Piret. "Measurement of ultrasonic forces for particle–liquid separations". In: *Aiche Journal* 43 (1997), pp. 1727–1736.
- [125] Toru Tuziuti, Teruyuki Kozuka, and Hideto Mitome. "Measurement of Distribution of Acoustic Radiation Force Perpendicular to Sound Beam Axis". In: *Japanese Journal of Applied Physics* 38.5B (May 1999), p. 3297. DOI: [10.1143/JJAP.38.3297](https://doi.org/10.1143/JJAP.38.3297).
- [126] G. Whitworth, M.A. Grundy, and W.T. Coakley. "Transport and harvesting of suspended particles using modulated ultrasound". In: *Ultrasonics* 29.6 (1991), pp. 439–444. DOI: [10.1016/0041-624X\(91\)90073-H](https://doi.org/10.1016/0041-624X(91)90073-H).
- [127] V. Bjerknes. *Fields of Force: Supplementary Lectures, Applications to Meteorology; ...* Publication of the Ernest Kempton Adams Fund for Physical Research. Columbia University Press, 1906.
- [128] Lawrence A. Crum. "Bjerknes forces on bubbles in a stationary sound field". In: *Journal of the Acoustical Society of America* 57 (1975), pp. 1363–1370.

- [129] Wesley L. Nyborg. *Biophysical Mechanisms of Ultrasound*. Ed. by Michael H. Repacholi and Deirdre A. Benwell. Totowa, NJ: Humana Press, 1982, pp. 35–75. ISBN: 978-1-4612-5805-6. DOI: [10.1007/978-1-4612-5805-6_2](https://doi.org/10.1007/978-1-4612-5805-6_2).
- [130] RE Apfel. “Acoustic radiation pressure-principles and application to separation science”. In: *Proc. of the DAGA conference, 1990*. 1990.
- [131] J. F. Spengler et al. “Observation of yeast cell movement and aggregation in a small-scale MHz-ultrasonic standing wave field”. In: *Bioseparation* 9.6 (2000), pp. 329–341. DOI: [10.1023/A:1011113826753](https://doi.org/10.1023/A:1011113826753).
- [132] S. M. Hagsäter et al. “Acoustic resonances in microfluidic chips: full-image micro-PIV experiments and numerical simulations”. In: *Lab Chip* 7 (10 2007), pp. 1336–1344. DOI: [10.1039/B704864E](https://doi.org/10.1039/B704864E).
- [133] Jeremy J. Hawkes et al. “Continuous cell washing and mixing driven by an ultrasound standing wave within a microfluidic channel”. In: *Lab Chip* 4 (5 2004), pp. 446–452. DOI: [10.1039/B408045A](https://doi.org/10.1039/B408045A).
- [134] Almudena Cabañas Sorando et al. “Patterns of particles aggregation and streaming in resonating fluids”. In: *AIP Conference Proceedings* 1433.1 (May 2012), pp. 757–760. DOI: [10.1063/1.3703291](https://doi.org/10.1063/1.3703291).
- [135] Wei Qiu et al. “Experimental Characterization of Acoustic Streaming in Gradients of Density and Compressibility”. In: *Physical Review Applied* 11.2 (2019). DOI: [10.1103/physrevapplied.11.024018](https://doi.org/10.1103/physrevapplied.11.024018).
- [136] Gabriel Dumy, Mauricio Hoyos, and Jean-Luc Aider. “Observation of selective optical manipulation of particles in acoustic levitation”. In: *The Journal of the Acoustical Society of America* 146.6 (Dec. 2019), pp. 4557–4568. DOI: [10.1121/1.5139640](https://doi.org/10.1121/1.5139640).
- [137] Marcin Kostur et al. “Chiral Separation in Microflows”. In: *Phys. Rev. Lett.* 96 (1 2006), p. 014502. DOI: [10.1103/PhysRevLett.96.014502](https://doi.org/10.1103/PhysRevLett.96.014502).
- [138] Sebastian Meinhardt et al. “Separation of Chiral Particles in Micro- or Nanofluidic Channels”. In: *Phys. Rev. Lett.* 108 (21 2012), p. 214504. DOI: [10.1103/PhysRevLett.108.214504](https://doi.org/10.1103/PhysRevLett.108.214504).
- [139] K. Beleke-Maxwell et al. “Numerical simulation of surface acoustic wave actuated enantiomer separation by the finite element immersed boundary method”. In: *Computers Fluids* 112 (2015), pp. 50–60. DOI: [10.1016/j.compfluid.2015.02.008](https://doi.org/10.1016/j.compfluid.2015.02.008).
- [140] Stefan Burger et al. “Numerical Simulation of Surface Acoustic Wave Actuated Separation of Rigid Enantiomers by the Fictitious Domain Lagrange Multiplier Method”. In: *Computational Methods in Applied Mathematics* 15.3 (2015), pp. 247–258. DOI: [10.1515/cmam-2015-0009](https://doi.org/10.1515/cmam-2015-0009).
- [141] Marcos et al. “Separation of Microscale Chiral Objects by Shear Flow”. In: *Phys. Rev. Lett.* 102 (15 2009), p. 158103. DOI: [10.1103/PhysRevLett.102.158103](https://doi.org/10.1103/PhysRevLett.102.158103).
- [142] Maria Aristov, Ralf Eichhorn, and Clemens Bechinger. “Separation of chiral colloidal particles in a helical flow field”. In: *Soft Matter* 9 (8 2013), pp. 2525–2530. DOI: [10.1039/C2SM27441H](https://doi.org/10.1039/C2SM27441H).
- [143] Freddy T. Rabouw et al. “Temporary Charge Carrier Separation Dominates the Photoluminescence Decay Dynamics of Colloidal CdSe Nanoplatelets”. In: *Nano Letters* 16.3 (2016). PMID: 26863992, pp. 2047–2053. DOI: [10.1021/acs.nanolett.6b00053](https://doi.org/10.1021/acs.nanolett.6b00053).
- [144] Abraham Fahn and Ella Werker. “4 - ANATOMICAL MECHANISMS OF SEED DISPERSAL”. In: *Seed Biology*. Ed. by T.T. KOZLOWSKI. Academic Press, 1972, pp. 151–221. ISBN: 978-0-12-424301-9. DOI: [10.1016/B978-0-12-424301-9.50010-3](https://doi.org/10.1016/B978-0-12-424301-9.50010-3).

- [145] E. Reyssat and L. Mahadevan. "Hygromorphs: from pine cones to biomimetic bilayers". In: *Journal of The Royal Society Interface* 6.39 (2009), pp. 951–957. DOI: [10.1098/rsif.2009.0184](https://doi.org/10.1098/rsif.2009.0184).
- [146] Rivka Elbaum et al. "The Role of Wheat Awns in the Seed Dispersal Unit". In: *Science* 316.5826 (2007), pp. 884–886. DOI: [10.1126/science.1140097](https://doi.org/10.1126/science.1140097).
- [147] Marion Dufour et al. "Halide Ligands To Release Strain in Cadmium Chalcogenide Nanoplatelets and Achieve High Brightness". In: *ACS Nano* 13.5 (2019), pp. 5326–5334. DOI: [10.1021/acsnano.8b09794](https://doi.org/10.1021/acsnano.8b09794).
- [148] Alexander W. Achtstein et al. "Linear Absorption in CdSe Nanoplates: Thickness and Lateral Size Dependency of the Intrinsic Absorption". In: *The Journal of Physical Chemistry C* 119.34 (2015), pp. 20156–20161. DOI: [10.1021/acs.jpcc.5b06208](https://doi.org/10.1021/acs.jpcc.5b06208).
- [149] G.K Sandhu et al. "Molar extinction coefficients of some fatty acids". In: *Radiation Physics and Chemistry* 65.3 (2002), pp. 211–215. DOI: [10.1016/S0969-806X\(02\)00269-4](https://doi.org/10.1016/S0969-806X(02)00269-4).
- [150] Emile Drijvers et al. "Ligand Displacement Exposes Binding Site Heterogeneity on CdSe Nanocrystal Surfaces". In: *Chemistry of Materials* 30.3 (2018), pp. 1178–1186. DOI: [10.1021/acs.chemmater.7b05362](https://doi.org/10.1021/acs.chemmater.7b05362).
- [151] Shalini Singh et al. "Colloidal CdSe Nanoplatelets, A Model for Surface Chemistry/Optoelectronic Property Relations in Semiconductor Nanocrystals". In: *Journal of the American Chemical Society* 140.41 (2018), pp. 13292–13300. DOI: [10.1021/jacs.8b07566](https://doi.org/10.1021/jacs.8b07566).
- [152] Yunhua Chen et al. "Revealing the Surface Structure of CdSe Nanocrystals by Dynamic Nuclear Polarization-Enhanced ⁷⁷Se and ¹¹³Cd Solid-State NMR Spectroscopy". In: *Journal of the American Chemical Society* 143.23 (2021), pp. 8747–8760. DOI: [10.1021/jacs.1c03162](https://doi.org/10.1021/jacs.1c03162).
- [153] Armando Rúa, Félix E. Fernández, and Nelson Sepúlveda. "Bending in VO₂-coated microcantilevers suitable for thermally activated actuators". In: *Journal of Applied Physics* 107.7 (Apr. 2010). DOI: [10.1063/1.3369282](https://doi.org/10.1063/1.3369282).
- [154] Hashem Mazaheri and Amin Khodabandehloo. "Behavior of an FG temperature-responsive hydrogel bilayer: Analytical and numerical approaches". In: *Composite Structures* 301 (2022), p. 116203. DOI: [10.1016/j.compstruct.2022.116203](https://doi.org/10.1016/j.compstruct.2022.116203).
- [155] K.F. Gauss and P. Petic. *General Investigations of Curved Surfaces*. Dover Books on Mathematics. Dover Publications, 2005. ISBN: 9780486446455.
- [156] S. Timoshenko. "Analysis of Bi-Metal Thermostats". In: *J. Opt. Soc. Am.* 11.3 (1925), pp. 233–255. DOI: [10.1364/JOSA.11.000233](https://doi.org/10.1364/JOSA.11.000233).
- [157] Minghuang Huang et al. "Nanomechanical architecture of semiconductor nanomembranes". In: *Nanoscale* 3 (1 2011), pp. 96–120. DOI: [10.1039/C0NR00648C](https://doi.org/10.1039/C0NR00648C).
- [158] W. Rawicz et al. "Effect of Chain Length and Unsaturation on Elasticity of Lipid Bilayers". In: *Biophysical Journal* 79.1 (2000), pp. 328–339. DOI: [10.1016/S0006-3495\(00\)76295-3](https://doi.org/10.1016/S0006-3495(00)76295-3).
- [159] Raj Kumar Gupta et al. "Langmuir–Blodgett films of octadecanethiol – properties and potential applications". In: *Analytica Chimica Acta* 568.1 (2006). Molecular Electronics and Analytical Chemistry, pp. 109–118. DOI: [10.1016/j.aca.2005.10.010](https://doi.org/10.1016/j.aca.2005.10.010).
- [160] E. Prince, ed. *International Tables for Crystallography Volume C: Mathematical, physical and chemical tables*. First Edition. International Union of Crystallography, 2006. ISBN: 978-1-4020-1900-5. DOI: [10.1107/97809553602060000103](https://doi.org/10.1107/97809553602060000103).

- [161] Stephen R. Martin and Maria J. Schilstra. "Circular Dichroism and Its Application to the Study of Biomolecules". In: *Methods in Cell Biology* 84 (2008), pp. 263–293. DOI: [10.1016/S0091-679X\(07\)84010-6](https://doi.org/10.1016/S0091-679X(07)84010-6).
- [162] Zhengtao Li et al. "Reversible Plasmonic Circular Dichroism of Au Nanorod and DNA Assemblies". In: *Journal of the American Chemical Society* 134.7 (2012), pp. 3322–3325. DOI: [10.1021/ja209981n](https://doi.org/10.1021/ja209981n).
- [163] Robert Schreiber et al. "Chiral plasmonic DNA nanostructures with switchable circular dichroism". In: *Nature Communications* 4.1 (2013), p. 2948. DOI: [10.1038/ncomms3948](https://doi.org/10.1038/ncomms3948).
- [164] Antti J. Karttunen et al. "Icosahedral Au₇₂: a predicted chiral and spherically aromatic golden fullerene". In: *Chem. Commun.* (4 2008), pp. 465–467. DOI: [10.1039/B715478J](https://doi.org/10.1039/B715478J).
- [165] Assaf Ben-Moshe et al. "Probing the Interaction of Quantum Dots with Chiral Capping Molecules Using Circular Dichroism Spectroscopy". In: *Nano Letters* 16.12 (2016), pp. 7467–7473. DOI: [10.1021/acs.nanolett.6b03143](https://doi.org/10.1021/acs.nanolett.6b03143).
- [166] Judith F. Specht et al. "Size-dependent exciton substructure in CdSe nanoplatelets and its relation to photoluminescence dynamics". In: *Nanoscale* 11 (25 2019), pp. 12230–12241. DOI: [10.1039/C9NR03161H](https://doi.org/10.1039/C9NR03161H).
- [167] Haoran Zhang et al. "Shape Evolution and Control of Wurtzite CdSe Nanocrystals through a Facile One-Pot Strategy". In: *The Journal of Physical Chemistry C* 125.34 (2021), pp. 18905–18915. DOI: [10.1021/acs.jpcc.1c04643](https://doi.org/10.1021/acs.jpcc.1c04643).
- [168] Yuan Gao and Xiaogang Peng. "Crystal Structure Control of CdSe Nanocrystals in Growth and Nucleation: Dominating Effects of Surface versus Interior Structure". In: *Journal of the American Chemical Society* 136.18 (2014), pp. 6724–6732. DOI: [10.1021/ja5020025](https://doi.org/10.1021/ja5020025).
- [169] Sameer Sapra, Jan Poppe, and Alexander Eychmüller. "CdSe Nanorod Synthesis: A New Approach". In: *Small* 3.11 (2007), pp. 1886–1888. DOI: [10.1002/smll.200700297](https://doi.org/10.1002/smll.200700297).
- [170] Liping Liu et al. "Shape Control of CdSe Nanocrystals with Zinc Blende Structure". In: *Journal of the American Chemical Society* 131.45 (2009), pp. 16423–16429. DOI: [10.1021/ja903633d](https://doi.org/10.1021/ja903633d).
- [171] Tobias Morris and Tykhon Zubkov. "Steric effects of carboxylic capping ligands on the growth of the CdSe quantum dots". In: *Colloids and Surfaces A: Physicochemical and Engineering Aspects* 443 (2014), pp. 439–449. DOI: [10.1016/j.colsurfa.2013.11.046](https://doi.org/10.1016/j.colsurfa.2013.11.046).
- [172] Maya Isarov et al. "Rashba Effect in a Single Colloidal CsPbBr₃ Perovskite Nanocrystal Detected by Magneto-Optical Measurements". In: *Nano Letters* 17.8 (2017), pp. 5020–5026. DOI: [10.1021/acs.nanolett.7b02248](https://doi.org/10.1021/acs.nanolett.7b02248).
- [173] Peter C. Sercel, Zeev Vally Vardeny, and Alexander L. Efros. "Circular dichroism in non-chiral metal halide perovskites". In: *Nanoscale* 12 (35 2020), pp. 18067–18078. DOI: [10.1039/D0NR05232A](https://doi.org/10.1039/D0NR05232A).
- [174] Do-Hoon Kwon, Pingjuan L. Werner, and Douglas H. Werner. "Optical planar chiral metamaterial designs for strong circular dichroism and polarization rotation". In: *Opt. Express* 16.16 (2008), pp. 11802–11807. DOI: [10.1364/OE.16.011802](https://doi.org/10.1364/OE.16.011802).
- [175] Wei Ma et al. "Attomolar DNA detection with chiral nanorod assemblies". In: *Nature Communications* 4.1 (2013), p. 2689. DOI: [10.1038/ncomms3689](https://doi.org/10.1038/ncomms3689).
- [176] Wei Ma et al. "Chiral Inorganic Nanostructures". In: *Chemical Reviews* 117.12 (2017), pp. 8041–8093. DOI: [10.1021/acs.chemrev.6b00755](https://doi.org/10.1021/acs.chemrev.6b00755).

- [177] Shaohua Liu et al. "Synthesis of chiral TiO₂ nanofibre with electron transition-based optical activity". In: *Nature Communications* 3.1 (2012), p. 1215. DOI: [10.1038/ncomms2215](https://doi.org/10.1038/ncomms2215).
- [178] Anastasia Visheratina et al. "Chirality Analysis of Complex Microparticles using Deep Learning on Realistic Sets of Microscopy Images". In: *ACS Nano* 17.8 (2023), pp. 7431–7442. DOI: [10.1021/acsnano.2c12056](https://doi.org/10.1021/acsnano.2c12056).
- [179] Nina Berova, Lorenzo Di Bari, and Gennaro Pescitelli. "Application of electronic circular dichroism in configurational and conformational analysis of organic compounds". In: *Chem. Soc. Rev.* 36 (6 2007), pp. 914–931. DOI: [10.1039/B515476F](https://doi.org/10.1039/B515476F).
- [180] Alexander O. Govorov et al. "Theory of Circular Dichroism of Nanomaterials Comprising Chiral Molecules and Nanocrystals: Plasmon Enhancement, Dipole Interactions, and Dielectric Effects". In: *Nano Letters* 10.4 (2010), pp. 1374–1382. DOI: [10.1021/nl100010v](https://doi.org/10.1021/nl100010v).
- [181] Mayank Puri and Vivian E. Ferry. "Circular Dichroism of CdSe Nanocrystals Bound by Chiral Carboxylic Acids". In: *ACS Nano* 11.12 (2017), pp. 12240–12246. DOI: [10.1021/acsnano.7b05690](https://doi.org/10.1021/acsnano.7b05690).
- [182] Takuya Nakashima, Yuki Kobayashi, and Tsuyoshi Kawai. "Optical Activity and Chiral Memory of Thiol-Capped CdTe Nanocrystals". In: *Journal of the American Chemical Society* 131.30 (2009), pp. 10342–10343. DOI: [10.1021/ja902800f](https://doi.org/10.1021/ja902800f).
- [183] Takuya Kurihara, Yasuto Noda, and K. Takegoshi. "Quantitative Solid-State NMR Study on Ligand–Surface Interaction in Cysteine-Capped CdSe Magic-Sized Clusters". In: *The Journal of Physical Chemistry Letters* 8.12 (2017), pp. 2555–2559. DOI: [10.1021/acs.jpcllett.7b00909](https://doi.org/10.1021/acs.jpcllett.7b00909).
- [184] Takuya Kurihara, Yasuto Noda, and Kiyonori Takegoshi. "Capping Structure of Ligand–Cysteine on CdSe Magic-Sized Clusters". In: *ACS Omega* 4.2 (2019), pp. 3476–3483. DOI: [10.1021/acsomega.8b02752](https://doi.org/10.1021/acsomega.8b02752).
- [185] Takuya Kurihara et al. "Rotational Motion of Ligand-Cysteine on CdSe Magic-Sized Clusters". In: *The Journal of Physical Chemistry C* 123.24 (2019), pp. 14993–14998. DOI: [10.1021/acs.jpcc.9b01181](https://doi.org/10.1021/acs.jpcc.9b01181).
- [186] Vera A. Kuznetsova et al. "Effect of Chiral Ligand Concentration and Binding Mode on Chiroptical Activity of CdSe/CdS Quantum Dots". In: *ACS Nano* 13.11 (2019), pp. 13560–13572. DOI: [10.1021/acsnano.9b07513](https://doi.org/10.1021/acsnano.9b07513).
- [187] Matthew T. Frederick, Victor A. Amin, and Emily A. Weiss. "Optical Properties of Strongly Coupled Quantum Dot–Ligand Systems". In: *The Journal of Physical Chemistry Letters* 4.4 (2013), pp. 634–640. DOI: [10.1021/jz301905n](https://doi.org/10.1021/jz301905n).
- [188] B. Göhler et al. "Spin Selectivity in Electron Transmission Through Self-Assembled Monolayers of Double-Stranded DNA". In: *Science* 331.6019 (2011), pp. 894–897. DOI: [10.1126/science.1199339](https://doi.org/10.1126/science.1199339).
- [189] Yingdan Xu and Wenbo Mi. "Chiral-induced spin selectivity in biomolecules, hybrid organic–inorganic perovskites and inorganic materials: a comprehensive review on recent progress". In: *Mater. Horiz.* (2023), pp. –. DOI: [10.1039/D3MH00024A](https://doi.org/10.1039/D3MH00024A).
- [190] Roald Hoffmann. "A chemical and theoretical way to look at bonding on surfaces". In: *Rev. Mod. Phys.* 60 (3 1988), pp. 601–628. DOI: [10.1103/RevModPhys.60.601](https://doi.org/10.1103/RevModPhys.60.601).
- [191] Matthew T. Frederick and Emily A. Weiss. "Relaxation of Exciton Confinement in CdSe Quantum Dots by Modification with a Conjugated Dithiocarbamate Ligand". In: *ACS Nano* 4.6 (2010), pp. 3195–3200. DOI: [10.1021/nn1007435](https://doi.org/10.1021/nn1007435).

- [192] Matthew T. Frederick et al. "Control of Exciton Confinement in Quantum Dot–Organic Complexes through Energetic Alignment of Interfacial Orbitals". In: *Nano Letters* 13.1 (2013), pp. 287–292. DOI: [10.1021/nl304098e](https://doi.org/10.1021/nl304098e).
- [193] Xiaoqing Gao et al. "Excitonic Circular Dichroism of Chiral Quantum Rods". In: *Journal of the American Chemical Society* 139.25 (2017), pp. 8734–8739. DOI: [10.1021/jacs.7b04224](https://doi.org/10.1021/jacs.7b04224).
- [194] John A. Schellman. "Symmetry Rules for Optical Rotation". In: *The Journal of Chemical Physics* 44.1 (May 1966), pp. 55–63. DOI: [10.1063/1.1726503](https://doi.org/10.1063/1.1726503).
- [195] John A. Schellman. "Symmetry rules for optical rotation". In: *Accounts of Chemical Research* 1.5 (1968), pp. 144–151. DOI: [10.1021/ar50005a003](https://doi.org/10.1021/ar50005a003).
- [196] Jon Applequist. "On the polarizability theory of optical rotation". In: *The Journal of Chemical Physics* (1973). Cited by: 89, 4251 – 4259. DOI: [10.1063/1.1678981](https://doi.org/10.1063/1.1678981).
- [197] Xiao Shao et al. "Chiral 3D CdSe Nanotetrapods". In: *Inorganic Chemistry* 59.19 (2020), pp. 14382–14388. DOI: [10.1021/acs.inorgchem.0c02179](https://doi.org/10.1021/acs.inorgchem.0c02179).
- [198] Brian P. Bloom et al. "Chirality Control of Electron Transfer in Quantum Dot Assemblies". In: *Journal of the American Chemical Society* 139.26 (2017), pp. 9038–9043. DOI: [10.1021/jacs.7b04639](https://doi.org/10.1021/jacs.7b04639).
- [199] Masakazu Matsubara et al. "Polarization-controlled tunable directional spin-driven photocurrents in a magnetic metamaterial with threefold rotational symmetry". In: *Nature Communications* 13.1 (2022), p. 6708. DOI: [10.1038/s41467-022-34374-7](https://doi.org/10.1038/s41467-022-34374-7).
- [200] Jun Zhang et al. "Identification of Facet-Dependent Coordination Structures of Carboxylate Ligands on CdSe Nanocrystals". In: *Journal of the American Chemical Society* 141.39 (2019), pp. 15675–15683. DOI: [10.1021/jacs.9b07836](https://doi.org/10.1021/jacs.9b07836).
- [201] George B. Kauffman. "The Discovery of Optically Active Coordination Compounds: A Milestone in Stereochemistry". In: *Isis* 66.1 (1975), pp. 38–62. (Visited on 06/02/2023).
- [202] Sander F. Wuister, Celso de Mello Donegá, and Andries Meijerink. "Influence of Thiol Capping on the Exciton Luminescence and Decay Kinetics of CdTe and CdSe Quantum Dots". In: *The Journal of Physical Chemistry B* 108.45 (2004), pp. 17393–17397. DOI: [10.1021/jp047078c](https://doi.org/10.1021/jp047078c).
- [203] Assaf Ben Moshe, Daniel Szwarcman, and Gil Markovich. "Size Dependence of Chiroptical Activity in Colloidal Quantum Dots". In: *ACS Nano* 5.11 (2011), pp. 9034–9043. DOI: [10.1021/nm203234b](https://doi.org/10.1021/nm203234b).
- [204] Bernd Fritzing et al. "Utilizing Self-Exchange To Address the Binding of Carboxylic Acid Ligands to CdSe Quantum Dots". In: *Journal of the American Chemical Society* 132.29 (2010), pp. 10195–10201. DOI: [10.1021/ja104351q](https://doi.org/10.1021/ja104351q).
- [205] Kim De Nolf et al. "Binding and Packing in Two-Component Colloidal Quantum Dot Ligand Shells: Linear versus Branched Carboxylates". In: *Journal of the American Chemical Society* 139.9 (2017), pp. 3456–3464. DOI: [10.1021/jacs.6b11328](https://doi.org/10.1021/jacs.6b11328).
- [206] G. B. Deacon and R. J. Phillips. "Relationships between the carbon-oxygen stretching frequencies of carboxylate complexes and the type of carboxylate coordination". English. In: *Coordination Chemistry Reviews* 33.3 (Jan. 1980), pp. 227–250. DOI: [10.1016/S0010-8545\(00\)80455-5](https://doi.org/10.1016/S0010-8545(00)80455-5).
- [207] Ilya V. Yudanov et al. "Size Dependence of the Adsorption Energy of CO on Metal Nanoparticles: A DFT Search for the Minimum Value". In: *Nano Letters* 12.4 (2012), pp. 2134–2139. DOI: [10.1021/nl300515z](https://doi.org/10.1021/nl300515z).

- [208] Matthew Pham and Alex Travesset. "Ligand structure and adsorption free energy of nanocrystals on solid substrates". In: *The Journal of Chemical Physics* 153.20 (Nov. 2020). DOI: [10.1063/5.0030529](https://doi.org/10.1063/5.0030529).
- [209] Shalini Singh et al. "Ligand Adsorption Energy and the Postpurification Surface Chemistry of Colloidal Metal Chalcogenide Nanocrystals". In: *Chemistry of Materials* 33.8 (2021), pp. 2796–2803. DOI: [10.1021/acs.chemmater.0c04761](https://doi.org/10.1021/acs.chemmater.0c04761).
- [210] Yang Zhou, Fudong Wang, and William E. Buhro. "Large Exciton Energy Shifts by Reversible Surface Exchange in 2D II–VI Nanocrystals". In: *Journal of the American Chemical Society* 137.48 (2015), pp. 15198–15208. DOI: [10.1021/jacs.5b09343](https://doi.org/10.1021/jacs.5b09343).
- [211] Haochen Sun and William E. Buhro. "Contrasting Ligand-Exchange Behavior of Wurtzite and Zinc-Blende Cadmium Telluride Nanoplatelets". In: *Chemistry of Materials* 33.5 (2021), pp. 1683–1697. DOI: [10.1021/acs.chemmater.0c04247](https://doi.org/10.1021/acs.chemmater.0c04247).
- [212] A.S. Mestre et al. "Activated carbons for the adsorption of ibuprofen". In: *Carbon* 45.10 (2007), pp. 1979–1988. DOI: [10.1016/j.carbon.2007.06.005](https://doi.org/10.1016/j.carbon.2007.06.005).
- [213] Rebecca Momper et al. "Kinetic Control over Self-Assembly of Semiconductor Nanoplatelets". In: *Nano Letters* 20.6 (2020), pp. 4102–4110. DOI: [10.1021/acs.nanolett.9b05270](https://doi.org/10.1021/acs.nanolett.9b05270).
- [214] Daria A. Kurtina et al. "Induction of Chirality in Atomically Thin ZnSe and CdSe Nanoplatelets: Strengthening of Circular Dichroism via Different Coordination of Cysteine-Based Ligands on an Ultimate Thin Semiconductor Core". In: *Materials* 16.3 (2023). DOI: [10.3390/ma16031073](https://doi.org/10.3390/ma16031073).
- [215] Junjie Hao et al. "Ligand-Induced Chirality in Asymmetric CdSe/CdS Nanostructures: A Close Look at Chiral Tadpoles". In: *ACS Nano* 14.8 (2020), pp. 10346–10358. DOI: [10.1021/acsnano.0c03909](https://doi.org/10.1021/acsnano.0c03909).
- [216] Xiaoqing Gao et al. "Distinct Excitonic Circular Dichroism between Wurtzite and Zincblende CdSe Nanoplatelets". In: *Nano Letters* 18.11 (2018), pp. 6665–6671. DOI: [10.1021/acs.nanolett.8b01001](https://doi.org/10.1021/acs.nanolett.8b01001).
- [217] Urice Tohgha, Krisztina Varga, and Milan Balaz. "Achiral CdSe quantum dots exhibit optical activity in the visible region upon post-synthetic ligand exchange with d- or l-cysteine". In: *Chem. Commun.* 49 (18 2013), pp. 1844–1846. DOI: [10.1039/C3CC37987F](https://doi.org/10.1039/C3CC37987F).
- [218] L. Addadi et al. "A chemical model for the cooperation of sulfates and carboxylates in calcite crystal nucleation: Relevance to biomineralization". In: *Proceedings of the National Academy of Sciences* 84.9 (1987), pp. 2732–2736. DOI: [10.1073/pnas.84.9.2732](https://doi.org/10.1073/pnas.84.9.2732).
- [219] A. Herman, L. Addadi, and S. Weiner. "Interactions of sea-urchin skeleton macromolecules with growing calcite crystals— a study of intracrystalline proteins". In: *Nature* 331.6156 (1988), pp. 546–548. DOI: [10.1038/331546a0](https://doi.org/10.1038/331546a0).
- [220] Stephen Mann et al. "Crystallization at Inorganic-organic Interfaces: Biominerals and Biomimetic Synthesis". In: *Science* 261.5126 (1993), pp. 1286–1292. DOI: [10.1126/science.261.5126.1286](https://doi.org/10.1126/science.261.5126.1286).
- [221] A. M. Belcher et al. "Control of crystal phase switching and orientation by soluble mollusc-shell proteins". In: *Nature* 381.6577 (1996), pp. 56–58. DOI: [10.1038/381056a0](https://doi.org/10.1038/381056a0).
- [222] C. A. Orme et al. "Formation of chiral morphologies through selective binding of amino acids to calcite surface steps". In: *Nature* 411.6839 (2001), pp. 775–779. DOI: [10.1038/35081034](https://doi.org/10.1038/35081034).

- [223] Shunai Che et al. "Synthesis and characterization of chiral mesoporous silica". In: *Nature* 429.6989 (2004), pp. 281–284. DOI: [10.1038/nature02529](https://doi.org/10.1038/nature02529).
- [224] Durga Acharya et al. "Phase Behavior and Effect of Enantiomerism on Potassium N-Dodecanoyl Alaninate/Water/Decanol Systems". In: *Journal of Oleo Science* 52 (July 2003), pp. 407–420. DOI: [10.5650/jos.52.407](https://doi.org/10.5650/jos.52.407).
- [225] R. Oda et al. "Tuning bilayer twist using chiral counterions". In: *Nature* 399.6736 (1999), pp. 566–569. DOI: [10.1038/21154](https://doi.org/10.1038/21154).
- [226] R. Zana and Y. Talmon. "Dependence of aggregate morphology on structure of dimeric surfactants". In: *Nature* 362.6417 (1993), pp. 228–230. DOI: [10.1038/362228a0](https://doi.org/10.1038/362228a0).
- [227] Aurélie Brizard et al. "Counterion, Temperature, and Time Modulation of Nanometric Chiral Ribbons from Gemini-Tartrate Amphiphiles". In: *Journal of the American Chemical Society* 129.12 (2007), pp. 3754–3762. DOI: [10.1021/ja0682172](https://doi.org/10.1021/ja0682172).
- [228] John J. Wendoloski and James B. Matthew. "Molecular dynamics effects on protein electrostatics". In: *Proteins: Structure, Function, and Bioinformatics* 5.4 (1989), pp. 313–321. DOI: [10.1002/prot.340050407](https://doi.org/10.1002/prot.340050407).
- [229] S. Karaborni et al. "Simulating the Self-Assembly of Gemini (Dimeric) Surfactants". In: *Science* 266.5183 (1994), pp. 254–256. DOI: [10.1126/science.266.5183.254](https://doi.org/10.1126/science.266.5183.254).
- [230] Sumeet Jain and Frank S. Bates. "On the Origins of Morphological Complexity in Block Copolymer Surfactants". In: *Science* 300.5618 (2003), pp. 460–464. DOI: [10.1126/science.1082193](https://doi.org/10.1126/science.1082193).
- [231] W.M. Gelbart, A. Ben-Shaul, and D. Roux. *Micelles, Membranes, Microemulsions, and Monolayers*. Partially Ordered Systems. Springer New York, 2012. ISBN: 9781461383895.
- [232] Naoya Ryu et al. "Memorized chiral arrangement of gemini surfactant assemblies in nanometric hybrid organic–silica helices". In: *Chem. Commun.* 52 (34 2016), pp. 5800–5803. DOI: [10.1039/C6CC01219A](https://doi.org/10.1039/C6CC01219A).
- [233] Peizhao Liu et al. "Optically Active Perovskite CsPbBr₃ Nanocrystals Helically Arranged on Inorganic Silica Nanohelices". In: *Nano Letters* 20.12 (2020), pp. 8453–8460. DOI: [10.1021/acs.nanolett.0c02013](https://doi.org/10.1021/acs.nanolett.0c02013).
- [234] Stephan Link and Mostafa A. El-Sayed. "Spectral Properties and Relaxation Dynamics of Surface Plasmon Electronic Oscillations in Gold and Silver Nanodots and Nanorods". In: *The Journal of Physical Chemistry B* 103.40 (1999), pp. 8410–8426. DOI: [10.1021/jp9917648](https://doi.org/10.1021/jp9917648).
- [235] H Rezvani Nikabadi et al. "Gradual growth of gold nanoseeds on silica for SiO₂@gold homogeneous nano core/shell applications by the chemical reduction method". In: *Physica Scripta* 87.2 (2013), p. 025802. DOI: [10.1088/0031-8949/87/02/025802](https://doi.org/10.1088/0031-8949/87/02/025802).
- [236] Pandian Senthil Kumar et al. "High-yield synthesis and optical response of gold nanostars". In: *Nanotechnology* 19.1 (2007), p. 015606. DOI: [10.1088/0957-4484/19/01/015606](https://doi.org/10.1088/0957-4484/19/01/015606).
- [237] Manoj Verma et al. "Differential role of PVP on the synthesis of plasmonic gold nanostructures and their catalytic and SERS properties". In: *RSC Adv.* 6 (83 2016), pp. 80342–80353. DOI: [10.1039/C6RA18345J](https://doi.org/10.1039/C6RA18345J).
- [238] Laura C. Straub, John A. Capobianco, and Mathias S. Wickleder. "Growing Gold Nanostars on SiO₂ Nanoparticles: Easily Accessible, NIR Active Core-dash, Shell Nanostructures from PVP/DMF Reduction". In: *Chemistry* 4.3 (2022), pp. 647–654. DOI: [10.3390/chemistry4030046](https://doi.org/10.3390/chemistry4030046).

- [239] S.F. Wei, J.S. Lian, and Q. Jiang. “Controlling growth of ZnO rods by polyvinylpyrrolidone (PVP) and their optical properties”. In: *Applied Surface Science* 255.15 (2009), pp. 6978–6984. DOI: [10.1016/j.apsusc.2009.03.023](https://doi.org/10.1016/j.apsusc.2009.03.023).
- [240] Brenda L. Sanchez-Gaytan and So-Jung Park. “Spiky Gold Nanoshells”. In: *Langmuir* 26.24 (2010), pp. 19170–19174. DOI: [10.1021/1a1038969](https://doi.org/10.1021/1a1038969).
- [241] Yueming Zhai et al. “Polyvinylpyrrolidone-induced anisotropic growth of gold nanoprisms in plasmon-driven synthesis”. In: *Nature Materials* 15.8 (2016), pp. 889–895. DOI: [10.1038/nmat4683](https://doi.org/10.1038/nmat4683).
- [242] Philippe Gay-Balmaz and Olivier J. F. Martin. “Electromagnetic scattering of high-permittivity particles on a substrate”. In: *Appl. Opt.* 40.25 (2001), pp. 4562–4569. DOI: [10.1364/AO.40.004562](https://doi.org/10.1364/AO.40.004562).
- [243] Patrick C. Chaumet, Adel Rahmani, and Manuel Nieto-Vesperinas. “Optical Trapping and Manipulation of Nano-objects with an Apertureless Probe”. In: *Phys. Rev. Lett.* 88 (12 2002), p. 123601. DOI: [10.1103/PhysRevLett.88.123601](https://doi.org/10.1103/PhysRevLett.88.123601).
- [244] T. Zhang et al. “Full-polarized Tomographic Diffraction Microscopy Achieves a Resolution about One-Fourth of the Wavelength”. In: *Phys. Rev. Lett.* 111 (24 2013), p. 243904. DOI: [10.1103/PhysRevLett.111.243904](https://doi.org/10.1103/PhysRevLett.111.243904).
- [245] Edward M. Purcell and Carlton R. Pennypacker. “Scattering and Absorption of Light by Nonspherical Dielectric Grains”. In: 186 (Dec. 1973), pp. 705–714. DOI: [10.1086/152538](https://doi.org/10.1086/152538).
- [246] Piotr J. Flatau, Graeme L. Stephens, and Bruce T. Draine. “Light scattering by rectangular solids in the discrete-dipole approximation: a new algorithm exploiting the Block-Toeplitz structure”. In: *J. Opt. Soc. Am. A* 7.4 (1990), pp. 593–600. DOI: [10.1364/JOSAA.7.000593](https://doi.org/10.1364/JOSAA.7.000593).
- [247] Bruce T. Draine and Piotr J. Flatau. “Discrete-Dipole Approximation For Scattering Calculations”. In: *J. Opt. Soc. Am. A* 11.4 (1994), pp. 1491–1499. DOI: [10.1364/JOSAA.11.001491](https://doi.org/10.1364/JOSAA.11.001491).
- [248] Marcus Huntemann, Georg Heygster, and Gang Hong. “Discrete dipole approximation simulations on GPUs using OpenCL—Application on cloud ice particles”. In: *Journal of Computational Science* 2.3 (2011). Social Computational Systems, pp. 262–271. DOI: [10.1016/j.jocs.2011.05.011](https://doi.org/10.1016/j.jocs.2011.05.011).
- [249] J. J. Goodman, B. T. Draine, and P. J. Flatau. “Application of fast-Fourier-transform techniques to the discrete-dipole approximation”. In: *Opt. Lett.* 16.15 (1991), pp. 1198–1200. DOI: [10.1364/OL.16.001198](https://doi.org/10.1364/OL.16.001198).
- [250] Dmitry A. Smunev, Patrick C. Chaumet, and Maxim A. Yurkin. “Rectangular dipoles in the discrete dipole approximation”. In: *Journal of Quantitative Spectroscopy and Radiative Transfer* 156 (2015), pp. 67–79. DOI: [10.1016/j.jqsrt.2015.01.019](https://doi.org/10.1016/j.jqsrt.2015.01.019).
- [251] Patrick Christian Chaumet. “The Discrete Dipole Approximation: A Review”. In: *Mathematics* 10.17 (2022). DOI: [10.3390/math10173049](https://doi.org/10.3390/math10173049).
- [252] Tun Cao et al. “Strongly tunable circular dichroism in gammadion chiral phase-change metamaterials”. In: *Opt. Express* 21.23 (2013), pp. 27841–27851. DOI: [10.1364/OE.21.027841](https://doi.org/10.1364/OE.21.027841).
- [253] Anton Kuzyk et al. “DNA-based self-assembly of chiral plasmonic nanostructures with tailored optical response”. In: *Nature* 483.7389 (2012), pp. 311–314. DOI: [10.1038/nature10889](https://doi.org/10.1038/nature10889).

- [254] Assaf Ben-Moshe et al. "Chirality and chiroptical effects in inorganic nanocrystal systems with plasmon and exciton resonances". In: *Chem. Soc. Rev.* 42 (16 2013), pp. 7028–7041. DOI: [10.1039/C3CS60139K](https://doi.org/10.1039/C3CS60139K).
- [255] Kevin Martens et al. "Long- and short-ranged chiral interactions in DNA-assembled plasmonic chains". In: *Nature Communications* 12.1 (2021), p. 2025. DOI: [10.1038/s41467-021-22289-8](https://doi.org/10.1038/s41467-021-22289-8).
- [256] Ralf Eichhorn. "Microfluidic Sorting of Stereoisomers". In: *Phys. Rev. Lett.* 105 (3 2010), p. 034502. DOI: [10.1103/PhysRevLett.105.034502](https://doi.org/10.1103/PhysRevLett.105.034502).
- [257] Debora Schamel et al. "Chiral Colloidal Molecules And Observation of The Propeller Effect". In: *Journal of the American Chemical Society* 135.33 (2013), pp. 12353–12359. DOI: [10.1021/ja405705x](https://doi.org/10.1021/ja405705x).
- [258] Ewald Benes et al. "Ultrasonic separation of suspended particles". In: vol. 1–2. Feb. 2001, 649–659 vol.1. ISBN: 0-7803-7177-1. DOI: [10.1109/ULTSYM.2001.991812](https://doi.org/10.1109/ULTSYM.2001.991812).
- [259] Tobias Lilliehorn et al. "Trapping of microparticles in the near field of an ultrasonic transducer". In: *Ultrasonics* 43 (Apr. 2005), pp. 293–303. DOI: [10.1016/j.ultras.2004.11.001](https://doi.org/10.1016/j.ultras.2004.11.001).
- [260] Salomé Gutiérrez-Ramos, Mauricio Hoyos, and J. C. Ruiz-Suárez. "Induced clustering of *Escherichia coli* by acoustic fields". In: *Scientific Reports* 8.1 (2018), p. 4668. DOI: [10.1038/s41598-018-22960-z](https://doi.org/10.1038/s41598-018-22960-z).
- [261] Nicolas Mordant, Emmanuel Lévêque, and Jean-François Pinton. "Experimental and numerical study of the Lagrangian dynamics of high Reynolds turbulence". In: *New Journal of Physics* 6.1 (2004), p. 116. DOI: [10.1088/1367-2630/6/1/116](https://doi.org/10.1088/1367-2630/6/1/116).
- [262] Nicholas T. Ouellette, Haitao Xu, and Eberhard Bodenschatz. "A quantitative study of three-dimensional Lagrangian particle tracking algorithms". In: *Experiments in Fluids* 40.2 (2006), pp. 301–313. DOI: [10.1007/s00348-005-0068-7](https://doi.org/10.1007/s00348-005-0068-7).
- [263] Federico Toschi and Eberhard Bodenschatz. "Lagrangian Properties of Particles in Turbulence". In: *Annual Review of Fluid Mechanics* 41.1 (2009), pp. 375–404. DOI: [10.1146/annurev.fluid.010908.165210](https://doi.org/10.1146/annurev.fluid.010908.165210).
- [264] Douglas H. Kelley and Nicholas T. Ouellette. "Using particle tracking to measure flow instabilities in an undergraduate laboratory experiment". In: *American Journal of Physics* 79.3 (Mar. 2011), pp. 267–273. DOI: [10.1119/1.3536647](https://doi.org/10.1119/1.3536647).
- [265] Hakan O. Caldag, Alperen Acemoglu, and Serhat Yesilyurt. "Experimental characterization of helical swimming trajectories in circular channels". In: *Microfluidics and Nanofluidics* 21.8 (2017), p. 136. DOI: [10.1007/s10404-017-1973-9](https://doi.org/10.1007/s10404-017-1973-9).
- [266] Masato Makino and Masao Doi. "Migration of twisted ribbon-like particles in simple shear flow". In: *Physics of Fluids* 17.10 (Oct. 2005). DOI: [10.1063/1.2107867](https://doi.org/10.1063/1.2107867).
- [267] L Petitjean et al. "Velocity fields in a collectively migrating epithelium". In: *Biophys J* 98.9 (2010), pp. 1790–1800. DOI: [10.1016/j.bpj.2010.01.030](https://doi.org/10.1016/j.bpj.2010.01.030).
- [268] Thomas E. Angelini et al. "Glass-like dynamics of collective cell migration". In: *Proceedings of the National Academy of Sciences* 108.12 (2011), pp. 4714–4719. DOI: [10.1073/pnas.1010059108](https://doi.org/10.1073/pnas.1010059108).
- [269] Diego Adolfo Santamaría Razo et al. "A version of Stöber synthesis enabling the facile prediction of silica nanospheres size for the fabrication of opal photonic crystals". In: *Journal of Nanoparticle Research* 10.7 (2008), pp. 1225–1229. DOI: [10.1007/s11051-008-9373-4](https://doi.org/10.1007/s11051-008-9373-4).

- [270] Danfeng Cai et al. "Modeling and analysis of collective cell migration in an in vivo three-dimensional environment". In: *Proceedings of the National Academy of Sciences* 113.15 (2016), E2134–E2141. DOI: [10.1073/pnas.1522656113](https://doi.org/10.1073/pnas.1522656113).
- [271] Dominic Arold and Michael Schmiedeberg. "Mean field approach of dynamical pattern formation in underdamped active matter with short-ranged alignment and distant anti-alignment interactions". In: *Journal of Physics: Condensed Matter* 32.31 (2020), p. 315403. DOI: [10.1088/1361-648X/ab849b](https://doi.org/10.1088/1361-648X/ab849b).
- [272] Gabriel Dumy, Mauricio Hoyos, and Jean-Luc Aider. "Influence of the temperature on the opto-acoustophoretic effect". In: *The Journal of the Acoustical Society of America* 149.1 (Jan. 2021), pp. 556–568. DOI: [10.1121/10.0003058](https://doi.org/10.1121/10.0003058).
- [273] Madhavi Krishnan, Victor M. Ugaz, and Mark A. Burns. "PCR in a Rayleigh-Bénard Convection Cell". In: *Science* 298.5594 (2002), pp. 793–793. DOI: [10.1126/science.298.5594.793](https://doi.org/10.1126/science.298.5594.793).
- [274] Radha Muddu, Yassin A. Hassan, and Victor M. Ugaz. "Chaotically Accelerated Polymerase Chain Reaction by Microscale Rayleigh–Bénard Convection". In: *Angewandte Chemie International Edition* 50.13 (2011), pp. 3048–3052. DOI: [10.1002/anie.201004217](https://doi.org/10.1002/anie.201004217).
- [275] Robert A. Houze. "Chapter 2 - Atmospheric Dynamics". In: *Cloud Dynamics*. Ed. by Robert A. Houze. Vol. 104. International Geophysics. Academic Press, 2014, pp. 25–46. DOI: [10.1016/B978-0-12-374266-7.00002-0](https://doi.org/10.1016/B978-0-12-374266-7.00002-0).
- [276] J. Salort et al. "Thermal boundary layer near roughnesses in turbulent Rayleigh–Bénard convection: Flow structure and multistability". In: *Physics of Fluids* 26.1 (Jan. 2014). DOI: [10.1063/1.4862487](https://doi.org/10.1063/1.4862487).
- [277] I. Rodriguez et al. "Fluid dynamics and heat transfer in the wake of a sphere". In: *International Journal of Heat and Fluid Flow* 76 (2019), pp. 141–153. DOI: [10.1016/j.ijheatfluidflow.2019.02.004](https://doi.org/10.1016/j.ijheatfluidflow.2019.02.004).
- [278] Saeed A. Alameri and Ahmed K. Alkaabi. "1 - Fundamentals of nuclear reactors". In: *Nuclear Reactor Technology Development and Utilization*. Ed. by Salah Ud-Din Khan and Alexander Nakhabov. Woodhead Publishing Series in Energy. Woodhead Publishing, 2020, pp. 27–60. ISBN: 978-0-12-818483-7. DOI: [10.1016/B978-0-12-818483-7.00001-9](https://doi.org/10.1016/B978-0-12-818483-7.00001-9).
- [279] M.E.H. Tijani. "Loudspeaker-driven thermo-acoustic refrigeration". PhD thesis. Applied Physics and Science Education, 2001. ISBN: 90-386-1829-8. DOI: [10.6100/IR547542](https://doi.org/10.6100/IR547542).
- [280] Ying Wang and Patricio F. Mendez. "Isotherm penetration depth under a moving Gaussian surface heat source on a thick substrate". In: *International Journal of Thermal Sciences* 172 (2022), p. 107334. DOI: [10.1016/j.ijthermalsci.2021.107334](https://doi.org/10.1016/j.ijthermalsci.2021.107334).
- [281] Taisei Goto et al. "Induction of Strong and Tunable Circularly Polarized Luminescence of Nonchiral, Nonmetal, Low-Molecular-Weight Fluorophores Using Chiral Nanotemplates". In: *Angewandte Chemie International Edition* 56.11 (2017), pp. 2989–2993. DOI: [10.1002/anie.201612331](https://doi.org/10.1002/anie.201612331).
- [282] J. F. Spengler, W. T. Coakley, and K. T. Christensen. "Microstreaming effects on particle concentration in an ultrasonic standing wave". In: *AIChE Journal* 49.11 (2003), pp. 2773–2782. DOI: [10.1002/aic.690491110](https://doi.org/10.1002/aic.690491110).
- [283] Junjun Lei, Peter Glynn-Jones, and Martyn Hill. "Acoustic streaming in the transducer plane in ultrasonic particle manipulation devices". In: *Lab Chip* 13 (11 2013), pp. 2133–2143. DOI: [10.1039/C3LC00010A](https://doi.org/10.1039/C3LC00010A).

- [284] Alessio Di Giacomo et al. "Colloidal Synthesis of Laterally Confined Blue-Emitting 3.5 Monolayer CdSe Nanoplatelets". In: *Chemistry of Materials* 32.21 (2020), pp. 9260–9267. DOI: [10.1021/acs.chemmater.0c03066](https://doi.org/10.1021/acs.chemmater.0c03066).
- [285] Aniket S. Mule et al. "Unraveling the Growth Mechanism of Magic-Sized Semiconductor Nanocrystals". In: *Journal of the American Chemical Society* 143.4 (2021), pp. 2037–2048. DOI: [10.1021/jacs.0c12185](https://doi.org/10.1021/jacs.0c12185).
- [286] Reiko Oda et al. "Gemini surfactants, the effect of hydrophobic chain length and dissymmetry". In: *Chem. Commun.* (21 1997), pp. 2105–2106. DOI: [10.1039/A704069E](https://doi.org/10.1039/A704069E).
- [287] Mahdi Samadi Khoshkhoo et al. "Multicolor Patterning of 2D Semiconductor Nanoplatelets". In: *ACS Nano* 15.11 (2021), pp. 17623–17634. DOI: [10.1021/acsnano.1c05400](https://doi.org/10.1021/acsnano.1c05400).
- [288] L. Bellebon. "Manipulation, caractérisation et reconcentration de cellules par force de radiation acoustique". PhD thesis. Laboratoire de Physique et Mécanique des Milieux Hétérogènes, 2021. URL: <https://www.theses.fr/2021SORUS569>.

RÉSUMÉ

Appartenant aux semi-conducteurs II-VI, les nanoplaquettes de chalcogénure de cadmium présentent des caractéristiques optiques fines dans la région visible. Ces particules peuvent mesurer jusqu'à des centaines de nanomètres en longueur et en largeur, tout en présentant quelques nanomètres le long de leur dimension d'épaisseur sous confinement quantique. Lors de la fonctionnalisation des ligands en surface sur ces nanofeuillets ultrafins, des corps sous contrainte résiduelle sont créés. Cela provient du désaccord entre le réseau cristallin inorganique et la couche d'ancrage des atomes, en plus de la répulsion stérique induite par les chaînes aliphatiques. Ces trois composants agissants sont capturés via une analyse mécanique quantitative pour aboutir à un modèle permettant de prédire l'enroulement des nanoplaquettes. Les rayons résultants des nanohélices peuvent être ajustés en faisant varier linéairement les longueurs de chaîne organique associées, pour une population d'épaisseur donnée de nanoplaquettes. Malgré la contrainte de surface importante induite par les groupes thiolates, le paramètre de maille dans le plan des nanocristaux reste en moyenne égal à celui du zinc blende massif, comme le démontrent des expériences et des simulations par diffraction des rayons X aux grands angles. L'orientation spécifique de ces objets anisotropes et déformés reflète un impact sur la forme et l'intensité de leurs pics correspondants en diffraction.

Les moyens d'obtenir des nanoplaquettes de chalcogénure de cadmium présentant des propriétés chiroptiques en absorption sont abordés. La voie la plus prometteuse consiste à substituer les carboxylates achiraux en surface par des énantiomères chiraux de l'acide tartrique. Les valeurs de dissymétrie semblent augmenter avec le nombre de stéréocentres et présentent des signaux polarisés beaucoup plus forts avec les groupes fonctionnels de carboxylate qu'avec les thiolates. Ces formes de courbe de type absorptif associées à la longueur d'onde de transition excitonique du cœur inorganique, résultent d'un effet d'hybridation entre leur niveau de trous et l'orbital moléculaire des ligands. D'autre part, les hélices de silice chirales décorées d'or, synthétisées à partir de l'auto-assemblage des molécules de tensioactif type gemini, sont également capables de montrer le dichroïsme circulaire dans leur région de résonance plasmonique. Cela augmente avec la force du couplage plasmonique interparticulaire, en accord avec les simulations réalisées selon l'approximation des dipôles discrets. Une ouverture vers le tri des objets chiraux par optoacoustophorèse est documentée. Cette preuve de concept démontre différentes vitesses de migration en moyenne dans le plan entre les énantiomères chiraux séparés, en fonction des conditions de travail acoustiques et optiques. L'effet de la forme et de la concentration des particules en solution montre qu'en cas d'empilement, la compressibilité d'un objet peut conduire à des comportements d'auto-organisation similaires à ceux des matières actives, des bactéries et des cellules.

MOTS CLÉS

semi-conducteur, nanoparticules, chiralité, chimie de surface, mécaniques, acoustiques

ABSTRACT

Belonging to II-VI semiconductors, cadmium chalcogenide nanoplatelets exhibit narrow optical features in the visible region. These particles can measure up to hundreds of nanometers in length and width, while presenting a few nanometers along their quantum confined thickness direction. During surface functionalization of ligands onto these ultrathin nanosheets, residually stressed bodies are created. This originates from the mismatch between the inorganic crystal lattice and layer of anchoring atoms, in addition to the steric repulsion brought by aliphatic chains. These three acting components are captured via a quantitative mechanical analysis to result in a model that allows for the prediction of curling in nanoplatelets. The resulting nanohelices radii are shown to be able to be tuned by linearly varying the associated organic chain lengths, for a given thickness population of nanoplatelets. Despite the important surface stress induced by thiolate headgroups, the average in-plane lattice parameter of these nanocrystals remains equal to that of zinc blende bulk as demonstrated experimentally and theoretically by wide-angle X-ray diffraction. Specific orientation of these anisotropic and distorted objects reflects an impact on the form and intensity of their corresponding scattered peaks.

Ways to obtaining cadmium chalcogenide nanoplatelets that display chiroptical properties in absorption are addressed. The most promising route consists in substituting pristine surface achiral carboxylates by chiral enantiomers of tartaric acid. The dissymmetry values appear to increase with the number of stereocenters and show much stronger polarized signals with carboxylate than thiolate functional groups. These absorptive-like line shapes associated to the excitonic transition wavelength of the inorganic core, result from a hybridization effect between their hole level and the ligands' molecular orbital. On the other hand, gold decorated chiral silica helices, synthesized from the benefit of the gemini surfactant molecules' self-assembly, are also capable of exhibiting circular dichroism in their plasmon resonance region. This increases with the strength of the interparticle plasmonic coupling, in agreement with simulations performed under discrete dipole approximation. An opening towards sorting chiral objects via optoacoustophoresis is documented. This proof-of-concept demonstrates distinct average in-plane migration speeds between separate chiral enantiomers, as a function of the acoustics and optical working conditions. The effect of particles' shape and concentration in solution show that upon jamming, an object's compressibility can lead to self-organizing behaviors similarly to cases of active matters, bacteria and cells.

KEYWORDS

semiconductor, nanoparticles, chirality, surface chemistry, mechanics, acoustics